ELECTRICAL AND STRUCTURAL REMODELLING IN ATRIAL FIBRILLATION: PHENOTYPES FOR PERSONALIZED THERAPY

EDITED BY: Vijay S. Chauhan, Sanjiv M. Narayan and Atul Verma

PUBLISHED IN: Frontiers in Physiology

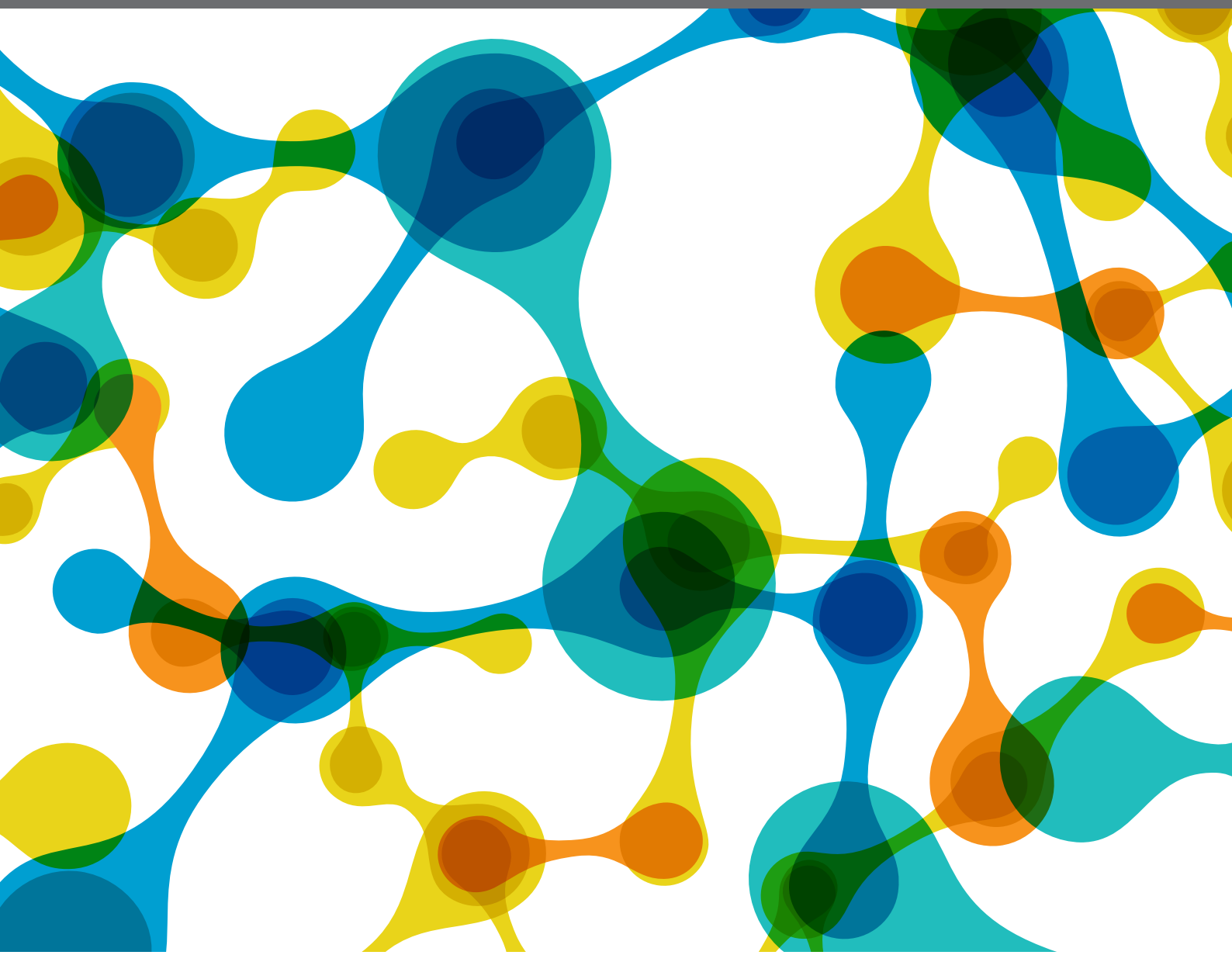

frontiers Research Topics

frontiers

ISSN 1664-8714
ISBN 978-2-88971-082-9
DOI 10.3389/978-2-88971-082-9

About Frontiers

Frontiers is more than just an open-access publisher of scholarly articles: it is a pioneering approach to the world of academia, radically improving the way scholarly research is managed. The grand vision of Frontiers is a world where all people have an equal opportunity to seek, share and generate knowledge. Frontiers provides immediate and permanent online open access to all its publications, but this alone is not enough to realize our grand goals.

Frontiers Journal Series

The Frontiers Journal Series is a multi-tier and interdisciplinary set of open-access, online journals, promising a paradigm shift from the current review, selection and dissemination processes in academic publishing. All Frontiers journals are driven by researchers for researchers; therefore, they constitute a service to the scholarly community. At the same time, the Frontiers Journal Series operates on a revolutionary invention, the tiered publishing system, initially addressing specific communities of scholars, and gradually climbing up to broader public understanding, thus serving the interests of the lay society, too.

Dedication to Quality

Each Frontiers article is a landmark of the highest quality, thanks to genuinely collaborative interactions between authors and review editors, who include some of the world's best academicians. Research must be certified by peers before entering a stream of knowledge that may eventually reach the public - and shape society; therefore, Frontiers only applies the most rigorous and unbiased reviews.
Frontiers revolutionizes research publishing by freely delivering the most outstanding research, evaluated with no bias from both the academic and social point of view. By applying the most advanced information technologies, Frontiers is catapulting scholarly publishing into a new generation.

What are Frontiers Research Topics?

Frontiers Research Topics are very popular trademarks of the Frontiers Journals Series: they are collections of at least ten articles, all centered on a particular subject. With their unique mix of varied contributions from Original Research to Review Articles, Frontiers Research Topics unify the most influential researchers, the latest key findings and historical advances in a hot research area! Find out more on how to host your own Frontiers Research Topic or contribute to one as an author by contacting the Frontiers Editorial Office: frontiersin.org/about/contact

ELECTRICAL AND STRUCTURAL REMODELLING IN ATRIAL FIBRILLATION: PHENOTYPES FOR PERSONALIZED THERAPY

Topic Editors:
Vijay S. Chauhan, Peter Munk Cardiac Centre, Canada
Sanjiv M. Narayan, Stanford University, United States
Atul Verma, University of Toronto, Canada

Citation: Chauhan, V. S., Narayan, S. M., Verma, A., eds. (2021). Electrical and Structural Remodelling in Atrial Fibrillation: Phenotypes for Personalized Therapy. Lausanne: Frontiers Media SA. doi: 10.3389/978-2-88971-082-9

Table of Contents

05 ***Editorial: Electrical and Structural Remodelling in Atrial Fibrillation: Phenotyping for Personalized Therapy***
Vijay S. Chauhan, Atul Verma and Sanjiv M. Narayan

07 ***Toward Mechanism-Directed Electrophenotype-Based Treatments for Atrial Fibrillation***
Fu Siong Ng, Balvinder S. Handa, Xinyang Li and Nicholas S. Peters

14 **In silico** ***Comparison of Left Atrial Ablation Techniques That Target the Anatomical, Structural, and Electrical Substrates of Atrial Fibrillation***
Caroline H. Roney, Marianne L. Beach, Arihant M. Mehta, Iain Sim, Cesare Corrado, Rokas Bendikas, Jose A. Solis-Lemus, Orod Razeghi, John Whitaker, Louisa O'Neill, Gernot Plank, Edward Vigmond, Steven E. Williams, Mark D. O'Neill and Steven A. Niederer

25 ***A Novel Tool for the Identification and Characterization of Repetitive Patterns in High-Density Contact Mapping of Atrial Fibrillation***
Stef Zeemering, Arne van Hunnik, Frank van Rosmalen, Pietro Bonizzi, Billy Scaf, Tammo Delhaas, Sander Verheule and Ulrich Schotten

37 ***Left Atrial Enhancement Correlates With Myocardial Conduction Velocity in Patients With Persistent Atrial Fibrillation***
Rheeda L. Ali, Norman A. Qureshi, Silvia Liverani, Caroline H. Roney, Steven Kim, P. Boon Lim, Jennifer H. Tweedy, Chris D. Cantwell and Nicholas S. Peters

46 ***Linking Electrical Drivers With Atrial Cardiomyopathy for the Targeted Treatment of Atrial Fibrillation***
Gordon Ho, Andrew Y. Lin and David E. Krummen

63 ***Apelin Inhibits Angiotensin II-Induced Atrial Fibrosis and Atrial Fibrillation via TGF-β1/Smad2/α-SMA Pathway***
Wenkui Lv, Ling Zhang, Xinchun Cheng, Hongli Wang, Wen Qin, Xianhui Zhou and Baopeng Tang

73 ***Comparison of Unipolar and Bipolar Voltage Mapping for Localization of Left Atrial Arrhythmogenic Substrate in Patients With Atrial Fibrillation***
Deborah Nairn, Heiko Lehrmann, Björn Müller-Edenborn, Steffen Schuler, Thomas Arentz, Olaf Dössel, Amir Jadidi and Axel Loewe

86 ***Impact of Left Atrial Bipolar Electrogram Voltage on First Pass Pulmonary Vein Isolation During Radiofrequency Catheter Ablation***
Lohit Garg, Naga Venkata K. Pothineni, J. Michael Daw, Matthew C. Hyman, Jeffrey Arkles, Cory M. Tschabrunn, Pasquale Santangeli and Francis E. Marchlinski

93 ***Transcriptomic Bioinformatic Analyses of Atria Uncover Involvement of Pathways Related to Strain and Post-translational Modification of Collagen in Increased Atrial Fibrillation Vulnerability in Intensely Exercised Mice***
Yena Oh, Sibao Yang, Xueyan Liu, Sayantan Jana, Farzad Izaddoustdar, Xiaodong Gao, Ryan Debi, Dae-Kyum Kim, Kyoung-Han Kim, Ping Yang, Zamaneh Kassiri, Robert Lakin and Peter H. Backx

115 ***Non-invasive Spatial Mapping of Frequencies in Atrial Fibrillation: Correlation With Contact Mapping***
Miguel Rodrigo, Kian Waddell, Sarah Magee, Albert J. Rogers, Mahmood Alhusseini, Ismael Hernandez-Romero, Alejandro Costoya-Sánchez, Alejandro Liberos and Sanjiv M. Narayan

frontiers in Physiology

EDITORIAL
published: 27 May 2021
doi: 10.3389/fphys.2021.697536

Editorial: Electrical and Structural Remodelling in Atrial Fibrillation: Phenotyping for Personalized Therapy

Vijay S. Chauhan[1]*, *Atul Verma*[2] and *Sanjiv M. Narayan*[3]

[1] Division of Cardiology, Peter Munk Cardiac Center, University Health Network, Toronto, ON, Canada, [2] Southlake Regional Health Center, Newmarket, ON, Canada, [3] Stanford University, Palo Alto, Stanford, CA, United States

Keywords: atrial fibrillation, structural remodelling, electrical remodelling, fibrotic atrial myopathy, personalized medicine, catheter ablation

Editorial on the Research Topic

Electrical and Structural Remodelling in Atrial Fibrillation: Phenotyping for Personalized Therapy

Atrial fibrillation (AF) is the most prevalent arrhythmia worldwide, afflicting millions of patients (Chugh et al., 2014). Unfortunately, the success of AF therapy remains modest, in part due to the challenges of translating advances in basic science to the bedside. Atrial remodelling is a widely acknowledged process that accelerates the susceptibility to and progression of AF, and comprises electrical and structural components (Nattel et al., 2008). An increasingly recognized structural component is fibrotic atrial myopathy (FAM), which describes interstitial and replacement fibrosis. However, it is unclear which clinical tools best define remodelling, and whether electrical and structural components progress independently or in concert. Delineation of electrical and structural remodelling of the atria may be central to breakthroughs in therapy and the foundation to tailor therapy for personalized medicine.

This Research Topic focuses on original research and reviews on the clinical implications of electrical and structural remodelling in AF. The 10 contributions cover cutting edge and emerging content areas. This includes electrical remodelling, delineated by clinical AF mapping or translational models. Structurally, this includes characterization of abnormalities including FAM. These contributions provide a foundation for personalized therapy of AF. In this editorial, each contribution is summarized along with its physiologic and clinical implications.

The importance of local atrial electrogram features to delineate FAM and its effect on pulmonary vein isolation (PVI) was investigated by Garg et al. In 20 patients with paroxysmal AF undergoing PVI, left atrial bipolar voltage mapping during sinus rhythm revealed lower global voltage and lower local voltage in those who failed to achieve first pass PVI. Their findings suggest that more global and segmental fibrosis may reduce the success of PVI with radiofrequency energy. Nairn et al. also performed high-resolution left atrial voltage mapping in 28 patients before AF catheter ablation. Bipolar and unipolar voltages were compared and were found to highly correlate both in sinus rhythm and AF. A unipolar voltage threshold was computed based on a linear transformation of bipolar voltage that provided high spatial concordance. The authors report that reduced bipolar inter-electrode distance from 6 to 2 mm did not significantly increase the correlation between mapped areas of low voltage compared to unipolar recordings, and suggested that spatial resolution may not be a clinically significant confounder of mapping low voltage aspects of FAM when using contemporary tools. In eight patients with persistent AF, Ali et al. evaluated left atrial FAM using late gadolinium enhanced magnetic resonance imaging (LGE MRI) and local conduction velocities as defined by bipolar activation mapping in

OPEN ACCESS

Edited and reviewed by:
Ruben Coronel,
University of Amsterdam, Netherlands

***Correspondence:**
Vijay S. Chauhan
vijay.chauhan@uhn.ca

Specialty section:
This article was submitted to Cardiac Electrophysiology, a section of the journal Frontiers in Physiology

Received: *19 April 2021*
Accepted: *26 April 2021*
Published: *27 May 2021*

Citation:
Chauhan VS, Verma A and Narayan SM (2021) Editorial: Electrical and Structural Remodelling in Atrial Fibrillation: Phenotyping for Personalized Therapy. Front. Physiol. 12:697536. doi: 10.3389/fphys.2021.697536

sinus rhythm. They found that LGE MRI signal intensity correlated with colocalized conduction velocity, but only at spatial scaling of a mapping catheter electrode. This finding extends work by Caixal et al. (2021) who recently showed that LGE MRI signal intensity correlated with atrial conduction velocity in sinus rhythm unless the atrium was markedly dilated. These studies suggest that LGE MRI may provide functional assessment of FAM in terms of conduction slowing and predisposition to reentry. Roney et al. constructed 50 AF patient-specific left atrial bi-layer models incorporating FAM based on their LGE MRIs and simulated AF in order to determine the location of electrical drivers. Several different ablation approaches were tested, including PVI, linear ablations, FAM ablation, driver ablation, or a combination thereof to determine the optimal approach to terminate AF or convert AF to an atrial tachycardia. The study demonstrated the need for a patient-specific ablation strategy based on their FAM and driver distribution.

The mechanisms of conditional AF structural modelling were further explored in two mechanistic studies. In a mouse model of exercise-induced AF, Oh et al. used transcriptomic bioinformatic analysis of atria to investigate novel collagen pathways that increase AF vulnerability. During 6 weeks of exercise, there was differential regulation of atrial genes linked to mechanosensing, extracellular matrix and tumor necrosis factor pathways, which was 2-fold higher than in the ventricles. Transcriptomics were temporally dynamic and related to increased preload and atrial stretch seen with exercise. Tang et al. also studied molecular modulation of structural remodelling, in particular the regulation of angiotensin 2-induced atrial fibrosis. In rats treated for 2-weeks with apelin, an inhibitor of fibrosis, there was a decrease in angiotensin 2-induced atrial fibrosis and AF inducibility with programmed stimulation. The protective effects of apelin were mediated by suppression of Smad2-dependent fibrosis, which may provide an effective up-stream therapy for atrial fibrosis and AF.

With respect to characterizing electrical modelling, Rodrigo et al. evaluated regional differences in activation rates during AF using non-invasive electrocardiographic imaging (ECGI) and contact mapping. ECGI provided a moderate estimation of intracardiac recording-based activation rates in AF after filtering by high spectral organization. The ECGI-derived highest dominant frequency predicted acute AF ablation success suggesting that this approach may provide an effective tool to identify patient responders for personalized ablation therapy. The importance of discerning repetitive AF propagation as putative targets for catheter ablation was also studied by Zeemering et al. These AF patterns were automatically identified from high-density-electrode array recordings in goat model of AF using a novel computational tool based on recurrence plots. Activation breakthrough and reentry were seen as repetitive conduction patterns which became shorter with more prolonged AF duration. Using this methodology with high-resolution clinical mapping catheters may delineate putative targets for AF catheter ablation.

The final two contributions by Ho et al. and Ng et al. provide a comprehensive review of electrophenotyping to improve our understanding of patient-specific AF mechanisms than may guide personalized therapy. This is necessary because AF mechanisms and propagation is dependent on the extent of structural and electrical remodelling, which can vary even among patients with comparable AF risk factors, AF duration, and cardiovascular disease.

In summary, improved therapy for AF is likely to require better delineation of FAM in individual patients, both in its structural and electrical components. Structural FAM is now widely appreciated, yet it is undefined whether to identify this by non-invasive imaging, by voltage mapping or via its functional effects such as conduction slowing. It is equally undefined how to treat structural FAM. Electrically, it is critical to delineate how FAM leads to functional arrhythmias. Identification of patient-specific AF triggers or AF sustaining substrates, such as localized drivers, is limited by the spatial resolution of clinical tools and lack of accepted gold standards for validation. Electrophenotyping of patients with AF may enable us to identify those in whom therapy should target FAM, and those in whom FAM and AF may progress and who may instead benefit from more general strategies. The 10 articles in this Research Topic add to our understanding of FAM, and provide exciting areas for further investigation. We congratulate the authors.

AUTHOR CONTRIBUTIONS

All authors contributed to content and critical review of this editorial.

REFERENCES

Caixal, G., Alarcon, F., Althoff, T., Nunez-Garcia, M., Benito, E., Borras, R., et al. (2021). Accuracy of left atrial fibrosis detection with cardiac magnetic resonance: correlation of late gadolinium enhancement with endocardial voltage and conduction velocity. *Europace* 23, 380–388. doi: 10.1093/europace/euaa313

Chugh, S., Havmoeller, R., Narayanan, K., Singh, D., Rienstra, M., Benjamin, E., et al. (2014). Worldwide epidemiology of atrial fibrillation: a global burden of disease 2010 study. *Circulation* 129, 837–847. doi: 10.1161/CIRCULATIONAHA.113.005119

Nattel, S., Burstein, B., and Dobrev, D. (2008). Atrial Remodeling and Atrial Fibrillation: Mechanisms and Implications. *Circ. Arrhythmia Electrophysiol.* 1, 62–73. doi: 10.1161/CIRCEP.107.754564

Conflict of Interest: The authors declare that the research was conducted in the absence of any commercial or financial relationships that could be construed as a potential conflict of interest.

frontiers in Physiology

MINI REVIEW
published: 28 August 2020
doi: 10.3389/fphys.2020.00987

Toward Mechanism-Directed Electrophenotype-Based Treatments for Atrial Fibrillation

Fu Siong Ng, Balvinder S. Handa, Xinyang Li and Nicholas S. Peters*

National Heart & Lung Institute, Imperial College London, London, United Kingdom

Current treatment approaches for persistent atrial fibrillation (AF) have a ceiling of success of around 50%. This is despite 15 years of developing adjunctive ablation strategies in addition to pulmonary vein isolation to target the underlying arrhythmogenic substrate in AF. A major shortcoming of our current approach to AF treatment is its predominantly empirical nature. This has in part been due to a lack of consensus on the mechanisms that sustain human AF. In this article, we review evidence suggesting that the previous debates on AF being *either* an organized arrhythmia with a focal driver *or* a disorganized rhythm sustained by multiple wavelets, may prove to be a false dichotomy. Instead, a range of fibrillation electrophenotypes exists along a continuous spectrum, and the predominant mechanism in an individual case is determined by the nature and extent of remodeling of the underlying substrate. We propose moving beyond the current empirical approach to AF treatment, highlight the need to prescribe AF treatments based on the underlying AF electrophenotype, and review several possible novel mapping algorithms that may be useful in discerning the AF electrophenotype to guide tailored treatments, including Granger Causality mapping.

Keywords: atrial fibrilation (AF), fibrillation, ablation, mapping, Granger analyses

OPEN ACCESS

Edited by:
Atul Verma,
University of Toronto, Canada

Reviewed by:
Ruben Coronel,
University of Amsterdam, Netherlands
David R. Van Wagoner,
Case Western Reserve University, United States

****Correspondence:***
Fu Siong Ng
f.ng@imperial.ac.uk

Specialty section:
This article was submitted to Cardiac Electrophysiology, a section of the journal Frontiers in Physiology

Received: *05 June 2020*
Accepted: *20 July 2020*
Published: *28 August 2020*

Citation:
Ng FS, Handa BS, Li X and Peters NS (2020) Toward Mechanism-Directed Electrophenotype-Based Treatments for Atrial Fibrillation. Front. Physiol. 11:987. doi: 10.3389/fphys.2020.00987

INTRODUCTION

Atrial fibrillation (AF) is the commonest arrhythmia, for which the direct costs alone are estimated to be up to 2.4% of the United Kingdom healthcare budget, with more than 5 million people in the United States and >8 million people in the European Union estimated to have AF in 2010 (Colilla et al., 2013; Krijthe et al., 2013). Catheter ablation currently forms the mainstay of treatment for patients with AF. Initial catheter ablation strategies were directed toward electrical isolation of the pulmonary veins, which were shown to harbor the triggers for AF (Haissaguerre et al., 1998). Pulmonary vein isolation (PVI) has therefore become a cornerstone of AF ablation, and in patients with paroxysmal AF, this has success rates of ∼70% with multiple procedures (Phlips et al., 2018; Knight et al., 2019).

The picture is more complex in persistent AF, where there are greater degrees of structural and electrophysiological remodeling (Heijman et al., 2014). AF is generally viewed as a progressive disease with "AF begetting AF" (Wijffels et al., 1995). There is evidence for significant remodeling of ionic currents, calcium handling and connexins, and structural remodeling in the form of increased

fibrosis, which combine to create a pro-arrhythmic substrate in persistent AF (Nattel et al., 2008). The accepted paradigm is that, whilst triggers are relatively more important in paroxysmal AF, the substrate becomes increasingly more important in relation to the triggers with the progression to persistent AF (Heijman et al., 2014). As a result, ablation targeting only the pulmonary veins has been associated with relatively poor success rates in persistent AF (Schreiber et al., 2015).

ADJUNCTIVE CATHETER ABLATION FOR PERSISTENT AF

In order to address and modify the pro-arrhythmic substrate in AF, several catheter ablation strategies have been tested over the past 15 years. Linear ablations were performed to compartmentalize the atria (Jaïs et al., 2004; Hocini et al., 2005), to mirror the surgical Maze procedure (Cox et al., 2000), with the rationale that a reduction of tissue mass may increase the likelihood of AF termination, based on the critical mass hypothesis for fibrillation (Lee et al., 2013). There was also significant interest in ablating sites with complex fractionated atrial electrograms (CFAE), with the assumption that these sites represent areas of interest that are critical to driving or sustaining AF (Nademanee et al., 2004). However, there is not a clear and direct relationship between electrogram fractionation and driver sites, with fractionation also seen at sites of passive wavefront collision and "zig-zag" activation through fibrotic regions (de Bakker and Wittkampf, 2010). Despite initial interest in these adjunctive ablation approaches, the STAR-AF 2 study showed that such empirical ablation did not improve ablation efficacy, and the success rates for linear lesions or CFAE ablation in addition to PVI were similar to that of PVI alone (Verma et al., 2015).

More recently, there have been efforts to directly map and ablate the drivers of AF. These include the use of bi-atrial basket catheters to perform endocardial mapping (Narayan et al., 2012; Baykaner et al., 2018) and the use of non-invasive electrocardiographic imaging (ECGI) to perform epicardial mapping (Haissaguerre et al., 2014; Knecht et al., 2017). Although these approaches initially held great promise, subsequent follow-up studies have not been able to reproduce the high success rates first reported for rotor ablation (Buch et al., 2016). Another adjunctive ablation strategy is to target areas of atrial scar, on the premise that these areas are key components of the atrial arrhythmic substrate. Efforts have been directed toward either ablating the areas of scar (Jadidi et al., 2016) or electrically isolating these regions of scar (Kottkamp et al., 2016). Such ablation approaches have yet to be proven to be effective, and have several issues, including the problem that electrogram voltage, used as a surrogate for regions of scar, often correlates poorly with scar identified using late-enhancement MRI imaging (Qureshi et al., 2019).

None of the adjunctive ablation strategies above have reproducibly improved success rates of catheter ablation of persistent AF. Several investigators have thus focused on improving ablation lesion creation as means to improving success rates, on the basis that some of the failures can be attributed to inadequate and incomplete lesion creation. This includes developing specific indices to guide ablation, for example Ablation Index, incorporating the effects of force, time and power of ablation (Phlips et al., 2018), or new approaches to ablation, such as the "high-power, short-duration" approach to ablation (Winkle et al., 2019).

However, despite these efforts, there remains a ceiling to AF ablation success rates for persistent ablation, at around 50% (Scherr et al., 2015). A significant limitation is that current ablation strategies for persistent AF are predominantly empirical in nature, and the lack of patient-specific tailored treatments, directed toward the specific AF mechanism, places a ceiling on success rates of current treatments.

CONFLICTING EVIDENCE ON THE MECHANISMS SUSTAINING AF

The electrophysiological mechanisms that sustain AF have long been disputed, with a consensus still lacking. The *anarchical* model of AF, held widely since Moe proposed the multiple-wavelet hypothesis in the 1960s (Moe et al., 1964), states that AF is sustained by multiple self-perpetuating activation wavelets propagating randomly through atrial tissue. Central to this model, supported by work from Allessie et al. (2010) and Eckstein et al. (2013), is an absence of localized sources, and would support an ablative strategy of creating globally distributed boundary lines confining and extinguishing wavelets (Jaïs et al., 2004; Hocini et al., 2005).

The apparently contrary *hierarchical* model of AF, states that AF is sustained by drivers, in the form of spiral waves or "rotors" (Krinskii, 1966; Pandit and Jalife, 2013), and is supported by work from the Jalife group in the 1990s (Davidenko et al., 1992), but despite a decade of clinical mapping experience, it was not until recently that any clinical evidence for such drivers, albeit disputed, has emerged (Narayan et al., 2012). Rotors are thought to be dynamic during AF and VF; initiating, meandering, terminating, and either re-emerging or superseded by others (Dharmaprani et al., 2019). At present, there is intense debate as to whether rotors, if they exist in humans, are predominantly stable, or short-lasting and mobile, in human AF. There has been a recent move away from the term "rotor" toward the more widely encompassing terms of "rotational driver" or "rotational activity," to include spiral wave re-entry, leading circle re-entry and micro-reentry. High-resolution optical mapping of AF in explanted human hearts has suggested some rotational drivers in human AF may in fact be micro-reentrant in nature (Hansen et al., 2015), with such rotational drivers having predilection for areas of fibrosis (Zahid et al., 2016).

Recent human AF mapping data have challenged the rotor hypothesis, with detailed high-resolution contact electrode mapping in human atria failing to confirm the existence of stable rotational drivers (Allessie et al., 2010; Lee et al., 2014, 2015, 2017). Some investigators have suggested that AF may be maintained because of the dissociation between the endocardial and epicardial layers of human atria (Allessie et al., 2010).

This endocardial-epicardial asynchrony of atrial activation gives rise to transmurally propagating waves, leading to the appearance of "new" focal waves at breakthrough sites in the opposite layer (Roney et al., 2018), and this continuous generation new fibrillation waves on both sides of the atrial wall contributes toward the stability and maintenance of AF.

It is evident that the current clinical literature on the mechanisms sustaining human AF is conflicting. Different investigators have reported a range of apparently contradictory electrophysiological mechanisms, as briefly discussed above. We previously reported that this discordance in findings may in part be explained by the different methodologies used in these studies (Roney et al., 2017; Li et al., 2019). We reported that the spatial resolution of data critically influences the interpretation of the underlying mechanism of fibrillation (Roney et al., 2017). There is a minimum spatial resolution requirement for correct identification of fibrillation mechanisms, with low-resolution data potentially leading to the false detection of non-existent rotational drivers. We also recently demonstrated that the specific analysis approach, including the pre-processing steps and parameterization of the analysis, can also significantly alter the interpretation of fibrillation data, with the lack of a standardized framework for fibrillation analysis contributing to the current conflicting evidence (Li et al., 2019). These challenges, amongst others, have thus far precluded any consensus on human AF mechanisms.

THE FIBRILLATION ELECTROPHENOTYPE SPECTRUM – A UNIFYING HYPOTHESIS FOR AF MECHANISMS?

Much of the above debate about anarchical versus hierarchical forms of AF, which raged in the early 2010s, may ultimately prove to be a false dichotomy. All the above-mentioned mechanisms may be relevant and important in sustaining AF, and the predominant AF mechanism in an individual is dependent on the specific nature of the underlying atrial substrate. We recently systematically demonstrated that a spectrum of ventricular fibrillation (VF) mechanisms exists, and that the mechanism sustaining VF is determined by the underlying substrate of the ventricular myocardium (Handa et al., 2020b). We reported a continuous range of fibrillation "electrophenoypes" that can sustain VF, influenced by the substrate spectrum that incorporates the degree of gap junction coupling and the specific pattern of fibrosis. For example, reduced gap junction coupling favors disorganized fibrillation, sustained by multiple

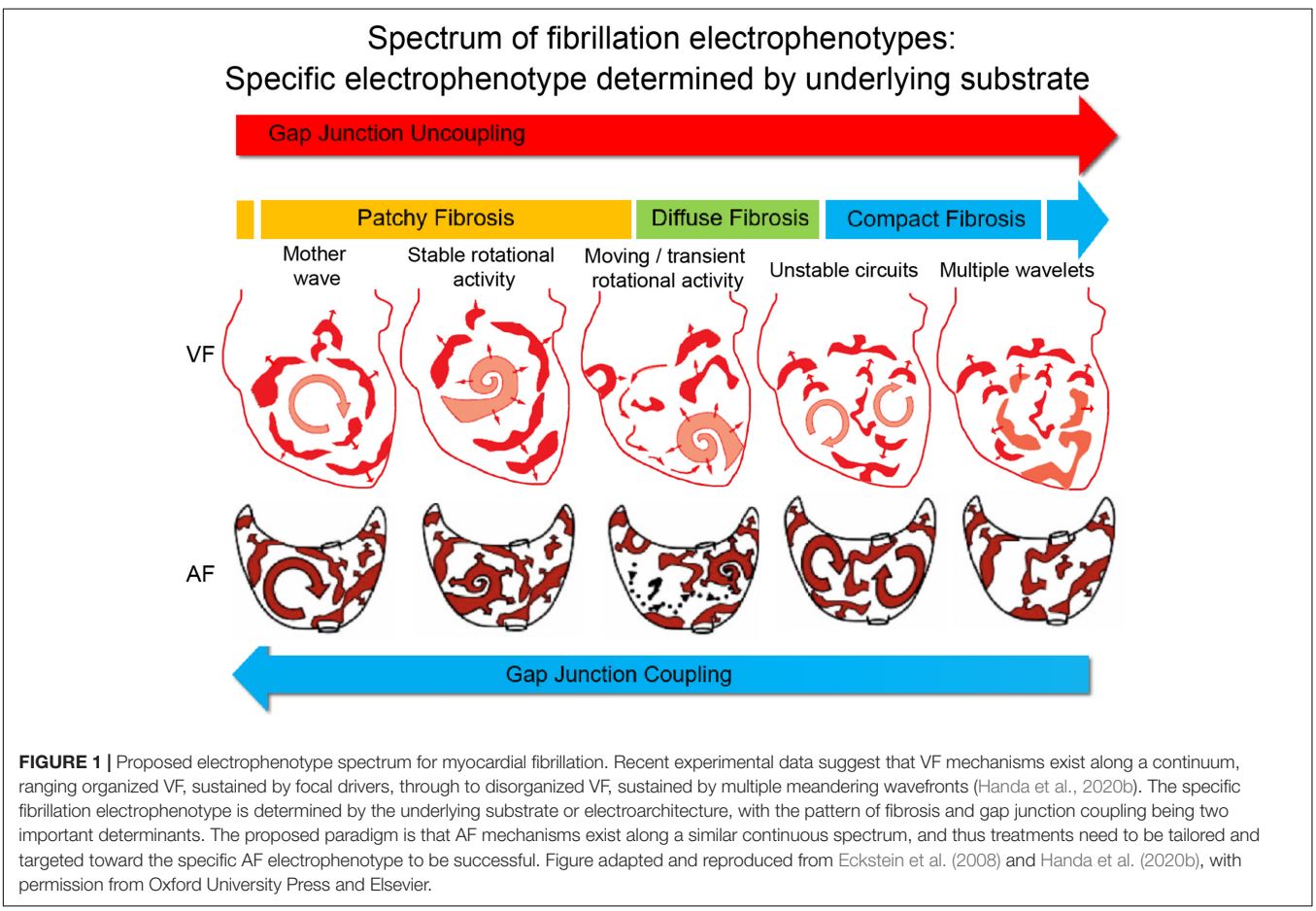

FIGURE 1 | Proposed electrophenotype spectrum for myocardial fibrillation. Recent experimental data suggest that VF mechanisms exist along a continuum, ranging organized VF, sustained by focal drivers, through to disorganized VF, sustained by multiple meandering wavefronts (Handa et al., 2020b). The specific fibrillation electrophenotype is determined by the underlying substrate or electroarchitecture, with the pattern of fibrosis and gap junction coupling being two important determinants. The proposed paradigm is that AF mechanisms exist along a similar continuous spectrum, and thus treatments need to be tailored and targeted toward the specific AF electrophenotype to be successful. Figure adapted and reproduced from Eckstein et al. (2008) and Handa et al. (2020b), with permission from Oxford University Press and Elsevier.

wavelets, while preserved gap junction coupling favors organized fibrillation, sustained by rotational drivers or foci. Patchy fibrosis favors fibrillation sustained by stable rotational drivers, while compact fibrosis favors disorganized fibrillation, with diffuse interstitial fibrosis causing an intermediate electrophenotype, sustained by a combination of unstable rotational drivers and meandering wavefronts (**Figure 1**).

We hypothesize that a similar electrophenotype spectrum exists for AF, with the AF electrophenotype also determined by the underlying atrial substrate (**Figure 1**). As we have demonstrated for VF, it is possible that the degree of remodeling of the atrial substrate, including remodeling of ionic currents (Samie et al., 2001; Kneller et al., 2005; Muñoz et al., 2007), calcium handling (Samie et al., 2000), connexins, and fibrosis, determines the specific AF electrophenotype and the predominant AF mechanism. Our own analysis of human persistent AF would appear to support this hypothesis (Handa et al., 2020a).

The electrophenotype spectrum is a direct correlate of the underlying substrate spectrum, which is what determines the fibrillation mechanism. Whilst it would be desirable to accurately describe the substrate for each patient, in terms of the degree of remodeling of ionic currents, calcium handling, gap junctions, and fibrosis, that is not currently possible. However, measuring the functional correlate of the sum of the arrhythmogenic remodeling of the substrate, i.e. the electrophenotype, is within our capabilities, using the current tools and technology in the clinical electrophysiology laboratory, and thus categorising AF into broad electrophenotype categories may be a helpful concept to facilitate the tailoring of treatments.

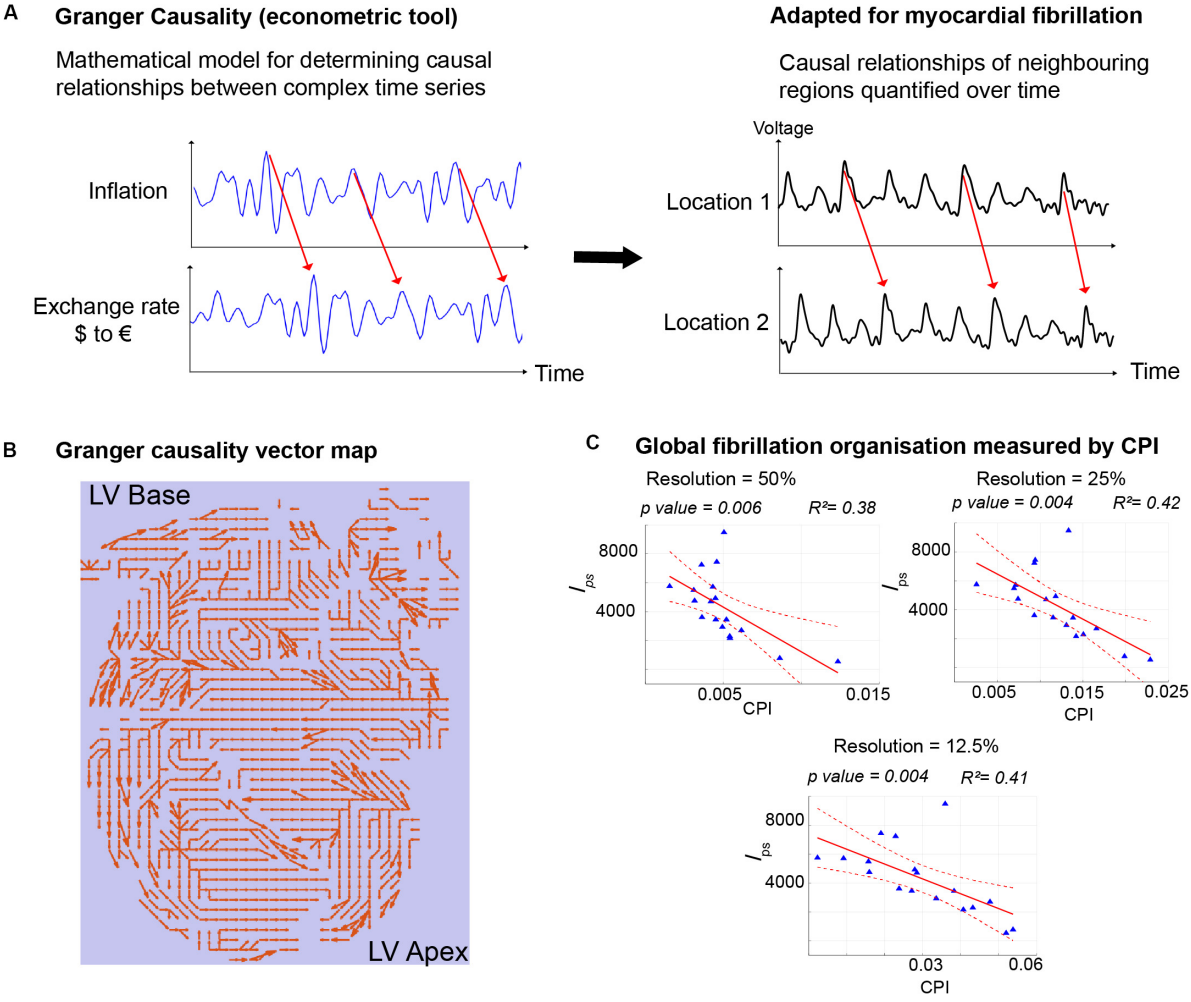

FIGURE 2 | Granger Causality mapping to discern AF electrophenotype. **(A)** Granger Causality analysis, an econometric tool that determines the causal relationships between two time series, was adapted for use in fibrillation, to determine the strength of causal relationships of signals from different regions of myocardium during fibrillation. **(B)** The entire mapping field is represented with arrows depicting the strongest casual relationships. **(C)** Quantification of the number of causal pairs above a set threshold of causality (Causality Pairing Index, CPI) is a method to discern the overall organization of fibrillation and the electrophenotype of fibrillation. Importantly CPI is effective even with low resolution data, downsampled to 25%, when compared to the gold-standard high-resolution mapping data. In this example, CPI using downsampled data correlates negatively with the full-resolution I_{ps}, which measures the number of short-lived phase singularities and is a measure of fibrillation disorganization. Figure adapted and reproduced from Handa et al. (2020a), in line with Creative Commons Attribution 4.0 (CC-BY 4.0).

MECHANISM-DIRECTED TREATMENT BASED ON AF ELECTROPHENOTYPE

If the electrophenotype spectrum exists for human AF, then a mechanism-directed therapeutic approach, based on the AF electrophenotype, would be expected to yield better success rates than current empirical treatment strategies. For example, AF on the organized end of the electrophenotype spectrum would be more amenable to mapping and ablation of focal drivers, and responsive to Class Ic antiarrhythmic agents, which have been shown to destabilize spiral waves (Kneller et al., 2005). AF on the disorganized end of the electrophenotype spectrum may be responsive to compartmentalization of the atria or Class III antiarrhythmic agents to prolong refractoriness. Conversely, the current approach to AF treatment, which at present is neither patient-specific nor mechanism-directed, neglects the underlying electrophenotype and would be expected to have overall poor success rates.

However, such a tailored approach to AF treatment is critically dependent on the ability to accurately identify the AF electrophenotype in patients. Much of the work on AF and VF mechanisms, including our own, has been performed with high-resolution optical mapping (Davidenko et al., 1992; Muñoz et al., 2007; Roney et al., 2018; Handa et al., 2020b). The problem of low spatial resolution clinical data, which has hampered the interpretation of human AF data (King et al., 2017; Roney et al., 2017), would need to be overcome, and novel approaches for handling fibrillation data would be required.

There are currently several candidate approaches to identify the AF electrophenotype to guide tailored treatments. We recently adapted Granger causality analysis, originally an econometric tool for quantifying causal relationships between complex time series data (Nobel Prize Economics 2003), for use on AF data (Handa et al., 2020a). By testing for causal relationships of electrical signals between neighboring regions of the heart over time and quantifying the number of causal relationships above a set "causality threshold," we can reliably measure global fibrillation organization and characterize the AF electrophenotype, even when applied to low spatial resolution clinical AF data (**Figure 2**). Other novel analysis approaches, such as wavefront field mapping, which can reveal the network of rotational and focal sites in AF (Leef et al., 2019), electrocardiographic flow mapping, which determines the main propagation patterns during AF (Bellmann et al., 2019), or mapping of connectivity between different regions of the atria usual mutual information analysis (Tao et al., 2017), may also be able to identify the AF electrophenotype to guide mechanism-directed treatments.

However, one drawback is that invasively acquired data, obtained during catheter ablation procedures, are required for these above approaches to work. The ideal scenario would be to have the ability to discern the underlying mechanism or electrophenotype of AF without the need to perform an invasive procedure, such as using data from a combination of the surface electrogram, ECGI and MRI imaging. However, these less invasive methods have their own associated limitations. Electrocardiographic imaging, has been used to map activation in both AF and VF to guide ablation of areas harboring supposed drivers, though there is ongoing debate about the degree of correlation of ECGI interpolated electrograms with those acquired with contact mapping (Cluitmans et al., 2018). Similarly, late gadolinium enhanced cardiac MRI (LGE-CMR) to detect atrial fibrosis holds promise with regards mapping the structural substrate of AF and guiding tailored therapy, though it is limited by a number of challenges in fibrosis detection posed in thin-walled atrial tissue (Siebermair et al., 2017).

CONCLUSION

Current treatments for persistent AF are predominantly based on empiricism and not tailored to target the underlying AF mechanism in individual patients. Recent data suggest that fibrillation mechanisms may exist along a continuous spectrum, with the specific electrophenotype determined by the degree of remodeling of the underlying myocardial substrate and electroarchitecture. Tailored mechanism-directed treatments based on the AF electrophenotype may help to improve the currently poor success rates in treating persistent AF. Several novel mapping algorithms, including Granger Causality mapping, may be able to determine the underlying AF electrophenotype to guide tailored treatments.

AUTHOR CONTRIBUTIONS

FSN drafted the manuscript. All authors critically reviewed and approved the manuscript.

FUNDING

This work was supported by the British Heart Foundation (RG/16/3/32175). FSN was also supported by the National Institute for Health Research (NIHR) Imperial Biomedical Research Centre.

REFERENCES

Allessie, M. A., De Groot, N. M. S., Houben, R. P. M., Schotten, U., Boersma, E., Smeets, J. L., et al. (2010). Electropathological substrate of long-standing persistent atrial fibrillation in patients with structural heart disease longitudinal dissociation. *Circ. Arrhythm. Electrophysiol.* 3, 606–615. doi: 10.1161/circep.109.910125

Baykaner, T., Rogers, A. J., Meckler, G. L., Zaman, J., Navara, R., Rodrigo, M., et al. (2018). Clinical implications of ablation of drivers for atrial fibrillation: a systematic review and meta-analysis. *Circ. Arrhythm. Electrophysiol.* 11:e006119.

Bellmann, B., Zettwitz, M., Lin, T., Ruppersberg, P., Guttmann, S., Tscholl, V., et al. (2019). Velocity characteristics of atrial fibrillation sources determined by electrographic flow mapping before and after

catheter ablation. *Int. J. Cardiol.* 286, 56–60. doi: 10.1016/j.ijcard.2019.02.006

Buch, E., Share, M., Tung, R., Benharash, P., Sharma, P., Koneru, J., et al. (2016). Long-term clinical outcomes of focal impulse and rotor modulation for treatment of atrial fibrillation: a multicenter experience. *Heart Rhythm* 13, 636–641. doi: 10.1016/j.hrthm.2015.10.031

Cluitmans, M., Brooks, D. H., MacLeod, R., Dössel, O., Guillem, M. S., Van Dam, P. M., et al. (2018). Validation and opportunities of electrocardiographic imaging: from technical achievements to clinical applications. *Front. Physiol.* 9:1305. doi: 10.3389/fphys.2018.01305

Colilla, S., Crow, A., Petkun, W., Singer, D. E., Simon, T., and Liu, X. (2013). Estimates of current and future incidence and prevalence of atrial fibrillation in the U.S. adult population. *Am. J. Cardiol.* 112, 1142–1147. doi: 10.1016/j.amjcard.2013.05.063

Cox, J. L., Schuessler, R. B., and Boineau, J. P. (2000). The development of the Maze procedure for the treatment of atrial fibrillation. *Semin. Thorac. Cardiovasc. Surg.* 12, 2–14.

Davidenko, J. M., Pertsov, A. V., Salomonsz, R., Baxter, W., and Jalife, J. (1992). Stationary and drifting spiral waves of excitation in isolated cardiac muscle. *Nature* 355, 349–351. doi: 10.1038/355349a0

de Bakker, J. M. T., and Wittkampf, F. H. M. (2010). The pathophysiologic basis of fractionated and complex electrograms and the impact of recording techniques on their detection and interpretation. *Circ. Arrhythmi. Electrophysiol.* 3, 204–213. doi: 10.1161/circep.109.904763

Dharmaprani, D., Schopp, M., Kuklik, P., Chapman, D., Lahiri, A., Dykes, L., et al. (2019). Renewal theory as a universal quantitative framework to characterize phase singularity regeneration in mammalian cardiac fibrillation. *Circ. Arrhythm. Electrophysiol.* 12, 1–12.

Eckstein, J., Verheule, S., de Groot, N., Allessie, M., and Schotten, U. (2008). Mechanisms of perpetuation of atrial fibrillation in chronically dilated atria. *Prog. Biophys. Mol. Biol.* 97, 435–451. doi: 10.1016/j.pbiomolbio.2008.02.019

Eckstein, J., Zeemering, S., Linz, D., Maesen, B., Verheule, S., van Hunnik, A., et al. (2013). Transmural conduction is the predominant mechanism of breakthrough during atrial fibrillation: evidence from simultaneous endo-epicardial high-density activation mapping. *Circ. Arrhythm. Electrophysiol.* 6, 334–341. doi: 10.1161/circep.113.000342

Haissaguerre, M., Hocini, M., Denis, A., Shah, A. J., Komatsu, Y., Yamashita, S., et al. (2014). Driver domains in persistent atrial fibrillation. *Circulation* 130, 530–538.

Haissaguerre, M., Jais, P., Shah, D. C., Takahashi, A., Hocini, M., Quiniou, G., et al. (1998). Spontaneous initiation of atrial fibrillation by ectopic beats originating in the pulmonary veins. *N. Engl. J. Med.* 339, 659–666. doi: 10.1056/nejm199809033391003

Handa, B. S., Li, X., Aras, K. K., Qureshi, N. A., Mann, I., Chowdhury, R. A., et al. (2020a). Granger causality-based analysis for classification of fibrillation mechanisms and localization of rotational drivers. *Circ. Arrhythm. Electrophysiol.* 13:e008237.

Handa, B. S., Li, X., Baxan, N., Roney, C., Shchendrygina, A., Mansfield, C. A., et al. (2020b). Ventricular fibrillation mechanism and global fibrillatory organisation are determined by gap junction coupling and fibrosis pattern. *Cardiovasc. Res.* doi: 10.1093/cvr/cvaa141 [online ahead of print].

Hansen, B. J., Zhao, J., Csepe, T. A., Moore, B. T., Li, N., Jayne, L. A., et al. (2015). Atrial fibrillation driven by micro-anatomic intramural re-entry revealed by simultaneous sub-epicardial and sub-endocardial optical mapping in explanted human hearts. *Eur. Heart J.* 36, 2390–2401. doi: 10.1093/eurheartj/ehv233

Heijman, J., Voigt, N., Nattel, S., and Dobrev, D. (2014). Cellular and molecular electrophysiology of atrial fibrillation initiation, maintenance, and progression. *Circ. Res.* 114, 1483–1499. doi: 10.1161/circresaha.114.302226

Hocini, M., Jaïs, P., Sanders, P., Takahashi, Y., Rotter, M., Rostock, T., et al. (2005). Techniques, evaluation, and consequences of linear block at the left atrial roof in paroxysmal atrial fibrillation: a prospective randomized study. *Circulation* 112, 3688–3696. doi: 10.1161/circulationaha.105.541052

Jadidi, A. S., Lehrmann, H., Keyl, C., Sorrel, J., Markstein, V., Minners, J., et al. (2016). Ablation of persistent atrial fibrillation targeting low-voltage areas with selective activation characteristics. *Circ. Arrhythm. Electrophysiol.* 9:e002962.

Jaïs, P., Hocini, M., Hsu, L. F., Sanders, P., Scavee, C., Weerasooriya, R., et al. (2004). Technique and results of linear ablation at the mitral isthmus. *Circulation* 110, 2996–3002. doi: 10.1161/01.cir.0000146917.75041.58

King, B., Porta-Sánchez, A., Massé, S., Zamiri, N., Balasundaram, K., Kusha, M., et al. (2017). Effect of spatial resolution and filtering on mapping cardiac fibrillation. *Heart Rhythm* 14, 608–615. doi: 10.1016/j.hrthm.2017.01.023

Knecht, S., Sohal, M., Deisenhofer, I., Albenque, J. P., Arentz, T., Neumann, T., et al. (2017). Multicentre evaluation of non-invasive biatrial mapping for persistent atrial fibrillation ablation: the AFACART study. *Europace* 19, 1302–1309. doi: 10.1093/europace/euw168

Kneller, J., Kalifa, J., Zou, R., Zaitsev, A. V., Warren, M., Berenfeld, O., et al. (2005). Mechanisms of atrial fibrillation termination by pure sodium channel blockade in an ionically-realistic mathematical model. *Circ. Res.* 96, e35–e47.

Knight, B. P., Novak, P. G., Sangrigoli, R., Champagne, J., Dubuc, M., Adler, S. W., et al. (2019). Long-term outcomes after ablation for paroxysmal atrial fibrillation using the second-generation cryoballoon: final results from STOP AF post-approval study. *JACC Clin. Electrophysiol.* 5, 306–314.

Kottkamp, H., Berg, J., Bender, R., Rieger, A., and Schreiber, D. (2016). Box isolation of fibrotic areas (BIFA): a patient-tailored substrate modification approach for ablation of atrial fibrillation. *J. Cardiovasc. Electrophysiol.* 27, 22–30. doi: 10.1111/jce.12870

Krijthe, B. P., Kunst, A., Benjamin, E. J., Lip, G. Y. H., Franco, O. H., Hofman, A., et al. (2013). Projections on the number of individuals with atrial fibrillation in the European Union, from 2000 to 2060. *Eur. Heart J.* 34, 2746–2751. doi: 10.1093/eurheartj/eht280

Krinskii, V. I. (1966). Excitation propagation in nonhomogenous medium (actions analogous to heart fibrillation). *Biofizika* 11, 676–683.

Lee, A. M., Aziz, A., Didesch, J., Clark, K. L., Schuessler, R. B., and Damiano, R. J. (2013). Importance of atrial surface area and refractory period in sustaining atrial fibrillation: testing the critical mass hypothesis. *J. Thorac. Cardiovasc. Surg.* 146, 593–598. doi: 10.1016/j.jtcvs.2012.04.021

Lee, G., Kumar, S., Teh, A., Madry, A., Spence, S., Larobina, M., et al. (2014). Epicardial wave mapping in human long-lasting persistent atrial fibrillation: transient rotational circuits, complex wavefronts, and disorganized activity. *Eur. Heart J.* 35, 86–97. doi: 10.1093/eurheartj/eht267

Lee, S., Sahadevan, J., Khrestian, C. M., Cakulev, I., Markowitz, A., and Waldo, A. L. (2015). Simultaneous biatrial high-density (510-512 Electrodes) epicardial mapping of persistent and long-standing persistent atrial fibrillation in patients: new insights into the mechanism of its maintenance. *Circulation* 132, 2108–2117. doi: 10.1161/circulationaha.115.017007

Lee, S., Sahadevan, J., Khrestian, C. M., Markowitz, A., and Waldo, A. L. (2017). Characterization of foci and breakthrough sites during persistent and long-standing persistent atrial fibrillation in patients: studies using high-density (510-512 Electrodes) biatrial epicardial mapping. *J. Am. Heart Assoc.* 6, 1–12.

Leef, G., Shenasa, F., Bhatia, N. K., Rogers, A. J., Sauer, W., Miller, J. M., et al. (2019). Wavefront field mapping reveals a physiologic network between drivers where ablation terminates atrial fibrillation. *Circ. Arrhythm. Electrophysiol.* 12:e006835.

Li, X., Roney, C. H., Handa, B. S., Chowdhury, R. A., Niederer, S. A., Peters, N. S., et al. (2019). Standardised framework for quantitative analysis of fibrillation dynamics. *Sci. Rep.* 9, 16610–16671.

Moe, G. K., Rheinboldt, W. C., and Abildskov, J. A. (1964). A computer model of atrial fibrillation. *Am. Heart J.* 67, 200–220. doi: 10.1016/0002-8703(64)90371-0

Muñoz, V., Grzeda, K. R., Desplantez, T., Pandit, S. V., Mironov, S., Taffet, S. M., et al. (2007). Adenoviral expression of IKs contributes to wavebreak and fibrillatory conduction in neonatal rat ventricular cardiomyocyte monolayers. *Circ. Res.* 101, 475–483. doi: 10.1161/circresaha.107.149617

Nademanee, K., McKenzie, J., Kosar, E., Schwab, M., Sunsaneewitayakul, B., Vasavakul, T., et al. (2004). A new approach for catheter ablation of atrial fibrillation: mapping of the electrophysiologic substrate. *J. Am. Coll Cardiol.* 43, 2044–2053.

Narayan, S. M., Krummen, D. E., Shivkumar, K., Clopton, P., Rappel, W.-J., and Miller, J. M. (2012). Treatment of atrial fibrillation by the ablation of localized sources: CONFIRM (Conventional Ablation for Atrial Fibrillation With or Without Focal Impulse and Rotor Modulation) trial. *J. Am. Coll Cardiol.* 60, 628–636.

Nattel, S., Burstein, B., and Dobrev, D. (2008). Atrial remodeling and atrial fibrillation: mechanisms and implications. *Circ. Arrhythm. Electrophysiol.* 1, 62–73. doi: 10.1161/circep.107.754564

Pandit, S. V., and Jalife, J. (2013). Rotors and the dynamics of cardiac fibrillation. *Circ. Res.* 112, 849–862. doi: 10.1161/circresaha.111.300158

Phlips, T., Taghji, P., El Haddad, M., Wolf, M., Knecht, S., Vandekerckhove, Y., et al. (2018). Improving procedural and one-year outcome after contact force-guided pulmonary vein isolation: the role of interlesion distance, ablation index, and contact force variability in the 'CLOSE'-protocol. *Europace* 20, f419–f427. doi: 10.1093/europace/eux376

Qureshi, N. A., Kim, S. J., Cantwell, C. D., Afonso, V. X., Bai, W., Ali, R. L., et al. (2019). Voltage during atrial fibrillation is superior to voltage during sinus rhythm in localizing areas of delayed enhancement on magnetic resonance imaging: an assessment of the posterior left atrium in patients with persistent atrial fibrillation. *Hear Rhythm* 16, 1357–1367. doi: 10.1016/j.hrthm.2019.05.032

Roney, C. H., Cantwell, C. D., Bayer, J. D., Qureshi, N. A., Lim, P. B., Tweedy, J. H., et al. (2017). Spatial resolution requirements for accurate identification of drivers of atrial fibrillation. *Circ. Electrophysiol.* 10:e004899.

Roney, C. H., Ng, F. S., Debney, M. T., Eichhorn, C., Nachiappan, A., Chowdhury, R. A., et al. (2018). Determinants of new wavefront locations in cholinergic atrial fibrillation. *Europace* 20, iii3–iii5.

Samie, F. H., Berenfeld, O., Anumonwo, J., Mironov, S. F., Udassi, S., Beaumont, J., et al. (2001). Rectification of the background potassium current: a determinant of rotor dynamics in ventricular fibrillation. *Circ. Res.* 89, 1216–1223. doi: 10.1161/hh2401.100818

Samie, F. H., Mandapati, R., Gray, R. A., Watanabe, Y., Zuur, C., Beaumont, J., et al. (2000). A mechanism of transition from ventricular fibrillation to tachycardia: effect of calcium channel blockade on the dynamics of rotating waves. *Circ. Res.* 86, 684–691. doi: 10.1161/01.res.86.6.684

Scherr, D., Khairy, P., Miyazaki, S., Aurillac-Lavignolle, V., Pascale, P., Wilton, S. B., et al. (2015). Five-year outcome of catheter ablation of persistent atrial fibrillation using termination of atrial fibrillation as a procedural endpoint. *Circ. Arrhythm. Electrophysiol.* 8, 18–24.

Schreiber, D., Rostock, T., Fröhlich, M., Sultan, A., Servatius, H., Hoffmann, B. A., et al. (2015). Five-year follow up after catheter ablation of persistent atrial fibrillation using the "Stepwise Approach" and prognostic factors for success. *Circ. Arrhythm Electrophysiol.* 8, 1–31.

Siebermair, J., Kholmovski, E. G., and Marrouche, N. (2017). Assessment of left atrial fibrosis by late gadolinium enhancement magnetic resonance imaging: methodology and clinical implications. *JACC Clin. Electrophysiol.* 3, 791–802. doi: 10.1016/j.jacep.2017.07.004

Tao, S., Way, S. F., Garland, J., Chrispin, J., Ciuffo, L. A., Balouch, M. A., et al. (2017). Ablation as targeted perturbation to rewire communication network of persistent atrial fibrillation. *PLoS One* 12:e0179459. doi: 10.1371/journal.pone.0179459

Verma, A., Jiang, C., Betts, T. R., Chen, J., Deisenhofer, I., Mantovan, R., et al. (2015). Approaches to catheter ablation for persistent atrial fibrillation. *N. Engl. J. Med.* 372, 1812–1822.

Wijffels, M. C., Kirchhof, C. J., Dorland, R., and Allessie, M. A. (1995). Atrial fibrillation begets atrial fibrillation. A study in awake chronically instrumented goats. *Circulation* 92, 1954–1968.

Winkle, R. A., Mohanty, S., Patrawala, R. A., Mead, R. H., Kong, M. H., Engel, G., et al. (2019). Low complication rates using high power (45–50 W) for short duration for atrial fibrillation ablations. *Heart Rhythm* 16, 165–169.

Zahid, S., Cochet, H., Boyle, P. M., Schwarz, E. L., Whyte, K. N., Vigmond, E. J., et al. (2016). Patient-derived models link re-entrant driver localization in atrial fibrillation to fibrosis spatial pattern. *Cardiovasc. Res.* 110, 443–454.

Conflict of Interest: The authors have a patent application pending on Granger Causality mapping (UK Patent Application No. 1903259.8).

frontiers in Physiology

ORIGINAL RESEARCH
published: 16 September 2020
doi: 10.3389/fphys.2020.572874

In silico Comparison of Left Atrial Ablation Techniques That Target the Anatomical, Structural, and Electrical Substrates of Atrial Fibrillation

*Caroline H. Roney[1], Marianne L. Beach[1], Arihant M. Mehta[1], Iain Sim[1], Cesare Corrado[1], Rokas Bendikas[1], Jose A. Solis-Lemus[1], Orod Razeghi[1], John Whitaker[1], Louisa O'Neill[1], Gernot Plank[2], Edward Vigmond[3], Steven E. Williams[1], Mark D. O'Neill[1] and Steven A. Niederer[1]**

[1]School of Biomedical Engineering and Imaging Sciences, King's College London, London, United Kingdom, [2]Department of Biophysics, Medical University of Graz, Graz, Austria, [3]IHU Liryc, Electrophysiology and Heart Modeling Institute, Fondation Bordeaux Université, Bordeaux, France

OPEN ACCESS

Edited by:
Atul Verma,
University of Toronto, Canada

Reviewed by:
Tong Liu,
Tianjin Medical University, China
Sanjay Ram Kharche,
University of Western Ontario, Canada

***Correspondence:**
Steven A. Niederer
steven.niederer@kcl.ac.uk

Specialty section:
This article was submitted to Cardiac Electrophysiology, a section of the journal Frontiers in Physiology

Received: *15 June 2020*
Accepted: *18 August 2020*
Published: *16 September 2020*

Citation:
Roney CH, Beach ML, Mehta AM, Sim I, Corrado C, Bendikas R, Solis-Lemus JA, Razeghi O, Whitaker J, O'Neill L, Plank G, Vigmond E, Williams SE, O'Neill MD and Niederer SA (2020) In silico Comparison of Left Atrial Ablation Techniques That Target the Anatomical, Structural, and Electrical Substrates of Atrial Fibrillation. Front. Physiol. 11:572874. doi: 10.3389/fphys.2020.572874

Catheter ablation therapy for persistent atrial fibrillation (AF) typically includes pulmonary vein isolation (PVI) and may include additional ablation lesions that target patient-specific anatomical, electrical, or structural features. Clinical centers employ different ablation strategies, which use imaging data together with electroanatomic mapping data, depending on data availability. The aim of this study was to compare ablation techniques across a virtual cohort of AF patients. We constructed 20 paroxysmal and 30 persistent AF patient-specific left atrial (LA) bilayer models incorporating fibrotic remodeling from late-gadolinium enhancement (LGE) MRI scans. AF was simulated and post-processed using phase mapping to determine electrical driver locations over 15 s. Six different ablation approaches were tested: (i) PVI alone, modeled as wide-area encirclement of the pulmonary veins; PVI together with: (ii) roof and inferior lines to model posterior wall box isolation; (iii) isolating the largest fibrotic area (identified by LGE-MRI); (iv) isolating all fibrotic areas; (v) isolating the largest driver hotspot region [identified as high simulated phase singularity (PS) density]; and (vi) isolating all driver hotspot regions. Ablation efficacy was assessed to predict optimal ablation therapies for individual patients. We subsequently trained a random forest classifier to predict ablation response using (a) imaging metrics alone, (b) imaging and electrical metrics, or (c) imaging, electrical, and ablation lesion metrics. The optimal ablation approach resulting in termination, or if not possible atrial tachycardia (AT), varied among the virtual patient cohort: (i) 20% PVI alone, (ii) 6% box ablation, (iii) 2% largest fibrosis area, (iv) 4% all fibrosis areas, (v) 2% largest driver hotspot, and (vi) 46% all driver hotspots. Around 20% of cases remained in AF for all ablation strategies. The addition of patient-specific and ablation pattern specific lesion metrics to the trained random forest classifier improved predictive capability from an accuracy of 0.73 to 0.83. The trained classifier results demonstrate that the surface areas of pre-ablation driver regions and of fibrotic tissue not isolated by the proposed ablation strategy are both important for predicting ablation outcome. Overall, our study demonstrates the need to select the optimal ablation

strategy for each patient. It suggests that both patient-specific fibrosis properties and driver locations are important for planning ablation approaches, and the distribution of lesions is important for predicting an acute response.

Keywords: atrial fibrillation, virtual cohort, catheter ablation, atrial fibrosis, phase singularity mapping

INTRODUCTION

Current treatment approaches for persistent atrial fibrillation (AF) are sub-optimal, with over 40% of patients exhibiting AF recurrence within 18 months of catheter ablation therapy (Verma et al., 2015). Catheter ablation typically includes pulmonary vein isolation (PVI) and may include additional lesions. These additional lesions may target patient-specific features of the anatomical, structural, or electrical substrates.

Anatomical ablation approaches aim to either isolate areas that are common sites of triggers or anatomical re-entry (Pambrun et al., 2019), or to reduce the space available for re-entry. Specifically, PVI aims to isolate triggered beats from the pulmonary veins. Linear ablation approaches may include additional ablation lines at the mitral isthmus or the roof of the left atrium; for example, Kottkamp et al. (2002) applied lesion lines from the mitral valve annulus to the pulmonary vein orifices to prevent anatomical reentrant circuits. Yu et al. (2017) demonstrated that linear lesions together with PVI demonstrate similar efficacy to PVI alone. Other anatomical approaches include box isolation, which includes additional ablation lines to isolate a box of tissue on the posterior wall and roof, and aims to reduce the spatial size of the atrial substrate, where fibrillatory wavefronts may persistently propagate (Hwang et al., 2015; Williams et al., 2019). Pambrun et al. (2019) used an ablation strategy that targeted the coronary sinus and vein of Marshall to eliminate potential sites of anatomical re-entry. The anatomical ablation lesion set applied will depend on individual patient anatomy; however, it will not necessarily take into account electrical or structural features of the atrial substrate. We simulate two anatomical ablation approaches: PVI and box isolation.

Structural ablation approaches aim to remove or isolate aberrant fibrotic tissue identified through either electroanatomic mapping or atrial imaging. For example, Kottkamp et al. (2016) performed box isolation of fibrotic areas to remove low voltage areas from electroanatomic voltage maps as a surrogate for fibrotic tissue. The Delayed-Enhancement MRI Determinant of Successful Radiofrequency Catheter Ablation of Atrial Fibrillation (DECAAF) study showed that atrial fibrosis detected on late-gadolinium enhancement MRI (LGE-MRI) was independently associated with AF recurrence (Marrouche et al., 2014; Chubb et al., 2019). The current DECAAFII clinical study aims to investigate whether ablation guided by LGE-MRI is superior to PVI. However, it is challenging to characterize atrial tissue from LGE-MRI imaging data and to use this characterization to decide which areas to ablate. As a further complication, recent studies demonstrate evidence both for and against the colocation of fibrillatory drivers with fibrotic tissue (Haissaguerre et al., 2016; Sohns et al., 2017). We simulate two structural ablation approaches: isolating the largest fibrotic area and isolating all fibrotic areas.

Electrical ablation approaches are personalized to target areas of electrogram fractionation (Nademanee et al., 2004) or to isolate electrical drivers identified using phase singularity (PS) analysis (Lim et al., 2017). Narayan et al. (2012) demonstrated high success rates by ablating focal and re-entrant drivers identified through phase and activation mapping of AF. However, these approaches require accurate mapping of atrial drivers, which is challenging (Handa et al., 2018), and are also complicated by the emergence of post-ablation drivers that may not be present pre-ablation. We simulate two electrical ablation approaches: isolating the largest driver region and isolating all driver regions.

Biophysical modeling provides essential mechanistic insights into the individual contribution of the anatomical, electrical, and structural substrates to AF, and each individual patient's response to multiple different ablation strategies. This allows the efficacy of specific ablation strategies and the relative effect of ablation strategy and atrial debulking to be predicted. However, biophysical models take a significant amount of time to construct and simulate and so are both compute and resource intensive, limiting their direct clinical applicability. Combining the mechanistic insights of biophysical models with machine learning techniques may lead to a more robust machine learning predictor, which is computationally efficient and allows fast prediction in the catheter laboratory on any desktop computer.

We aimed to compare AF ablation techniques that target features of the anatomical, structural, and electrical AF substrates for patient-specific simulations of paroxysmal and persistent AF. Specifically, we applied different anatomical, structural, and electrical ablation strategies to a cohort of 20 virtual paroxysmal AF patients and 30 virtual persistent AF patients. Subsequently, we trained a machine learning random forest classifier to predict ablation response using (a) imaging metrics alone, (b) imaging and electrical metrics, or (c) imaging, electrical, and ablation lesion metrics.

MATERIALS AND METHODS

Patient Cohort

Computational models were constructed from cardiac MRI data for 20 paroxysmal AF and 30 persistent AF patients treated at St Thomas' Hospital. Paroxysmal and persistent AFs were defined following HRS/EHRA/ECAS/APHRS/SOLAECE guidelines: paroxysmal AF is AF that terminates spontaneously or with intervention within 7 days; persistent AF is continuous AF that is sustained beyond 7 days (Calkins et al., 2018). MRI data consisted of contrast enhanced magnetic resonance

angiogram (CE-MRA) scans, which were used to delineate the left atrial (LA) endocardial wall, together with LGE-MRI data, which were processed for fibrosis tissue distribution. Image acquisition details have been previously published (Sim et al., 2019) and are described in the **Supplementary Material**. Ethical approval was granted by regional ethics committee (17/LO/0150 and 15/LO/1803).

Geometry Construction

To build an anatomical model for each patient, the left atrium was segmented from the CE-MRA images using semi-automated tools within CemrgApp software[1] (Sim et al., 2019; Razeghi et al., 2020, see **Figure 1A**). LGE-MRI scans were registered with CE-MRA images to inform the distribution of fibrotic tissue incorporated into each virtual patient model (see **Figure 1B**). Each LA segmentation mesh was post-processed using multiple steps, to create a mesh suitable for electrophysiology simulations (See **Figure 1C**). To create a closed surface, the following filters were applied using Meshlab software[2]: Poisson surface reconstruction, marching cubes, and quadric edge collapse decimation (Cignoni et al., 2008; Kazhdan and Hoppe, 2013). Paraview software (Kitware, Clifton Park, NY, United States[3]; Ahrens et al., 2005) was used to clip the closed surface mesh at the mitral valve and four pulmonary veins, and to label each of the four pulmonary veins and LA appendage (Roney et al., 2019). The clipped and labeled mesh was then re-meshed using mmgtools software[4] to create triangular elements of approximately equal average edge length (0.34 mm). These steps are shown in **Supplementary Figure 1**. This endocardial surface mesh was then duplicated and projected 0.1 mm epicardially to produce an epicardial surface, and these were coupled using linear elements to produce a bilayer model (Labarthe et al., 2014). The projection distance is an arbitrary value, since the atrial wall thickness is incorporated in the simulations through the choice of coupling coefficient, following (Labarthe et al., 2014).

Endocardial and epicardial fibers from a human atrial *ex-vivo* diffusion tensor MRI atlas (Pashakhanloo et al., 2016; Roney et al., 2020) were registered to each anatomical mesh using the universal atrial coordinate system (Roney et al., 2019). Specifically, the fiber fields corresponding to diffusion tensor MRI dataset 1 were used because these were shown to optimally predict arrhythmia properties (Roney et al., 2020). Fiber streamlines are shown in **Figure 1D**. More details on fiber field assignment are given in the **Supplementary Material** and **Supplementary Figure 2**. Meshalyzer software[5] was used to visualize simulation data.

Biophysical Modeling Details

Biophysical simulations were run using Cardiac Arrhythmia Research Package CARPentry simulator (Vigmond et al., 2003), with the monodomain model for excitation propagation.

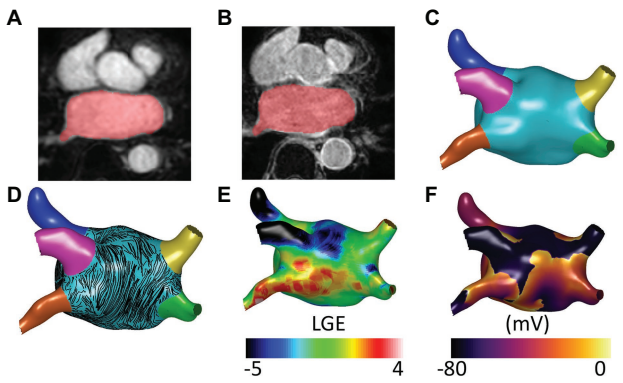

FIGURE 1 | Model construction and atrial fibrillation (AF) simulation. **(A)** Contrast enhanced magnetic resonance angiogram (CE-MRA) imaging showing semi-automatic segmentation of atrial imaging. **(B)** Late-gadolinium enhancement (LGE) imaging with registered segmentation overlaid in red. Anatomical models for each patient were segmented from CE-MRA images and post-processed to create meshes suitable for running biophysical simulations. **(C)** Atrial regions were labeled as follows: left atrial (LA) body (light blue), LA appendage (dark blue), left superior pulmonary vein (pink), left inferior pulmonary vein (orange), right superior pulmonary vein (yellow), and right inferior pulmonary vein (green). **(D)** Atrial fibers from a human atrial *ex-vivo* DTMRI atlas were incorporated using the universal atrial coordinate system, and endocardial fibers are visualized here as streamlines. **(E)** Fibrotic tissue was added through registration of LGE-MRI data. **(F)** AF simulation. AF simulations were run on the models using Cardiac Arrythmia Research package (CARPentry) software. The images included in this figure are an example of one of the virtual patient models of the cohort.

The Courtemanche–Ramirez–Nattel human atrial ionic model (Courtemanche et al., 1998) was used with the following changes: maximal I_{Kr} conductance was multiplied by 1.6 to represent LA tissue; maximal I_{Na} conductance was multiplied by 2 to ensure physiological action potential upstroke velocities; and maximal I_{K1} conductance was multiplied by 0.8 for a closer agreement with clinical restitution data (Krummen et al., 2012). To incorporate the effects of electrical heterogeneity, the cell model for the LA model was modified as follows for the LA appendage region: maximal I_{CaL} conductance was multiplied by 1.06 and maximal I_{to} conductance was multiplied by 0.67 (Seemann et al., 2006). For the PV region, the following changes were applied to the LA model maximal conductances: $g_{to} \times 0.75$, $g_{CaL} \times 0.75$, $g_{Kr} \times 1.5$, and $g_{Ks} \times 0.67$ (Dorn et al., 2012; Roney et al., 2016). AF electrical remodeling was incorporated in all atrial regions by reducing the maximal ionic conductances of I_{to}, I_{Kur}, and I_{CaL} by 50, 50, and 70%, respectively, following Courtemanche et al. (1999). Longitudinal conductivity was assigned as 0.4 S/m and transverse as 0.1 S/m.

Fibrosis Modeling

The effects of fibrotic remodeling were included for each anatomy according to LGE-MRI intensity values (see **Figure 1E**). Fibrotic remodeling was modeled as regions of conduction slowing together with electrophysiological changes. LGE intensity was normalized for assigning tissue conductivity regions using the maximum and minimum values. Tissue conductivities were

[1]www.cemrgapp.com
[2]www.meshlab.net
[3]www.paraview.org
[4]www.mmgtools.org
[5]https://git.opencarp.org/openCARP/meshalyzer

then modified to result in 100% conduction velocity in regions of 0–56% normalized LGE intensity; 80% conduction velocity for 56–60% LGE; 60% conduction velocity for 60–64% LGE, and 40% conduction velocity for >64% normalized LGE intensity (Krueger et al., 2014). For electrophysiological remodeling, LGE intensity was rescaled by subtracting the mean blood pool intensity and dividing by the standard deviation (SD). Ionic properties were modified to represent the effects of elevated TGF-ß1 (maximal ionic conductances were rescaled in regions with LGE intensity >3 SDs above the mean of the blood pool as follows: 50% of the regional ionic model value of gK1, 60% of gNa, and 50% of gCaL; Avila et al., 2007; Ramos-Mondragón et al., 2011; Roney et al., 2016; Zahid et al., 2016a). To identify fibrotic regions, LGE-MRI maps were thresholded at 3 SDs above the blood pool mean and separated into different regions using a connected component analysis (Roney et al., 2016).

AF Induction and Post-processing

Atrial fibrillation was equivalently initiated for each anatomy (see **Figure 1F**) by setting initial conditions for each simulation which corresponded to four spiral wave re-entries (Matene et al., 2014; Roney et al., 2020). This set-up was defined using the universal atrial coordinate system (Roney et al., 2019) as an activation time field with two Archimedean spirals on each of the posterior and anterior walls, with opposite chirality for adjacent spirals. AF induction is described in more detail in the **Supplementary Material** and **Supplementary Figure 3**.

Arrhythmia simulations were post-processed to identify the PS locations for 15 s of arrhythmia data. Spatial PS density maps were calculated using our previous methodology (Roney et al., 2016). To identify regions of high PS density, termed *PS hotspots*, PS density maps were thresholded at 1 SD above the mean and separated into different regions using a connected component analysis.

Ablation Modeling

We tested six different ablation approaches: (i) PVI alone, modeled as wide-area encirclement of the pulmonary veins; PVI together with: (ii) roof and inferior lines to model posterior wall box isolation (*box* ablation); (iii) isolating the largest fibrotic area (identified as high LGE-MRI intensity; *single fibrosis* ablation); (iv) isolating all fibrotic areas (*all fibrosis* ablation); (v) isolating the largest driver region (identified as high PS density; *single PS hotspot* ablation); and (vi) isolating all driver regions (*all PS hotspots* ablation).

To automate ablation lesion application and to produce consistent lesions across anatomies, the six different ablation approaches (see **Supplementary Figure 4**) were defined as follows. PVI was applied at a fixed distance threshold from the junction of the LA body with the pulmonary veins. Roof and inferior lines for the box isolation approach were defined using the universal atrial coordinate system at the same coordinate locations across the virtual cohort (Roney et al., 2019). To identify fibrotic areas for ablation, LGE-MRI maps were first thresholded at 3 SDs above the blood pool mean (Roney et al., 2016). Thresholded tissue was then separated into connected component regions, and the area of each region was calculated. To isolate the largest fibrotic area, the region with the largest area was selected for ablation and joined to the closest mesh boundary or ablation lesion – in this case, either the mitral valve or the PVI lesions. To isolate all fibrotic areas, a lesion set was constructed as PVI together with each fibrotic region joined to either the closest mesh boundary or lesion within the set. Driver region ablation lesions were performed in the same way as fibrosis region ablation but according to PS density maps thresholded at 1 SD above the mean. **Figure 2** shows the six ablation approaches for one anatomy in the cohort.

Ablation responses were automatically classified as either termination, macroreentry, or AF. Macroreentry was classified as cases with dominant frequency <4.7 Hz, and AF as cases with dominant frequency >4.7 Hz (Ng et al., 2006; Jarman et al., 2012).

Random Forest Classifier

Random forest classifiers were trained to predict binary ablation response for three sets of input variables, corresponding to (a) imaging metrics alone; (b) imaging and electrical metrics; and (c) imaging, electrical, and lesion metrics. The imaging metrics used were the total LA body surface area (the surface area of the light blue region in **Figure 1A**), the total pulmonary vein surface area (the sum of the surface areas of the pink, orange, yellow, and green regions in **Figure 1A**), and the total fibrotic tissue surface area (thresholded at 3 SDs above the blood pool mean).

The electrical metrics were measured from pre-ablation AF simulations and included the mean dominant frequency and the total PS hotspot area (thresholded at 1 SD above the mean). Five lesion metrics were calculated on the atrial mesh after ablated tissue was removed. Three metrics were calculated in the largest connected region post-ablation as the remaining hotspot area, LA surface area, and fibrosis area (calculated as the remaining tissue area with reduced conductivity values i.e.,

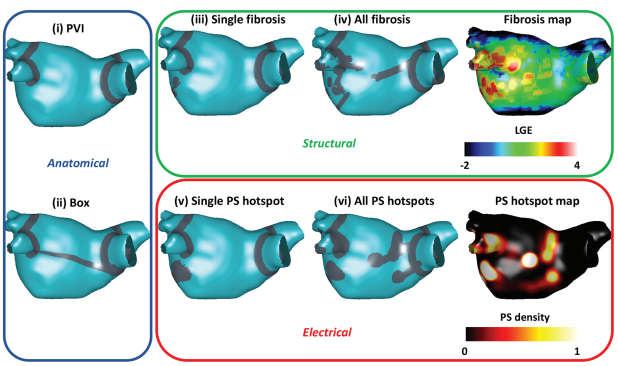

FIGURE 2 | Anatomical, electrical, and structural ablation approaches. The six ablation approaches are indicated by the gray ablation lesions. Anatomical approaches, shown in the blue box, include pulmonary vein isolation (PVI) and box ablation. Structural ablation approaches, shown in the green box, include ablating either a single fibrosis area or all areas of fibrosis on the LGE intensity map. Electrical approaches, shown in the red box, include ablating either a single phase singularity (PS) hotspot or all PS hotspots based on the pre-ablation PS hotspot map.

normalized LGE intensity value >56%). The width of the roof metric was calculated as the width of the largest connected region measured at a universal atrial coordinate value of 0.5 (this is zero in the case of box isolation as the roof is not in the largest connected region post-ablation). The metric corresponding to the smallest channel height post-ablation was calculated as the minimum Euclidean distance between the mitral valve and ablation lesions of significant size (defined as those with area greater than 80% of the second largest ablation lesion).

We split the dataset into training and test sets as a 70:30 split ensuring that all ablation types for a given anatomical model were in the same set. To select hyperparameters for the random forest classifiers, we performed 5-fold cross validation with a balanced-accuracy criterion on the number of estimators, the maximum depth, and the minimum number of samples per leaf. The values tested are given in **Table 1**. These hyperparameters were then used for the random forest model that was trained using a balanced weighting. Accuracy, precision, and recall were calculated on the test set for the three random forest classifiers. To assess the importance of the input features to the trained random forest classifier, we used the SHapley Additive exPlanations (SHAP) methodology (Štrumbelj and Kononenko, 2014). This was performed using scikit-learn in python, using the functions RandomForestClassifier and GridSearchCV (Varoquaux et al., 2015), and the SHAP toolbox (available at: https://github.com/slundberg/shap).

We compared random forest classification to both logistic regression (LogisticRegression in scikit-learn) and support vector machine classifiers (SVCs in scikit-learn), following 5-fold cross-validation to select the optimal hyperparameters.

TABLE 1 | Hyperparameter values tested using cross-validation for training random forest classifiers.

Hyperparameter	Values tested
Number of estimators	10, 20, 50, 70, 80, 100
Maximum depth	4, 8, 16
Minimum number of samples per leaf	5, 10, 20

TABLE 2 | Patient characteristics calculated from the atrial models for the paroxysmal and persistent AF cohorts.

	Paroxysmal (n = 20)	Persistent (n = 30)
Left atrial surface area (cm^2)	102.1 ± 19.0	120.1 ± 23.3
Pulmonary vein surface area (cm^2)	28.1 ± 7.29	30.4 ± 8.73
Fibrotic tissue surface area (cm^2)	23.2 ± 7.89	26.2 ± 5.78

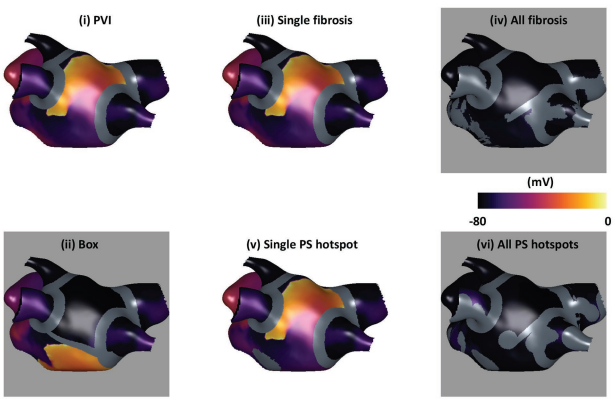

FIGURE 3 | Example transmembrane voltage snapshots demonstrating the six ablation approaches. Plots are shown 1.5 s post-ablation, with ablation lesions overlaid in gray. Ablation response is indicated by background color: responders (AT or termination) are shown with a gray background, and non-responders (AF) with white.

RESULTS

Paroxysmal and Persistent AF Model Ablation Outcomes

Patient characteristics including LA, pulmonary vein and fibrotic tissue surface area calculated from the atrial models are given in **Table 2** for each of the paroxysmal and persistent AF cohorts. **Supplementary Figure 5** shows that LGE-MRI intensity values and distributions vary across the cohort.

The average electrical metrics measured pre-ablation for the cohort were a mean dominant frequency of 4.86 ± 0.11 Hz and a mean total PS hotspot area of 27.7 ± 9.12 cm^2. **Supplementary Figure 6** shows that AF duration varies between models in the cohort. The mean AF duration is 11.0 ± 4.77 s, with 11 cases between 2–5 s, 6 between 5–10 s, 10 between 10–14.9 s, and 23 over 15 s.

Ablation simulations demonstrated a range of outcomes, which were classified as AF, atrial tachycardia (AT), or termination. **Figure 3** shows transmembrane voltage snapshots 1.5 s after each of the six ablation approaches for one virtual patient. For this example, AF continued after three of the ablation strategies (PVI, single PS hotspot ablation, and single fibrosis area ablation); AF converted to AT after box isolation; and the arrhythmia terminated after all PS hotspot ablation and after all fibrosis area ablation. The three AF cases were labeled acute ablation non-responders, and AT and termination cases were labeled acute ablation responders.

Table 3 shows the average lesion metrics for the cohort, calculated as properties of the mesh with ablation lesion sets. These include the following metrics calculated in the largest connected region post-ablation: the remaining hotspot area, LA surface area, and fibrosis area; as well as the width of the roof and the smallest channel height in the post-ablation mesh.

Ablation outcomes, classified as AF, AT, or termination, are shown in **Figure 4** for the whole virtual paroxysmal and persistent AF cohort with the six ablation strategies. The ablation approaches are ordered by the largest area of connected non-ablated LA tissue in the post-ablation mesh, with PVI resulting in the largest connected area (corresponding to the smallest ablation area), and box resulting in the smallest connected area on average across the cases. This plot shows that ablating all PS hotspots results, on average, in a larger connected area post-ablation than box isolation, but more of the cases converted to AT or terminated. This demonstrates that it is not simply the area of

TABLE 3 | Average lesion metrics across the virtual cohort for the different ablation approaches.

Property	PVI	Box	Single hotspot	All hotspots	Single fibrosis	All fibrosis
Remaining LA surface area (cm^2)	90.1 ± 22.4	70.2 ± 19.2	87.1 ± 22.2	80.2 ± 20.6	88.3 ± 21.8	82.9 ± 20.2
Remaining fibrosis area (cm^2)	32.6 ± 22.9	25.3 ± 19,6	30.1 ± 22.5	25.6 ± 20.5	30.9 ± 23.1	27.1 ± 22.4
Remaining hotspot area (cm^2)	21.0 ± 8.02	19.6 ± 7.40	15.4 ± 7.08	0.00 ± 0.00	17.9 ± 7.29	13.1 ± 7.05
Conducting roof width (cm)	2.84 ± 1.05	0.00 ± 0.00	2.75 ± 1.14	2.60 ± 1.13	2.83 ± 1.05	2.81 ± 1.06
Smallest post-ablation channel height (cm)	1.96 ± 0.81	1.87 ± 0.79	1.89 ± 0.89	1.02 ± 0.87	1.96 ± 0.82	1.34 ± 0.98

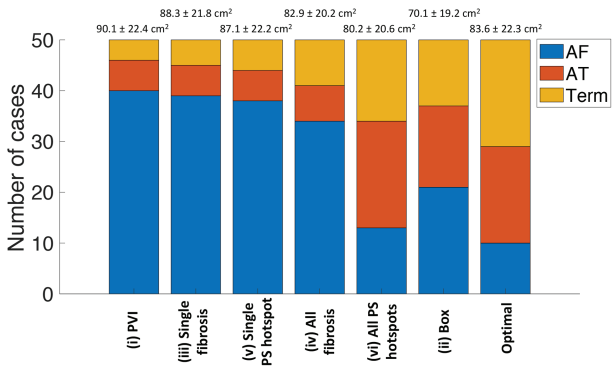

FIGURE 4 | Simulated ablation outcomes classified as AF, AT, or termination varies between the six ablation approaches. The strategies are ordered by the largest area of connected non-ablated tissue in the post-ablation mesh, which are listed as mean and standard deviation (SD) values above the bar chart. The number of outcomes classified as AF is in blue, AT in red, and termination in yellow. The final bar shows the distribution of outcomes if the optimal treatment was chosen for each virtual patient. AF, atrial fibrillation; AT, atrial tachycardia; Term, termination; PVI, pulmonary vein isolation; PS, phase singularity.

ablated tissue that is important, but also the spatial location of ablation lesions. The final bar of **Figure 4** shows the distribution of outcomes if the optimal treatment was chosen for each virtual patient. The optimal treatment was defined as the strategy that results in termination, or if no termination was possible, strategies that resulted in AT were selected. If multiple strategies resulted in the same outcome, the strategy that resulted in the smallest ablation burden was selected. Selecting the optimal treatment for each patient has a greater number of termination and AT cases than any of the six ablation approaches, and results in a larger connected surface area than ablating all PS hotspots.

For 10 of the virtual patients, all ablation strategies tested resulted in AF continuation. These cases are therefore non-responders to the six strategies used. Conversely, for nine of the virtual patients, AF converted to AT or terminated for all six strategies. For each case, we ranked all strategies that result in an acute ablation response by decreasing remaining tissue surface area. Optimal ablation approaches were all driver regions (46%), PVI (20%), box (6%), all fibrosis areas (4%), single driver regions (2%), and single fibrosis area (2%). Twenty percentage of cases remained in AF for all ablation strategies.

Supplementary Table 1 shows that the methodology used for modeling atrial fibrosis and tuning model properties affects the predicted ablation outcome.

Predicting Outcome Using Random Forest Classifiers

There are many factors that contribute to the continuation of AF. We used a machine learning classifier to identify the factors that predicted response to ablation strategies. To predict ablation response for the virtual patients, we trained random forest classifiers with the following input variables: (a) imaging metrics alone; (b) imaging and electrical metrics; and (c) imaging, electrical, and lesion metrics. Optimal hyperparameters were 50 estimators, a maximum depth of 8, and a minimum number of samples per leaf of 5. The accuracy, precision, and recall measured on the test set were as follows for each of the three classifiers: (a) 0.72, 0.73, and 0.72; (b) 0.73, 0.74, and 0.73; and (c) 0.83, 0.85, and 0.83. As such, the addition of lesion metrics to the model improves its predictive capability compared to simply including the ablation type. The effects of the choice of classifier were tested by also training a logistic regression and SVC. Using all input variables (imaging, electrical, and lesion metrics), the accuracy, precision, and recall on the test set were lower for the trained logistic regression: 0.67, 0.69, and 0.67, and for the trained SVC: 0.76, 0.76, and 0.76.

SHapley Additive exPlanations analysis was performed to determine the relative importance of each variable to the classifier prediction. For classifiers (a) and (b), the type of ablation applied was the most important feature for the prediction. For the imaging metric model, the total fibrosis area and the total LA surface area were the next most important variables, where higher values of each were more likely to be associated with AF post-ablation. For the imaging and electrical metric model, this was also the case, and electrical metrics were less important.

Figure 5 shows the SHAP summary plot for the combined imaging, electrical, and lesion metrics model. Each point represents a variable value for one of the 300 cases. The horizontal location indicates whether the effect leads to a higher or lower predicted probability (with 0 as responder and 1 as non-responder). Blue points indicate a low value, and red points indicate a high value for an observation. Each of the following lesion metrics was found to be positively correlated with positive prediction (AF, non-responder): remaining hotspot area, remaining fibrosis area, post-ablation roof width, and remaining LA surface area.

Effects of Lesion Metrics on Acute Ablation Response

The SHAP analysis highlighted that the remaining pre-ablation PS hotspot area following ablation is a key determinant of AF termination. As an example of this, **Figure 6** shows PS

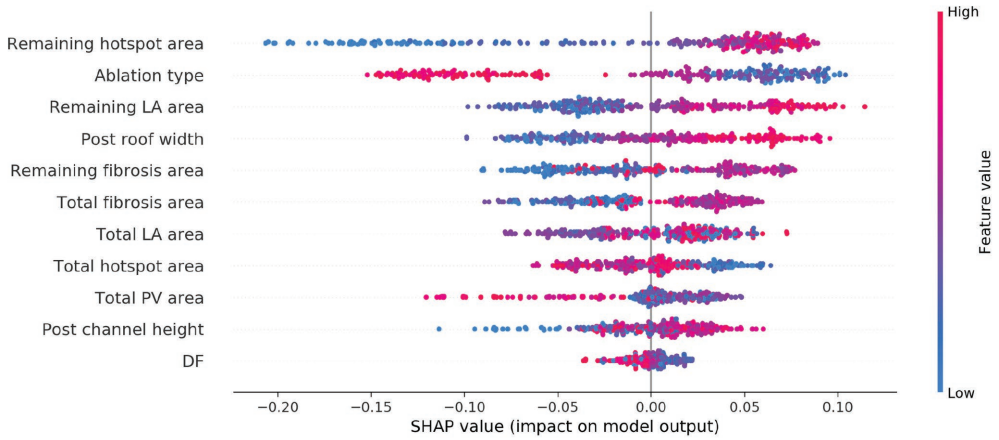

FIGURE 5 | SHapley Additive exPlanations (SHAP) variable importance plot for the trained classifier using imaging, modeling, and ablation lesion metrics. Variables are ranked by the SHAP analysis in descending order of importance, with a red or blue color indicating a high or low value for the observation, respectively.

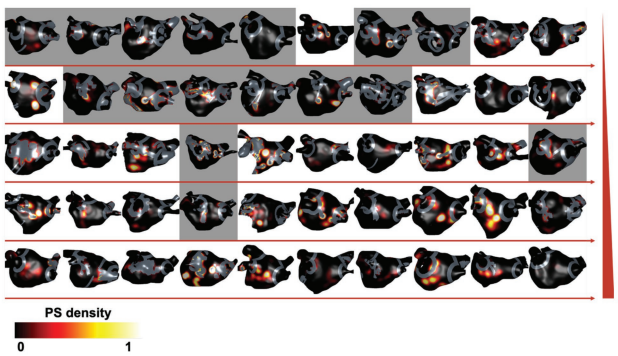

FIGURE 6 | Remaining PS hotspot areas affect ablation outcome. Pre-ablation PS hotspot maps are shown for each virtual patient with ablation lesions targeting all fibrosis regions (ablation strategy iv) overlaid in gray. Cases are ordered by increasing remaining PS hotspot area, shown by directions of horizontal red arrows and increasing by row, indicated by the red vertical ramp. The background color indicates acute ablation outcome: gray for responders (AT or termination) and white for non-responders (AF). There are more acute responders for cases with low than high remaining PS hotspot areas.

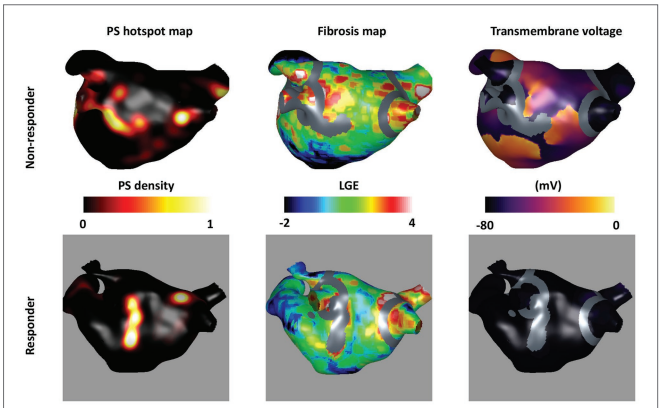

FIGURE 7 | Non-isolated fibrosis area affects ablation outcome. The top row shows an acute non-responder and the bottom row shows an acute responder to the single PS hotspot ablation strategy (strategy number v). For each, the pre-ablation PS hotspot map is shown in the first column; the fibrosis intensity map in the second column; and a transmembrane voltage map at 1.5 s post-ablation in the third column. Ablation lesions corresponding to the largest PS hotspot are shown in gray overlaid on the fibrosis maps and transmembrane voltage maps. There is a larger area of non-ablated fibrosis for the largest post-ablation tissue region in the top row (47.9 cm^2) than the bottom row (1.57 cm^2) suggesting that non-isolated fibrosis area affects ablation outcome.

hotspot maps with ablation lesions that targeted all fibrosis regions indicated in gray on the atrial shell. The maps are shown in order of increasing remaining PS hotspot area, with background color indicating acute ablation outcome (gray for responders and white for non-responders). There are more acute responders for low than high remaining PS hotspot areas. This is indicated by a higher number of maps with a gray background in the upper rows of the figure.

The area of fibrosis remaining post-ablation was also found to be an important factor for predicting ablation outcome. **Figure 7** shows an example of cases with high and low remaining fibrosis area following single PS hotspot ablation. The case with a larger non-isolated fibrosis area (47.9 cm^2) shown in the top row is an acute ablation non-responder since AF continues post-ablation, while a case with a smaller non-isolated fibrosis area (1.57 cm^2) converts post-single PS hotspot ablation.

DISCUSSION

Main Findings

This virtual patient cohort study demonstrates the use of a simulation and a machine learning platform for trialing and analyzing different ablation approaches. We present an efficient pipeline for constructing models from LGE-MRI imaging data (4.5 h from imaging to patient-specific model with DTMRI fibers, regional heterogeneity, and fibrotic remodeling), which we utilized to generate the first cohort of atrial models with fibers from a DTMRI atlas and the largest cohort of atrial models constructed from LGE-MRI data. Specifically, we automatically applied six ablation approaches that target features of the anatomical, structural,

or electrical AF substrates to 20 paroxysmal and 30 persistent patient-specific models. Optimal ablation approaches in order of prevalence were all driver regions (46%), PVI (20%), box (6%), all fibrosis areas (4%), single driver regions (2%), and single fibrosis area (2%). Around 20% of cases remained in AF for all ablation strategies. Randomized controlled trials have answered some of the questions regarding ablation of long-standing persistent AF; however, the critical question of technique over debulking persists (Brooks et al., 2010). We show that optimal outcomes require targeting different ablation strategies in different patients and that targeting the AF substrate can be effective beyond its effect on debulking the atria. Overall, our study suggests that both patient-specific fibrosis properties and driver locations are important for planning ablation approaches, and the distribution of lesions is important for predicting an acute response.

Anatomical Ablation Approaches

We observed a variation in the outcome of the six ablation approaches used across the cohort of models constructed (**Figures 3, 4**). For example, PVI ablation alone was sufficient for an acute response – and hence the optimal ablation approach – for 20% of the virtual patient models. Lim et al. (2015) reported a higher acute AF termination rate with PVI of 30–60% across multiple clinical trials. This value may be lower in our study because we only studied the ability of the atria to sustain rather than initiate AF; the significant impact of trigger removal on outcome is therefore not captured by our current model. The box ablation lesion set applied in our study converted AF to either AT or termination for 58% of the virtual patient models (**Figure 4**). However, the box approach removes a large area of LA tissue and so this approach was optimal for only 6% of these models. This success rate could be improved by applying a patient-specific box size and location depending on the individual patient conduction and repolarization properties. Williams et al. (2019) proposed an approach for targeting box ablation lesion sets depending on the patient-specific electrical size. This proposition should also be considered when aiming to achieve a greater success rate.

Structural Ablation Approaches

Several clinical centers target the fibrotic substrate during ablation therapy to remove or isolate fibrotic tissue which may or may not anchor electrical drivers. Fibrotic tissue can be identified through either electroanatomic mapping (Kottkamp et al., 2016) or atrial imaging (Cochet et al., 2015). In our study, we simulated ablation of fibrotic areas identified from LGE-MRI data. The area of fibrotic tissue in the largest remaining tissue region post-ablation was found to be important for predicting ablation response (**Figure 7**). This suggests that identifying fibrotic tissue either through imaging or electroanatomic mapping is important, and the choice of measuring modality is likely to affect the identified substrate. However, our findings also indicate that structural ablation approaches targeting fibrotic tissue areas were not as successful as electrical ablation approaches targeting PS driver hotspots. Thus, it may be important to map or predict using simulations, the distribution of electrical drivers when planning ablation therapy and fibrosis imaging alone may not be sufficient to guide ablation in all cases.

Electrical Ablation Approaches

Ablating all PS driver hotspots was the most effective ablation strategy in our study; resulting in a positive response for 74% of cases and represented the optimal approach for 46% of cases. This suggests that PS hotspots play a key role in driving AF (**Figure 7**). However, despite ablating all the PS hotspots identified through pre-ablation simulation processing, 26% of cases were still able to sustain AF. This suggests that not all possible PS hotspots are identified during a single AF episode, motivating the methodology of Boyle et al. (2019) that identifies different driver locations through different AF initiation protocols. Narayan et al. (2012) demonstrated high success rates by ablating focal and re-entrant drivers identified through phase and activation mapping of basket catheter data (Schricker and Zaman, 2015). Ensuring the correct classification of phase singularities is critical for targeting ablations because wavefront break up does not represent an equal target to a stable rotor. An optimal method of ablation likely involves an appropriate combination of anatomical, structural, and electrical ablation approaches.

Comparison With Other Ablation Simulation Studies

There is a variation between both clinical and simulation studies in the ablation approaches utilized. We joined ablation lesions to their closest boundary similar to the study of Weiss et al. (2016) which showed that ablating from the center of a mother rotor to a boundary terminated the arrhythmia. Shim et al. (2017) compared persistent AF ablation using empirically chosen ablation lesion sets (n = 55) to simulation guided lesion sets (n = 53), chosen from five different lesion sets (PVI, three linear ablations, and one electrogram-guided ablation). They demonstrated that ablation guided by simulations was feasible in clinical practice and not inferior to empirically chosen ablation lesion sets. Bayer et al. (2016) performed a simulation study to compare (1) PVI with roof and mitral lines; (2) circles, lines, or crosses near rotor locations; and (3) 4–8 lines applied to streamline the patient-specific sinus rhythm activation sequence. They found that streamlining activation sequences is a robust alternative ablation approach for cases where other approaches do not terminate AF. This represents a further ablation pattern that could be tested using our simulation and machine learning methodology. In addition, Roney et al. (2018) used a virtual pilot clinical study to predict whether ablating interatrial connections would return the right atrium to sinus rhythm. Our current study could be extended to biatrial meshes to investigate the importance of the right atrium in AF. In a pioneering clinical trial, the optimal target identification *via* modeling of arrhythmogenesis approach clinically ablates fibrotic tissue identified as an ablation target using computational simulations (Boyle et al., 2019).

Designing Patient-Specific Lesion Sets

We have developed a virtual patient cohort that can be used to predict the optimal ablation strategy for a given patient. Our results (**Figure 4**) demonstrate that it is not simply the area of ablated tissue that is important in determining ablation outcome, but also the spatial location of ablation lesions in relation to the anatomy, fibrotic tissue distribution and driver positions, and necessitating patient-specific therapy. While providing mechanistic understanding, current simulation strategies take extensive time to create, simulate, and analyze the model output. We have shown that with a limited dataset we can create a classifier with accuracy of 0.83. Increasing the dataset size or number of features may increase the classifier accuracy. Alternately, the simulation-trained classifier could be used to initialize a classifier based on clinical data to accelerate learning from smaller clinical data sets. In addition, the classifier could be used together with a minimal cut analysis to find a successful ablation approach that minimizes ablation area and maximizes the area of conducting tissue (Zahid et al., 2016b).

Limitations

The results of our simulation predictions need to be compared to the clinical ablation approach and outcome. Our study investigates whether an arrhythmia can be sustained and does not include the effects of triggered beats. There was no significant difference between paroxysmal and persistent virtual patient ablation outcomes in our study. This may be because we did not simulate the effects of triggered beats for initiating AF. We did not include personalized electrophysiology in our simulations, and this may affect AF properties and ablation outcome. Similar to previous studies (Roney et al., 2016), our current study shows that the modeling methodology used for incorporating the effects of atrial fibrosis affects simulation outcome. Future studies should optimize the choice of fibrosis modeling methodology through comparison with clinical outcome. In addition, we did not model the effects of variable wall thickness, which has been shown to affect PS stability and meander (Roy et al., 2018). We performed monodomain simulations, and although the differences with bidomain simulations for paced activation have been shown to be small (Potse et al., 2006), differences for our AF simulations should be investigated. We only included 50 patient-specific models which are insufficient to predict optimal ablation pattern for the six approaches simulated. We simulated and predicted acute outcome, which while correlated with, is not equivalent to long term outcome (Lim et al., 2015). We joined ablated regions to their closest region with additional ablation lines to avoid islands of ablated tissue causing re-entry; however, how best to do this requires further investigation.

CONCLUSION

Overall, our virtual cohort study has demonstrated the importance of considering the effect of patient-specific fibrosis properties and driver locations when planning ablation approaches. It is important to consider these factors and the distribution of lesions in order to select the optimal ablation strategy for each patient.

DATA AVAILABILITY STATEMENT

The raw data supporting the conclusions of this article will be made available by the authors, without undue reservation.

ETHICS STATEMENT

The studies involving human participants were reviewed and approved by regional ethics committee (17/LO/0150 and 15/LO/1803). The patients/participants provided their written informed consent to participate in this study.

AUTHOR CONTRIBUTIONS

CR and SN conceived and designed the study. CR, MB, and SN drafted the manuscript. CR, MB, and AM constructed atrial models. CR developed the model construction pipeline, ran the simulations, and analyzed the data. CC and RB helped build the fiber atlas used in this study. OR and JS-L developed CemrgApp segmentation software. EV developed meshalyzer visualization software. EV and GP developed CARPentry simulation software. IS, JW, LO'N, and SW collected and segmented atrial imaging data. SN, SW, and MO'N provided supervision. All authors contributed to the article and approved the submitted version.

FUNDING

CR is funded by a Medical Research Council Skills Development Fellowship (MR/S015086/1). SW is supported by a British Heart Foundation Fellowship (FS 20/26/34952). SN acknowledges support from the UK Engineering and Physical Sciences Research Council (EP/M012492/1, NS/A000049/1, and EP/P01268X/1), the British Heart Foundation (PG/15/91/31812, PG/13/37/30280), and Kings Health Partners London National Institute for Health Research (NIHR) Biomedical Research Centre. This work was supported by the Wellcome/EPSRC Centre for Medical Engineering (WT 203148/Z/16/Z).

ACKNOWLEDGMENTS

We thank NVIDIA for donating a Titan V GPU for our research. We acknowledge support from King's College London *via* King's Undergraduate Research Fellowships and the KCL Parents' & Carer's Fund.

SUPPLEMENTARY MATERIAL

The Supplementary Material for this article can be found online at: https://www.frontiersin.org/articles/10.3389/fphys.2020.572874/full#supplementary-material

REFERENCES

Ahrens, J., Geveci, B., and Law, C. (2005). "ParaView: An end-user tool for large-data visualization" in *Visualization Handbook*. Elsevier Munchen.

Avila, G., Medina, I. M., Jiménez, E., Elizondo, G., and Aguilar, C. I. (2007). Transforming growth factor-β1 decreases cardiac muscle L-type Ca^{2+} current and charge movement by acting on the Cav1.2 mRNA. *Am. J. Physiol. Heart Circ. Physiol.* 292, H622–H631. doi: 10.1152/ajpheart.00781.2006

Bayer, J. D., Roney, C. H., Pashaei, A., Jaïs, P., and Vigmond, E. J. (2016). Novel radiofrequency ablation strategies for terminating atrial fibrillation in the left atrium: a simulation study. *Front. Physiol.* 7:108. doi: 10.3389/fphys.2016.00108

Boyle, P. M., Zghaib, T., Zahid, S., Ali, R. L., Deng, D., Franceschi, W. H., et al. (2019). Computationally guided personalized targeted ablation of persistent atrial fibrillation. *Nat. Biomed. Eng.* 3, 870–879. doi: 10.1038/s41551-019-0437-9

Brooks, A. G., Stiles, M. K., Laborderie, J., Lau, D. H., Kuklik, P., Shipp, N. J., et al. (2010). Outcomes of long-standing persistent atrial fibrillation ablation: a systematic review. *Heart Rhythm* 7, 835–846. doi: 10.1016/j.hrthm.2010.01.017

Calkins, H., Hindricks, G., Cappato, R., Kim, Y. H., Saad, E. B., Aguinaga, L., et al. (2018). 2017 HRS/EHRA/ECAS/APHRS/SOLAECE expert consensus statement on catheter and surgical ablation of atrial fibrillation. *Europace* 20, e1–e160. doi: 10.1093/europace/eux274

Chubb, H., Karim, R., Mukherjee, R., Williams, S. E., Whitaker, J., Harrison, J., et al. (2019). A comprehensive multi-index cardiac magnetic resonance-guided assessment of atrial fibrillation substrate prior to ablation: prediction of long-term outcomes. *J. Cardiovasc. Electrophysiol.* 30, 1894–1903. doi: 10.1111/jce.14111

Cignoni, P., Callieri, M., Corsini, M., Dellepiane, M., Ganovelli, F., and Ranzuglia, G. (2008). MeshLab: an open-source mesh processing tool in 6th Eurographics Italian Chapter Conference 2008 - Proceedings; July 2, 2008.

Cochet, H., Mouries, A., Nivet, H., Sacher, F., Derval, N., Denis, A., et al. (2015). Age, atrial fibrillation, and structural heart disease are the main determinants of left atrial fibrosis detected by delayed-enhanced magnetic resonance imaging in a general cardiology population. *J. Cardiovasc. Electrophysiol.* 26, 484–492. doi: 10.1111/jce.12651

Courtemanche, M., Ramirez, R. J., and Nattel, S. (1998). Ionic mechanisms underlying human atrial action potential properties: insights from a mathematical model. *Am. J. Phys.* 275, H301–H321. doi: 10.1152/ajpheart.1998.275.1.H301

Courtemanche, M., Ramirez, R. J., and Nattel, S. (1999). Ionic targets for drug therapy and atrial fibrillation-induced electrical remodeling: insights from a mathematical model. *Cardiovasc. Res.* 42, 477–489. doi: 10.1016/s0008-6363(99)00034-6

Dorn, A., Krueger, M. W., Seemann, G., and Doessel, O. (2012). Modelling of heterogeneous human atrial electrophysiology. *Biomed. Tech.* 57, 350–353. doi: 10.1515/bmt-2012-4215

Haissaguerre, M., Shah, A. J., Cochet, H., Hocini, M., Dubois, R., Vigmond, E., et al. (2016). Intermittent drivers anchoring to structural heterogeneities as a major pathophysiologic mechanism of human persistent atrial fibrillation. *J. Physiol.* 9, 2387–2398. doi: 10.1113/JP270617

Handa, B. S., Roney, C. H., Houston, C., Qureshi, N. A., Li, X., Pitcher, D. S., et al. (2018). Analytical approaches for myocardial fibrillation signals. *Comput. Biol. Med.* 102, 315–326. doi: 10.1016/j.compbiomed.2018.07.008

Hwang, M., Park, J., Lee, Y., Park, J. H., Choi, S. H., Shim, E. B., et al. (2015). Fibrillation number based on wavelength and critical mass in patients who underwent radiofrequency catheter ablation for atrial fibrillation. *IEEE Trans. Biomed. Eng.* 62, 673–679. doi: 10.1109/TBME.2014.2363669

Jarman, J. W. E., Wong, T., Kojodjojo, P., Spohr, H., Davies, J. E., Roughton, M., et al. (2012). Spatiotemporal behavior of high dominant frequency during paroxysmal and persistent atrial fibrillation in the human left atrium. *Circ. Arrhythm. Electrophysiol.* 5, 650–658. doi: 10.1161/CIRCEP.111.967992

Kazhdan, M., and Hoppe, H. (2013). Screened poisson surface reconstruction. *ACM Trans. Graph.* 32, 1–13. doi: 10.1145/2487228.2487237

Kottkamp, H., Berg, J., Bender, R., Rieger, A., and Schreiber, D. (2016). Box isolation of fibrotic areas (BIFA): a patient-tailored substrate modification approach for ablation of atrial fibrillation. *J. Cardiovasc. Electrophysiol.* 27, 22–30. doi: 10.1111/jce.12870

Kottkamp, H., Hindricks, G., Autschbach, R., Krauss, B., Strasser, B., Schirdewahn, P., et al. (2002). Specific linear left atrial lesions in atrial fibrillation: intraoperative radiofrequency ablation using minimally invasive surgical techniques. *J. Am. Coll. Cardiol.* 40, 475–480. doi: 10.1016/S0735-1097(02)01993-9

Krueger, M. W., Rhode, K. S., O'Neill, M. D., Rinaldi, C. A., Gill, J., Razavi, R., et al. (2014). Patient-specific modeling of atrial fibrosis increases the accuracy of sinus rhythm simulations and may explain maintenance of atrial fibrillation. *J. Electrocardiol.* 47, 324–328. doi: 10.1016/j.jelectrocard.2013.11.003

Krummen, D. E., Bayer, J. D., Ho, J., Ho, G., Smetak, M. R., Clopton, P., et al. (2012). Mechanisms of human atrial fibrillation initiation: clinical and computational studies of repolarization restitution and activation latency. *Circ. Arrhythm. Electrophysiol.* 5, 1149–1159. doi: 10.1161/CIRCEP.111.969022

Labarthe, S., Bayer, J., Coudière, Y., Henry, J., Cochet, H., Jaïs, P., et al. (2014). A bilayer model of human atria: mathematical background, construction, and assessment. *Europace* 16, iv21–iv29. doi: 10.1093/europace/euu256

Lim, H. S., Derval, N., Komatsu, Y., Zellerhoff, S., Denis, A., Shah, A. J., et al. (2015). Is ablation to termination the best strategy for ablation of persistent atrial fibrillation. *Circ. Arrhythm. Electrophysiol.* 8, 963–970. doi: 10.1161/CIRCEP.114.001721

Lim, H. S., Hocini, M., Dubois, R., Denis, A., Derval, N., Zellerhoff, S., et al. (2017). Complexity and distribution of drivers in relation to duration of persistent atrial fibrillation. *J. Am. Coll. Cardiol.* 69, 1257–1269. doi: 10.1016/j.jacc.2017.01.014

Marrouche, N. F., Wilber, D., Hindricks, G., Jais, P., Akoum, N., Marchlinski, F., et al. (2014). Association of atrial tissue fibrosis identified by delayed enhancement MRI and atrial fibrillation catheter ablation: the DECAAF study. *JAMA* 311, 498–506. doi: 10.1001/jama.2014.3

Matene, E., Vinet, A., and Jacquemet, V. (2014). Dynamics of atrial arrhythmias modulated by time-dependent acetylcholine concentration: a simulation study. *Europace* 16, iv11–iv20. doi: 10.1093/europace/euu255

Nademanee, K., McKenzie, J., Kosar, E., Schwab, M., Sunsaneewitayakul, B., Vasavakul, T., et al. (2004). A new approach for catheter ablation of atrial fibrillation: mapping of the electrophysiologic substrate. *J. Am. Coll. Cardiol.* 43, 2044–2053. doi: 10.1016/j.jacc.2003.12.054

Narayan, S. M., Patel, J., Mulpuru, S., and Krummen, D. E. (2012). Focal impulse and rotor modulation ablation of sustaining rotors abruptly terminates persistent atrial fibrillation to sinus rhythm with elimination on follow-up: a video case study. *Heart Rhythm* 9, 1436–1439. doi: 10.1016/j.hrthm.2012.03.055

Ng, J., Kadish, A. H., and Goldberger, J. J. (2006). Effect of electrogram characteristics on the relationship of dominant frequency to atrial activation rate in atrial fibrillation. *Heart Rhythm* 3, 1295–1305. doi: 10.1016/j.hrthm.2006.07.027

Pambrun, T., Denis, A., Duchateau, J., Sacher, F., Hocini, M., Jaïs, P., et al. (2019). MARSHALL bundles elimination, pulmonary veins isolation and lines completion for ANatomical ablation of persistent atrial fibrillation: MARSHALL-PLAN case series. *J. Cardiovasc. Electrophysiol.* 30, 7–15. doi: 10.1111/jce.13797

Pashakhanloo, F., Herzka, D. A., Ashikaga, H., Mori, S., Gai, N., Bluemke, D. A., et al. (2016). Myofiber architecture of the human atria as revealed by submillimeter diffusion tensor imaging. *Circ. Arrhythm. Electrophysiol.* 9:e004133. doi: 10.1161/CIRCEP.116.004133

Potse, M., Dubé, B., Richer, J., Vinet, A., and Gulrajani, R. M. (2006). A comparison of monodomain and bidomain reaction-diffusion models for action potential propagation in the human heart. *IEEE Trans. Biomed. Eng.* 53, 2425–2435. doi: 10.1109/TBME.2006.880875

Ramos-Mondragón, R., Vega, A. V., and Avila, G. (2011). Long-term modulation of Na^+ and K^+ channels by TGF-β1 in neonatal rat cardiac myocytes. *Pflugers Arch.* 461, 235–247. doi: 10.1007/s00424-010-0912-3

Razeghi, O., Solís-lemus, J. A., Lee, A. W. C., Karim, R., Corrado, C., Roney, C. H., et al. (2020). SoftwareX cemrgApp: an interactive medical imaging application with image processing, computer vision, and machine learning toolkits for cardiovascular research. *SoftwareX* 12:100570. doi: 10.1016/j.softx.2020.100570

Roney, C. H., Bayer, J. D., Zahid, S., Meo, M., Boyle, P. M. J., Trayanova, N. A., et al. (2016). Modelling methodology of atrial fibrosis affects rotor dynamics and electrograms. *Europace* 18, iv146–iv155. doi: 10.1093/europace/euw365

Roney, C. H., Bendikas, R., Pashakhanloo, F., Corrado, C., Vigmond, E. J., McVeigh, E. R., et al. (2020). Constructing a human atrial fibre atlas. *Ann. Biomed. Eng.* doi: 10.1007/s10439-020-02525-w [Epub ahead of print]

Roney, C. H., Pashaei, A., Meo, M., Dubois, R., Boyle, P. M., Trayanova, N. A., et al. (2019). Universal atrial coordinates applied to visualisation, registration and construction of patient specific meshes. *Med. Image Anal.* 55, 65–75. doi: 10.1016/j.media.2019.04.004

Roney, C. H., Williams, S. E., Cochet, H., Mukherjee, R. K., O'Neill, L., Sim, I., et al. (2018). Patient-specific simulations predict efficacy of ablation of interatrial connections for treatment of persistent atrial fibrillation. *Europace* 20, iii55–iii68. doi: 10.1093/europace/euy232

Roy, A., Varela, M., and Aslanidi, O. (2018). Image-based computational evaluation of the effects of atrial wall thickness and fibrosis on re-entrant drivers for atrial fibrillation. *Front. Physiol.* 9:1352. doi: 10.3389/fphys.2018.01352

Schricker, A. A., and Zaman, J. (2015). Role of rotors in the ablative therapy of persistent atrial fibrillation. *Arrhythmia Electrophysiol. Rev.* 4, 47–52. doi: 10.15420/aer.2015.4.1.47

Seemann, G., Höper, C., Sachse, F. B., Dössel, O., Holden, A. V., and Zhang, H. (2006). Heterogeneous three-dimensional anatomical and electrophysiological model of human atria. *Philos. Trans. A Math. Phys. Eng. Sci.* 364, 1465–1481. doi: 10.1098/rsta.2006.1781

Shim, J., Hwang, M., Song, J. S., Lim, B., Kim, T. H., Joung, B., et al. (2017). Virtual in-silico modeling guided catheter ablation predicts effective linear ablation lesion set for longstanding persistent atrial fibrillation: multicenter prospective randomized study. *Front. Physiol.* 8:792. doi: 10.3389/fphys.2017.00792

Sim, I., Razeghi, O., Karim, R., Chubb, H., Whitaker, J., O'Neill, L., et al. (2019). Reproducibility of atrial fibrosis assessment using CMR imaging and an open source platform. *JACC Cardiovasc. Imaging* 12, 2076–2077. doi: 10.1016/j.jcmg.2019.03.027

Sohns, C., Lemes, C., Metzner, A., Fink, T., Chmelevsky, M., Maurer, T., et al. (2017). First-in-man analysis of the relationship between electrical rotors from noninvasive panoramic mapping and atrial fibrosis from magnetic resonance imaging in patients with persistent atrial fibrillation. *Circ. Arrhythm. Electrophysiol.* 10:e004419. doi: 10.1161/CIRCEP.116.004419

Štrumbelj, E., and Kononenko, I. (2014). Explaining prediction models and individual predictions with feature contributions. *Knowl. Inf. Syst.* 41, 647–665. doi: 10.1007/s10115-013-0679-x

Varoquaux, G., Buitinck, L., Louppe, G., Grisel, O., Pedregosa, F., and Mueller, A. (2015). Scikit-learn: machine learning in python. *GetMobile Mob. Comput. Commun.* 19, 29–33. doi: 10.1145/2786984.2786995

Verma, A., Jiang, C. -Y., Betts, T. R., Chen, J., Deisenhofer, I., Mantovan, R., et al. (2015). Approaches to catheter ablation for persistent atrial fibrillation. *N. Engl. J. Med.* 372, 1812–1822. doi: 10.1056/NEJMoa1408288

Vigmond, E. J., Hughes, M., Plank, G., and Leon, L. J. (2003). Computational tools for modeling electrical activity in cardiac tissue. *J. Electrocardiol.* 36, 69–74. doi: 10.1016/j.jelectrocard.2003.09.017

Weiss, J. N., Qu, Z., and Shivkumar, K. (2016). Ablating atrial fibrillation: a translational science perspective for clinicians. *Heart Rhythm* 13, 1868–1877. doi: 10.1016/j.hrthm.2016.05.026

Williams, S. E., O'Neill, L., Roney, C. H., Julia, J., Metzner, A., Reißmann, B., et al. (2019). Left atrial effective conducting size predicts atrial fibrillation vulnerability in persistent but not paroxysmal atrial fibrillation. *J. Cardiovasc. Electrophysiol.* 30, 1416–1427. doi: 10.1111/jce.13990

Yu, H. T., Shim, J., Park, J., Kim, I. S., Kim, T. H., Uhm, J. S., et al. (2017). Pulmonary vein isolation alone versus additional linear ablation in patients with persistent atrial fibrillation converted to paroxysmal type with antiarrhythmic drug therapy: a multicenter, prospective, randomized study. *Circ. Arrhythm. Electrophysiol.* 10:e004915. doi: 10.1161/CIRCEP.116.004915

Zahid, S., Cochet, H., Boyle, P. M., Schwarz, E. L., Whyte, K. N., Vigmond, E. J., et al. (2016a). Patient-derived models link re-entrant driver localization in atrial fibrillation to fibrosis spatial pattern. *Cardiovasc. Res.* 110, 443–454. doi: 10.1093/cvr/cvw073

Zahid, S., Whyte, K. N., Schwarz, E. L., Blake, R. C., Boyle, P. M., Chrispin, J., et al. (2016b). Feasibility of using patient-specific models and the minimum cut algorithm to predict optimal ablation targets for left atrial flutter. *Heart Rhythm* 13, 1687–1698. doi: 10.1016/j.hrthm.2016.04.009

Conflict of Interest: The authors declare that the research was conducted in the absence of any commercial or financial relationships that could be construed as a potential conflict of interest.

frontiers in Physiology

ORIGINAL RESEARCH
published: 15 October 2020
doi: 10.3389/fphys.2020.570118

A Novel Tool for the Identification and Characterization of Repetitive Patterns in High-Density Contact Mapping of Atrial Fibrillation

Stef Zeemering[1]†, Arne van Hunnik[1†], Frank van Rosmalen[2], Pietro Bonizzi[3], Billy Scaf[1], Tammo Delhaas[2], Sander Verheule[1] and Ulrich Schotten[1]*

[1] Department of Physiology, Maastricht University Medical Center, Cardiovascular Research Institute Maastricht, Maastricht, Netherlands, [2] Department of Biomedical Engineering, Maastricht University Medical Center, Cardiovascular Research Institute Maastricht, Maastricht, Netherlands, [3] Department of Data Science and Knowledge Engineering, Maastricht University, Maastricht, Netherlands

OPEN ACCESS

Edited by:
Atul Verma,
University of Toronto, Canada

Reviewed by:
Flavia Ravelli,
University of Trento, Italy
Jason D. Bayer,
Université de Bordeaux, France

***Correspondence:**
Stef Zeemering
s.zeemering@maastrichtuniversity.nl

† These authors have contributed equally to this work

Specialty section:
This article was submitted to Cardiac Electrophysiology, a section of the journal Frontiers in Physiology

Received: *06 June 2020*
Accepted: *22 September 2020*
Published: *15 October 2020*

Citation:
Zeemering S, van Hunnik A, van Rosmalen F, Bonizzi P, Scaf B, Delhaas T, Verheule S and Schotten U (2020) A Novel Tool for the Identification and Characterization of Repetitive Patterns in High-Density Contact Mapping of Atrial Fibrillation. Front. Physiol. 11:570118. doi: 10.3389/fphys.2020.570118

Introduction: Electrical contact mapping provides a detailed view of conduction patterns in the atria during atrial fibrillation (AF). Identification of repetitive wave front propagation mechanisms potentially initiating or sustaining AF might provide more insights into temporal and spatial distribution of candidate AF mechanism and identify targets for catheter ablation. We developed a novel tool based on recurrence plots to automatically identify and characterize repetitive conduction patterns in high-density contact mapping of AF.

Materials and Methods: Recurrence plots were constructed by first transforming atrial electrograms recorded by a multi-electrode array to activation-phase signals and then quantifying the degree of similarity between snapshots of the activation-phase in the electrode array. An AF cycle length dependent distance threshold was applied to discriminate between repetitive and non-repetitive snapshots. Intervals containing repetitive conduction patterns were detected in a recurrence plot as regions with a high recurrence rate. Intervals that contained similar repetitive patterns were then grouped into clusters. To demonstrate the ability to detect and quantify the incidence, duration and size of repetitive patterns, the tool was applied to left and right atrial recordings in a goat model of different duration of persistent AF [3 weeks AF (3 wkAF, n = 8) and 22 weeks AF (22 wkAF, n = 8)], using a 249-electrode mapping array (2.4 mm inter-electrode distance).

Results: Recurrence plots identified frequent recurrences of activation patterns in all recordings and indicated a strong correlation between recurrence plot threshold and AF cycle length. Prolonged AF duration was associated with shorter repetitive pattern duration [mean maximum duration 3 wkAF: 74 cycles, 95% confidence interval (54–94) vs. 22 wkAF: 41 cycles (21–62), p = 0.03], and smaller recurrent regions within repetitive patterns [3 wkAF 1.7 cm^2 (1.0–2.3) vs. 22 wkAF 0.5 cm^2 (0.0–1.2), p = 0.02]. Both breakthrough patterns and re-entry were identified as repetitive conduction patterns.

Conclusion: Recurrence plots provide a novel way to delineate high-density contact mapping of AF. Dominant repetitive conduction patterns were identified in a goat model of sustained AF. Application of the developed methodology using the new generation of multi-electrode catheters could identify additional targets for catheter ablation of AF.

Keywords: atrial fibrillation, mapping, recurrence plots, repetitive conduction patterns, mechanisms

INTRODUCTION

During atrial fibrillation (AF) electrical conduction patterns in the atria are divers, variable, and often complex. The complexity of these wave front patterns, i.e., the number of waves that propagate through the atria during each AF cycle, typically increases with AF duration (Allessie et al., 2010). Catheter ablation of AF aims at isolation of triggers for AF and at elimination of a dominant electrical mechanism that initiates or sustains AF. Current success rates of various approaches to catheter ablation of AF in patients show that there is a need to systematically identify additional targets besides the pulmonary veins (PV), especially in patients undergoing redo procedures after initially successful PV isolation. Several candidate mechanisms, associated detection algorithms, and ablation strategies have been proposed and applied in the last few decades, but this has not yet led to significantly improved long-term ablation outcome (Verma et al., 2015; Wong et al., 2015).

Proposed candidate sources of AF often show a high degree of repetitiveness. Repetitive focal patterns of activation detected in high-density mapping have been reported in patients with persistent AF (Holm et al., 1997; Lee et al., 2015), but others found repetitive focal events to be rare (de Groot and Allessie, 2019). Highly repetitive microreentrant sources were found using optical mapping, both in sheep (Mandapati et al., 2000) and in a small diverse set of human explanted hearts (Hansen et al., 2015), but also using panoramic contact mapping (Swarup et al., 2014). Other studies suggest more unstable spatiotemporal behavior of reentrant circuits, driven by an underlying stochastic process of wave generation (Dharmaprani et al., 2019) or clustered at the borders of fibrotic atrial regions (Haïssaguerre et al., 2016). Repetitive AF sources were also identified in several anatomical locations with a more general approach based on high electrogram morphology similarity and short AF cycle length (Ravelli et al., 2012, 2014).

Repetitive conduction is also to be expected in the vicinity of such local drivers. A local source may not always conduct 1:1 to its vicinity but this region is nonetheless expected to exhibit repetitive conduction patterns driven by the source. The presence of repetitive patterns in a region of the atria may furthermore reveal a structure-function relationship at that site, impacted by atrial anatomy (Hansen et al., 2015; van Hunnik et al., 2018) or by structural remodeling associated with AF (Verheule et al., 2010; Maesen et al., 2013). A repetitive pattern may also be the precursor to (spontaneous) termination of AF (Ortiz et al., 1993), or give an indication of the overall state of atrial conduction, i.e., the dynamics of linking of conduction between consecutive activations in different atrial regions (Gerstenfeld et al., 1992). Therefore techniques to reliably identify repetitive conduction patterns can be very instrumental, particularly in the light of recent advances toward electro-anatomical mapping tools with increased spatiotemporal resolution.

In this paper we introduce a method to analyze the incidence and characteristics of repetitive conduction patterns in contact mapping of AF using a recurrence plot, a well-established technique to study the dynamics of complex non-linear systems (Marwan et al., 2007). We demonstrate the ability of this novel computational tool to detect and quantify repetitive conduction patterns in high-density epicardial mapping in a goat model of AF.

MATERIALS AND METHODS

High-Density Contact Mapping in a Goat Model of AF

In this study we made use of a retrospective dataset, comprised of baseline measurements from a drug provocation study in two groups of 8 goats, in which AF was induced by left atrial burst pacing and maintained for either 3 weeks (3 wkAF) or 22 weeks (22 wkAF). High-density contact mapping was performed during an open-chest experiment, using a 249-electrode circular mapping array (2.4 mm inter-electrode distance, sampling frequency 1039 Hz). One-minute recordings of unipolar atrial electrograms were made simultaneously on the right atrial (RA) and left atrial (LA) epicardial wall. Further experimental details can be found in van Hunnik et al. (2018). The study protocol was approved by the local ethics committee and complied with the Dutch and European directives.

Recurrence Plot Construction to Visualize Repetitive Pattern Incidence

Recurrence plots provide a general way to visualize and analyze the temporal behavior of complex non-linear dynamical systems (Marwan et al., 2007). It requires the definition of a phase-space trajectory of the dynamical system and a distance function that measures the similarity or distance between any pair of time points on the trajectory. A recurrence then occurs when the distance between two points in time is below a certain threshold. The recurrence rate *RR* is defined as the fraction of detected recurrences over all comparisons.

We adapted this general definition of recurrence plots to the analysis of atrial electrograms and conduction patterns. The approach is illustrated in **Figure 1** on a recording of beats that were regularly paced from four cardinal directions. First, unipolar atrial electrograms were transformed to activation-phase signals

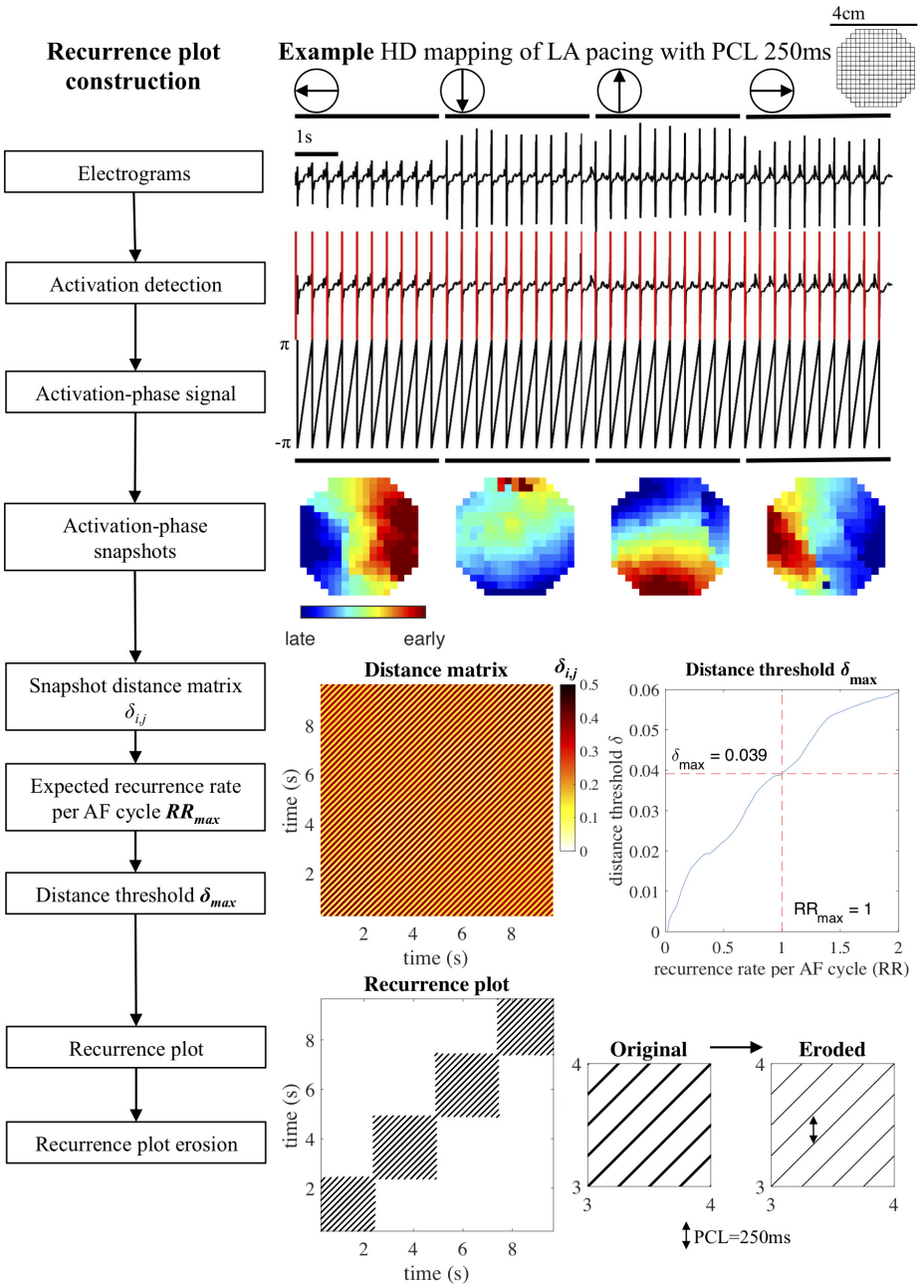

FIGURE 1 | Recurrence plot construction. Block diagram and example of recurrence plot reconstruction for a recording of a paced rhythm. Unipolar electrograms were annotated, converted to activation-phase signals and used to create activation phase snapshots. Next, the distances $\delta_{i,j}$ between all pairs of snapshots (*i,j*) were used to construct a distance matrix. The distance threshold δ_{max} was computed based on the maximum recurrence rate per AF cycle RR_{max} (default RR_{max} = 1) and applied to the distance matrix to construct a recurrence plot. Consecutive recurrences were eroded, removing false positives from the recurrence plot. HD, high density; LA, left atrium; PCL, pacing cycle length.

by local activation time annotation, employing a previously published algorithm that assigns local atrial deflections to maximize the likelihood of atrial deflection intervals given an estimated AF cycle length distribution (Zeemering et al., 2012). Activation-phase signals (in the range $[-\pi, \pi)$] were constructed by linear interpolation, taking the local activation time as the moment of phase inversion. The phase-space was then defined as the snapshot of the activation-phase of all mapping array electrodes at individual time points. This snapshot can be interpreted as still frame of the local conduction pattern at a given time point. The distance $\delta_{i,j}$ between two time points *i* and *j* on the phase-space trajectory was determined based on the phase angle difference at every electrode, by taking the average of the cosine of each difference, transformed back to a fraction

of the activation-phase duration of a single AF cycle (2π). This distance measure was chosen so that the range of differences between two snapshots [$(-2\pi, 2\pi)$] was mapped appropriately: maximum similarity occurred at differences (0, -2π, and 2π), while maximum dissimilarity occurred at π and $-\pi$. This also meant that the distance between two snapshots was always symmetric. The resulting distance measure ranged from 0 (two snapshots that were completely in phase) to 0.5 (two snapshots that were half an AF cycle length out of phase).

This transformation of electrograms to activation-phase snapshots, also known as the phase-space embedding, together with the distance function was subsequently used to create a distance matrix in which all activation-phase snapshots within a recording were compared. The distance matrix was transformed to a recurrence plot by imposing an adaptive maximum distance threshold δ_{max}. The distance threshold δ_{max} can be interpreted as the maximum degree to which two snapshots were allowed to be out of phase for a recurrence to occur. This threshold was computed by requiring the recurrence plot to have a recurrence rate that corresponded to a maximum recurrence rate per AF cycle RR_{max}. Default value for RR_{max} was set to 1, equivalent to the recurrence rate per AF cycle that would occur if a single conduction pattern were repeating for the whole length of the recording. The resulting δ_{max} and recurrence rate of the recurrence plot therefore depended on the AF cycle length, the number of time points in the recording, and the distribution of distances in the distance matrix. A formal definition of the distance matrix, recurrence plot construction, and distance threshold computation is provided in the section "Distance Matrix and Distance Threshold Computation" of **Supplementary Methods**. Note that this choice for the threshold constituted a sensitive detection of recurrences, which on the one hand ensured that completely regular patterns were detected correctly, but on the other hand also caused false positive recurrence detections (also known as false nearest neighbors in recurrence plot analysis) in recordings with a lower degree of regularity.

Recurrence Plot Analysis to Detect Repetitive Patterns

Recurrence plots were analyzed to detect the incidence and duration of repetitive patterns. There are a few general features of a recurrence plot that are worth mentioning here. A recurrence plot is always symmetric as it compares all pairs of snapshot within a recording in both directions of time, past and future. The main diagonal represents the comparison of a snapshot with itself and hence is always recurrent. A repeating conduction pattern will form a sequence of consecutive recurrences, i.e., if two activation-phase snapshots are similar, these two snapshots will also be similar when shifted equal (small) amounts in time. This phenomenon is visible in a recurrence plot as a diagonal line (Marwan et al., 2007). A conduction pattern that repeats consistently for several consecutive AF cycles will show up in the recurrence plot as a square block of diagonal lines around the main diagonal. Due to the sensitive detection of recurrences, diagonal lines may exhibit some "thickness" when the distance between consecutive activation-phase snapshots still falls within the imposed threshold, which leads to aforementioned false positive recurrences. In our analysis this effect was removed by eroding the recurrence plot, effectively replacing consecutive horizontal or vertical snapshot recurrences by a single recurrence at the time point with minimum distance.

The resulting eroded recurrence plot was then used to detect intervals that contained repetitive patterns, as illustrated in **Figure 2**. These intervals were detected by an algorithm that traversed the main diagonal of a recurrence plot and computed the recurrence rate per AF cycle in square blocks of increasing duration around the diagonal at each time point. Recurrence rate was again normalized to the AF cycle length, so that a value of 1 indicated a single recurrence occurring each AF cycle on average. For each time point we stored the duration of the interval that was formed by the square block in the recurrence plot with the maximum recurrence rate. Intervals that contained repetitive patterns were defined as local maxima in the interval duration, with a minimum recurrence rate per AF cycle RR_{min}. The default value of RR_{min} was set to 0.9, corresponding to an average of 0.9 recurrences per AF cycle, to account for short-lasting pattern interruptions and small deviations in AF cycle length. In case of two identified intervals with more than 50% overlap in time, the interval with the longest duration was selected.

Clustering of Similar Repetitive Patterns

To investigate which identified intervals on the main diagonal of the recurrence plot containing repetitive patterns represented similar or distinct activation patterns, patterns were grouped based on the cross-recurrence rate between intervals. Cross-recurrence rate between two intervals was determined by computing the recurrence rate in the rectangular block in the recurrence plot formed by the respective intervals. The resulting interval similarity matrix, describing the cross-recurrence rate between all pairs of intervals containing repetitive patterns, was clustered using agglomerative hierarchical clustering, a commonly used clustering technique that builds a tree of linked pairs of most similar intervals using a bottom-up approach (Hastie et al., 2009). Groups of similar patterns were extracted from the hierarchical cluster tree using the same recurrence rate threshold RR_{min} applied in the detection of repetitive patterns.

Repetitive Pattern Visualization

Repetitive (clustered) patterns were visualized by computing the average of activation-phase snapshots corresponding to recurrences on a vertical line within the corresponding intervals in the recurrence plot. The average activation-phase snapshot was converted to an average activation time map using the estimated AF cycle length, setting the earliest activation time to zero. To identify spatial regions within the mapping array that contributed most to the recurrent behavior of the average pattern, a heat map was constructed that indicated the average recurrent activation-phase distance δ_k^p for a pattern (p) for each electrode (k) separately (see section "Average Pattern Activation-Phase Distance" in **Supplementary Methods**). The size of the most recurrent region was defined as the area covered by electrodes with an average activation-phase distance below the computed adaptive distance threshold δ_{max}, or a fixed time difference threshold Δt, after

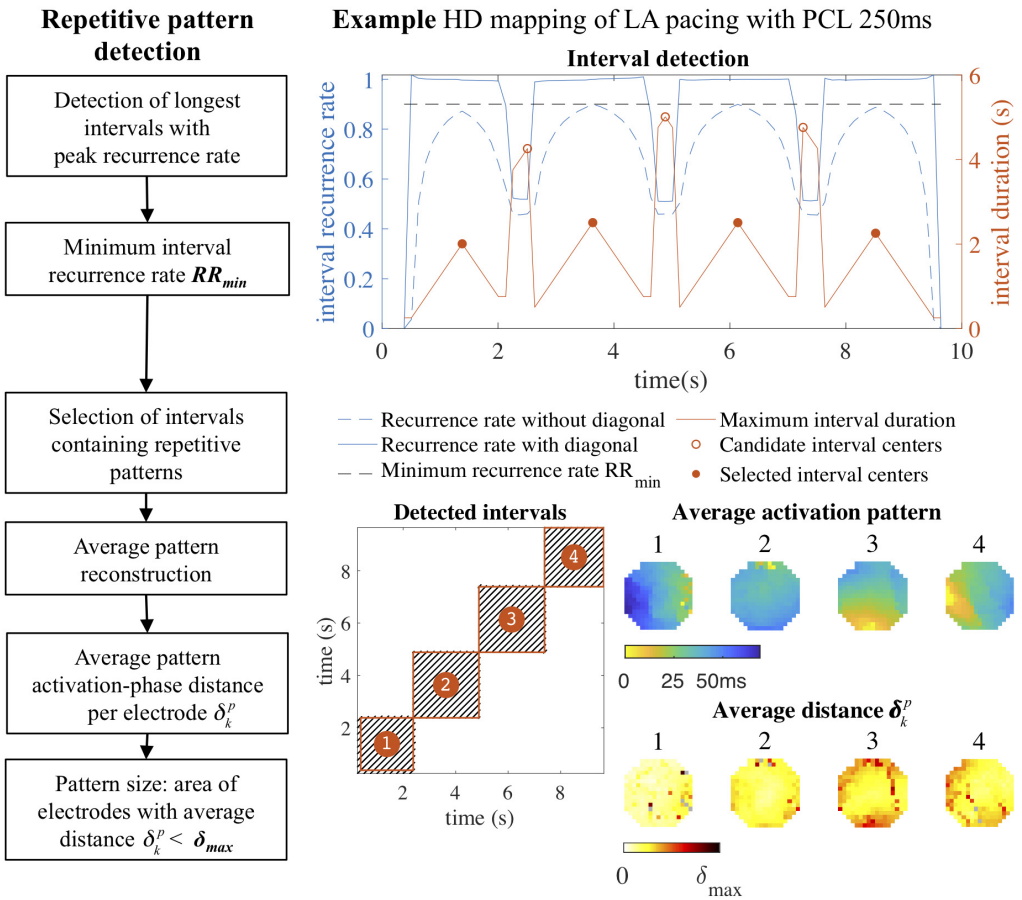

FIGURE 2 | Repetitive pattern detection. Intervals containing repetitive patterns were detected by traversing the main diagonal of the recurrence plot and computing the duration of the square block surrounding the diagonal with the maximum recurrence rate at each time point. Intervals with peak duration and a recurrence rate above a minimum recurrence rate per AF cycle RR_{min} (0.9) were selected. In the four detected intervals the average activation time map was constructed, representing the original four pacing directions. For each pattern a heat map was constructed that indicated the average recurrent activation-phase distance δ_k^p for a pattern (p) for each electrode (k) separately. From this heat map the pattern size was computed by determining the area of the electrodes with $\delta_k^p < \delta_{max}$. In this example of a paced rhythm the repetitive patterns were very consistent: almost all electrodes contributed to the repetitive pattern with an average activation-phase distance below the distance threshold. HD, high density; LA, left atrium; PCL, pacing cycle length.

converting the average activation-phase distance per electrode to a time difference by multiplying δ_k^p by the AF cycle length.

Statistics

Based on the recurrence plot analysis we determined for each individual recording the adaptive distance threshold δ_{max}, the number and duration of intervals containing repetitive patterns and clusters of similar patterns, and the size of most recurrent region. Sensitivity analysis was performed to assess the effect of the thresholds RR_{max} and RR_{min} on the detection of repetitive patterns (see section "Sensitivity Analysis" in **Supplementary Methods**). Differences between 3 and 22 wkAF and LA and RA were tested using mixed ANOVA, employing a significance threshold of 0.05. Correlations between parameters were computed using Spearman's rank correlation coefficient, controlling for AF group and atrium. Algorithms for recurrence plot construction and repetitive pattern detection were implemented in MATLAB (2019). Statistical tests were performed using R (R Core Team, 2019) and the package *emmeans* (Lenth, 2020).

RESULTS

Application to High-Density Recordings of AF

The procedure of electrogram activation-phase and snapshot distance matrix computation, recurrence plot construction and repetitive pattern detection was applied to recordings during AF in the goat model. The result of this automated analysis scheme in simultaneous left and right atrial recordings in a single animal is illustrated in **Figure 3**. Intervals containing repetitive patterns are indicated as red square blocks around the diagonal. For both atria, the detected intervals were clustered into groups of similar patterns, of which the three clusters with the longest combined duration (in AF cycles) are shown. For each clustered pattern the

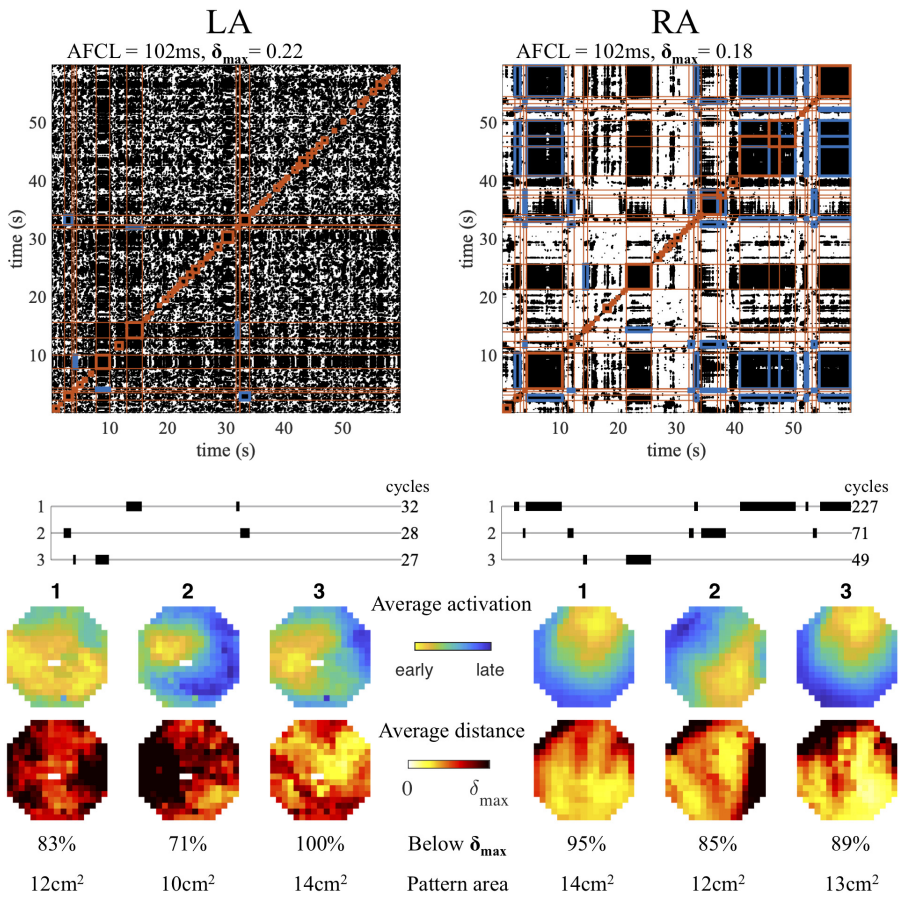

FIGURE 3 | Example of repetitive pattern detection in simultaneous **left** (LA) and **right** (RA) atrial recordings. For both locations the recurrence plot and interval detection (red blocks) are depicted. Those intervals are shown that belong to the three clustered patterns with longest duration (in cycles). Cross-recurrence between intervals belonging to the same cluster is indicated in blue in the recurrence plot. The average activation pattern for each pattern is illustrated, together with the heat map of the average activation-phase distance per electrode.

average activation time map was determined together with the heat map of the average activation-phase distance per electrode. In this case the right atrium showed a repetitive pattern for many cycles (227), a wave entering from the northeast of the mapping area, alternated with a different pattern (71 cycles), again a wave entering the field of view, but now from the southeast. The third pattern resembled the first, but the distance heat map indicated a more variable pattern at the entrance point of the wave. In contrast, at the same time in the left atrium, the three most prevalent patterns were short lasting, with 32, 28, and 27 cycles, respectively. Here the first pattern represented two peripheral waves that collided in the center of the mapping area, and the second and third repetitive focal/breakthrough waves at distinct locations. The heat maps of the patterns in the left atrium indicated a more variable or unstable pattern compared to the right.

Sensitivity Analysis of RR_{max} and RR_{min}

First, we varied RR_{max} between 0.25 and 2, around the default value of 1, and quantified the effect on the recurrence plot construction: the distance threshold δ_{max} and the recurrence rate of the eroded recurrence plot. We also evaluated the effect of RR_{max} on the detection of repetitive patterns (keeping RR_{min} fixed at the default value 0.9): number of intervals, maximum duration of an interval, maximum pattern duration and pattern size (using the adaptive distance threshold δ_{max} that is determined by the choice of RR_{max}). We repeated this analysis for a range of fixed δ_{max}. Results show that most parameters are moderately affected by changes in RR_{max}. Recurrence plot parameters show an approximately linear response (**Supplementary Figures 1A,B**), while the parameters related to the detection of repetitive patterns show either a linear (maximum interval and pattern duration), a weak biphasic (number of intervals), or almost no response (pattern size) (**Supplementary Figure 2**). In contrast, using a range of fixed δ_{max} [0.1, 0.25] that corresponded to the range of observed values for the δ_{max} computed from RR_{max}, we observed a much stronger, non-linear response in the eroded recurrence plot recurrence rate (**Supplementary Figure 1C**) and the pattern detection parameters (**Supplementary Figure 3**). **Supplementary Figure 4** provides an example of recurrence plot construction and repetitive pattern detection for varying values of RR_{max}.

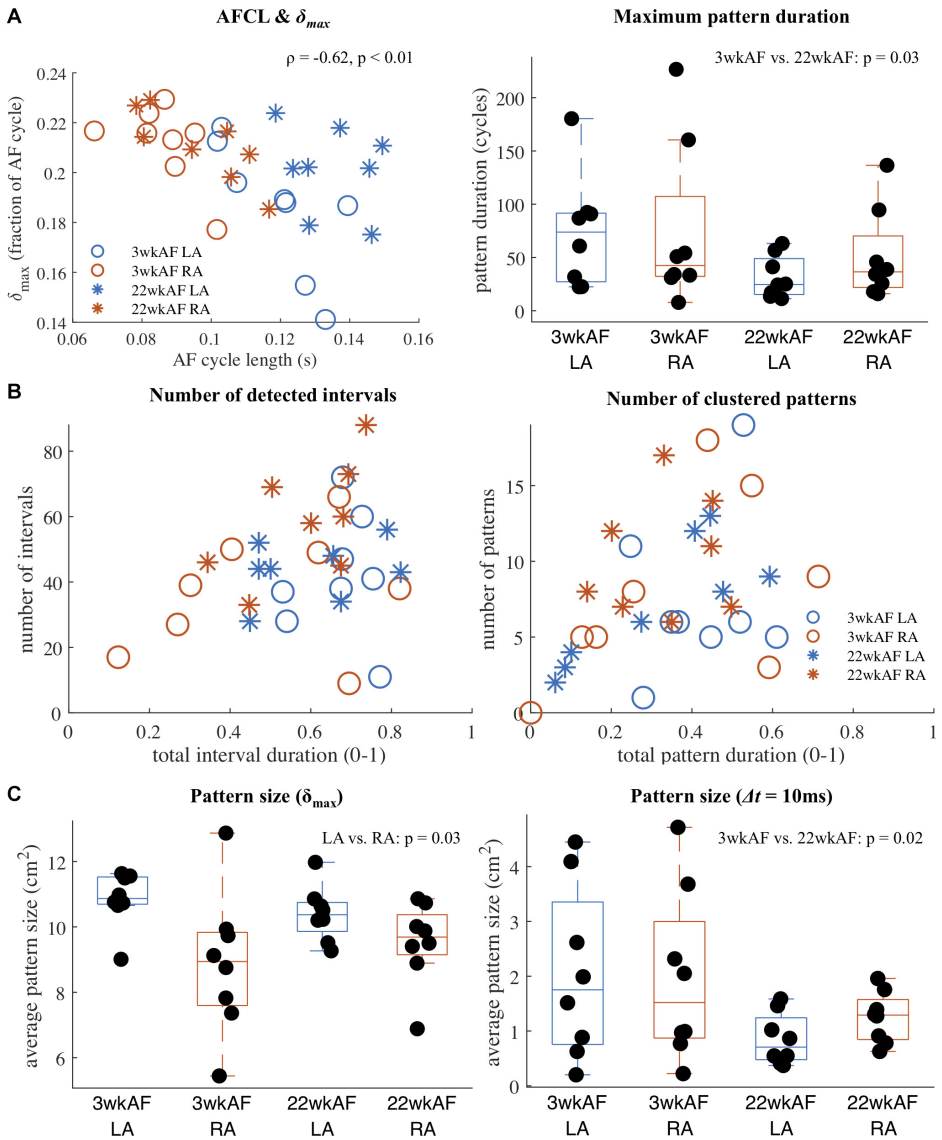

FIGURE 4 | Recurrence detection results in 3 and 22 wkAF goats. **(A)** Correlation between AF cycle length (AFCL) and the adaptive distance threshold δ_{max}, and maximum pattern duration per recording in AF cycles. **(B)** Variety of number of detected intervals containing a repetitive interval and clustered patterns compared to the total recording coverage. Only clustered patterns with a combined duration exceeding 10 AF cycles were included. **(C)** Average size of the most recurrent pattern region within each recording, computed using the adaptive distance threshold δ_{max} (left) and a fixed maximum time difference Δt (10 ms) applied to the average activation time difference between pattern recurrences (right).

Second, we varied RR_{min} between 0.5 and 1.5, while keeping RR_{max} fixed at $RR_{max} = 1$. Results show that choices for RR_{min} close to the default value 0.9 do not change the qualitative interpretation of the results of the pattern identification, most notably for the maximum duration of patterns and the pattern size (**Supplementary Figure 5**).

Repetitive Patterns in a Goat Model of Different AF Duration

Using $RR_{max} = 1$ and $RR_{min} = 0.9$, repetitive pattern detection was performed in all recordings at baseline in the two groups of 3 and 22 wkAF goats to investigate the incidence of repetitive patterns and to detect any potential differences in recurrence characteristics associated with AF duration and atrium. Our main results are summarized in **Figure 4**. The computed distance threshold δ_{max} was strongly correlated with the AF cycle length (correlation −0.62, $p < 0.01$, **Figure 4A**). The maximum duration (in number of AF cycles) of clustered patterns was longer in 3 wkAF than in 22 wkAF (mean maximum duration 74 cycles [95% confidence interval (54–94) vs. 41 (21–62) cycles, $p = 0.03$]. In **Figure 4B** we illustrated the diversity in the number of intervals that contained repetitive patterns, as well as the total duration of these intervals during a recording. We observed a wide variety of interval incidence and prevalence,

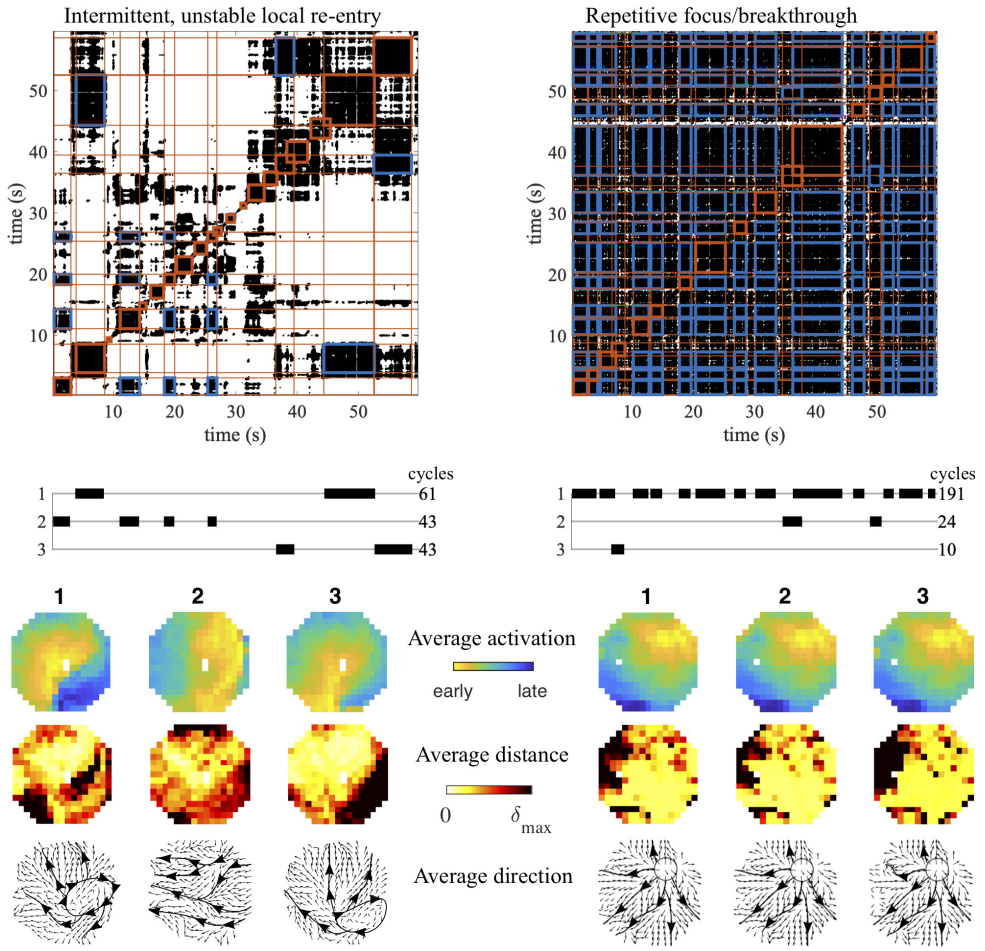

FIGURE 5 | Examples of AF mechanisms detected using recurrence analysis. Two conduction patterns associated with candidate AF mechanisms are depicted: an intermittent, unstable local re-entry within the mapping area **(left)** and a repetitive focal/breakthrough wave **(right)**. Intervals containing recurrent patterns are indicated in red blocks, while cross-recurrences between clustered intervals are indicated in blue. The average activation pattern for each pattern is illustrated, together with the heat map of the average activation-phase distance per electrode and the average conduction direction during the pattern duration.

from recordings that showed a low number of intervals that covered only a small portion of the recording duration, to recordings with a small to large amount of intervals that covered almost the entire recording. The number of patterns, where multiple intervals could be grouped into one clusters representing a single pattern, compared to the total coverage of the recording showed similar diversity. Here we only included clusters of patterns where the total duration of the combined intervals exceeded 10 AF cycles. The average size of the most recurrent region per recording (**Figure 4C**) was slightly smaller in the right atrium [mean size LA 10.9 cm^2 (10.0–11.4) vs. RA 9.5 cm^2 (8.8–10.3), p = 0.03], when computed based on the number of electrodes with an average activation-phase distance below the adaptive distance threshold δ_{max}. Pattern region size was much smaller when applying a fixed maximum activation time difference threshold Δt of 10 ms between recurrences in detected patterns. Here, differences were found between 3 and 22 wkAF [3 wkAF 1.7 cm^2 (1.0–2.3) vs. 22 wkAF 0.5 cm^2 (0.0–1.2), p = 0.02]. Sensitivity analysis of Δt indicated that this difference in regions with low average temporal dissociation was consistent for values of Δt between 10 and 30 ms (**Supplementary Figure 5B**).

Examples of Mechanisms Detected by Recurrence Analysis

In **Figure 5** we show two examples to illustrate how this method can detect and visualize candidate AF source patterns. These were selected recordings from the same study in goats, but during infusion of different dosages of the antiarrhythmic drug used. The first example shows a recording that started with a peripheral wave entering from the east (pattern 2), but then switched to a local re-entry within the mapping area (pattern 1). Pattern 2 returned after a while, but was intermitted by other, less stable and frequent patterns. Then pattern 3 arose, again a local re-entry within the mapping area, comparable to pattern 1, but following a slightly different trajectory. Finally pattern 1 reappeared, followed by pattern 3. The dominant

conduction direction per electrode for each of the patterns confirmed their interpretation. The second example shows an extreme case of a repetitive focal/breakthrough wave, where the most spatiotemporal stable pattern (pattern 1) appeared intermittently for a total of 191 cycles. In this example the other intermittent patterns (patterns 2 and 3) were very similar to pattern 1, and only differed slightly in the variation of the radial spread of activation, as indicated by the activation-phase distance heat maps. The dominant conduction direction per electrode for each of the patterns highlights this radial spread originating from the site of the focus/breakthrough activation.

DISCUSSION

We developed a method to automatically identify repetitive patterns of conduction in high-density mapping of AF. This method can be used to detect the incidence of time intervals containing repetitive patterns, to group intermittent intervals that exhibit similar repetitive patterns, and to visualize these distinct patterns to interpret the mechanism the conduction pattern represents. As an application, repetitive conduction patterns were identified in HD mapping recordings in a goat model of sustained AF, where we identified repetitive patterns in almost all recordings. We also show that the maximum duration of repetitive patterns and the size of the regions containing the most dominant repetitive pattern decreased with prolonged AF duration.

Recurrence Analysis as a Tool to Identify Repetitive Patterns During AF

Recurrence analysis has been applied to investigate AF characteristics in invasive measurements, based on single electrode bipolar electrogram morphology. Recurrence plots were used to assess the degree of organization present during AF (Censi et al., 2000). Recurrence quantification analysis was applied to detect complex fractionated atrial electrograms (Navoret et al., 2013), to quantify the dynamics of beat-to-beat deflection morphology similarity at several locations in the left and right atrium (Ng et al., 2014), and to distinguish spiral wave reentry from multiple wavelets in bipolar electrograms (Hummel et al., 2017). Recurrence plots derived from consecutive AF cycle lengths from an electrogram recorded in the coronary sinus suggested that the underlying AF process is deterministic, rather than stochastic (Aronis et al., 2018). Also alternative methods for the detection of local bipolar electrogram regularity were proposed, again using electrogram morphology, but also by integrating electrogram coupling to quantify local organization (Faes and Ravelli, 2007), or by quantifying the repetitiveness of the pattern of complex fractionated atrial electrograms using frequency domain parameters (Ciaccio et al., 2011). The use of a single electrode and bipolar electrograms, however, limits the amount of spatiotemporal information that can be incorporated in the assessment of the dynamics of the underlying recurrent conduction pattern. In our approach we aimed to not only include temporal dynamics, but also detailed local spatial coherence, by analyzing electrograms from a high-resolution grid of electrodes. Our approach further relies on unipolar electrograms that are insensitive to the direction of conduction. We adopted an activation-phase representation of the electrograms to enable the computation of the distance, or difference, between two snapshots of conduction in time. Other approaches may also be chosen to arrive at this phase-space representation of the conduction patterns, for instance methods that rely on the Hilbert transform of the filtered electrogram (Kuklik et al., 2015). Caution should be applied, however, when interpreting the resulting averaged activation-phase patterns, as these approaches tend to blur the true underlying activation patterns, which can lead to the elimination of conduction block (Podziemski et al., 2018).

Interpretation and Implications of the Adaptive Recurrence Threshold

In our approach we adopted an adaptive distance threshold to transform the distance matrix that describes the difference in activation-phase between each pair of snapshots, to a recurrence plot, that only contains the moments in time when two conduction patterns are sufficiently in phase. The choice for a recurrence plot threshold has to be made carefully: applying a too restrictive threshold will not identify existing recurrences and can lead to the detection of many short, interrupted intervals; a too tolerant threshold will lead to many false positive recurrences, that obscure the underlying structure of the recurrence plot (Marwan, 2011). There are several approaches to choosing a recurrence threshold (Zbilut et al., 2002). We used the *a priori* knowledge of the AF cycle length to choose a threshold that led to a number of recurrences that was to be expected if the underlying pattern was completely regular and repetitive for the whole duration of the recording. In the case of AF this threshold was often too tolerant, which led to sensitive, but not specific detection of recurrent snapshots. The post processing of the resulting recurrence plot, together with the constraints imposed on the detection of repetitive patterns, ensured that these false positives detections were disregarded. Sensitivity analysis indicated that this approach to compute an adaptive distance threshold is a relatively robust choice compared to setting a fixed distance threshold: a small change in $RR_{\max}$ led to relatively small and predictable change in $\delta_{\max}$ and associated pattern detection results, whereas changes in a fixed $\delta_{\max}$, that was applied to all recordings, led to much more pronounced and unpredictable changes in pattern detection results.

A higher recurrence threshold that still leads to the detection of intervals that contain repetitive intervals can indicate two things: either repetitive patterns are more variable, but still stand out from other intervals with even more disorganized activity, and/or the spatial region within the mapping area where the repetitive pattern is localized is smaller. The application of our method on the goat model data revealed that the threshold is strongly associated with the AF cycle length. This correlation indicated less stable or smaller repetitive patterns in recordings with shorted AF cycle lengths, which corroborates the findings of Schuessler et al. (1992) where in a cholinergic model of

AF the shortening of the effective refractory period (and cycle length) resulted in an increased number of wave fronts and local re-entry circuits.

Repetitive Patterns in AF

Applying the developed methodology to recordings in a goat model of AF, we found that there was a large diversity both in the number of repetitive patterns as well as in the total duration of the recording covered by repetitive patterns. Stability of patterns, however, seemed to decrease with AF duration, with a lower maximum pattern duration in 22 wkAF. The size of the region within the mapping area responsible for the recurrent behavior did also decrease with AF duration (using a fixed threshold of 10ms for the maximum allowed activation time difference between recurrences). This suggests that, while repetitive patterns are still present, the size of the repetitive process becomes smaller with prolonged AF duration. This is largely in line with findings in a comparable goat model of AF (Verheule et al., 2010). Interestingly we observed switching between different repetitive patterns in several of the examples (**Figures 3**, **5**). This suggests the existence of different states of the atrial conduction during AF, and sudden transitions between these states, as also observed in simulations of AF (Iravanian and Langberg, 2017; Marcotte and Grigoriev, 2017).

In this study we analyzed mapping data from the epicardium of both atria. Since conduction during AF is a 3D process, signals measured simultaneously on the endocardial wall may show some degree of uncoupling (Eckstein et al., 2013; Gutbrod et al., 2015; de Groot et al., 2016). Independent epi-endocardial repetitive patterns might point to separate drivers in the two layers. It would be of great interest to further investigated whether epi-endocardial coupling occurs during episodes of repetitive activity. Furthermore, electrode array resolution has been shown to significantly impact AF driver identification (Roney et al., 2017). Computation modeling of AF can help to investigate the effect of 3D conduction, dissociation and mapping device on pattern detection, providing that the model incorporates the 3D nature of the atrial anatomy and bundle structure, and exhibits epi-endocardial dissociation to an extent that 3D conduction patterns can be simulated [see for instance (Gharaviri et al., 2020)].

Recurrence Analysis to Identify and Target AF Sources

The detection of AF sources during an AF ablation is a possible extension of the current approach. The examples in **Figure 5** show that our approach – in principle – can detect and visualize local candidate mechanism that may drive or initiate AF (e.g., a local re-entry or a repetitive focal/breakthrough wave). In patients, ablation of such driver sites may restore sinus rhythm or prevent AF recurrence. As a future perspective, during an ablation procedure, several regions of the atria could be mapped sequentially and repetitive patterns can then be reconstructed for each region. With the use of a common reference, or spatial overlap between asynchronous recordings at different sites, repetitive patterns can be "stitched" together to form a more complete picture of whole atrial repetitive conduction. A similar approach was recently demonstrated in the RADAR trial (Choudry et al., 2020), where a catheter placed in the coronary sinus (CS) served as the common reference. A potential limitation of that specific setup is that intervals containing repetitive patterns were detected using only the electrograms from the CS catheter. In contrast, identification of repetitive patterns at partially overlapping sites also enables the detection of candidate AF drivers that do not lead to repetitive electrogram morphology in the CS. Multi-site identification of repetitive patterns will, however, require recordings with longer duration than currently acquired during an ablation procedure, together with a sufficient incidence and duration of repetitive patterns.

LIMITATIONS

The result of the recurrence plot construction and repetitive pattern detection were dependent on the chosen phase-space embedding (local activation-phase computation) and recurrence rate thresholds $RR_{\max}$ and $RR_{\min}$. Optimal embedding and threshold values were not investigated in this study. Sensitivity analysis of $RR_{\max}$ and $RR_{\min}$ indicated that results obtained in the goat model of AF were moderately insensitive with respect to the exact choice for these thresholds. Recordings evaluated in this study were from a goat model of AF, where although AF was persistent, the amount of structural remodeling was most likely limited and the differences between groups subtle. A similar study in patients in different stages of AF (paroxysmal and persistent) is needed to investigate the relationship between AF duration and associated structural remodeling and repetitive pattern incidence and size.

DATA AVAILABILITY STATEMENT

The raw data supporting the conclusions of this article will be made available by the authors, without undue reservation. Requests to access these datasets should be directed to SZ, s.zeemering@maastrichtuniversity.nl.

ETHICS STATEMENT

The animal study was reviewed and approved by the Local Ethical Board for animal experimentation of Maastricht University.

AUTHOR CONTRIBUTIONS

SZ developed the concept, developed analysis tools, analyzed and interpreted the data, and wrote the article. AH conducted the experiments, analyzed the data, and contributed to the scientific interpretation and the writing of the article. FR and PB developed analysis tools and contributed to the writing of the article. BS conducted the experiments. TD contributed to the scientific interpretation and the writing of the article. SV contributed to the scientific interpretation and the writing of the article. US developed the concept and contributed to the

scientific interpretation and the writing of the article. All authors contributed to the article and approved the submitted version.

FUNDING

This study was funded by the Netherlands Heart Foundation (CVON2014-09, RACE V Reappraisal of Atrial Fibrillation: Interaction between hyper Coagulability, Electrical remodeling, and Vascular Destabilization in the Progression of AF) and was performed within the framework of CTMM, the Center for Translational Molecular Medicine (www.ctmm.nl), project COHFAR (Grant 01C-203).

SUPPLEMENTARY MATERIAL

The Supplementary Material for this article can be found online at: https://www.frontiersin.org/articles/10.3389/fphys.2020.570118/full#supplementary-material

REFERENCES

Allessie, M. A., de Groot, N. M. S., Houben, R. P. M., Schotten, U., Boersma, E., Smeets, J. L., et al. (2010). Electropathological substrate of long-standing persistent atrial fibrillation in patients with structural heart disease: longitudinal dissociation. *Circ. Arrhythm. Electrophysiol.* 3, 606–615. doi: 10.1161/CIRCEP.109.910125

Aronis, K. N., Berger, R. D., Calkins, H., Chrispin, J., Marine, J. E., Spragg, D. D., et al. (2018). Is human atrial fibrillation stochastic or deterministic?-Insights from missing ordinal patterns and causal entropy-complexity plane analysis. *Chaos* 28:063130. doi: 10.1063/1.5023588

Censi, F., Barbaro, V., Bartolini, P., Calcagnini, G., Michelucci, A., Gensini, G. F., et al. (2000). Recurrent patterns of atrial depolarization during atrial fibrillation assessed by recurrence plot quantification. *Ann. Biomed. Eng.* 28, 61–70. doi: 10.1114/1.248

Choudry, S., Mansour, M., Sundaram, S., Nguyen, D. T., Dukkipati, S. R., Whang, W., et al. (2020). RADAR: a multicenter food and drug administration investigational device exemption clinical trial of persistent atrial fibrillation. *Circ. Arrhythm. Electrophysiol.* 13:e007825. doi: 10.1161/CIRCEP.119.007825

Ciaccio, E. J., Biviano, A. B., Whang, W., Vest, J. A., Gambhir, A., Einstein, A. J., et al. (2011). Differences in repeating patterns of complex fractionated left atrial electrograms in longstanding persistent atrial fibrillation as compared with paroxysmal atrial fibrillation. *Circ. Arrhythm. Electrophysiol.* 4, 470–477. doi: 10.1161/01.cir.0000146917.75041.58

de Groot, N., van der Does, L., Yaksh, A., Lanters, E., Teuwen, C., Knops, P., et al. (2016). Direct proof of endo-epicardial asynchrony of the atrial wall during atrial fibrillation in humans. *Circ. Arrhythm. Electrophysiol.* 9:e003648. doi: 10.1161/CIRCEP.115.003648

de Groot, N. M. S., and Allessie, M. A. (2019). Pathophysiology of atrial fibrillation: focal patterns of activation. *Pacing Clin. Electrophysiol.* 42, 1312–1319. doi: 10.1111/pace.13777

Dharmaprani, D., Schopp, M., Kuklik, P., Chapman, D., Lahiri, A., Dykes, L., et al. (2019). Renewal theory as a universal quantitative framework to characterize phase singularity regeneration in mammalian cardiac fibrillation. *Circ. Arrhythm. Electrophysiol.* 12:e007569. doi: 10.1161/CIRCEP.119.007569

Eckstein, J., Zeemering, S., Linz, D., Maesen, B., Verheule, S., van Hunnik, A., et al. (2013). Transmural conduction is the predominant mechanism of breakthrough during atrial fibrillation: evidence from simultaneous endo-epicardial high-density activation mapping. *Circ. Arrhythm. Electrophysiol.* 6, 334–341. doi: 10.1161/CIRCEP.113.000342

Faes, L., and Ravelli, F. (2007). A morphology-based approach to the evaluation of atrial fibrillation organization. *IEEE Eng. Med. Biol. Mag.* 26, 59–67. doi: 10.1109/memb.2007.384097

Gerstenfeld, E. P., Sahakian, A. V., and Swiryn, S. (1992). Evidence for transient linking of atrial excitation during atrial fibrillation in humans. *Circulation* 86, 375–382. doi: 10.1161/01.cir.86.2.375

Gharaviri, A., Bidar, E., Potse, M., Zeemering, S., Verheule, S., Pezzuto, S., et al. (2020). Epicardial fibrosis explains increased endo–epicardial dissociation and epicardial breakthroughs in human atrial fibrillation. *Front. Physiol.* 11:68. doi: 10.3389/fphys.2020.00068

Gutbrod, S. R., Walton, R., Gilbert, S., Meillet, V., Jaïs, P., Hocini, M., et al. (2015). Quantification of the transmural dynamics of atrial fibrillation by simultaneous endocardial and epicardial optical mapping in an acute sheep model. *Circ. Arrhythm. Electrophysiol.* 8, 456–465. doi: 10.1161/CIRCEP.114.002545

Haïssaguerre, M., Shah, A. J., Cochet, H., Hocini, M., Dubois, R., Efimov, I., et al. (2016). Intermittent drivers anchoring to structural heterogeneities as a major pathophysiological mechanism of human persistent atrial fibrillation. *J. Physiol.* 594, 2387–2398. doi: 10.1016/j.hrcr.2014.10.004

Hansen, B. J., Zhao, J., Csepe, T. A., Moore, B. T., Li, N., Jayne, L. A., et al. (2015). Atrial fibrillation driven by micro-anatomic intramural re-entry revealed by simultaneous sub-epicardial and sub-endocardial optical mapping in explanted human hearts. *Eur. Heart J.* 36, 2390–2401. doi: 10.1093/eurheartj/ehv233

Hastie, T., Tibshirani, R., and Friedman, J. (2009). "Hierarchical clustering," in *The Elements of Statistical Learning*, ed. Springer series in statistics (New York: Springer), 520–528.

Holm, M., Johansson, R., Brandt, J., Lührs, C., and Olsson, S. B. (1997). Epicardial right atrial free wall mapping in chronic atrial fibrillation. Documentation of repetitive activation with a focal spread–a hitherto unrecognised phenomenon in man. *Eur. Heart J.* 18, 290–310. doi: 10.1093/oxfordjournals.eurheartj.a015233

Hummel, J. P., Baher, A., Buck, B., Fanarjian, M., Webber, C. L., and Akar, J. G. (2017). A method for quantifying recurrent patterns of local wavefront direction during atrial fibrillation. *Comput. Biol. Med.* 89, 497–504. doi: 10.1016/j.compbiomed.2017.08.027

Iravanian, S., and Langberg, J. J. (2017). Critical phase transitions during ablation of atrial fibrillation. *Chaos* 27:093925. doi: 10.1161/CIRCEP.115.003337

Kuklik, P., Zeemering, S., Maesen, B., Maessen, J., Crijns, H. J., Verheule, S., et al. (2015). Reconstruction of instantaneous phase of unipolar atrial contact electrogram using a concept of sinusoidal recomposition and Hilbert transform. *IEEE Trans. Biomed. Eng.* 62, 296–302. doi: 10.1109/TBME.2014.2350029

Lee, S., Lee, S., Sahadevan, J., Sahadevan, J., Khrestian, C. M., Khrestian, C. M., et al. (2015). Simultaneous biatrial high-density (510-512 Electrodes) epicardial mapping of persistent and long-standing persistent atrial fibrillation in patients: new insights into the mechanism of its maintenance. *Circulation* 132, 2108–2117. doi: 10.1161/CIRCULATIONAHA.115.017007

Lenth, R. (2020). *emmeans: Estimated Marginal Means, aka Least-Squares Means*. Available online at: https://CRAN.R-project.org/package=emmeans (accessed May 10, 2020).

Maesen, B., Zeemering, S., Afonso, C., Eckstein, J., Burton, R. A. B., van Hunnik, A., et al. (2013). Rearrangement of atrial bundle architecture and consequent changes in anisotropy of conduction constitute the 3-dimensional substrate for atrial fibrillation. *Circ. Arrhythm. Electrophysiol.* 6, 967–975. doi: 10.1161/CIRCEP.113.000050

Mandapati, R., Skanes, A., Chen, J., Berenfeld, O., and Jalife, J. (2000). Stable microreentrant sources as a mechanism of atrial fibrillation in the isolated sheep heart. *Circulation* 101, 194–199. doi: 10.1161/01.cir.101.2.194

Marcotte, C. D., and Grigoriev, R. O. (2017). Dynamical mechanism of atrial fibrillation: a topological approach. *Chaos* 27:093936. doi: 10.1016/j.jtbi.2008.03.029

Marwan, N. (2011). How to avoid potential pitfalls in recurrence plot based data analysis. *Int. J. Bifurcation Chaos* 21, 1003–1017. doi: 10.1142/S0218127411029008

Marwan, N., Romano, M. C., Thiel, M., and Kurths, J. (2007). Recurrence plots for the analysis of complex systems. *Phys. Rep.* 438, 237–329. doi: 10.1016/j.physrep.2006.11.001

MATLAB (2019). *MATLAB Release 2019a*. Natick, MA: The MathWorks Inc.

Navoret, N., Jacquir, S., Laurent, G., and Binczak, S. (2013). Detection of complex fractionated atrial electrograms using recurrence quantification analysis. *IEEE Trans. Biomed. Eng.* 60, 1975–1982. doi: 10.1109/TBME.2013.2247402

Ng, J., Gordon, D., Passman, R. S., Knight, B. P., Arora, R., and Goldberger, J. J. (2014). Electrogram morphology recurrence patterns during atrial fibrillation. *Heart Rhythm.* 11, 2027–2034. doi: 10.1016/j.hrthm.2014.08.002

Ortiz, J., Igarashi, M., Gonzalez, H. X., Laurita, K., Rudy, Y., and Waldo, A. L. (1993). Mechanism of spontaneous termination of stable atrial flutter in the canine sterile pericarditis model. *Circulation* 88, 1866–1877. doi: 10.1161/01.cir.88.4.1866

Podziemski, P., Zeemering, S., Kuklik, P., van Hunnik, A., Maesen, B., Maessen, J., et al. (2018). Rotors detected by phase analysis of filtered, epicardial atrial fibrillation electrograms colocalize with regions of conduction block. *Circ. Arrhythm. Electrophysiol.* 11:e005858. doi: 10.1161/CIRCEP.117.005858

R Core Team (2019). *R: A Language and Environment for Statistical Computing*. Vienna: R Foundation for Statistical Computing.

Ravelli, F., Mase, M., Cristoforetti, A., Del Greco, M., Centonze, M., Marini, M., et al. (2012). Anatomic localization of rapid repetitive sources in persistent atrial fibrillation – fusion of biatrial ct images with wave similarity/cycle length maps. *JACC Cardiovasc. Imaging* 5, 1211–1220. doi: 10.1016/j.jcmg.2012.07.016

Ravelli, F., Masè, M., Cristoforetti, A., Marini, M., and Disertori, M. (2014). The logical operator map identifies novel candidate markers for critical sites in patients with atrial fibrillation. *Prog. Biophys. Mol. Biol.* 115, 186–197. doi: 10.1016/j.pbiomolbio.2014.07.006

Roney, C. H., Cantwell, C. D., Bayer, J. D., Qureshi, N. A., Lim, P. B., Tweedy, J. H., et al. (2017). Spatial resolution requirements for accurate identification of drivers of atrial fibrillation. *Circ. Arrhythm. Electrophysiol.* 10:e004899. doi: 10.1161/CIRCEP.116.004899

Schuessler, R. B., Grayson, T. M., Bromberg, B. I., Cox, J. L., and Boineau, J. P. (1992). Cholinergically mediated tachyarrhythmias induced by a single extrastimulus in the isolated canine right atrium. *Circ. Res.* 71, 1254–1267. doi: 10.1161/01.res.71.5.1254

Swarup, V., Baykaner, T., Rostamian, A., Daubert, J. P., Hummel, J., Krummen, D. E., et al. (2014). Stability of rotors and focal sources for human atrial fibrillation: focal impulse and rotor mapping (FIRM) of AF sources and fibrillatory conduction. *J. Cardiovasc. Electrophysiol.* 25, 1284–1292. doi: 10.1111/jce.12559

van Hunnik, A., Zeemering, S., Podziemski, P., Simons, J., Gatta, G., Hannink, L., et al. (2018). Stationary atrial fibrillation properties in the goat do not entail stable or recurrent conduction patterns. *Front. Physiol.* 9:947. doi: 10.3389/fphys.2018.00947

Verheule, S., Tuyls, E., van Hunnik, A., Kuiper, M., Schotten, U., and Allessie, M. (2010). Fibrillatory conduction in the atrial free walls of goats in persistent and permanent atrial fibrillation. *Circ. Arrhythm. Electrophysiol.* 3, 590–599. doi: 10.1161/CIRCEP.109.931634

Verma, A., Jiang, C.-Y., Betts, T. R., Chen, J., Deisenhofer, I., Mantovan, R., et al. (2015). Approaches to catheter ablation for persistent atrial fibrillation. *N. Engl. J. Med.* 372, 1812–1822. doi: 10.1056/NEJMoa1408288

Wong, K. C. K., Paisey, J. R., Sopher, M., Balasubramaniam, R., Jones, M., Qureshi, N., et al. (2015). No benefit of complex fractionated atrial electrogram ablation in addition to circumferential pulmonary vein ablation and linear ablation: benefit of complex ablation study. *Circ. Arrhythm. Electrophysiol.* 8, 1316–1324. doi: 10.1161/CIRCEP.114.002504

Zbilut, J. P., Zaldivar-Comenges, J.-M., and Strozzi, F. (2002). Recurrence quantification based Liapunov exponents for monitoring divergence in experimental data. *Phys. Lett. A* 297, 173–181. doi: 10.1016/S0375-9601(02)00436-X

Zeemering, S., Maesen, B., Nijs, J., Lau, D. H., Granier, M., Verheule, S., et al. (2012). Automated quantification of atrial fibrillation complexity by probabilistic electrogram analysis and fibrillation wave reconstruction. *Conf. Proc. IEEE Eng. Med. Biol. Soc.* 2012, 6357–6360. doi: 10.1109/EMBC.2012.6347448

Conflict of Interest: US is co-founder and shareholder of YourRhythmics BV, a spin-off company of the University Maastricht, holds intellectual property with Roche and YourRhythmics BV, received consultancy fees or honoraria from Johnson & Johnson, Roche Diagnostics (Switzerland), and Bayer Healthcare (Germany).

The remaining authors declare that the research was conducted in the absence of any commercial or financial relationships that could be construed as a potential conflict of interest.

frontiers in Physiology

ORIGINAL RESEARCH
published: 12 November 2020
doi: 10.3389/fphys.2020.570203

Left Atrial Enhancement Correlates With Myocardial Conduction Velocity in Patients With Persistent Atrial Fibrillation

Rheeda L. Ali[1,2,3†‡], Norman A. Qureshi[1,2†], Silvia Liverani[4], Caroline H. Roney[1,2,3,7], Steven Kim[5], P. Boon Lim[1,2], Jennifer H. Tweedy[1,3], Chris D. Cantwell[1,6] and Nicholas S. Peters[1,2*]*

[1] ElectroCardioMaths Programme of The Imperial Centre for Cardiac Engineering, Imperial College London, London, United Kingdom, [2] National Heart & Lung Institute, Imperial College London, London, United Kingdom, [3] Department of Bioengineering, Imperial College London, London, United Kingdom, [4] School of Mathematical Sciences, Queen Mary University of London, London, United Kingdom, [5] Abbot Medical, St. Paul, MN, United States, [6] Department of Aeronautics, Imperial College London, London, United Kingdom, [7] School of Biomedical Engineering and Imaging Sciences, King's College London, London, United Kingdom

OPEN ACCESS

Edited by:
Atul Verma,
University of Toronto, Canada

Reviewed by:
Mihail G. Chelu,
Baylor College of Medicine, United States
Nassir Marrouche,
Tulane University, United States

***Correspondence:**
Nicholas S. Peters
n.peters@imperial.ac.uk
Rheeda L. Ali
rali13@jhu.edu;
rheeda.ali@gmail.com

[†] These authors have contributed equally to this work

[‡] **Present address:**
Rheeda L. Ali,
Johns Hopkins University, Baltimore, MD, United States

Specialty section:
This article was submitted to Cardiac Electrophysiology, a section of the journal Frontiers in Physiology

Received: 06 June 2020
Accepted: 16 October 2020
Published: 12 November 2020

Citation:
Ali RL, Qureshi NA, Liverani S, Roney CH, Kim S, Lim PB, Tweedy JH, Cantwell CD and Peters NS (2020) Left Atrial Enhancement Correlates With Myocardial Conduction Velocity in Patients With Persistent Atrial Fibrillation. Front. Physiol. 11:570203. doi: 10.3389/fphys.2020.570203

Background: Conduction velocity (CV) heterogeneity and myocardial fibrosis both promote re-entry, but the relationship between fibrosis as determined by left atrial (LA) late-gadolinium enhanced cardiac magnetic resonance imaging (LGE-CMRI) and CV remains uncertain.

Objective: Although average CV has been shown to correlate with regional LGE-CMRI in patients with persistent AF, we test the hypothesis that a localized relationship exists to underpin LGE-CMRI as a minimally invasive tool to map myocardial conduction properties for risk stratification and treatment guidance.

Method: 3D LA electroanatomic maps during LA pacing were acquired from eight patients with persistent AF following electrical cardioversion. Local CVs were computed using triads of concurrently acquired electrograms and were co-registered to allow correlation with LA wall intensities obtained from LGE-CMRI, quantified using normalized intensity (NI) and image intensity ratio (IIR). Association was evaluated using multilevel linear regression.

Results: An association between CV and LGE-CMRI intensity was observed at scales comparable to the size of a mapping electrode: −0.11 m/s per unit increase in NI ($P < 0.001$) and −0.96 m/s per unit increase in IIR ($P < 0.001$). The magnitude of this change decreased with larger measurement area. Reproducibility of the association was observed with NI, but not with IIR.

Conclusion: At clinically relevant spatial scales, comparable to area of a mapping catheter electrode, LGE-CMRI correlates with CV. Measurement scale is important in accurately quantifying the association of CV and LGE-CMRI intensity. Importantly, NI, but not IIR, accounts for changes in the dynamic range of CMRI and enables quantitative reproducibility of the association.

Keywords: LGE-MRI, image segmentation, fibrosis, electro anatomical mapping, conduction velocities, Atrial fibrillation, left atrium

INTRODUCTION

Success rates of catheter ablation for persistent AF is hindered by our poor understanding of the underlying mechanisms of AF persistence. Central to improving this understanding is the relationship between local myocardial conduction properties and the underlying tissue architecture, determined clinically by estimating myocardial fibrotic burden using late-gadolinium enhanced cardiac magnetic resonance imaging (LGE-CMRI). The challenges to determining this relationship are in part due to limitations and inconsistencies in the acquisition, interpretation and the registration of high-resolution imaging and electroanatomic mapping (EAM) data to allow correlative analyses.

It has previously been established that an electro-architectural relationship exists between myocardial fibrosis and CV on a regional and whole-heart level (Badger et al., 2009; Fukumoto et al., 2016). However, if such a relationship exists on a localized level, LGE-CMRI may fulfill its potential as a non-invasive tool to map myocardial conduction properties for risk stratification and treatment guidance.

Current 3D EAM systems with high-density multi-electrode contact mapping catheters can provide detailed spatio-temporal information on the functional behavior of the endocardium. Local CV can give a clear interpretation of underlying tissue health and identify the presence of non-conducting fibrotic tissue through the analysis of wave-front propagation patterns (Spach and Kootsey, 1983; Tanaka et al., 2007). The accurate evaluation of local CV requires invasive contact mapping with subsequent laborious post-processing of acquired electrograms.

Late-gadolinium enhanced cardiac magnetic resonance imaging is a well-established non-invasive technique to visualize myocardial fibrosis and has been corroborated with histomorphometric validation (Schmidt et al., 2007). Fibrotic atrial imaging has had mixed success due to the current limits of MRI resolution, the patchy nature of atrial fibrosis and difficulties in inter-patient scar-thresholding. As a consequence, several post-processing algorithms and intensity normalization approaches have been developed to improve the robustness of LA fibrosis-mapping from LGE-CMRI (Pontecorboli et al., 2017). Although the extent of enhancement has been associated with conventional markers of atrial structural remodeling such as LA dimension (Habibi et al., 2015), and clinical outcomes following catheter ablation (McGann et al., 2011), there is continued uncertainty surrounding the exact nature and pathological state of the atrial myocardium delineated by high-intensity regions.

We sought to test the hypothesis that a systematic and objective approach to the acquisition and spatial correlation of CV and LGE-CMRI data can define a reproducible electro-architectural relationship at clinically relevant scales.

Abbreviations: CL, Cycle length; CV, Conduction velocity; EAM, Electro anatomical mapping; IIR, Image Intensity Ratio; LGE-CMRI, Late gadolinium enhanced cardiac MRI; NI, Normalized Intensity.

MATERIALS AND METHODS

A diagram showing the key steps of the data collection and analysis methodology used in the study is shown in **Figure 1**.

Study Population

Patients with symptomatic persistent AF (based on the classification of AF by published guidelines from the AHA/ACC/HRS/ESC) presenting for their first ablation to Imperial College Healthcare NHS Trust were prospectively enrolled. The study was approved by the Local Research and Ethics Committee for Imperial College Healthcare NHS Trust and written informed consent was obtained from each patient. Patients with contraindications to undergoing LGE-CMRI were excluded from the study.

Data Acquisition

Each patient underwent LGE-CMRI prior to the ablation procedure. MRI acquisition was performed using a 1.5T Philips Achieva MR system, and a 5- or 32-element phased-array cardiac coil. LGE-CMRI was performed in the axial orientation 12–20 min following the 20 ml bolus of gadobenate dimeglumine contrast agent, using an ECG triggered, free-breathing navigator-gated whole heart 3D spoiled gradient echo acquisition sequence. Resolution was at 1.5 × 1.5 × 4 mm and reconstructed to 1.25 × 1.25 × 2 mm. Complete LA coverage was obtained with 40–50 slices. Data were acquired within a window of 100–150 ms within each R-R interval depending on heart rates, with a low-high k-space ordering and spectral pre-saturation with inversion recovery (SPIR) for fat suppression. The inversion recovery delay was determined from a Look-Locker sequence, with an inversion time chosen to null myocardial signal. MRI scans were performed in patients in rate-controlled AF. To assess the robustness and reproducibility of the methodology, two patients (denoted throughout as patients G and H) underwent two pre-ablation LGE-CMRI scans, 2 weeks apart.

Catheter ablation was performed within 2 weeks from the LGE-CMRI scan. All anti-arrhythmic drugs were discontinued for at least 5 half-lives, and amiodarone was discontinued at least 60 days prior to the ablation procedure. All procedures were performed in the post-absorptive state under general anesthesia. Transesophageal echocardiography was performed in all patients once anesthetized to exclude LA appendage clot, and to subsequently guide transseptal puncture. A deflectable decapolar catheter (Inquiry^{TM}, St Jude Medical, St. Paul, MN, United States) was positioned in the coronary sinus to record electrograms, pace the atrium, and serve as a temporal reference. Single *trans*-septal punctures were performed using a Brokenbrough needle through a fixed curve long-sheath (SL0, St Jude Medical, MN, United States). Unfractionated heparin was administered to achieve an activated clotting time of 300–350 s throughout the procedure.

An impedance-based EAM system (NavX EnsiteTM Velocity, St Jude Medical, MN, United States) was used. The LA geometry and all subsequent data were acquired using a 20-pole (1 mm electrodes) double-loop catheter (Inquiry^{TM} AFocusII^{TM}, St Jude Medical, MN, United States) with 4 mm electrode spacing. Before

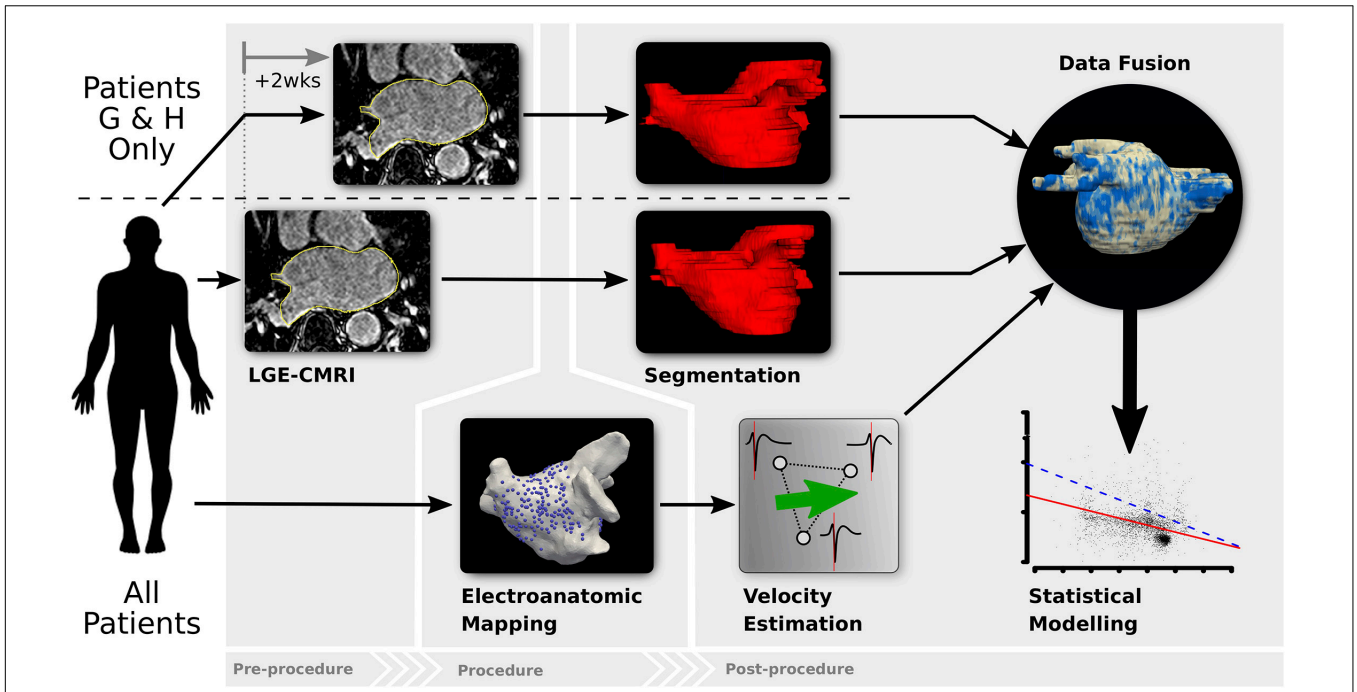

FIGURE 1 | Diagram of the analysis methodology. All patients undergo LGE-CMRI prior to the ablation procedure (patients G and H had 2 pre-procedural LGE-CMRI to assess reproducibility of LA fibrosis-mapping). Prior to any ablation, LA EAM during pacing is performed. Localized CV is estimated from EAM data and LGE-CMRI images are segmented to estimate fibrosis density. Data is co-registered and fused, after which statistical modeling is undertaken.

each acquisition, the AFocusII catheter was held tangentially to the endocardial surface, enabling stable tissue contact. Patients presenting in AF underwent external DCCV before any mapping was conducted. Following the acquisition of the LA geometry, high-density LA activation mapping was performed. The left atrium was paced from one of more sites [i.e., the coronary sinus, roof of left atrium and left atrial (LA) appendage] at pacing rates of 250, 300, 350, and 600 ms. The pacing protocol included a drive train of 8 beats to ensure that LA capture and activation was consistent (avoiding latency and decrementation), and also to facilitate the stability of AFocusII catheter at the particular site of the left atrium that was being interrogated/mapped.

The LA was paced using a drive train protocol of 8 beats from the coronary sinus, roof, and/or LA appendage. Unipolar electrograms were recorded and displayed at filter settings of 0.5–100 Hz during the procedure, where the 20 recordings together form a kernel as shown in **Figure 2A**. The electrode positions were projected to the geometry by the EAM system (**Figures 2E,F**). Electrodes more than 5 mm away from the surface were disregarded.

Data were acquired at multiple locations on the LA, focused mainly on the posterior endocardial wall where the highest propensity of fibrosis was expected to be found (Cochet et al., 2015). Local activation times (LATs) were calculated by the EAM system relative to a reference electrode and assigned as the time of the maximum negative gradient of the unipolar electrogram. Electrograms were assessed post-procedurally by an experienced Cardiac Electrophysiologist and those indicative of poor contact or high noise were rejected. Following mapping, pulmonary vein isolation was achieved. All patients were observed for a further 24 h prior to discharge. No complications were observed in this cohort of patients.

MRI/EAM Segmentation and Registration

The LA epicardial surface on LGE-CMRI images was manually segmented by an experienced Cardiac Radiologist, as shown in **Figure 2B**, and the epicardial surface was extracted. The EAM surface was co-registered to the MRI surface (Rueckert et al., 1999; Studholme et al., 1999; Schnabel et al., 2001; Ali et al., 2015). The accuracy of the registration process was estimated by target registration error (Fitzpatrick and West, 2001). Projected EAM surface electrode positions were mapped under the computed surface transformation to the MRI surface. The operators performing the ablation procedure were blinded to the generated LA scar-maps derived from the LGE-CMRI.

Local and Regional Conduction Velocity Estimation

Conduction velocity (CV) was estimated both locally and regionally. Regional CV was estimated by fitting a model of an ideal circular propagating wavefront to the positions and LATs of the 20 electrodes of a given kernel. Additionally, the wavefront radius, r, and residual error, η, of the fit were calculated (Roney et al., 2014). High η indicate that the wavefront is not sufficiently smooth within the kernel. Kernels with $\eta < 5$ s/mm were rejected as the wavefront violated the planarity assumptions required by the local CV analysis below.

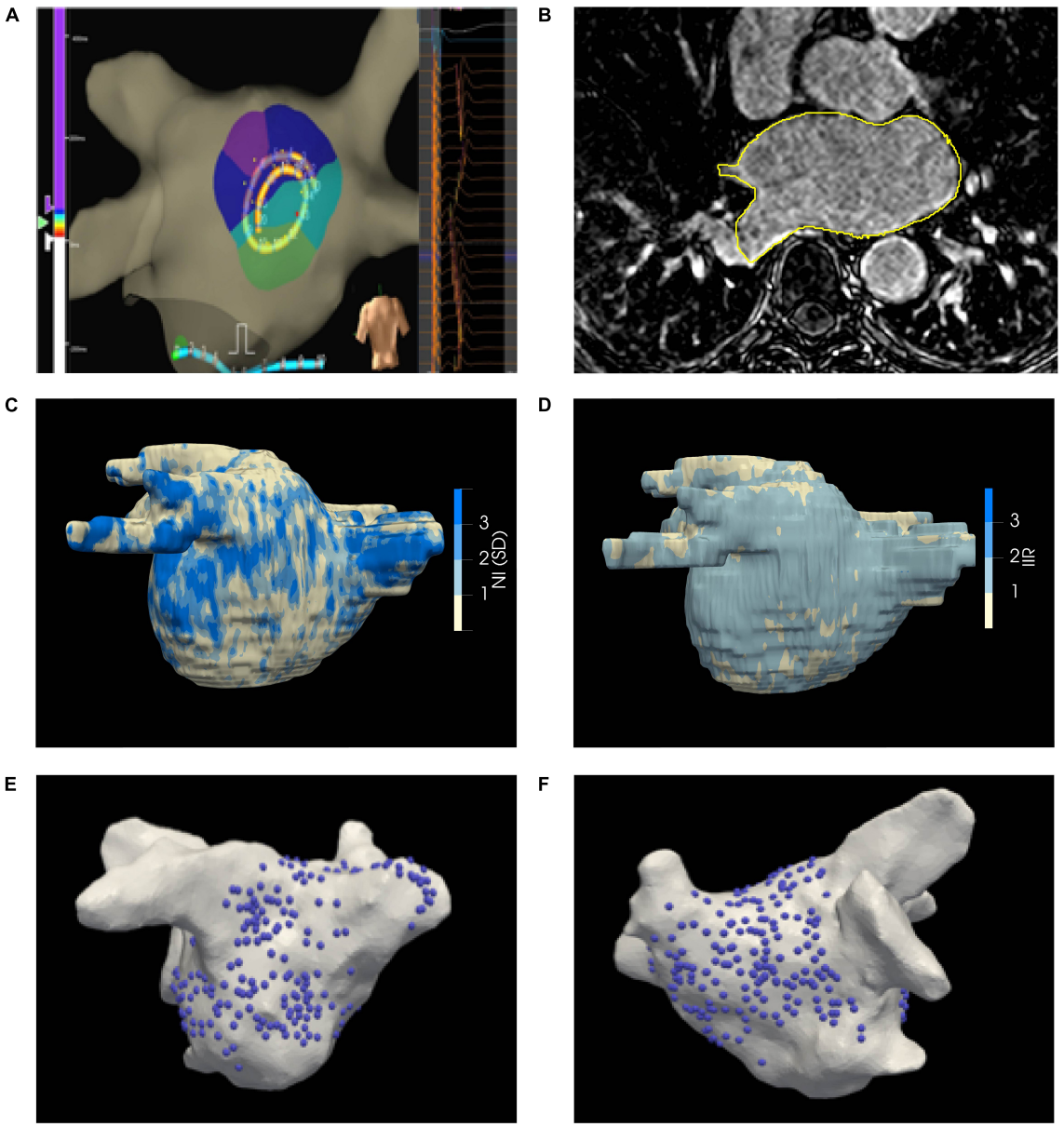

FIGURE 2 | (A) Ensite^{TM} Velocity mapping system used for collecting endocardial electrograms. The LA was paced over a range of CLs and the acquired unipolar electrograms are shown in the right panel. **(B)** LGE-CMRI axial slice with manual segmentation delineated in yellow **(C)** Illustrative patient-specific map NI. **(D)** Illustrative patient-specific map of IIR for same patient as **(C, E, F)** Distribution of electrograms on the posterior and anterior walls of the LA, respectively.

The local CV is calculated using the principle of triangulation which uses the differences in LATs across unique groups of 3 mapping electrodes (triads) and their interelectrode distance (Kojodjojo et al., 2005). This approach provides accurate estimates of velocities in areas of just a few mm (Badger et al., 2009), but assumes planar propagating wavefronts (Cantwell et al., 2014). Triads were only chosen between concurrent recordings within the same kernel to avoid any inter-beat variability of wavefront propagation. The minimum interelectrode distance between any pair of electrodes in a triad was constrained to be greater than the registration error.

Detection and Evaluation of Left Atrial Wall Intensities From LGE-CMRI

Raw absolute LA wall image intensities were extracted from the LGE-CMRI image as the maximum voxel intensity along a 3 mm inward-facing normal from the segmented epicardial surface.

Left atrial wall LGE-CMRI intensities are acquired in arbitrary units and their average brightness and dynamic range varies between images, even between multiple scans of the same subject. Local gadolinium uptake was quantitatively evaluated through two intensity normalization techniques: (1) Normalized intensity (NI) is calculated from the raw intensity by subtracting the mean

intensity of the LA blood pool and dividing by the standard deviation (SD) of the blood pool voxels (Kolipaka et al., 2005; Fukumoto et al., 2016) Image Intensity Ratio (IIR) is calculated as the ratio of raw intensity values and the mean intensity of the LA blood pool (Khurram et al., 2014). Both these metrics convert the raw intensities to quantities which can be compared, and are routinely utilized in LA scar-mapping with LGE-CMRI (McGann et al., 2011; Khurram et al., 2014; Fukumoto et al., 2016). The mean and SD of the blood pool were calculated by shrinking the segmented epicardial surface by 5 voxels (3 mm). The average NI or IIR value on the area enclosed by each triad of transformed electrode positions was then calculated (Ali et al., 2014). A representative map of NI on the segmented surface is shown in **Figure 2C**.

Reproducibility

A sub-group of two patients had two pre-ablation LGE-CMRI scans, separated by 2 weeks. Segmentation, registration and construction of the LA scar map were performed independently on each image. A single EAM dataset was used per patient for determining association. The data from each scan were included in the statistical analysis as separate datasets. If the image processing and registration methodology is reproducible, the estimated association should not be significantly different between the two scans of the same patient.

Statistical Analysis

Continuous variables are given as mean ± SD; categorical variables are given as percentages. A linear mixed-effects model was used to characterize the relationship between LA wall intensity, using either NI or IIR, and CV. Likelihood-ratio tests were used to compare if models, fit by maximum likelihood, were significantly different. The inclusion of CL did not significantly improve the model fit and was excluded from the final model.

A multilevel model was used to characterize the relationship between LA wall intensity and CV. Multilevel models provide a mechanism to account for, and quantify, variation in model intercepts and slopes across patients and cycle lengths. The association between normalized intensity, I, and CV, V was modeled as

$$V_{ijk} = (\beta_0 + u_j + v_k) + (\beta_1 + \beta_{2j})\, I_{ijk} + \varepsilon_{ijk}$$

where β_0 is the overall intercept, and u_j and v_k are random effects associated with patients and cycle lengths. β_1 captures the effect due to intensity and is the primary parameter of interest in this study, representing the overall association between CV and intensity across all patients and cycle lengths. The β_{2j} values represent per-patient random slopes; that is, the patient-specific deviation from β_1. Likelihood-ratio tests were used to compare if models, fit by maximum likelihood, were significantly different. The model reported here was statistically significant ($p < 0.001$) compared to all other simpler models without random intercepts or slopes. The inclusion of a random slope for cycle length did not significantly improve the model fit.

Two-sided p-values with $p < 0.05$ were considered to indicate statistical significance. Statistical analyses were performed using R version 3.4.3 (The R Foundation for Statistical Computing).

RESULTS

Study Population

Due to the large number of data points collected per patient at multiple paced CL, a total of 8 patients provided sufficient data for the purposes of this study. A summary of the clinical characteristics is given in **Table 1**. Patients are denoted as A-H.

Data Quality

All EAM surfaces were registered to their corresponding MRI surfaces for co-localization of image intensity with CV. Average target registration errors were 3.08 mm (range 1.94–5.71 mm).

A total of 267 kernels were acquired across all patients, comprising a total of 5340 mapping points. In total 171 kernels were rejected due to non-planarity of the underlying wavefront ($\eta < 5$ s/mm). A total of 96 complete or partial kernels (mean 12 kernels/patient, range 2–13) remained. An average of 435 triads were formed per kernel (range 1–1140 triads/kernel).

Distribution of Conduction Velocities and Left Atrial Wall Intensities

An overview of the data used in this study is shown in **Figure 3** and summary statistics for CV and NI for each patient are given in **Supplementary Table 1**. The CV sampled across all patients is given in **Figure 3A**. The mean CV was 0.85 m/s. A representative example of the distribution of calculated CV is shown in **Figure 3B** for a kernel from Patient H, paced at a cycle-length of 600 ms, with the corresponding regional CV estimate indicated by the red line. Good coherence between the local and regional algorithms was observed across all kernels in the study.

An example of the distribution of gadolinium enhancements using NI (Patient H, second scan) is shown in **Figure 3C**. The distributions of NI across the entire segmented atrial surface

TABLE 1 | Clinical demographics of patients.

Patient characteristics (n = 8)	
Age (y)	62 ± 11
Male	5 (62.5)
Mean LA size on TTE (mm)	41 ± 6
MeanCHADS2 score	2.4 (0–5)
Mean left ventricular EF (%)	62 ± 8
Hypertension	3 (37.5)
Diabetes mellitus	1 (12.5)
Cerebrovascular disease	1 (12.5)
Coronary artery disease	2 (25)
History of heart failure	0 (0)
Duration of persistent AF (months)	19 ± 10.7
Anti-arrhythmic drug therapy (beta-blocker, flecainide, and amiodarone)	6 (75)

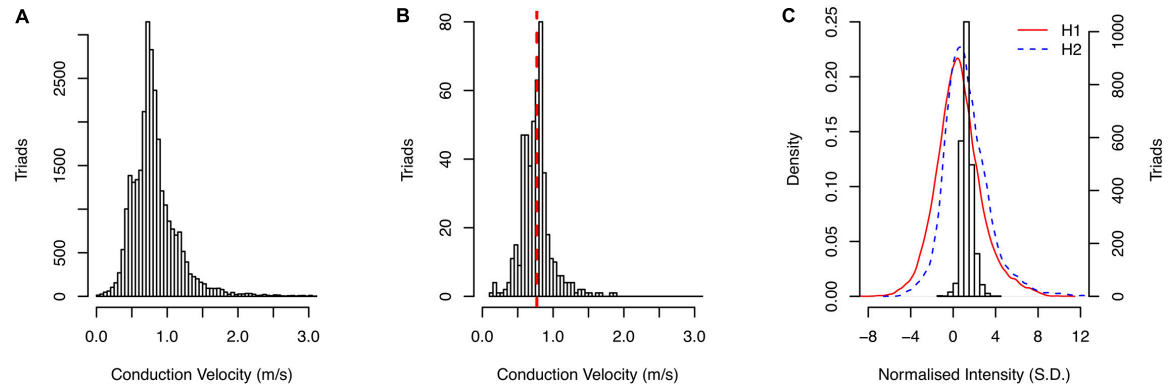

FIGURE 3 | (A) Distribution of CV measurements in the study. **(B)** Comparison of local CV measurement distribution with regional CV estimate (red dashed line). **(C)** Distribution of sampled NI for patient H second scan and the density of NI across entire atrial surface for both scans.

for the first and second scans are shown by the red and blue lines, respectively.

Influence of Triad Area

Triads were only formed within individual kernels from those electrodes in good contact with the myocardium. Triad areas ranged from 0.12 mm^2 to 590 mm^2. The change in CV per unit increase in LGE-CMRI intensity, denoted β_1, was measured across all patients and CL. The effect of measurement area on this slope was studied by binning triads by their area and fitting the model to those triads within each bin separately. Bins were chosen as 10 mm^2 wide non-overlapping intervals in the range 0–160 mm^2. Beyond this range there were insufficient data to generate reliable statistical models. **Figure 4** shows the change in the slope with increasing triad area. The magnitude of the slope was found to decrease with increasing area. To address the hypothesis that CV is associated with LGE-CMRI enhancement, specifically at small scales, only those triads with area <80 mm^2 were considered for the remainder of the study.

Association of Localized LGE Intensity With CV

Conduction velocity correlated with LGE-CMRI intensity (slope = −0.104 m/s change in CV per unit increase of NI, $p < 0.001$). The CV at 0 S.D. (model intercept) was 1.00 m/s, which is within the expected physiological range of healthy myocardium (Ramanathan et al., 2006; Cantwell et al., 2015). Per-patient slopes and intercepts are shown in **Figure 5A**. Six of the per-patient slopes are significantly different from the overall slope (p-values < 0.05). **Supplementary Figure 1** shows corresponding CV and NI at each triad for all kernels from Patient G, scan 2. The overall association and patient-specific association from the statistical model are also highlighted.

No random effect relating CL with NI was included in the model (based on the outcome of likelihood-ratio tests). Only one CL (350 ms) had an intercept significantly different from the overall intercept. Variations in the intercepts with CL were two orders of magnitude smaller than the overall intercept, suggesting there is negligible change in the relationship with respect to CL.

Reproducibility of LGE-CV Evaluation

For Patients G and H, who underwent two LGE-CMRI scans, the images were independently segmented, registered with the clinical data and fused to examine reproducibility. These are shown as G1, G2, H1, and H2 in **Figure 5A**. For both patients, the slope and intercept for the first and second scans did not differ with statistical significance when using NI.

Comparison of Left Atrial Wall Normalization (NI vs IIR)

Left atrial wall intensity was assessed using NI and IIR. The statistical model was modified to also examine the relationship between IIR with CV. This identified a change in CV of −0.942 m/s per unit increase in IIR ($p < 0.001$). The CV was estimated as 1.00 m/s at an IIR value of 1.0, which corresponds to an NI value of 0 S.D. Per-patient slopes and intercepts for the association of CV with IIR are shown in **Figure 5B**. As for NI, six of the patients have slopes which are significantly different from the overall slope. However, the confidence intervals are larger and reproducibility is poor, as evidenced by a significant difference in the random slopes of H1 and H2.

DISCUSSION

Main Findings

We have demonstrated a localized relationship between local myocardial CV and LA wall LGE in patients with persistent AF on clinically relevant scales comparable to a mapping catheter electrode or ablation lesion. Higher normalized LA intensities represent increased structural fibrotic remodeling and this corresponds to slower CV. The overall estimate for the change in CV with each unit increase in LA intensity was found to be substantially larger in magnitude than previously reported over larger spatial scales. Triad size was found to quantitatively affect the slope, with larger area measurements reducing the magnitude of the corresponding relationship. NI was identified to be a more effective intra- and inter-patient measure of LA intensity normalization compared to IIR, leading to increased confidence

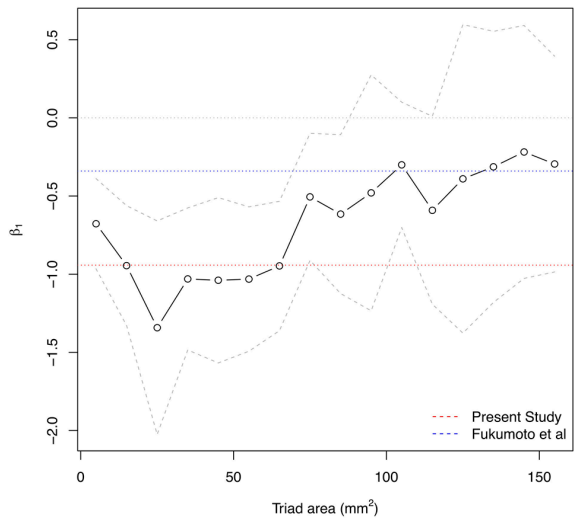

FIGURE 4 | Influence of measurement area on the overall β_1 estimate for association of CV with NI. Solid area denotes 95% confidence intervals. Larger measurement areas lead to lower magnitude β_1 estimate. The dotted red line indicates final β_1 estimate from present model for localized measurements with areas <80 mm^2. The dotted blue line indicates beta estimate from Fukumoto et al[1].

in the estimate of and improved intra-patient reproducibility. There were no significant differences in the relationship across multiple scans of the same patient.

Conduction Velocity and LGE-CMRI Defined Fibrosis

Lower local CV were observed in LA regions with increased fibrotic change as defined by the higher extent of gadolinium enhancement. The conduction delay can be explained by several underlying pathophysiological mechanisms including gap junctional remodeling, Na + channel abnormalities and heterogeneous cell-coupling between myocytes and fibroblasts (Rook et al., 1992; Maleckar et al., 2009; King et al., 2013).

Measurement Scale

The area subtended by the triads used in the analysis had a clear influence on the resulting beta estimate. In this study, the association is determined using triads of area <80 mm^2, allowing for a more direct translation and relevance to catheter ablation in clinical practice. At the upper end of this range (70–80 mm^2), the average maximal edge length of each triad was 15.4 mm (range 5.9–20.0 mm). For comparison, the typical contact area of the ablation electrode is approximately 10 mm^2 (3.5 mm diameter). Intuitively, averaging over larger areas diffuses the effect of small-scale variations in the quantities of interest and potentially masks the true localized association between them. In the atrium this is crucial, due to the patchy and non-uniform nature of atrial fibrosis (Frustaci et al., 2007). As shown in **Figure 2**, gadolinium uptake varies on scales as small as 5 mm such as in narrow isthmuses which can promote slow conduction and re-entry (Ciaccio et al., 2008). Fukumoto et al evaluated intensities for each of 20 sectors of the atrial wall in each axial slice. The length of each sector is approximately 20 mm, which is at the upper end of maximal triad edge length used in the present study and correspondingly the larger values of area in **Figure 4**. Consequently, at larger areas, localized variations in CV would be averaged out leading to a reduction in the magnitude of the association between CV and intensity. This factor may explain the apparent discrepancy between the association (beta estimate) of the present study (β_1: −0.942 m/s/IIR), at smaller spatial scales of areas <80 mm^2, and that of Fukumoto et al. (β_1:

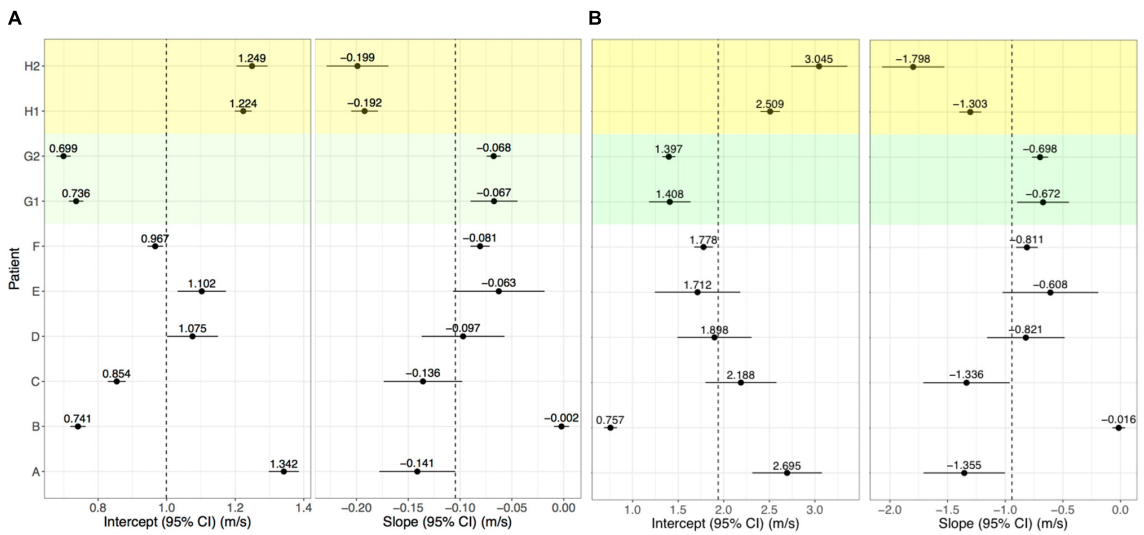

FIGURE 5 | Per-patient model intercepts (left) and slopes (right) for NI **(A)** and IIR **(B)**. Values indicate the per-patient difference from the model's overall intercept () and slope (NI: 1.00 m/s, = −0.104; IIR: = 1.94 m/s, and = −0.942. G1, G2 and H1, H2 correspond to repeat analyses of patients G and H for assessing reproducibility.

−0.34 m/s/IIR). To explain this, **Figure 4** also shows the same area dependency plot expressed in terms of IIR where the red and blue dotted lines mark the beta estimates from our study and that of Fukumoto et al., respectively. The IIR beta estimate of −0.34, found in Fukumoto et al. for persistent AF patients, is of smaller magnitude than the IIR beta estimate of −0.94 reported here, but is consistent with our findings, if measurement area is taken into consideration. This further emphasizes the importance of resolution when quantitatively comparing quantities.

Reproducibility

While both scans for each patient in the reproducibility sub-study were compared with the same EAM data, our experience suggests that the segmentation and co-registration steps are most prone to the introduction of errors. Importantly, the relationship between CV and NI within each pair of datasets were statistically indistinguishable, confirming the accuracy and reproducibility of our approach.

Intensity Normalization

One significant contribution of our study is a comparison between the IIR and NI metrics for the qualitative assessment of independently acquired MR images.

By its definition, IIR accounts for underlying shifts in the intensity spectrum, while NI includes the standard deviation of the blood pool to account for inter- and intra-patient differences and accordingly for differences in the dynamic range of the images. Consequently, NI led to a more robust statistical model for elucidating the relationship between CV and intensity, compared with IIR, as well as improved reproducibility of the patient-specific association. In particular, the 95% confidence intervals on the intercept and slope estimates for IIR, shown in **Figure 5B**, were generally larger than the corresponding confidence intervals for NI in **Figure 5A**. Reproducibility of patient-specific slopes was observed for NI, but not for IIR.

Conduction Velocity Restitution

No statistically significant effects due to CL were observed, indicating no identifiable CV restitution.

Limitations

In order to obtain high fidelity electrograms, electroanatomical data were limited to the posterior LA, which was anatomically consistent, conducive to placement of the AFocusII mapping catheter tangential to the endocardial surface, and contained a predilection of fibrosis. Sampling from the posterior wall may have potentially introduced sampling bias. Future studies should incorporate contact sensing catheters to increase robustness of the data collection protocol.

This study investigated a persistent AF cohort which has been shown to have more extensive structural and electrical remodeling compared to paroxysmal AF patients. Future studies should include a more heterogeneous group of patients.

The image MR images used in this study were manually segmented to delineate the epicardial wall of the left atrium. As such, errors may have been introduced during the segmentation process.

Image intensity ratio is defined as the ratio of the wall intensity of the sector to the blood pool mean (Khurram et al., 2014). However, in this study, IIR was evaluated point-wise as the ratio of the epicardial wall intensity and the mean blood intensity.

CONCLUSION

Higher LA intensities correspond to lower local myocardial conduction velocities. The scale of measurement of CV and LA wall intensity is crucial in accurately quantifying this relationship, which is found to be of a higher magnitude than previously reported[1]. Importantly, NI, but not IIR, accounts for changes in the dynamic range of LGE-CMRI and improves the quantitative reproducibility of the relationship. Evaluation of the LA substrate with the use of normalized intensity from LGE-CMRI can be potentially used as a minimally invasive tool to predict atrial myocardial conduction properties.

DATA AVAILABILITY STATEMENT

The raw data supporting the conclusions of this article will be made available by the authors, without undue reservation.

ETHICS STATEMENT

The studies involving human participants were reviewed and approved by Local Research and Ethics Committee for Imperial College Healthcare NHS Trust. The patients/participants provided their written informed consent to participate in this study.

AUTHOR CONTRIBUTIONS

RA, NQ, and CC conceived and planned the experiments. RA developed and implemented the algorithms. NQ obtained the clinical data and segmented the MRIs. SL and CC developed the statistical model and performed the statistical analysis. CR and SK contributed to the interpretation of the results. PL, JT, and NP helped supervise the project. All authors provided critical feedback and helped shape the research, analysis and manuscript.

FUNDING

This work was supported by the British Heart Foundation (BHF), grants FS/11/22/28745 and RG/10/11/28457, Rosetrees Trust Interdisciplinary Prize 2016 (Grant No. M577), the ElectroCardioMaths Program of the Imperial Centre for Cardiac Engineering and NIHR Imperial Biomedical Research Center.

SUPPLEMENTARY MATERIAL

The Supplementary Material for this article can be found online at: https://www.frontiersin.org/articles/10.3389/fphys.2020.570203/full#supplementary-material

REFERENCES

Ali, R. L., Cantwell, C. D., Roney, C. H., Qureshi, N. A., Lim, B., Siggers, J. H., et al. (2014). A novel method for quantifying localised correlation of late-gadolinium intensity with conduction velocity. *Comput. Cardiol.* 41, 193–196.

Ali, R. L., Cantwell, C. D., Qureshi, N. A., Roney, C. H., Lim, B., Sherwin, S. J., et al. (2015). "Automated fiducial point selection for reducing registration error in the co-localisation of left atrium electroanatomic and imaging data," in *Proceedings of the 2015 37th Annual International Conference of the IEEE Engineering in Medicine and Biology Society (EMBC)*, (Milan: IEEE), 1989–1992. doi: 10.1109/EMBC.2015.7318775

Badger, T. J., Oakes, R. S., Daccarett, M., Burgon, N. S., Akoum, N., Fish, E. N., et al. (2009). Temporal left atrial lesion formation after ablation of atrial fibrillation. *Heart Rhythm.* 6, 161–168. doi: 10.1016/j.hrthm.2008.10.042

Cantwell, C. D., Roney, C. H., Ng, F. S., Siggers, J. H., Sherwin, S. J., and Peters, N. S. (2015). Techniques for automated local activation time annotation and conduction velocity estimation in cardiac mapping. *Comput. Biol. Med.* 65, 229–242. doi: 10.1016/j.compbiomed.2015.04.027

Cantwell, C. D., Roney, C. H., Ali, R. L., Qureshi, N. A., Lim, B., and Peters, N. S. (2014). A software platform for the comparative analysis of electroanatomic and imaging data including conduction velocity mapping. *Conf. Proc. IEEE. Eng. Med. Biol. Soc.* 2014, 1591–1594. doi: 10.1109/EMBC.2014.6943908

Ciaccio, E. J., Chow, A. W., Kaba, R. A., Davies, D. W., Segal, O. R., and Peters, N. S. (2008). Detection of the diastolic pathway, circuit morphology, and inducibility of human postinfarction ventricular tachycardia from mapping in sinus rhythm. *Heart Rhythm.* 5, 981–991. doi: 10.1016/j.hrthm.2008.03.062

Cochet, H., Mouries, A., Nivet, H., Sacher, F., Derval, N., Denis, A., et al. (2015). Age, atrial fibrillation, and structural heart disease are the main determinants of left atrial fibrosis detected by delayed-enhanced magnetic resonance imaging in a general cardiology population. *J. Cardiovasc. Electrophysiol.* 26, 484–492. doi: 10.1111/jce.12651

Fitzpatrick, J. M., and West, J. B. (2001). The distribution of target registration error in rigid-body point-based registration. *IEEE. Trans. Med. Imag.* 20, 917–927. doi: 10.1109/42.952729

Frustaci, A., Chimenti, C., Bellocci, F., Morgante, E., Russo, M. A., and Maseri, A. (2007). Histological substrate of atrial biopsies in patients with lone atrial fibrillation. *Circulation* 96, 1180–1184. doi: 10.1161/01.cir.96.4.1180

Fukumoto, K., Habibi, M., Ipek, E. G., Zahid, S., Khurram, I. M., Zimmerman, S. L., et al. (2016). Association of left atrial local conduction velocity with late gadolinium enhancement on cardiac magnetic resonance in patients with atrial fibrillation. *Circulat. Arrhythm. Electrophysiol.* 9:e002897. doi: 10.1161/CIRCEP.115.002897

Habibi, M., Lima, J. A., Khurram, I. M., Zimmerman, S. L., Zipunnikov, V., Fukumoto, K., et al. (2015). Association of left atrial function and left atrial enhancement in patients with atrial fibrillation: cardiac magnetic resonance study. *Circ. Cardiovasc. Imag.* 8:e002769. doi: 10.1161/CIRCIMAGING.114.002769

Khurram, I. M., Beinart, R., Zipunnikov, V., Dewire, J., Yarmohammadi, H., Sasaki, T., et al. (2014). Magnetic resonance image intensity ratio, a normalized measure to enable interpatient comparability of left atrial fibrosis. *Heart Rhythm.* 11, 85–92. doi: 10.1016/j.hrthm.2013.10.007

King, J. H., Huang, C. L., and Fraser, J. A. (2013). Determinants of myocardial conduction velocity: implications for arrhythmogenesis. *Front. Physiol.* 4:154. doi: 10.3389/fphys.2013.00154

Kojodjojo, P., Kanagaratnam, P., Markides, V., Davies, D. W., and Peters, N. S. (2005). Age-related changes in human left and right atrial conduction. *J. Cardiovas. Electrophysiol.* 17, 120–127. doi: 10.1111/j.1540-8167.2005.00293.x

Kolipaka, A., Chatzimavroudis, G. P., White, R. D., O'Donnell, T. P., and Setser, R. M. (2005). Segmentation of non-viable myocardium in delayed enhancement magnetic resonance images. *Int. J. Cardiovasc. Imag.* 21, 303–311. doi: 10.1007/s10554-004-5806-z

Maleckar, M. M., Greenstein, J. L., Giles, W. R., and Trayanova, N. A. (2009). K+ current changes account for the rate dependence of the action potential in the human atrial myocyte. *Am. J. Physiol. Heart Circ. Physiol.* 297, H1398–H1410. doi: 10.1152/ajpheart.00411.2009

McGann, C., Kholmovski, E., Blauer, J., Vijayakumar, S., Haslam, T., Cates, J., et al. (2011). Dark regions of no-reflow on late gadolinium enhancement magnetic resonance imaging result in scar formation after atrial fibrillation ablation. *J. Am. Coll. Cardiol.* 58, 177–185. doi: 10.1016/j.jacc.2011.04.008

Pontecorboli, G., Figueras, I. V. R. M., Carlosena, A., Benito, E., Prat-Gonzales, S., Padeletti, L., et al. (2017). Use of delayed-enhancement magnetic resonance imaging for fibrosis detection in the atria: a review. *Europace* 19, 180–189. doi: 10.1093/europace/euw053

Ramanathan, C., Ping, J., Ghanem, R., Ryu, K., and Rudy, Y. (2006). Activation and repolarization of the normal human heart under complete physiological conditions. *Proc. Natl. Acad. Sci. U S A.* 103, 6309–6315. doi: 10.1073/pnas.0601533103

Roney, C. H., Cantwell, C. D., Qureshi, N. A., Ali, R. L., Chang, ETy, et al. (2014). An automated algorithm for determining conduction velocity, wavefront direction and origin of focal cardiac arrhythmias using a multipolar catheter. *Conf. Proc. IEEE. Eng. Med. Biol. Soc.* 2014, 1583–1586. doi: 10.1109/EMBC.2014.6943906

Rook, M. B., van Ginneken, A. C., de Jonge, B., el Aoumari, A., Gros, D., and Jongsma, H. J. (1992). Differences in gap junction channels between cardiac myocytes, fibroblasts, and heterolo-gous pairs. *Am. J. Physiol.* 263, C959–C977. doi: 10.1152/ajpcell.1992.263.5.C959

Rueckert, D., Sonoda, L. I., Hayes, C., Hill, D. L., Leach, M. O., and Hawkes, D. J. (1999). Nonrigid registration using free-form deformations: application to breast MR images. *IEEE. Trans. Med. Imag.* 18, 712–721. doi: 10.1109/42.796284

Schmidt, A., Azevedo, C. F., Cheng, A., Gupta, S. N., Bluemke, D. A., Foo, T. K., et al. (2007). Infarct tissue heterogeneity by magnetic resonance imaging identifies enhanced cardiac arrhythmia susceptibility in patients with left ventricular dysfunction. *Circulation* 115, 2006–2014. doi: 10.1161/circulationaha.106.653568

Schnabel, J. A., Rueckert, D., Quist, M., Blackall, J. M., Castellano-Smith, A. D., Hartkens, T., et al. (2001). A generic framework for non-rigid registration based on non-uniform multi-level free-form deformations. *Med. Image Comput. Comp. Assisted Intervent. MICCAI.* 2001, 573–581. doi: 10.1007/3-540-45468-3_69

Spach, M. S., and Kootsey, J. M. (1983). The nature of electrical propagation in cardiac muscle. *Am. J. Physiol.* 244, H3–H22. doi: 10.1152/ajpheart.1983.244.1.H3

Studholme, C., Hill, D. L., and Hawkes, D. J. (1999). An overlap invariant entropy measure of 3D medical image alignment. *Pattern Recogn.* 32, 71–86. doi: 10.1016/s0031-3203(98)00091-0

Tanaka, K., Zlochiver, S., Vikstrom, K. L., Yamazaki, M., Moreno, J., Klos, M., et al. (2007). Spatial distribution of fibrosis governs fibrillation wave dynamics in the posterior left atrium during heart failure. *Circ. Res.* 101, 839–847. doi: 10.1161/circresaha.107.153858

Conflict of Interest: SK was employed by the company Abbott United States.

The remaining authors declare that the research was conducted in the absence of any commercial or financial relationships that could be construed as a potential conflict of interest.

frontiers in Physiology

REVIEW
published: 12 November 2020
doi: 10.3389/fphys.2020.570740

Linking Electrical Drivers With Atrial Cardiomyopathy for the Targeted Treatment of Atrial Fibrillation

*Gordon Ho[1,2], Andrew Y. Lin[1,2] and David E. Krummen[1,2]**

[1] Division of Cardiology, Department of Medicine, University of California, San Diego, San Diego, CA, United States, [2] Division of Cardiology, Veterans Affairs San Diego Medical Center, San Diego, CA, United States

The relationship between atrial fibrillation (AF) and underlying functional and structural abnormalities has received substantial attention in the research literature over the past decade. Significant progress has been made in identifying these changes using non-invasive imaging, voltage mapping, and electrical recordings. Advances in computed tomography and cardiac magnetic resonance imaging can now provide insight regarding the presence and extent of cardiac fibrosis. Additionally, multiple technologies able to identify electrical targets during AF have emerged. However, an organized strategy to employ these resources in the targeted treatment of AF remains elusive. In this work, we will discuss the basis for mechanistic importance of atrial fibrosis and scar as potential sites promoting AF and emerging technologies to identify and target these structural and functional substrates in the electrophysiology laboratory. We also propose an approach to the use of such technologies to serve as a basis for ongoing work in the field.

Keywords: atrial fibillation, fibrosis, cardiac imaging, electrophysiologic mapping, electrical rotors, focal sources

OPEN ACCESS

Edited by:
Atul Verma,
University of Toronto, Canada

Reviewed by:
Dawood Darbar,
University of Illinois at Chicago, United States
Haibo Ni,
University of California, Davis, United States

***Correspondence:**
David E. Krummen
dkrummen@health.ucsd.edu

Specialty section:
This article was submitted to Cardiac Electrophysiology, a section of the journal Frontiers in Physiology

Received: *08 June 2020*
Accepted: *22 September 2020*
Published: *12 November 2020*

Citation:
Ho G, Lin AY and Krummen DE (2020) Linking Electrical Drivers With Atrial Cardiomyopathy for the Targeted Treatment of Atrial Fibrillation. Front. Physiol. 11:570740. doi: 10.3389/fphys.2020.570740

INTRODUCTION

Atrial fibrillation (AF) is the most common cardiac arrhythmia in the United States (Chugh et al., 2014). Catheter ablation is offered for patients with symptomatic AF despite medical therapy (January et al., 2014, 2019; Calkins et al., 2017), but success rates for ablation of persistent AF continues to be suboptimal with recurrent AF occurring in around 40–60% of patients in the landmark CABANA (Packer et al., 2019) and STAR-AF2 (Verma et al., 2015) trials. Potential contributing factors to the suboptimal success rates are the diverse phenotypes of atrial structural and functional abnormalities seen in patients with AF (Kottkamp, 2013; Krummen et al., 2015). While emerging technologies are now able to detect, classify, and target abnormal atrial substrate, their use is not well guided by existing guidelines or supported by randomized clinical trials (Quintanilla et al., 2016; Calkins et al., 2017). The purpose of this review is to propose a personalized AF ablation strategy utilizing emerging mapping and imaging techniques to target electrical drivers with or without associated atrial fibrosis. First, electrical and structural mechanisms of AF are summarized, followed by a review of the evidence linking fibrosis with electrical drivers of AF. Second, contemporary electrical invasive and non-invasive mapping and imaging techniques are discussed to localize electrical drivers and fibrosis. Finally, a proposed algorithm is proposed to help

guide personalized clinical treatment using these technologies and guide further clinical research.

DIVERSE ATRIAL SUBSTRATES UNDERLYING AF

In clinical practice, AF patients present with a spectrum of atrial electrical and structural substrates (Everett and Olgin, 2007; Kottkamp, 2013; Goette et al., 2016). **Figure 1** compares two patients from our electrophysiology laboratory with contrasting degrees of atrial cardiomyopathy. Patient 1 presented with persistent AF who remained symptomatic despite medical management and was referred for ablation. Voltage and activation mapping revealed relatively preserved bi-atrial voltages (**Figure 1A**) and a rapid left upper pulmonary vein electrical driver perpetuating AF (**Figure 1B**). Localized ablation terminated AF, which was subsequently non-inducible. In this patient with normal structural substrate, the AF was likely driven by an electrical driver from the pulmonary veins, as classically described (Haïssaguerre et al., 1998).

Patient 2 presented with recurrent persistent AF despite prior pulmonary vein isolation ablation. Voltage mapping revealed diffuse low voltage in the left atrium (**Figure 1C**), while panoramic multielectrode catheter mapping identified a rotational AF driver at the LA roof (**Figure 1D**). Limited ablation in the region of this driver terminated AF (**Figure 2C**), and the patient has remained in sinus rhythm during follow-up. In this patient with significant atrial fibrosis, extra-pulmonary vein drivers arising from the fibrotic substrate likely contributed to AF maintenance. These two examples demonstrate a broad spectrum of the structural and electrical substrate that may underly AF. While increasing atrial fibrosis typically correlates with a greater prevalence of extra-pulmonary vein sources (Angel et al., 2015; Cochet et al., 2018), counterintuitively, patients without fibrosis may have persistent AF while patients with extensive atrial fibrosis due to atrial cardiomyopathy may only have brief paroxysms of AF (Kottkamp, 2013). In a study by Kircher et al. (2018) in which invasive substrate mapping was performed in 119 patients, only 40% of persistent AF patients had low voltage zones, yet low voltage zones were still found in 18% of paroxysmal AF patients. While the AF source in the first patient would have been accounted for with guideline-directed pulmonary vein isolation (Haïssaguerre et al., 1998; Narayan et al., 2008), the driver located at the left atrial roof in patient 2 would not. Such examples, prevalent in the literature (Narayan et al., 2012a; Shivkumar et al., 2012) demonstrate the need for additional guidance regarding the use of patient-specific mapping and targeting strategies to treat AF.

MECHANISMS OF ATRIAL FIBRILLATION

There remains controversy surrounding the exact mechanisms of AF. This is likely due to multiple phenotypes of the arrhythmia and reflects a heterogeneous substrate (Krummen et al., 2015; Quintanilla et al., 2016; Calkins et al., 2017). Both abnormal electrical (Krummen et al., 2012; Baykaner et al., 2014, 2018; Haissaguerre et al., 2014; Schricker et al., 2014; Quintanilla et al., 2016) and structural/fibrotic abnormalities (Everett and Olgin, 2007; McDowell et al., 2013, 2015; Gonzales et al., 2014; Hansen et al., 2015, 2018; Sohns and Marrouche, 2020) have been implicated as mechanisms of AF, and may be different for each patient.

Electrical Substrate

Abnormal electrical substrate underlying AF may exist with or without the presence of fibrosis, and can be divided into 3 phases: initiation, transition and maintenance (Heijman et al., 2014; Krummen et al., 2015).

1. Initiation: The initiation of AF is thought to arise from rapid activation from a source, including the pulmonary veins (Haïssaguerre et al., 1998), superior vena cava, or other rapid foci (Gerstenfeld et al., 2003; Lin et al., 2003; Chen and Tai, 2005; Van Campenhout et al., 2013; Hayashi et al., 2015). This rapid ectopic activity can be caused by triggered activity [abnormalities in calcium handling leading to delayed afterdepolarizations (Dobrev et al., 2011) or loss of K + currents and delayed repolarization leading to early afterdepolarizations (Zellerhoff et al., 2009)] and abnormal automaticity, which have all been described around the LA/PV junction (Chou et al., 2005; Numata et al., 2012). At present, the standard of care for AF ablation is directed primarily at targeting triggers of AF from the pulmonary veins only. While reasonably effective, long-term elimination of AF triggers may be difficult or impossible, depending upon the rate of trigger formation, the dispersal of AF sources, and their frequency during invasive mapping and ablation procedures.
2. Transition: The transition period is the time during which the rapid activations from a focal source interact with regions with heterogeneous repolarization properties resulting in regional wavefront block, wavefront slowing, and the initiation of reentry (Krummen et al., 2012; Lalani et al., 2012; Schricker et al., 2014). This tissue heterogeneity can be manifested by both spatial dispersion of atrial fibrosis (Li et al., 1999; Chang et al., 2007) and ion currents [such as density of the rapid delayed rectifier current IKr (Li et al., 2001)], causing differences in conduction slowing, tissue refractoriness, and steep APD restitution (Krummen et al., 2012) to favor reentry.
3. Maintenance: Although the precise mechanisms of AF maintenance are incompletely understood, there is increasing evidence that AF is maintained by organized mechanisms. The exact type of organization is a topic of controversy, as some groups have proposed that AF is maintained via dissociated endo-epicardial breakthroughs (de Groot et al., 2010) or focal or rotational drivers (Jalife, 2003; Baykaner et al., 2014; Haissaguerre et al., 2014; Lalani et al., 2014; Schricker et al., 2014; Hansen et al., 2015, 2017, 2018; Quintanilla et al., 2016; Zahid et al., 2016; Csepe et al., 2017; Nattel et al., 2017; Zhao et al., 2017). Recent seminal work has demonstrated that rotational and

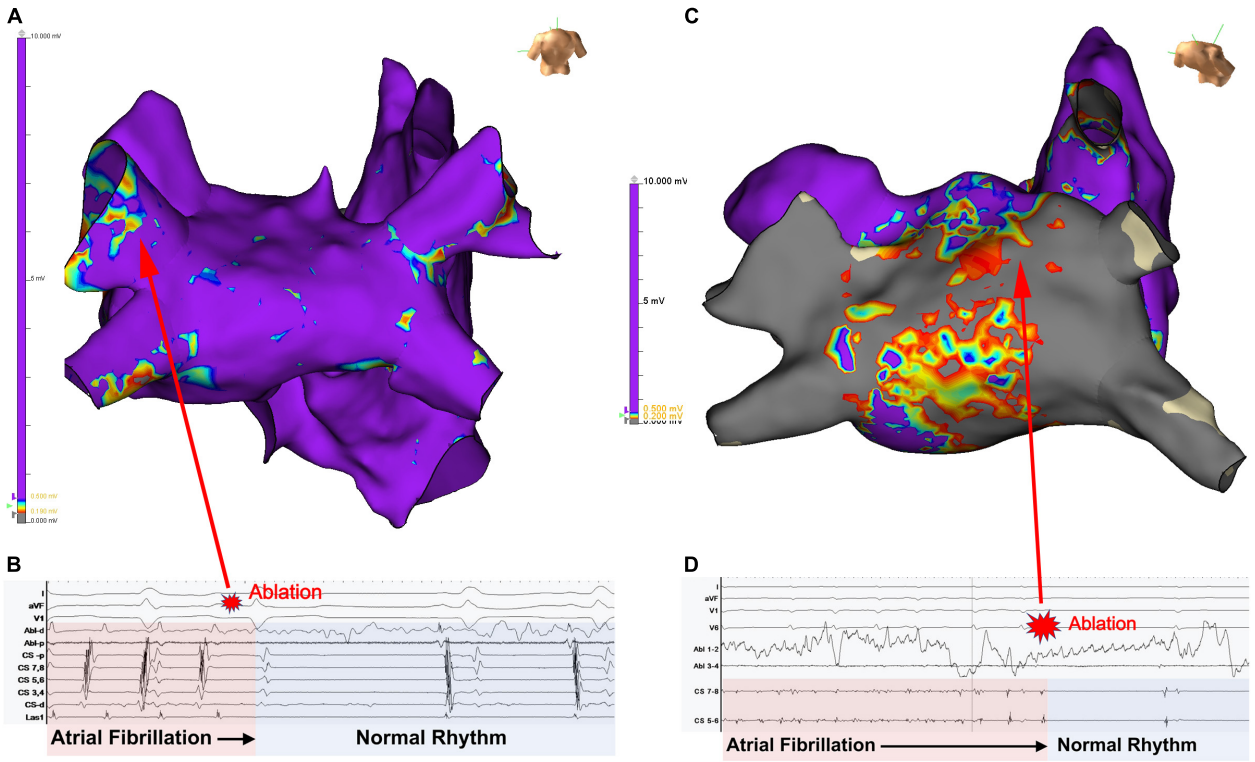

FIGURE 1 | Panel **(A)** shows the left atrial voltage map of a patient with persistent atrial fibrillation for 4 months. Panel **(B)** illustrates electrogram recordings from the ablation catheter showing a rapid driver site in the left upper pulmonary vein. Ablation at this site abruptly terminated AF. Panel **(C)** Bi-atrial voltage map of a patient with persistent atrial fibrillation s/p prior ablation with diffuse low-voltage and scar in the left atrium. Panel **(B)** shows a left atrial driver site in the LA roof. Panel **(D)** shows termination of AF with targeted ablation. Unpublished work from our laboratory.

focal drivers exist at sites that terminate AF when ablated, reinforcing the role of organized drivers maintain (Zhao et al., 2017; Kowalewski et al., 2018; Zaman et al., 2018; Leef et al., 2019).

Contribution of Fibrosis to Tissue Electrical Remodeling

Fibrotic atrial myopathy is associated with alterations in ionic currents, calcium cycling, and gap junctions leading to electrophysiologic remodeling and increased atrial susceptibility to triggered activity, automaticity, and reentry (Nattel et al., 2008; Shen et al., 2019). First, triggered activity may result from direct myofibroblast-cardiomyocyte interactions via gap junction coupling and diastolic depolarization of atrial myocytes by fibroblasts (Yue et al., 2011; Heijman et al., 2014). Secondly, fibroblast ion channel remodeling may also promote AF, with increased expression of Ca + + permeable TRPC3 channels and direct myofibroblast-cardiomyocyte interactions which cause conduction slowing due to Na + channel inactivation and impaired cell-cell coupling (Heijman et al., 2014). Changes in ionic channel properties occur with significant heterogeneity between the left and right atria, which may explain the propensity of AF to originate from the left atrium (Caballero et al., 2010). Remodeling of gap junctions such as connexin 40 and 43 and their expression, distribution, and intercellular orientation in atrial myopathy causing anisotropic conduction leading to reentry has been attributed to sustained AF (Shin et al., 2015). Finally, fibrosis and collagen deposition directly causes conduction slowing and heterogeneity.

Linking Fibrosis to Electrical AF Drivers

Advances in understanding the effects of fibrosis on electrical remodeling described above has provided a cellular basis that support recent observations correlating regions of fibrosis with focal and reentrant AF drivers. Prior work has demonstrated the relationship between functional electrical reentry and atrial structural heterogeneities such as fibrosis (Morgan et al., 2016) and fiber-angle discontinuities (Gonzales et al., 2014). Elegant *ex vivo* studies by Fedorov and colleagues reveal that AF re-entrant drivers are anchored to micro-anatomic regions of interstitial fibrosis (Hansen et al., 2015, 2016, 2017, 2018; Csepe et al., 2017; Zhao et al., 2017). In explanted human bi-atrial tissue sections shown in **Figure 2**, reentrant drivers were identified with high resolution optical activation mapping (**Figure 2A**) and colocalized using endocardial basket catheters (**Figure 2B**, left and center panels) with a clinical phase mapping system (FIRM, Abbott, Illinois) (Hansen et al., 2018). These drivers were anchored in regions of interstitial fibrosis imaged using high resolution 9T MRI (**Figure 2B**, right panel). Notably, epicardial electrodes revealed

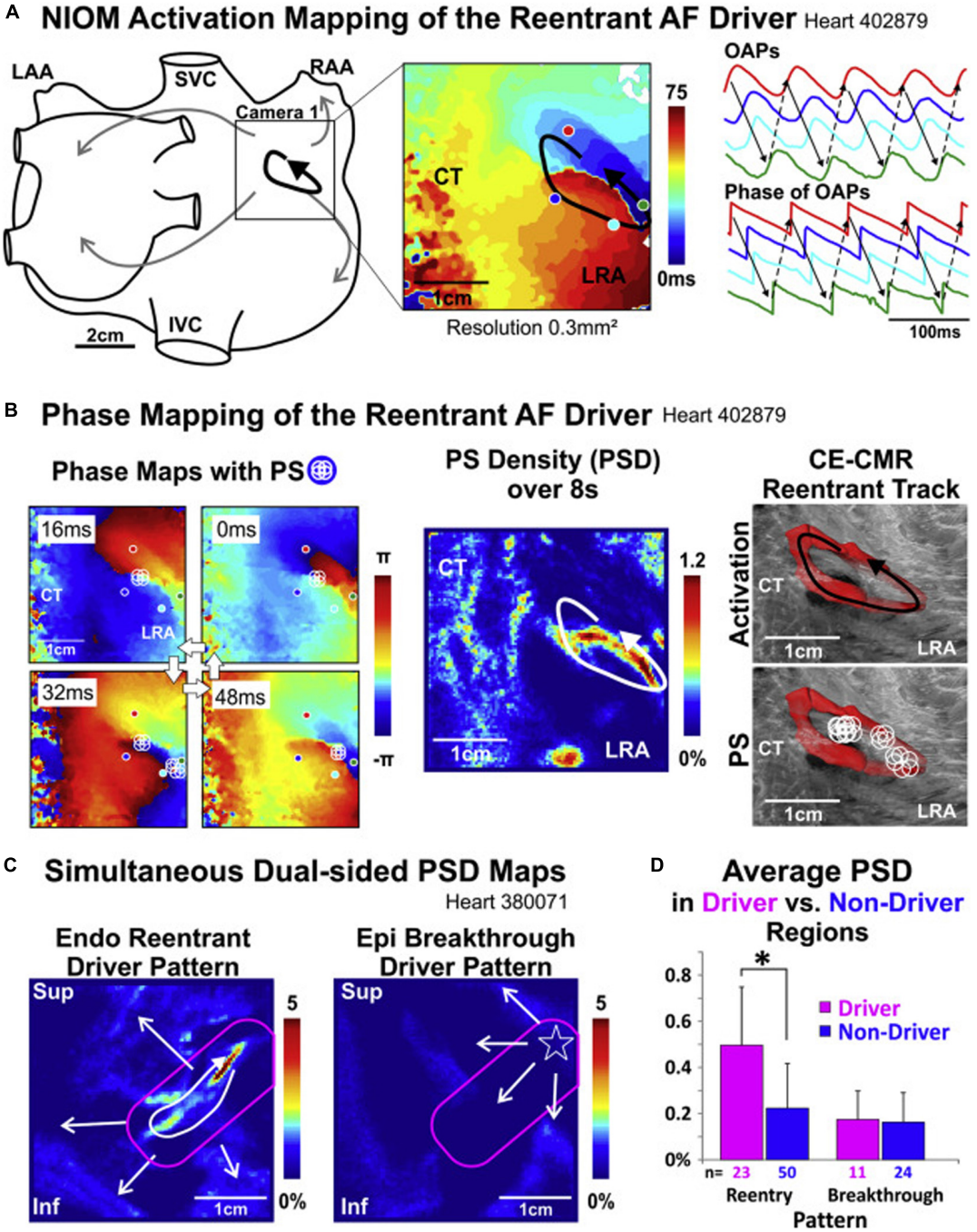

FIGURE 2 | Re-entrant drivers visualized with high resolution optical activation mapping **(A)** are colocalized with endocardial phase mapping using FIRMap basket catheters [**(B)**, left and center panels], and are anchored to regions of intramural fibrosis imaged with 9.4 T MRI [**(B)**, right panel]. Notably, endocardial re-entrant drivers result in epicardial focal breakthrough patterns when imaged with simultaneous endo-epi phase mapping **(C)**, with higher phase singularity density in regions with reentrant drivers identified **(D)**. NIOM, near-infrared optical mapping; CT, crista terminalis; LRA, low right atrium; OAP, optical action potentials; PS, phase singularities; CE-CMR, contrast-enhanced magnetic resonance; Endo, endocardium; Epi, epicardium; Inf, inferior; IVC, inferior vena cava; LAA, left atrial appendage; LRA, lateral right atrium; RAA, right atrial appendage; Sup, superior; SVC, superior vena cava. Hansen et al. (2018), reprinted with permission.

epicardial breakthroughs at sites of the endocardial reentrant drivers (**Figure 2C**). Ablation of these re-entrant drivers terminated AF, verifying their dominant role in AF (Hansen et al., 2015; Zhao et al., 2017). These findings confirm that the rotational drivers identified with phase mapping truly exist with high resolution optical activation mapping and reconcile how intramural rotational drivers may result in epicardial breakthroughs. Furthermore, these findings link

TABLE 1 | Clinical technologies to localize areas of fibrosis.

Technique	Advantages	Disadvantages	Landmark clinical studies
Cardiac MRI	Non-invasive, high signal-to-noise ratio	Artifact from cardiac devices, reproducibility of segmentation/windowing	DECAAF, Marrouche et al., 2014
Perfusion CT	High resolution, quick	Radiation, contrast	Ling et al., 2015
MRI-based computer modeling	Non-invasive, functional data in addition to structural data	Assumptions in computational model, variabilities with segmentation	Boyle et al., 2019
Electro-anatomic voltage mapping	High resolution, real-time	Invasive, time-intensive, assumptions of electrode recordings	Jadidi et al., 2016; Kottkamp et al., 2016; Yagishita et al., 2017

these electrical drivers with regions of fibrosis identified with high resolution MRI.

Likewise, clinical studies using non-invasive electrocardiographic imaging (ECGi) (Cochet et al., 2018) also correlated re-entrant drivers to late gadolinium-enhanced (LGE) areas on MRI. However, other clinical studies failed to correlate rotational drivers identified using invasive phase mapping with LGE on MRI (Chrispin et al., 2016) and electroanatomic voltage mapping (Schade et al., 2016). This discrepancy may reflect differences in mapping and imaging technologies, but may also highlight the possibility that electrical drivers can arise from (1) a purely electrical substrate [electrical remodeling altering cellular gap junction distribution (Fry et al., 2014; Shin et al., 2015) without fibrosis or shortened atrial refractory period (Wijffels et al., 1995)] or (2) structural heterogeneities such as fiber angle discontinuities found in the pulmonary vein antra (Narayan et al., 2008; Pashakhanloo et al., 2016) or crista terminalis (Gonzales et al., 2014), creating anisotropic conduction which may lead to reentry.

STRATEGIES TO ATTENUATE AND RISK-STRATIFY ATRIAL FIBRILLATION PRIOR TO ABLATION

Risk Factor Modification

Recent studies have shown that risk factor modification can reduce or suppress AF (Pathak et al., 2014, 2015; Lau et al., 2017). Obstructive sleep apnea (OSA) may lead to atrial electrophysiologic remodeling with increased atrial fibrosis and downregulation of connexin-43 due to repeated apneic episodes (Iwasaki et al., 2014). In a rat model, this resulted in substantial atrial conduction slowing and increased inducibility and duration of AF. Patients with OSA undergoing clinical AF ablation were found to have a reduction in bi-atrial voltage, widespread conduction abnormalities and longer sinus node recovery times (Dimitri et al., 2012).

Multiple studies have demonstrated the strong link between obesity and risk of developing AF. In sheep models, those with more significant obesity were found to have increased cytoplasmic transforming growth factor β1, platelet-derived growth factor, and larger left atrial size (Mahajan et al., 2015). Furthermore, there was also increased atrial fibrosis, infiltration of the epicardial fat into the posterior left atrial wall, heterogenous and slowed atrial conduction velocity, and higher rates of inducible and spontaneous AF in the obese group in both sheep and humans (Munger et al., 2012; Abed et al., 2013). Weight reduction is associated with improved AF control. In the LEGACY study, weight loss of $\geq$10% resulted in a 6-fold increased probability of arrhythmia-free survival (Pathak et al., 2015). Similarly, the ARREST-AF study showed that weight reduction with other risk factor modifications resulted in longer arrhythmia-free survival after AF ablation (Pathak et al., 2014). These studies suggest that atrial remodeling associated with obesity may be reversible with weight reduction (Aldaas et al., 2019).

Varying degrees of alcohol consumption has been associated with risk of incident AF and recurrence of AF after catheter ablation. This may be partly contributed by alcohol's association with other known risk factors for AF such as obesity, hypertension, and disordered sleep pattern. However, prior work has shown acute changes in atrial electrophysiology as a direct result of alcohol consumption and binge drinking, including shortening of the effective refractory period, slowed intra-atrial conduction, and prolonged p wave duration (Voskoboinik et al., 2016). Additionally, chronic drinking is an independent multivariate predictor of discrete atrial fibrosis (Qiao et al., 2015). Regarding the effect of alcohol cessation on burden of AF, the ARREST-AF study demonstrated decreased AF recurrence and symptom severity in patients with risk factor management including decreased alcohol consumption (Pathak et al., 2014).

Identify Fibrosis

Atrial fibrosis can be identified with a range of imaging and mapping technologies, of which some are detailed in a 2016 EHRA consensus statement (Donal et al., 2016). **Table 1** lists techniques that have been developed to characterize atrial substrate. However, it is important to note that all modalities identify indirect surrogates for atrial fibrosis, and use of fibrosis to guide ablation may be non-specific and as fibrosis is not synonymous with arrhythmogenicity.

Cardiac MRI

In some centers, cardiac MRI is used pre-procedurally to characterize atrial anatomy and burden of fibrosis in preparation for catheter ablation (Mahnkopf et al., 2010; Daccarett et al., 2011; Malcolme-Lawes et al., 2013; McGann et al., 2014; Calkins et al., 2017; Sohns and Marrouche, 2020). The multicenter prospective DECAAF trial (Marrouche et al., 2014) has established the role of MRI as a prognostic tool to predict success of PVI ablation based on the degree of atrial fibrosis (**Figure 3**). Additionally, other

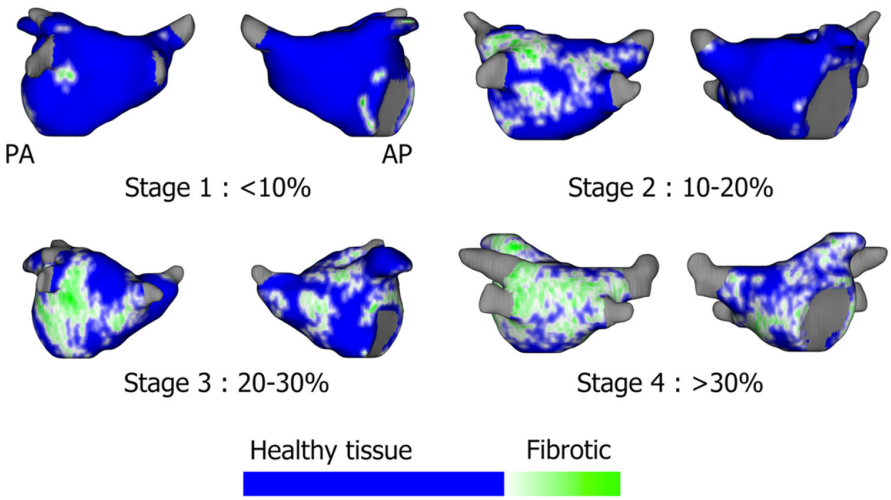

FIGURE 3 | Assessment of left atrial fibrosis burden using segmented gadolinium-enhanced MRI scans based on the Utah stages: Utah 1: <10%, Stage 2: 10–20%, Stage 3: 20–30%, Stage 4: >30% fibrotic tissue. Sohns and Marrouche (2020), reprinted with permission.

studies have evaluated the ability of MRI to detect gaps in PVI lesions in order to identify PV reconnections (Bisbal et al., 2014). However, the utility of MRI to localize fibrotic areas as potential targets for ablation is still unknown and is under investigation with the DECAAF-2 trial (NCT 02529319). A limitation of current cardiac MRI technology is artifact from cardiac devices and variability in acquisition sequences and thresholding (Karim et al., 2013; Calkins et al., 2017). A second challenge is that fibrotic areas may not always correlate with arrhythmogenicity. Additional work is required to determine the optimal role of MRI in AF procedural planning.

MRI based computer simulations

One proposed method to identify areas of fibrosis with potential arrhythmogenicity is building computer simulations using fibrotic areas derived from MRI combined with electroanatomic computer simulations to identify re-entrant drivers. This technique was described in a proof-of-concept clinical study showing feasibility of this non-invasive method (Zahid et al., 2016; Boyle et al., 2019). Prospective studies are needed to see whether this technique may improve AF ablation outcomes.

Cardiac CT

A proposed technique using perfusion cardiac computed tomography (CT) to identify surrogate regions of fibrosis was described by Ling and colleagues (Ling et al., 2015). In this technique, contrast-enhanced gated cardiac CT were segmented by degree of contrast attenuation, and areas of low attenuation correlated with low voltage points obtained from invasive electroanatomic bipolar voltage maps ($p = 0.04$) and qualitative agreement in about 80% of patients. Contemporary cardiac CT provides improved resolution (∼0.5 mm) as compared to MRI (∼1.5–2.0 mm) (Saeed et al., 2015), but has a lower signal-to-noise ratio. Although cardiac CT imaging is routinely obtained for evaluation of gross atrial anatomy prior to AF ablation, additional work is needed to both improve the ability of CT perfusion imaging to detect fibrosis and define its role in targeting AF-sustaining substrate.

Electro-Anatomic mapping

Invasive electroanatomic mapping is an established method of characterizing electrical substrate to identify regions as a surrogate for fibrosis. Improvements in electroanatomic mapping systems and multi-electrode mapping catheters have enabled spatial resolution down to 2–3 mm and higher density maps. Similar to substrate homogenization-based strategies to ablate ventricular tachycardia, individually tailored substrate ablation has been proposed and studied for AF. However, unlike ventricular tachycardia in which substrate mapping can be used to define the critical isthmus of a scar-based monomorphic VT circuit, the precise fibrotic microstructure underlying AF is less well characterized.

The efficacy of a substrate modification approach utilizing box isolation of fibrotic areas (BIFA) was tested in 28 patients with both paroxysmal and persistent AF who had low voltage areas <0.5 mV identified using a contact force ablation catheter (Kottkamp et al., 2016). The BIFA approach entails surrounding low voltage areas with linear ablation lines anchored to non-conducting regions such as wide area circumferential (WACA) ablation circles. This resulted in a 90% 1 year freedom in 10 paroxysmal AF patients and 72% 1 year freedom in 18 persistent AF patients. In another study by Kircher et al. (2018), 124 patients with either paroxysmal or persistent AF undergoing PVI were randomized to additional standard linear ablation versus an individually tailored approach to target low voltage areas. Voltage mapping was performed using a circular mapping catheter (1 mm electrode spacing) with low voltage cut-offs of <0.5 mV. Ablation of these voltage areas either in a cluster, linear ablation anchored to non-excitable regions or box isolation resulted in a significant improvement in freedom from atrial arrhythmia (68 vs 42%) after a single procedure. Although there was an improvement in this technique over empiric linear ablation, the recurrence in almost a

third of patients suggests that the underlying etiology of AF in these patients still has not been fully addressed. Disadvantages to substrate homogenization include the non-specificity of low voltage zones without integrated functional data and limitations of invasive voltage mapping described below.

Several clinical studies have attempted to characterize voltage cut-offs to represent the spectrum of atrial fibrosis (**Table 2**). In general, these studies used either ablation catheters with 4 mm electrodes (Oakes et al., 2009; Spragg et al., 2012) or multi-electrode catheters (Verma et al., 2005; Kapa et al., 2014; Rolf et al., 2014; Anter et al., 2015; Kottkamp et al., 2016) with 1 mm electrodes and 2–6 mm electrode spacing to define: dense scar at <0.2 mV, borderzone fibrosis at <0.5 mV and normal tissue >0.5 mV when compared in AF patients with healthy or abnormal atria, by the presence of LGE on MRI in 4 studies (Oakes et al., 2009; Spragg et al., 2012; Kapa et al., 2014; Anter et al., 2015). However, some investigators have argued abnormal tissue can exist with voltages <1.5 mV and viable tissue exists at >0.05 mV. This discrepancy could be contributed by several limitations and misconceptions of interpreting low voltage as a surrogate for fibrosis as described by Josephson and Anter (2015). Electrogram voltage may be affected by conduction velocity, fiber orientation and curvature, relationship of fiber orientation to the propagating wavefront, tissue contact, edema, fat and characteristics of the recording catheter such as electrode size, interelectrode spacing. Newer multielectrode catheters have been developed which could potentially address some of these issues, such as the orthogonal grid catheters and high-density baskets with 0.4 mm electrodes; however, these have not been systematically studied in this regard.

Identifying AF Triggers

Patients who have a high burden of atrial flutter or supraventricular tachycardias (SVT) may undergo atrial remodeling and develop both electrical and fibrotic substrate for AF (Franz et al., 1997). Thus, identifying a defined, consistent trigger is an important component of an AF ablation strategy (Calkins et al., 2017).

Supraventricular Tachycardias and Atrial Tachycardia/Flutters

Prior studies have shown an association between AF and supraventricular tachycardia (SVT) (Sauer et al., 2006) and cavo-tricuspid isthmus dependent atrial flutters (TAFL) (Pérez et al., 2009). Based upon these studies, it is recommended to evaluate for co-existing SVT or atrial tachycardia/flutter mechanisms either before or after AF ablation.

Pulmonary Vein Triggers

Foundational work in AF ablation demonstrated the importance of pulmonary vein (PV) triggers to AF (Haïssaguerre et al., 1998). The initial approach to PV trigger ablation was to perform segmental pulmonary vein isolation. A subsequent randomized study by Arentz et al. (2007) demonstrated improved outcomes with wide area circumferential ablation (WACA) compared to segmental ablation, potentially by disrupting other sustaining AF mechanisms at the PV antra characterized by fiber angle discontinuities (Pashakhanloo et al., 2016) and increased repolarization restitution (Narayan et al., 2008).

Non-PV Triggers

Ongoing work has revealed that non-PV ectopic beats and PACs may be present in 10–33% of patients with AF (Chen and Tai, 2005; Takigawa et al., 2015; Santangeli et al., 2016; Hojo et al., 2017), and suggested the potential utility of aggressive trigger induction with high dose isoproterenol. These triggers may originate from the posterior LA wall, superior vena cava (SVC), crista terminalis, coronary sinus (CS), Eustachian ridge, Ligament of Marshall, and left atrial appendage (Lin et al., 2003; Chen and Tai, 2005; Calkins et al., 2017). Additional work is required to determine the significance of these triggers to perpetuation of AF and whether this approach yield long-term improvement in AF-free survival after ablation.

Identify Drivers

A challenge in mapping drivers of AF is that standard activation mapping techniques using point by point mapping are unable to fully resolve the evolving wavefront propagation patterns during

TABLE 2 | Studies of bipolar voltage cutoffs.

Voltage cut-off (mV)	Study	Mapping catheter used	Gold standard for fibrosis	Patients	Rhythm
<0.2: dense scar <0.5: diseased	Verma et al., 2005	Circular (2-6-2 mm spacing)	Clinical history	700	NSR
<0.1: dense scar >0.5: normal	Oakes et al., 2009	Linear (4 mm tip, 1-7-4 mm)	LGE-MRI	54	60% NSR
>0.5 mV: normal	Spragg et al., 2012	Linear (3.5 mm tip, 2 mm)	LGE-MRI	10	?
<0.27: scar >0.45: normal	Kapa et al., 2014	Circular (2-6-2 mm)	LGE-MRI	20	NSR
<0.2: scar >0.5: normal	Rolf et al., 2014	Circular (2-6-2 mm or 2-4-2 mm)	Clinical history	178	NSR
<0.25: dense scar >0.48: normal	Anter et al., 2015	Multi-spline (2-6-2 mm)	LGE-MRI	30	NSR
<0.5: scar >1.5: normal	Kottkamp et al., 2016	Circular (2-6-2 mm)	Clinical history	41	NSR

NSR, normal sinus rhythm; AF, atrial fibrillation.

AF due to lack of having a standard reference. A second challenge is that AF drivers potentially utilize several sites of abnormal substrate during ongoing AF.

To address these challenges, an increasing number of specialized electrogram processing techniques and panoramic mapping methods have been developed. The variety of technologies, their requirements, risks and available data are illustrated in **Table 3**.

Focal Impulse and Rotor Modulation

One of the first technologies developed to specifically target the sustaining mechanisms of AF was focal impulse and rotor modulation (FIRM) mapping (Narayan et al., 2012a,b,c, 2013). This technique utilizes 64-electrode basket catheter recordings during AF analyzed by computational activation and phase analysis to identify semi-stable focal (centripetal activation) and rotational activation patterns. The results from the initial trial of this approach were reported in the CONFIRM trial (Narayan et al., 2012d), in which 92 patients undergoing AF ablation underwent pulmonary vein isolation alone versus PVI plus rotor ablation. Patients undergoing PVI + FIRM ablation experienced a greater number of AF terminations during ablation and had a greater AF-free survival at a median of 273 days after ablation. Subsequent work demonstrated that these results were durable, improving AF-free survival over a median follow-up of 870 days (Narayan et al., 2014). These outcomes were reproduced in independent studies from more than 10 sites (Miller et al., 2014) including Miller et al. (2017) who reported their results for 170 consecutive patients undergoing AF ablation employing PVI plus AF rotor ablation. Freedom from all atrial arrhythmias was 75% in patients with persistent AF and 57% in longstanding persistent AF at 1 year, off antiarrhythmic drug therapy. A meta-analysis by Baykaner et al. (2018) analyzed all published studies of FIRM mapping and ablation found a significant improvement in freedom from atrial arrhythmia recurrence in patients undergoing pulmonary vein isolation plus FIRM ablation. Ongoing work is required to determine the precise population who maximally benefit from this approach.

Electrocardiographic Imaging

Electrocardiographic imaging (ECGVue, Medtronic, Minneapolis, MN) is a non-invasive technique utilizing a 252-electrode vest integrated with a non-contrast CT has been used to record unipolar epicardial potentials during AF using inverse solution modeling (Ramanathan et al., 2004). Similarly, phase mapping has been applied to these potentials (Haissaguerre et al., 2014), and in a study of 103 patients with persistent AF, identified rotational and focal drivers (**Figure 4**).

Although changing wavefronts and transient reentrant activity were observed, AF drivers occurred repetitively in the defined regions. Ablation of such regions terminated persistent AF in 75% of patients and resulted in 1 year freedom from AF in 85% of patients. In the AFACART study (Knecht et al., 2017) of 118 patients with persistent AF, a step-wise ablation approach (driver only then PVI then linear ablation) showed that driver-only ablation terminated AF in 64% of patients, and this step-wise approach resulted in single procedure 1 year freedom from AF in 78% of patients, though 49% experienced atrial tachycardia.

Dipole Density Mapping

A system using dipole density mapping combined with ultrasound (Grace et al., 2017; Shi et al., 2020) (AcQMap, Acutus Medical Inc., Carlsbad, CA, United States) has been developed to create high resolution endocardial activation maps (150,000 points per second). AcQMap consists of a basket catheter with 48 ultrasound transducers and electrodes to sample the intracardiac potential field to create an instantaneous activation map using a non-contact, inverse solution algorithm (**Figure 5**). This basket is placed via a 16 French steerable sheath.

The AcQMap system was validated with contact mapping in 20 patients (Shi et al., 2020) showing good agreement for points up to 4 cm away from the center of the catheter. It was prospectively studied in 127 patients with persistent AF in the multicenter UNCOVER-AF trial (Willems et al., 2019) and identified organized sources including localized irregular activation (repetitive conduction through a confined zone, **Figure 5C**), focal sources and rotational

TABLE 3 | Clinical technologies to Localize AF drivers.

Technique	First clinical study	Methodology	Equipment needed	Access	Disadvantages
FIRM	2012	Phase mapping	64-electrode basket	8.5 Fr sheath	Basket catheter tissue contact, false-positive rotors
ECGi	2014	Activation and phase mapping	252-electrode disposable vest	Non-invasive	Epicardial potentials only/misses septal sites
Localized Electrogram Organization	2016	Activation, voltage & EGM characteristics	Multi-electrode catheter	8.5 Fr sheath	Subjective qualititative EGM assessment, non-panoramic
CARTOFINDER	2018	Activation mapping	64-electrode basket	8.5 Fr sheath	Basket catheter tissue contact, activation mapping limited by low temporo-spatial resolution
Acutus	2019	Activation mapping	48 electrode basket	16 Fr sheath	Large 16 Fr trans-septal sheath risks
Wavefront Mapping	2019	Propagation vector mapping	64-electrode basket	8.5 Fr sheath	Basket catheter tissue contact
FAST	2020	Spectral and unipolar EGM	Multi-electrode catheter	8.5 Fr sheath	Non-panoramic method, time consuming

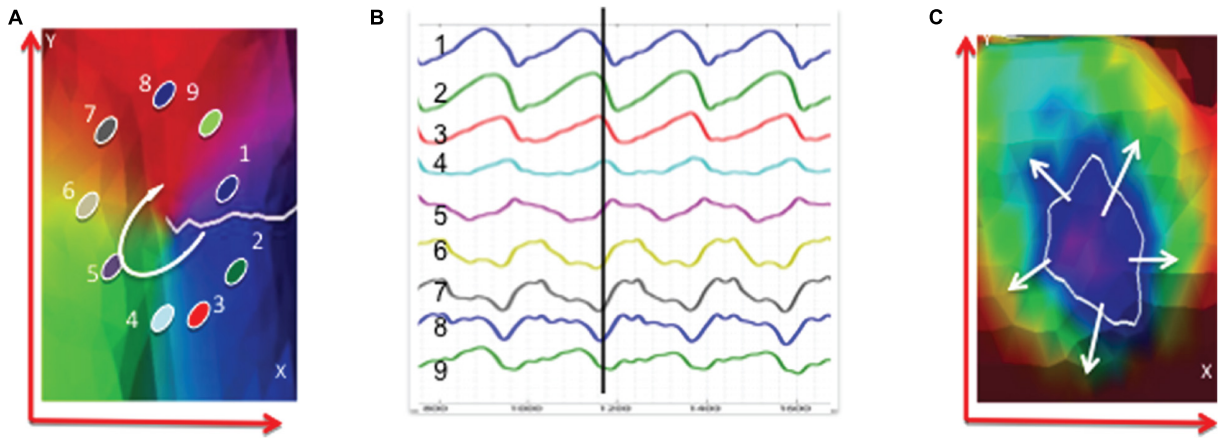

FIGURE 4 | Examples of an atrial rotor **(A)** and a focal driver **(C)** which were identified using the inverse solution computer modeling and phase mapping of body surface epicardial potentials **(B)**. Knecht et al. (2017), reprinted with permission.

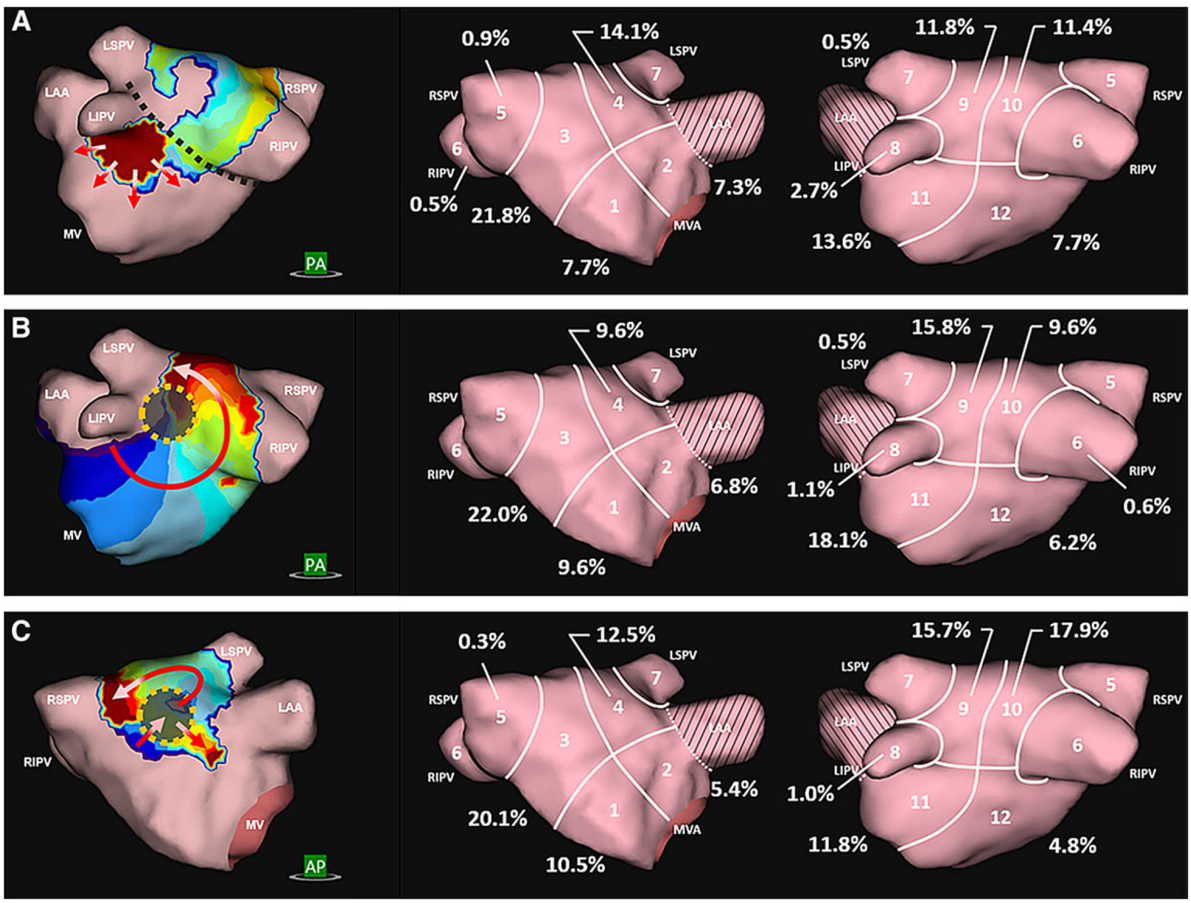

FIGURE 5 | Dipole density mapping reveals 3 distinct activation patterns: **(A)** focal activity originating from the mitral isthmus, **(B)** rotational activity originating from the posterior wall, and **(C)** localized irregular activation characterized by repetitive multidirectional entry, exit, and pivoting through a fixed site. Willems et al. (2019), reprinted with permission.

activation were found with an average of 5 sources per patient. Ablation of these sources resulted in termination in 32% of patients and 1-year freedom from AF in 73% with a single procedure and 93% with a second procedure. Randomized studies are still needed to establish a clear benefit using this strategy.

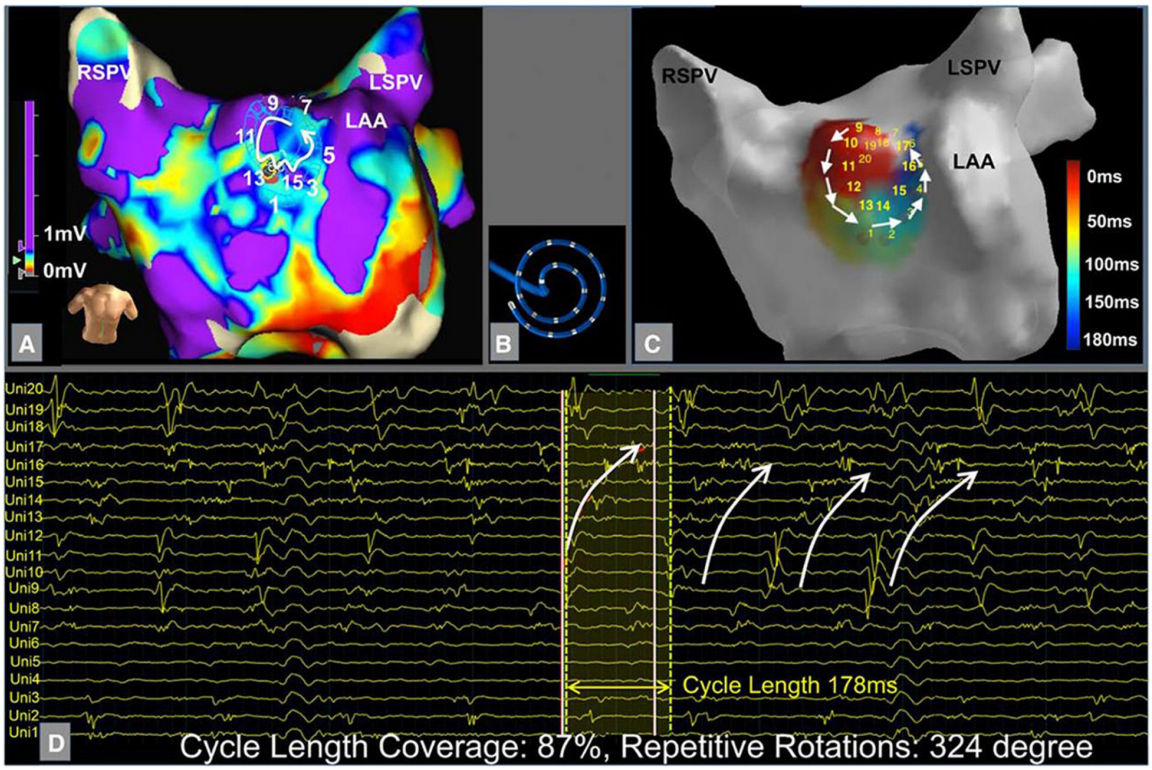

FIGURE 6 | Example of localized electrogram dispersion. **(A)** Bipolar voltage map with site of rotational activity. **(B)** Orientation of the multielectrode circular mapping catheter. **(C)** Activation sequence of rotational activity where ablation terminated atrial fibrillation. **(D)** Corresponding unipolar electrograms show repetitive rotational activation sequence. Jadidi et al. (2016) reprinted with permission.

Localized Electrogram Dispersion

A few methods have been proposed using qualitative analysis of electrogram temporospatial organization obtained from standard circular or multi-spline catheters. These methods expand upon complex fractionated atrial electrogram (CFAE) mapping by further evaluating propagation of electrograms on neighboring electrodes in an organized fashion to determine the presence of an active driver. Jadidi et al. (2016) proposed a method to identify regions with low voltage (<0.5 mV, **Figure 6A**) and electrograms spanning >70% of the AF cycle length over neighboring electrodes (**Figures 6B,C**) to identify a surrogate of an AF driver.

In a prospective study of 62 patients with persistent AF, ablation of these low voltage areas in addition to PVI led to acute AF termination in 73% and single procedure 1 year freedom from AF in 69%, compared to 47% in a matched PVI only control group ($p < 0.001$).

Another method described by Seitz et al. (2017) involves localization of regions of temporal and spatial dispersion of electrograms (minimum of 3 adjacent bipoles with activation spanning the entire AF cycle length) using a multi-spline catheter (Pentaray, Biosense-Webster, CA, United States). In the SUBSTRATE HD study (Seitz et al., 2017) of 105 patients (77% persistent AF), ablation of only driver regions terminated AF in 95% of patients, and 1.5-year freedom from atrial arrhythmias (median 1.4 procedures) was 85% compared to 59% of a validation control group who underwent step-wise PVI and linear ablation approach. Further randomized and multicenter centers with inexperienced operators are needed to confirm these promising results for localized driver ablation.

CARTOFINDER™

The CARTOFINDER™ system (Daoud et al., 2017) is an activation mapping based algorithm that records unipolar endocardial electrograms from 64-electrode basket catheters (**Figure 7**, left panel). The system calculates the percentage of the atrial surface geometry that is covered by the basket to guide repositioning. Activation patterns are then analyzed on the CARTO system to identify focal or reentrant drivers (**Figures 7A–D**).

In a study of 20 patients with persistent AF, CARTOFINDER identified rotational or focal drivers in all patients and AF terminated in half of the patients with driver ablation (Honarbakhsh et al., 2018). Randomized, longer-term outcome studies are needed to determine whether this method may effectively identify drivers to improve freedom from AF.

Focal Source and Trigger Mapping (FaST)

A novel quantitative algorithm (Gizurarson et al., 2016; Daoud et al., 2017) identifying sites with periodicity

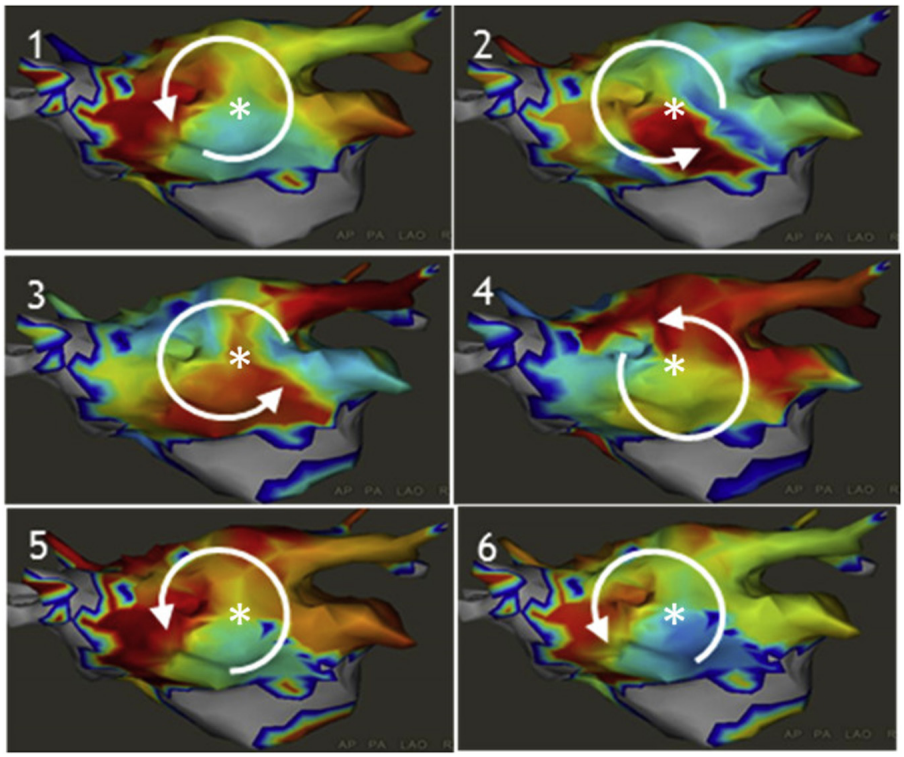

FIGURE 7 | Example of CARTOFINDER showing a counter clockwise rotational repetitive activation pattern through time (panels 1–6). Daoud et al. (2017) reprinted with permission.

and QS unipolar electrogram morphology was described by Chauhan et al. (2020). From bipolar and unipolar electrograms collected from a circular mapping electrode (Lasso, Biosense-Webster), the electrograms are analyzed by an algorithm (**Figure 8A**) that assesses bipolar EGM periodicity (segments with a spectral peak >10% of the total spectral power) and assesses the presence of QS morphology on the unipolar EGMs as a surrogate for organized focal drivers (**Figure 8B**).

This algorithm was tested in a randomized study of 80 patients (Chauhan et al., 2020) (48% persistent AF) to PVI + FAST versus PVI only, and resulted in a trend toward improved 1-year freedom from AF (74% with PVI + FAST compared to 51% with PVI-only, $p = 0.06$). Larger multicenter trials are needed to see if this method may significantly improve AF ablation success.

Wavefront Field Mapping

A promising technique was recently proposed using wavefront field mapping (Leef et al., 2019) to reveal organized areas of control during AF (**Figures 9A,B**). This novel vector mapping method computes activation times to calculate phase (**Figure 9C**), activation fronts, and gradient matching to display the vector fields (**Figures 9D–F**) to describe propagation of these fronts.

An advantage of this method is the ability to identify regions that control larger areas of the atria during AF, and thus distinguish true driver of AF compared to passive organized areas. This concept was studied retrospectively in 54 patients (Leef et al., 2019) in whom ablation of proposed drivers (from phase mapping) terminated AF, and all sites that were found to control larger atrial areas terminated AF with ablation. Prospective studies are ongoing to evaluate the ability of this method to identify critical drivers of AF to improve the targeted therapy of AF.

WHAT IS THE OPTIMAL ABLATION STRATEGY TO TARGET MECHANISMS OF AF?

The plethora of new imaging and mapping technologies reviewed above attempt to provide a personalized approach to improve the treatment of AF. Although there is a strong link between atrial fibrosis and electrical drivers (Cochet et al., 2018; Hansen et al., 2018), they do not always co-exist (Chrispin et al., 2016; Schade et al., 2016), suggesting electrical remodeling and structural heterogeneities other than fibrosis are also important AF mechanisms (Stiles et al., 2009; Lalani et al., 2012; Schricker et al., 2014; Zaman and Narayan, 2015). There are some patients who may have only an electrical substrate without fibrosis (such as lone AF due to a pulmonary vein driver), and there are other patients who have extensive atrial fibrosis with multiple AF

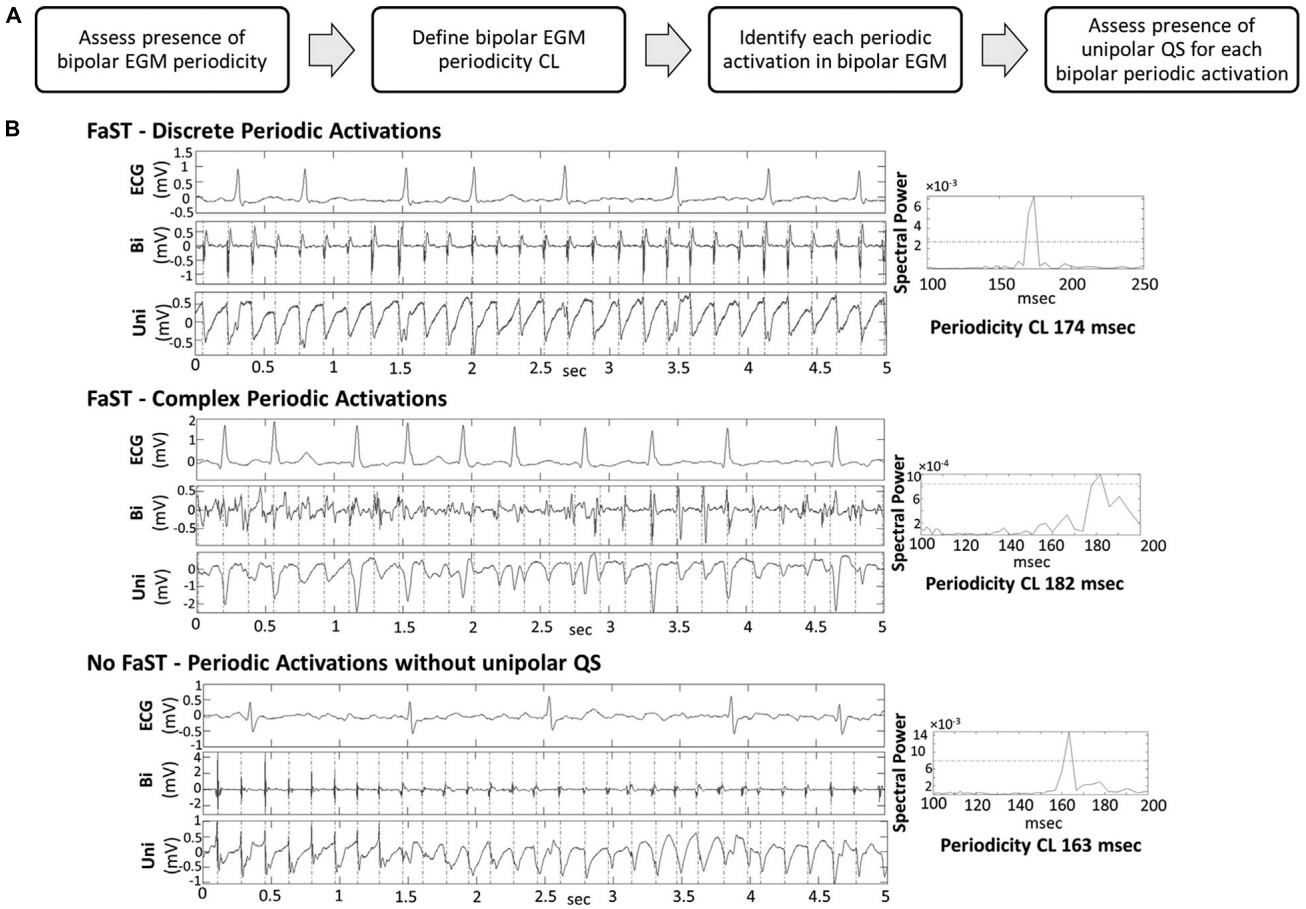

FIGURE 8 | (A) Workflow of algorithm in the FaST system. **(B)** Periodic activation of electrograms during AF and spectral analysis. Chauhan et al. (2020) reprinted with permission.

drivers (such as a patient with familial atrial cardiomyopathy). In the first case, PVI alone or driver mapping-guided ablation may be enough to eliminate the AF mechanism, but may not be enough in the second case. While meta-analysis of driver ablation studies show a benefit toward driver ablation (Baykaner et al., 2018), AF recurrence still recurs in ∼30%. This may be partly due to technological shortcomings and operator inexperience, but a possibility is that new drivers may recur in certain patients with progressive primary atrial cardiomyopathies.

More work is needed to determine how to identify patients with progressive underlying atrial cardiomyopathies and how to incorporate a substrate modification strategies in addition to AF drivers. However, importantly, more ablation is not necessarily better particularly with empiric atrial debulking strategies, as STAR-AF2 showed a proarrhythmic effect of empiric linear ablation primarily due to creation of substrate for atypical atrial flutters (Verma et al., 2015) and development of stiff atrial syndrome (Gibson et al., 2011).

Based upon the above discussion, we propose the following strategy for the management of drug-refractory AF (**Figure 10**), incorporating an organized approach to manage and reduce risk factors, and to use imaging to reveal the diverse types of AF. First, reversible clinical risk factors, such as obesity, hypertension, obstructive sleep apnea, and excessive alcohol use should be optimized in all patients to help reverse atrial remodeling (Lau et al., 2017). Second, PVI should usually be performed in all patients as an initial strategy. In the most recent 2017 expert consensus document for AF ablation, pulmonary vein isolation is the only ablation strategy given a Class 1 indication (Calkins et al., 2017). Third, elimination of AF triggers such as frequent PACs/atrial tachycardias should also be strongly considered, which is given a Class 2A indication. Fourth, in patients in whom AF sustains or remains inducible, adjunctive strategies addressing patient-specific AF mechanisms may be needed to improve the success of ablation. To address the potential for fibrotic mechanisms discussed previously, pre-procedural imaging or comprehensive invasive voltage mapping should be considered to determine the presence of significant atrial fibrosis which may prognosticate a need to perform electrical driver ablation and/or substrate modification to eliminate extra-PV AF mechanisms. Finally, in patients with persistent AF in whom AF is more likely to recur after PVI alone, electrical driver mapping should be considered to eliminate extra pulmonary

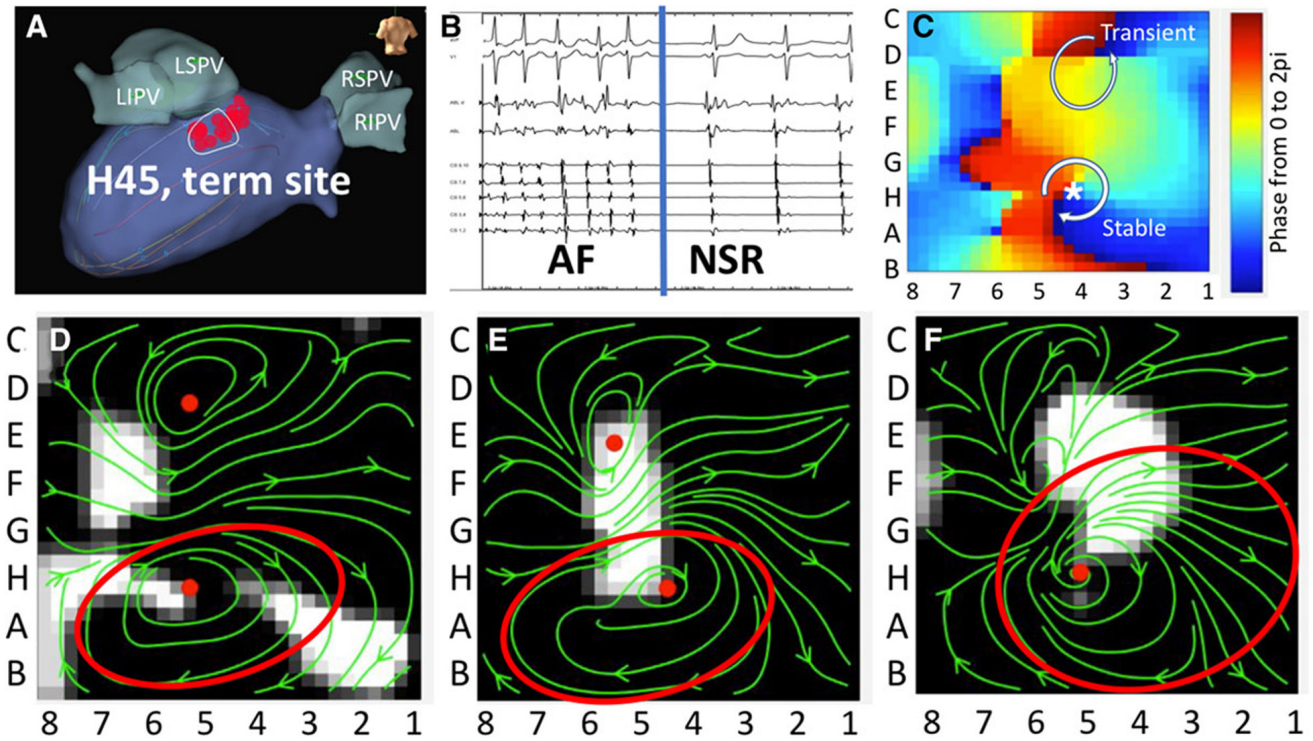

FIGURE 9 | (A) Targeted ablation of a rotor in the left posterior left atrium resulting in panel **(B)** AF termination in a patient with clinical AF. Activation times are converted to phase analysis **(C)**. **(D–F)** Vector fields of potential AF driver during AF. Leef et al. (2019) reprinted with permission.

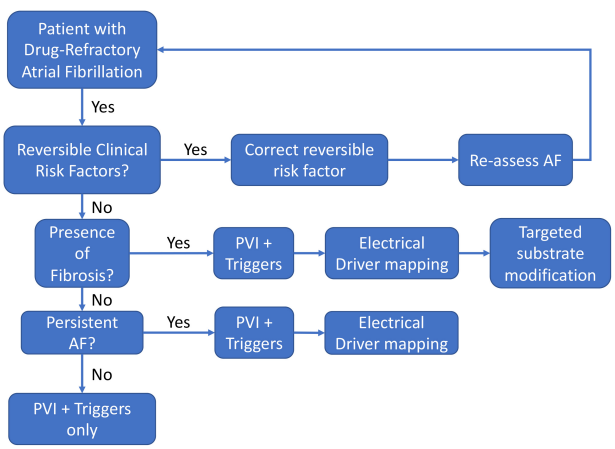

FIGURE 10 | Flowchart of a decision-support strategy regarding the use of supplemental AF mapping and targeting technologies.

vein AF mechanisms in a targeted, patient-specific approach. At present, the choice of adjunction functional mapping should in part be determined by operator experience and electrophysiology laboratory factors in the absence of definitive clinical trial data evaluating the new adjunctive technologies. While the current AF ablation consensus guidelines do discuss some of the earlier imaging and driver technologies, they are given a Class IIb indication due to lack of good quality clinical data. With improvements in mapping and imaging technologies discussed above, we await clinical trials to confirm the optimistic preliminary clinical studies supporting these mechanistic AF treatment strategies.

CONCLUSION

This review summarizes data linking fibrotic atrial cardiomyopathy with AF drivers and summarizes current clinical approaches for the targeted therapy of substrate and electrical mechanisms underlying atrial fibrillation. As the two patients presented at the beginning demonstrate, causes of AF may be heterogeneous; it is possible that AF in patient 1 may have been caused by electrical substrate only (triggered activity from an ectopic pulmonary vein source). In contrast, patient 2 may have an underlying primary atrial cardiomyopathy, compounded by the presence of scar from prior ablation, and although driver ablation terminated AF, he may have recurrence of AF with new driver sites. Similar to scar-based VT, a combination of substrate modification guided by electrical driver mapping may be needed in certain patients.

We believe that current data support an approach in which risk factor modification is addressed in all patients, and a patient specific strategy incorporating targeted therapy of structural and electrical substrate is considered in particular for

patients with anatomic and functional remodeling suggestive of advanced atrial remodeling and AF drivers outside the pulmonary vein anatomy. Ongoing work is required to determine the optimal combination of imaging and AF functional mapping to optimize procedural results in the management of patients with refractory arrhythmias.

DISCLOSURES

Dr. Ho receives grant support from the American Heart Association (AHA 19CDA34760021), National Institutes of Health (NIH 1KL2TR001444-06), and reports equity in Vektor Medical Inc. unrelated to this work. Dr. Krummen receives grant support from the UCSD Galvanizing Engineering in Medicine Foundation. He also reports equity in Vektor Medical unrelated to this work.

AUTHOR CONTRIBUTIONS

GH reviewed the current literature for the present manuscript, wrote the outline, identified important figures, composed the manuscript, and provided critical editing of the manuscript. AL performed background research for the manuscript and provided critical editing of the manuscript. DK reviewed the literature, composed the manuscript, and provided critical editing of the manuscript. All authors contributed to the article and approved the submitted version.

FUNDING

This work was partially supported by the American Heart Association (AHA 19CDA34760021) and the National Institutes of Health (NIH 1KL2TR001444-06).

REFERENCES

Abed, H. S., Samuel, C. S., Lau, D. H., Kelly, D. J., Royce, S. G., Alasady, M., et al. (2013). Obesity results in progressive atrial structural and electrical remodeling: implications for atrial fibrillation. *Hear. Rhythm* 10, 90–100. doi: 10.1016/j.hrthm.2012.08.043

Aldaas, O. M., Lupercio, F., Han, F. T., Hoffmayer, K. S., Krummen, D., Ho, G., et al. (2019). Meta-analysis of effect of modest (=10%) weight loss in management of overweight and obese patients with atrial fibrillation. *Am. J. Cardiol.* 124, 1568–1574. doi: 10.1016/j.amjcard.2019.08.009

Angel, N., Li, L., MacLeod, R. S., Marrouche, N., Ranjan, R., and Dosdall, D. J. (2015). Diverse fibrosis architecture and premature stimulation facilitate initiation of reentrant activity following chronic atrial fibrillation. *J. Cardiovasc. Electrophysiol.* 26, 1352–1360. doi: 10.1111/jce.12773

Anter, E., Tschabrunn, C. M., and Josephson, M. E. (2015). High-resolution mapping of scar-related atrial arrhythmias using smaller electrodes with closer interelectrode spacing. *Circ. Arrhythmia Electrophysiol.* 8, 537–545. doi: 10.1161/circep.114.002737

Arentz, T., Weber, R., Bürkle, G., Herrera, C., Blum, T., Stockinger, J., et al. (2007). Clinical perspective. *Circulation* 115, 3057–3063.

Baykaner, T., Lalani, G. G., Schricker, A., Krummen, D. E., and Narayan, S. M. (2014). Mapping and ablating stable sources for atrial fibrillation: summary of the literature on Focal Impulse and Rotor Modulation (FIRM). *J. Interv. Card Electrophysiol.* 40, 237–244. doi: 10.1007/s10840-014-9889-8

Baykaner, T., Rogers, A. J., Meckler, G. L., Zaman, J., Navara, R., Rodrigo, M., et al. (2018). Clinical implications of ablation of drivers for atrial fibrillation: a systematic review and meta-analysis. *Circ. Arrhythm. Electrophysiol.* 11:e006119.

Bisbal, F., Guiu, E., Cabanas-Grandío, P., Berruezo, A., Prat-Gonzalez, S., Vidal, B., et al. (2014). CMR-guided approach to localize and ablate gaps in repeat AF ablation procedure. *JACC Cardiovasc. Imaging* 7, 653–663. doi: 10.1016/j.jcmg.2014.01.014

Boyle, P. M., Zghaib, T., Zahid, S., Ali, R. L., Deng, D., Franceschi, W. H., et al. (2019). Computationally guided personalized targeted ablation of persistent atrial fibrillation. *Nat. Biomed. Eng.* 3, 870–879.

Caballero, R., De La Fuente, M. G., Gómez, R., Barana, A., Amorós, I., Dolz-Gaitón, P., et al. (2010). In humans, chronic atrial fibrillation decreases the transient outward current and ultrarapid component of the delayed rectifier current differentially on each atria and increases the slow component of the delayed rectifier current in both. *J. Am. Coll. Cardiol.* 55, 2346–2354. doi: 10.1016/j.jacc.2010.02.028

Calkins, H., Hindricks, G., Cappato, R., Kim, Y. H., Saad, E. B., Aguinaga, L., et al. (2017). 2017 HRS/EHRA/ECAS/APHRS/SOLAECE expert consensus statement on catheter and surgical ablation of atrial fibrillation. *Hear. Rhythm* 14, e275–e444.

Chang, S., Tai, C., Lin, Y., Wongcharoen, W., Lo, L., Tuan, T., et al. (2007). Biatrial substrate properties in patients with atrial fibrillation. *J. Cardiovasc. Electrophysiol.* 18, 1134–1139. doi: 10.1111/j.1540-8167.2007.00941.x

Chauhan, V. S., Verma, A., Nayyar, S., Timmerman, N., Tomlinson, G., Porta-Sanchez, A., et al. (2020). Focal source and trigger mapping in atrial fibrillation: randomized controlled trial evaluating a novel adjunctive ablation strategy. *Hear. Rhythm* 17, 683–691. doi: 10.1016/j.hrthm.2019.12.011

Chen, S. A., and Tai, C. T. (2005). Catheter ablation of atrial fibrillation originating from the non-pulmonary vein foci. *J. Cardiovasc. Electrophysiol.* 16, 229–232. doi: 10.1046/j.1540-8167.2005.40665.x

Chou, C. C., Nihei, M., Zhou, S., Tan, A., Kawase, A., Macias, E. S., et al. (2005). Intracellular calcium dynamics and anisotropic reentry in isolated canine pulmonary veins and left atrium. *Circulation* 111, 2889–2897. doi: 10.1161/circulationaha.104.498758

Chrispin, J., Ipek, E. G., Zahid, S., Prakosa, A., Habibi, M., Spragg, D., et al. (2016). Lack of regional association between atrial late gadolinium enhancement on cardiac magnetic resonance and atrial fibrillation rotors. *Hear. Rhythm* 13, 654–660. doi: 10.1016/j.hrthm.2015.11.011

Chugh, S. S., Havmoeller, R., Narayanan, K., Singh, D., Rienstra, M., Benjamin, E. J., et al. (2014). Worldwide epidemiology of atrial fibrillation: a global burden of disease 2010 study. *Circulation* 129, 837–847. doi: 10.1161/circulationaha.113.005119

Cochet, H., Dubois, R., Yamashita, S., Al Jefairi, N., Berte, B., Sellal, J. M., et al. (2018). Relationship between fibrosis detected on late gadolinium-enhanced cardiac magnetic resonance and re-entrant activity assessed with electrocardiographic imaging in human persistent atrial fibrillation. *JACC Clin. Electrophysiol.* 4, 17–29. doi: 10.1016/j.jacep.2017.07.019

Csepe, T. A., Hansen, B. J., and Fedorov, V. V. (2017). Atrial fibrillation driver mechanisms: insight from the isolated human heart. *Trends Cardiovasc. Med.* 27, 1–11. doi: 10.1016/j.tcm.2016.05.008

Daccarett, M., Badger, T. J., Akoum, N., Burgon, N. S., Mahnkopf, C., Vergara, G., et al. (2011). Association of left atrial fibrosis detected by delayed-enhancement magnetic resonance imaging and the risk of stroke in patients with atrial fibrillation. *J. Am. Coll. Cardiol.* 57, 831–838. doi: 10.1016/j.jacc.2010.09.049

Daoud, E. G., Zeidan, Z., Hummel, J. D., Weiss, R., Houmsse, M., Augostini, R., et al. (2017). Identification of repetitive activation patterns using novel computational analysis of multielectrode recordings during atrial fibrillation and flutter in humans. *JACC Clin. Electrophysiol.* 3, 207–216. doi: 10.1016/j.jacep.2016.08.001

de Groot, N. M. S., Houben, R. P. M., Smeets, J. L., Boersma, E., Schotten, U., Schalij, M. J., et al. (2010). Electropathological substrate of longstanding persistent atrial fibrillation in patients with structural heart disease: epicardial breakthrough. *Circulation* 122, 1674–1682. doi: 10.1161/circulationaha.109.910901

Dimitri, H., Ng, M., Brooks, A. G., Kuklik, P., Stiles, M. K., Lau, D. H., et al. (2012). Atrial remodeling in obstructive sleep apnea: implications for atrial fibrillation. *Hear. Rhythm* 9, 321–327. doi: 10.1016/j.hrthm.2011.10.017

Dobrev, D., Voigt, N., and Wehrens, X. H. T. (2011). The ryanodine receptor channel as a molecular motif in atrial fibrillation: pathophysiological and therapeutic implications. *Cardiovasc. Res.* 89, 734–743. doi: 10.1093/cvr/cvq324

Donal, E., Lip, G. Y. H., Galderisi, M., Goette, A., Shah, D., Marwan, M., et al. (2016). EACVI/EHRA expert consensus document on the role of multi-modality imaging for the evaluation of patients with atrial fibrillation. *Eur. Heart J. Cardiovasc. Imaging* 17, 355–383. doi: 10.1093/ehjci/jev354

Everett, T. H. IV, and Olgin, J. E. (2007). Atrial fibrosis and the mechanisms of atrial fibrillation. *Hear. Rhythm* 4, 22–24.

Franz, M. R., Karasik, P. L., Li, C., Moubarak, J., and Chavez, M. (1997). Electrical remodeling of the human atrium: similar effects in patients with chronic atrial fibrillation and atrial flutter. *J. Am. Coll. Cardiol.* 30, 1785–1792. doi: 10.1016/s0735-1097(97)00385-9

Fry, C. H., Gray, R. P., Dhillon, P. S., Jabr, R. I., Dupont, E., Patel, P. M., et al. (2014). Architectural correlates of myocardial conduction: changes to the topography of cellular coupling, intracellular conductance, and action potential propagation with hypertrophy in Guinea-pig ventricular myocardium. *Circ. Arrhythmia Electrophysiol.* 7, 1198–1204. doi: 10.1161/circep.114.001471

Gerstenfeld, E. P., Callans, D. J., Dixit, S., Zado, E., and Marchlinski, F. E. (2003). Incidence and location of focal atrial fibrillation triggers in patients undergoing repeat pulmonary vein isolation: implications for ablation strategies. *J. Cardiovasc. Electrophysiol.* 14, 685–690. doi: 10.1046/j.1540-8167.2003.03013.x

Gibson, D. N., Di Biase, L., Mohanty, P., Patel, J. D., Bai, R., Sanchez, J., et al. (2011). Stiff left atrial syndrome after catheter ablation for atrial fibrillation: clinical characterization, prevalence, and predictors. *Hear. Rhythm* 8, 1364–1371. doi: 10.1016/j.hrthm.2011.02.026

Gizurarson, S., Dalvi, R., Das, M., Ha, A. C. T., Suszko, A., and Chauhan, V. S. (2016). Hierarchical schema for identifying focal electrical sources during human atrial fibrillation: implications for catheter-based atrial substrate ablation. *JACC Clin. Electrophysiol.* 2, 656–666. doi: 10.1016/j.jacep.2016.02.009

Goette, A., Kalman, J. M., Aguinaga, L., Akar, J., Cabrera, J. A., Chen, S. A., et al. (2016). EHRA/HRS/APHRS/SOLAECE expert consensus on atrial cardiomyopathies: definition, characterization, and clinical implication. *Europace* 18, 1455–1490. doi: 10.1093/europace/euw161

Gonzales, M. J., Vincent, K. P., Rappel, W. J., Narayan, S. M., and McCulloch, A. D. (2014). Structural contributions to fibrillatory rotors in a patient-derived computational model of the atria. *Europace* 16, iv3–iv10.

Grace, A., Verma, A., and Willems, S. (2017). Dipole density mapping of atrial fibrillation. *Eur. Heart J.* 38, 5–9. doi: 10.1093/eurheartj/ehw585

Haissaguerre, M., Hocini, M., Denis, A., Shah, A. J., Komatsu, Y., Yamashita, S., et al. (2014). Driver domains in persistent atrial fibrillation. *Circulation* 130, 530–538.

Haïssaguerre, M., Jaïs, P., Shah, D. C., Takahashi, A., Hocini, M., Quiniou, G., et al. (1998). Spontaneous initiation of atrial fibrillation by ectopic beats originating in the pulmonary veins. *N. Engl. J. Med.* 339, 659–666. doi: 10.1056/nejm199809033391003

Hansen, B. J., Csepe, T. A., Zhao, J., Ignozzi, A. J., Hummel, J. D., and Fedorov, V. V. (2016). Maintenance of atrial fibrillation: are reentrant drivers with spatial stability the key? *Circ. Arrhythmia Electrophysiol.* 9, 1–12.

Hansen, B. J., Zhao, J., Csepe, T. A., Moore, B. T., Li, N., Jayne, L. A., et al. (2015). Atrial fibrillation driven by micro-anatomic intramural re-entry revealed by simultaneous sub-epicardial and sub-endocardial optical mapping in explanted human hearts. *Eur. Heart J.* 36, 2390–2401. doi: 10.1093/eurheartj/ehv233

Hansen, B. J., Zhao, J., and Fedorov, V. V. (2017). Fibrosis and atrial fibrillation: computerized and optical mapping: a view into the human atria at submillimeter resolution. *JACC Clin. Electrophysiol.* 3, 531–546. doi: 10.1016/j.jacep.2017.05.002

Hansen, B. J., Zhao, J., Li, N., Zolotarev, A., Zakharkin, S., Wang, Y., et al. (2018). Human atrial fibrillation drivers resolved with integrated functional and structural imaging to benefit clinical mapping. *JACC Clin. Electrophysiol.* 4, 1501–1515. doi: 10.1016/j.jacep.2018.08.024

Hayashi, K., An, Y., Nagashima, M., Hiroshima, K., Ohe, M., Makihara, Y., et al. (2015). Importance of nonpulmonary vein foci in catheter ablation for paroxysmal atrial fibrillation. *Hear. Rhythm* 12, 1918–1924. doi: 10.1016/j.hrthm.2015.05.003

Heijman, J., Voigt, N., Nattel, S., and Dobrev, D. (2014). Cellular and molecular electrophysiology of atrial fibrillation initiation, maintenance, and progression. *Circ. Res.* 114, 1483–1499. doi: 10.1161/circresaha.114.302226

Hojo, R., Fukamizu, S., Kitamura, T., Aomyama, Y., Nishizaki, M., Kobayashi, Y., et al. (2017). Development of nonpulmonary vein foci increases risk of atrial fibrillation recurrence after pulmonary vein isolation. *JACC Clin. Electrophysiol.* 3, 547–555. doi: 10.1016/j.jacep.2016.12.008

Honarbakhsh, S., Schilling, R. J., Dhillon, G., Ullah, W., Keating, E., Providencia, R., et al. (2018). A novel mapping system for panoramic mapping of the left atrium: application to detect and characterize localized sources maintaining atrial fibrillation. *JACC Clin. Electrophysiol.* 4, 124–134.

Iwasaki, Y., Kato, T., Xiong, F., Shi, Y.-F., Naud, P., Maguy, A., et al. (2014). Atrial fibrillation promotion with long-term repetitive obstructive sleep apnea in a rat model. *J. Am. Coll. Cardiol.* 64, 2013–2023. doi: 10.1016/j.jacc.2014.05.077

Jadidi, A. S., Lehrmann, H., Keyl, C., Sorrel, J., Markstein, V., Minners, J., et al. (2016). Ablation of persistent atrial fibrillation targeting low-voltage areas with selective activation characteristics. *Circ. Arrhythmia Electrophysiol.* 9, 1–11.

Jalife, J. (2003). Rotors and spiral waves in atrial fibrillation. *J. Cardiovasc. Electrophysiol.* 14, 776–780. doi: 10.1046/j.1540-8167.2003.03136.x

January, C. T., Wann, L. S., Alpert, J. S., Calkins, H., Cigarroa, J. E., Cleveland, J. C., et al. (2014). 2014 AHA/ACC/HRS guideline for the management of patients with atrial fibrillation: a report of the American college of Cardiology/American heart association task force on practice guidelines and the heart rhythm society. *J. Am. Coll. Cardiol.* 64, e1–e76.

January, C. T., Wann, L. S., Calkins, H., Chen, L. Y., Cigarroa, J. E., Cleveland, J. C., et al. (2019). 2019 AHA/ACC/HRS focused update of the 2014 AHA/ACC/HRS guideline for the management of patients with atrial fibrillation: a report of the american college of cardiology/American heart association task force on clinical practice guidelines and the heart R. *Hear. Rhythm* 16, e66–e93.

Josephson, M. E., and Anter, E. (2015). Substrate mapping for ventricular tachycardia: assumptions and misconceptions. *JACC Clin. Electrophysiol.* 1, 341–352.

Kapa, S., Desjardins, B., Callans, D. J., Marchlinski, F. E., and Dixit, S. (2014). Contact electroanatomic mapping derived voltage criteria for characterizing left atrial scar in patients undergoing ablation for atrial fibrillation. *J. Cardiovasc. Electrophysiol.* 25, 1044–1052. doi: 10.1111/jce.12452

Karim, R., Housden, R. J., Balasubramaniam, M., Chen, Z., Perry, D., Uddin, A., et al. (2013). Evaluation of current algorithms for segmentation of scar tissue from late Gadolinium enhancement cardiovascular magnetic resonance of the left atrium: an open-access grand challenge. *J. Cardiovasc. Magn. Reson.* 15, 1–17.

Kircher, S., Arya, A., Altmann, D., Rolf, S., Bollmann, A., Sommer, P., et al. (2018). Individually tailored vs. standardized substrate modification during radiofrequency catheter ablation for atrial fibrillation: a randomized study. *Europace* 20, 1766–1775. doi: 10.1093/europace/eux310

Knecht, S., Sohal, M., Deisenhofer, I., Albenque, J. P., Arentz, T., Neumann, T., et al. (2017). Multicentre evaluation of non-invasive biatrial mapping for persistent atrial fibrillation ablation: the AFACART study. *Europace* 19, 1302–1309. doi: 10.1093/europace/euw168

Kottkamp, H. (2013). Human atrial fibrillation substrate: towards a specific fibrotic atrial cardiomyopathy. *Eur. Heart J.* 34, 2731–2738. doi: 10.1093/eurheartj/eht194

Kottkamp, H., Berg, J., Bender, R., Rieger, A., and Schreiber, D. (2016). Box isolation of fibrotic areas (BIFA): a patient-tailored substrate modification approach for ablation of atrial fibrillation. *J. Cardiovasc. Electrophysiol.* 27, 22–30. doi: 10.1111/jce.12870

Kowalewski, C. A. B., Shenasa, F., Rodrigo, M., Clopton, P., Meckler, G., Alhusseini, M. I., et al. (2018). Interaction of localized drivers and disorganized activation in persistent atrial fibrillation: reconciling putative mechanisms using multiple mapping techniques. *Circ. Arrhythmia Electrophysiol.* 11, 1–12.

Krummen, D. E., Bayer, J. D., Ho, J., Ho, G., Smetak, M. R., Clopton, P., et al. (2012). Mechanisms of human atrial fibrillation initiation clinical and computational studies of repolarization restitution and activation latency. *Circ. Arrhythmia Electrophysiol.* 5, 1149–1159. doi: 10.1161/circep.111.969022

Krummen, D. E., Hebsur, S., Salcedo, J., Narayan, S. M., Lalani, G. G., and Schricker, A. A. (2015). Mechanisms underlying AF: triggers, rotors, other? *Curr. Treat. Options Cardiovasc. Med.* 17:371.

Lalani, G. G., Schricker, A., Gibson, M., Rostamian, A., Krummen, D. E., and Narayan, S. M. (2012). Atrial conduction slows immediately before the onset of human atrial fibrillation: a bi-atrial contact mapping study of transitions to atrial fibrillation. *J. Am. Coll. Cardiol.* 59, 595–606. doi: 10.1016/j.jacc.2011.10.879

Lalani, G. G., Trikha, R., Krummen, D. E., and Narayan, S. M. (2014). Rotors and focal sources for human atrial fibrillation–Mechanistic paradigm with direct clinical relevance. *Circ. J.* 78, 2357–2366. doi: 10.1253/circj.cj-14-0478

Lau, D. H., Nattel, S., Kalman, J. M., and Sanders, P. (2017). Modifiable risk factors and atrial fibrillation. *Circulation* 136, 583–596. doi: 10.1161/circulationaha.116.023163

Leef, G., Shenasa, F., Bhatia, N. K., Rogers, A. J., Sauer, W., Miller, J. M., et al. (2019). Wavefront field mapping reveals a physiologic network between drivers where ablation terminates atrial fibrillation. *Circ. Arrhythmia Electrophysiol.* 12, 1–10.

Li, D., Fareh, S., Leung, T. K., and Nattel, S. (1999). Promotion of atrial fibrillation by heart failure in dogs: atrial remodeling of a different sort. *Circulation* 100, 87–95. doi: 10.1161/01.cir.100.1.87

Li, D., Zhang, L., Kneller, J., and Nattel, S. (2001). Potential ionic mechanism for repolarization differences between canine right and left atrium. *Circ. Res.* 88, 1168–1175. doi: 10.1161/hh1101.091266

Lin, W. S., Tai, C. T., Hsieh, M. H., Tsai, C. F., Lin, Y. K., Tsao, H. M., et al. (2003). Catheter ablation of paroxysmal atrial fibrillation initiated by non-pulmonary vein ectopy. *Circulation* 107, 3176–3183. doi: 10.1161/01.cir.0000074206.52056.2d

Ling, Z., McManigle, J., Zipunnikov, V., Pashakhanloo, F., Khurram, I. M., Zimmerman, S. L., et al. (2015). The association of left atrial low-voltage regions on electroanatomic mapping with low attenuation regions on cardiac computed tomography perfusion imaging in patients with atrial fibrillation. *Hear. Rhythm* 12, 857–864. doi: 10.1016/j.hrthm.2015.01.015

Mahajan, R., Lau, D. H., Brooks, A. G., Shipp, N. J., Manavis, J., Wood, J. P. M., et al. (2015). Electrophysiological, electroanatomical, and structural remodeling of the atria as consequences of sustained obesity. *J. Am. Coll. Cardiol.* 66, 1–11. doi: 10.1016/j.jacc.2015.04.058

Mahnkopf, C., Badger, T. J., Burgon, N. S., Daccarett, M., Haslam, T. S., Badger, C. T., et al. (2010). Evaluation of the left atrial substrate in patients with lone atrial fibrillation using delayed-enhanced MRI: implications for disease progression and response to catheter ablation. *Hear. Rhythm* 7, 1475–1481. doi: 10.1016/j.hrthm.2010.06.030

Malcolme-Lawes, L. C., Juli, C., Karim, R., Bai, W., Quest, R., Lim, P. B., et al. (2013). Automated analysis of atrial late gadolinium enhancement imaging that correlates with endocardial voltage and clinical outcomes: A 2-center study. *Hear. Rhythm* 10, 1184–1191. doi: 10.1016/j.hrthm.2013.04.030

Marrouche, N. F., Wilber, D., Hindricks, G., Jais, P., Akoum, N., Marchlinski, F., et al. (2014). Association of atrial tissue fibrosis identified by delayed enhancement MRI and atrial fibrillation catheter ablation: the DECAAF study. *JAMA J. Am. Med. Assoc.* 311, 498–506. doi: 10.1001/jama.2014.3

McDowell, K. S., Vadakkumpadan, F., Blake, R., Blauer, J., Plank, G., Macleod, R. S., et al. (2013). Mechanistic inquiry into the role of tissue remodeling in fibrotic lesions in human atrial fibrillation. *Biophys. J.* 104, 2764–2773. doi: 10.1016/j.bpj.2013.05.025

McDowell, K. S., Zahid, S., Vadakkumpadan, F., Blauer, J., MacLeod, R. S., and Trayanova, N. A. (2015). Virtual electrophysiological study of atrial fibrillation in fibrotic remodeling. *PLoS One* 10, 1–16.

McGann, C., Akoum, N., Patel, A., Kholmovski, E., Revelo, P., Damal, K., et al. (2014). Atrial fibrillation ablation outcome is predicted by left atrial remodeling on MRI. *Circ. Arrhythmia Electrophysiol.* 7, 23–30.

Miller, J. M., Kalra, V., Das, M. K., Jain, R., Garlie, J. B., Brewster, J. A., et al. (2017). Clinical benefit of ablating localized sources for human atrial fibrillation: the indiana university FIRM registry. *J. Am. Coll. Cardiol.* 69, 1247–1256. doi: 10.1016/j.jacc.2016.11.079

Miller, J. M., Kowal, R. C., Swarup, V., Daubert, J. P., Daoud, E. G., Day, J. D., et al. (2014). Initial independent outcomes from focal impulse and rotor modulation ablation for atrial fibrillation: multicenter FIRM registry. *J. Cardiovasc. Electrophysiol.* 25, 921–929. doi: 10.1111/jce.12474

Morgan, R., Colman, M. A., Chubb, H., Seemann, G., and Aslanidi, O. V. (2016). Slow conduction in the border zones of patchy fibrosis stabilizes the drivers for atrial fibrillation: Insights from multi-scale human atrial modeling. *Front. Physiol.* 7, 1–15.

Munger, T. M., Dong, Y.-X., Masaki, M., Oh, J. K., Mankad, S. V., Borlaug, B. A., et al. (2012). Electrophysiological and hemodynamic characteristics associated with obesity in patients with atrial fibrillation. *J. Am. Coll. Cardiol.* 60, 851–860.

Narayan, S. M., Baykaner, T., Clopton, P., Schricker, A., Lalani, G. G., Krummen, D. E., et al. (2014). Ablation of rotor and focal sources reduces late recurrence of atrial fibrillation compared with trigger ablation alone: extended follow-up of the CONFIRM trial (conventional ablation for atrial fibrillation with or without focal impulse and rotor modulat. *J. Am. Coll. Cardiol.* 63, 1761–1768. doi: 10.1016/j.jacc.2014.02.543

Narayan, S. M., Kazi, D., Krummen, D. E., and Rappel, W. J. (2008). Repolarization and activation restitution near human pulmonary veins and atrial fibrillation initiation: a mechanism for the initiation of atrial fibrillation by premature beats. *J. Am. Coll. Cardiol.* 52, 1222–1230. doi: 10.1016/j.jacc.2008.07.012

Narayan, S. M., Krummen, D. E., Enyeart, M. W., and Rappel, W. J. (2012a). Computational mapping identifies localized mechanisms for ablation of atrial fibrillation. *PLoS One* 7:e46034. doi: 10.1371/journal.pone.0046034

Narayan, S. M., Krummen, D. E., and Rappel, W. J. (2012b). Clinical mapping approach to diagnose electrical rotors and focal impulse sources for human atrial fibrillation. *J. Cardiovasc. Electrophysiol.* 23, 447–454. doi: 10.1111/j.1540-8167.2012.02332.x

Narayan, S. M., Krummen, D. E., Shivkumar, K., Clopton, P., Rappel, W. J., and Miller, J. M. (2012c). Treatment of atrial fibrillation by the ablation of localized sources: CONFIRM (Conventional Ablation for Atrial Fibrillation with or Without Focal Impulse and Rotor Modulation) trial. *J. Am. Coll. Cardiol.* 60, 628–636.

Narayan, S. M., Patel, J., Mulpuru, S., and Krummen, D. E. (2012d). Focal impulse and rotor modulation ablation of sustaining rotors abruptly terminates persistent atrial fibrillation to sinus rhythm with elimination on follow-up: a video case study. *Hear. Rhythm* 9, 1436–1439. doi: 10.1016/j.hrthm.2012.03.055

Narayan, S. M., Shivkumar, K., Krummen, D. E., Miller, J. M., and Rappel, W. J. (2013). Panoramic electrophysiological mapping but not electrogram morphology identifies stable sources for human atrial fibrillation: stable atrial fibrillation rotors and focal sources relate poorly to fractionated electrograms. *Circ. Arrhythm. Electrophysiol.* 6, 58–67. doi: 10.1161/circep.111.977264

Nattel, S., Burstein, B., and Dobrev, D. (2008). Atrial remodeling and atrial fibrillation: mechanisms and implications. *Circ. Arrhythmia Electrophysiol.* 1, 62–73. doi: 10.1161/circep.107.754564

Nattel, S., Xiong, F., and Aguilar, M. (2017). Demystifying rotors and their place in clinical translation of atrial fibrillation mechanisms. *Nat. Rev. Cardiol.* 14, 509–520. doi: 10.1038/nrcardio.2017.37

Numata, A., Miyauchi, Y., Ono, N., Fishbein, M. C., Mandel, W. J., Lin, S., et al. (2012). Spontaneous atrial fibrillation initiated by tyramine in canine atria with increased sympathetic nerve sprouting. *J. Cardiovasc. Electrophysiol.* 23, 415–422. doi: 10.1111/j.1540-8167.2011.02197.x

Oakes, R. S., Badger, T. J., Kholmovski, E. G., Akoum, N., Burgon, N. S., Fish, E. N., et al. (2009). Detection and quantification of left atrial structural remodeling with delayed-enhancement magnetic resonance imaging in patients with atrial fibrillation. *Circulation* 119, 1758–1767. doi: 10.1161/circulationaha.108.811877

Packer, D. L., Mark, D. B., Robb, R. A., Monahan, K. H., Bahnson, T. D., Poole, J. E., et al. (2019). Effect of catheter ablation vs antiarrhythmic drug therapy on mortality, stroke, bleeding, and cardiac arrest among patients with atrial fibrillation: the CABANA randomized clinical trial. *JAMA J. Am. Med. Assoc.* 321, 1261–1274.

Pashakhanloo, F., Herzka, D. A., Ashikaga, H., Mori, S., Gai, N., Bluemke, D. A., et al. (2016). Myofiber architecture of the human atria as revealed by submillimeter diffusion tensor imaging. *Circ. Arrhythmia Electrophysiol.* 9:e004133.

Pathak, R. K., Middeldorp, M. E., Lau, D. H., Mehta, A. B., Mahajan, R., Twomey, D., et al. (2014). Aggressive risk factor reduction study for atrial fibrillation and implications for the outcome of ablation: the ARREST-AF cohort study. *J. Am. Coll. Cardiol.* 64, 2222–2231. doi: 10.1016/j.jacc.2014.09.028

Pathak, R. K., Middeldorp, M. E., Meredith, M., Mehta, A. B., Mahajan, R., Wong, C. X., et al. (2015). Long-term effect of goal-directed weight management in an

atrial fibrillation cohort: a long-term follow-up study (LEGACY). *J. Am. Coll. Cardiol.* 65, 2159–2169.

Pérez, F. J., Schubert, C. M., Parvez, B., Pathak, V., Ellenbogen, K. A., and Wood, M. A. (2009). Long-term outcomes after catheter ablation of cavo-tricuspid isthmus dependent atrial flutter: a meta-analysis. *Circ. Arrhythmia Electrophysiol.* 2, 393–401. doi: 10.1161/circep.109.871665

Qiao, Y., Shi, R., Hou, B., Wu, L., Zheng, L., Ding, L., et al. (2015). Impact of alcohol consumption on substrate remodeling and ablation outcome of paroxysmal atrial fibrillation. *J. Am. Heart Assoc.* 4:e002349.

Quintanilla, J. G., Pérez-Villacastín, J., Pérez-Castellano, N., Pandit, S. V., Berenfeld, O., Jalife, J., et al. (2016). Mechanistic approaches to detect, target, and ablate the drivers of atrial fibrillation. *Circ. Arrhythmia Electrophysiol.* 9, 1–11.

Ramanathan, C., Ghanem, R. N., Jia, P., Ryu, K., and Rudy, Y. (2004). Noninvasive electrocardiographic imaging for cardiac electrophysiology and arrhythmia. *Nat. Med.* 10, 422–428. doi: 10.1038/nm1011

Rolf, S., Kircher, S., Arya, A., Eitel, C., Sommer, P., Sergio, R., et al. (2014). Tailored atrial substrate modification based on low-voltage areas in catheter ablation of atrial fibrillation. *Circ. Arrhythmia Electrophysiol.* 7, 825–833. doi: 10.1161/circep.113.001251

Saeed, M., Van, T. A., Krug, R., Hetts, S. W., and Wilson, M. W. (2015). Cardiac MR imaging: current status and future direction. *Cardiovasc. Diagn. Ther.* 5, 290–310.

Santangeli, P., Zado, E. S., Hutchinson, M. D., Riley, M. P., Lin, D., Frankel, D. S., et al. (2016). Prevalence and distribution of focal triggers in persistent and long-standing persistent atrial fibrillation. *Hear. Rhythm* 13, 374–382. doi: 10.1016/j.hrthm.2015.10.023

Sauer, W. H., Alonso, C., Zado, E., Cooper, J. M., Lin, D., Dixit, S., et al. (2006). Atrioventricular nodal reentrant tachycardia in patients referred for atrial fibrillation ablation: response to ablation that incorporates slow-pathway modification. *Circulation* 114, 191–195. doi: 10.1161/circulationaha.106.621896

Schade, A., Nentwich, K., Costello-Boerrigter, L. C., Halbfass, P., Mueller, P., Roos, M., et al. (2016). Spatial relationship of focal impulses, rotors and low voltage zones in patients with persistent atrial fibrillation. *J. Cardiovasc. Electrophysiol.* 27, 507–514. doi: 10.1111/jce.12913

Schricker, A. A., Lalani, G. G., Krummen, D. E., Rappel, W. J., and Narayan, S. M. (2014). Human atrial fibrillation initiates via organized rather than disorganized mechanisms. *Circ. Arrhythm Electrophysiol.* 7, 816–824. doi: 10.1161/circep.113.001289

Seitz, J., Bars, C., Théodore, G., Beurtheret, S., Lellouche, N., Bremondy, M., et al. (2017). AF ablation guided by spatiotemporal electrogram dispersion without pulmonary vein isolation: a wholly patient-tailored approach. *J. Am. Coll. Cardiol.* 69, 303–321. doi: 10.1016/j.jacc.2016.10.065

Shen, M. J., Arora, R., and Jalife, J. (2019). Atrial myopathy. *JACC Basic Transl. Sci.* 4, 640–654.

Shi, R., Parikh, P., Chen, Z., Angel, N., Norman, M., Hussain, W., et al. (2020). Validation of dipole density mapping during atrial fibrillation and sinus rhythm in human left atrium. *JACC Clin. Electrophysiol.* 6, 171–181. doi: 10.1016/j.jacep.2019.09.012

Shin, S. Y., Jo, W.-M., Min, T. J., Kim, B.-K., Song, D. H., Hyeon, S. H., et al. (2015). Gap junction remodelling by chronic pressure overload is related to the increased susceptibility to atrial fibrillation in rat heart. *Ep. Eur.* 17, 655–663. doi: 10.1093/europace/euu294

Shivkumar, K., Ellenbogen, K. A., Hummel, J. D., Miller, J. M., and Steinberg, J. S. (2012). Acute termination of human atrial fibrillation by identification and catheter ablation of localized rotors and sources: first multicenter experience of focal impulse and rotor modulation (FIRM) ablation. *J. Cardiovasc. Electrophysiol.* 23, 1277–1285. doi: 10.1111/jce.12000

Sohns, C., and Marrouche, N. F. (2020). Atrial fibrillation and cardiac fibrosis. *Eur. Heart J.* 41, 1123–1131. doi: 10.1093/eurheartj/ehz786

Spragg, D. D., Khurram, I., Zimmerman, S. L., Yarmohammadi, H., Barcelon, B., Needleman, M., et al. (2012). Initial experience with magnetic resonance imaging of atrial scar and co-registration with electroanatomic voltage mapping during atrial fibrillation: success and limitations. *Hear. Rhythm* 9, 2003–2009. doi: 10.1016/j.hrthm.2012.08.039

Stiles, M. K., John, B., Wong, C. X., Kuklik, P., Brooks, A. G., Lau, D. H., et al. (2009). Paroxysmal lone atrial fibrillation is associated with an abnormal atrial substrate. Characterizing the 'second factor'. *J. Am. Coll. Cardiol.* 53, 1182–1191.

Takigawa, M., Takahashi, A., Kuwahara, T., Okubo, K., Takahashi, Y., Nakashima, E., et al. (2015). Impact of non-pulmonary vein foci on the outcome of the second session of catheter ablation for paroxysmal atrial fibrillation. *J. Cardiovasc. Electrophysiol.* 26, 739–746. doi: 10.1111/jce.12681

Van Campenhout, M. J. H., Yaksh, A., Kik, C., De Jaegere, P. P., Ho, S. Y., Allessie, M. A., et al. (2013). Bachmann's bundle a key player in the development of atrial fibrillation? *Circ. Arrhythmia Electrophysiol.* 6, 1041–1046. doi: 10.1161/circep.113.000758

Verma, A., Jiang, C. Y., Betts, T. R., Chen, J., Deisenhofer, I., Mantovan, R., et al. (2015). Approaches to catheter ablation for persistent atrial fibrillation. *N. Engl. J. Med.* 372, 1812–1822.

Verma, A., Wazni, O. M., Marrouche, N. F., Martin, D. O., Kilicaslan, F., Minor, S., et al. (2005). Pre-existent left atrial scarring in patients undergoing pulmonary vein antrum isolation: an independent predictor of procedural failure. *J. Am. Coll. Cardiol.* 45, 285–292. doi: 10.1016/j.jacc.2004.10.035

Voskoboinik, A., Prabhu, S., Ling, L., Kalman, J. M., and Kistler, P. M. (2016). Alcohol and atrial fibrillation: a sobering review. *J. Am. Coll. Cardiol.* 68, 2567–2576.

Wijffels, M. C. E. F., Kirchhof, C. J. H. J., Dorland, R., and Allessie, M. A. (1995). Atrial fibrillation begets atrial fibrillation: a study in awake chronically instrumented goats. *Circulation* 92, 1954–1968. doi: 10.1161/01.cir.92.7.1954

Willems, S., Verma, A., Betts, T. R., Murray, S., Neuzil, P., Ince, H., et al. (2019). Targeting nonpulmonary vein sources in persistent atrial fibrillation identified by noncontact charge density mapping: UNCOVER AF trial. *Circ. Arrhythmia Electrophysiol.* 12, 1–12.

Yagishita, A., Gimbel, J. R., De Oliveira, S., Manyam, H., Sparano, D., Cakulev, I., et al. (2017). Long-term outcome of left atrial voltage-guided substrate ablation during atrial fibrillation: a novel adjunctive ablation strategy. *J. Cardiovasc. Electrophysiol.* 28, 147–155. doi: 10.1111/jce.13122

Yue, L., Xie, J., and Nattel, S. (2011). Molecular determinants of cardiac fibroblast electrical function and therapeutic implications for atrial fibrillation. *Cardiovasc. Res.* 89, 744–753. doi: 10.1093/cvr/cvq329

Zahid, S., Cochet, H., Boyle, P. M., Schwarz, E. L., Whyte, K. N., Vigmond, E. J., et al. (2016). Patient-derived models link re-entrant driver localization in atrial fibrillation to fibrosis spatial pattern. *Cardiovasc. Res.* 110, 443–454. doi: 10.1093/cvr/cvw073

Zaman, J. A. B., and Narayan, S. M. (2015). When is structure, function? Revisiting an old concept in atrial fibrillation. *J. Cardiovasc. Electrophysiol.* 26, 1361–1363. doi: 10.1111/jce.12836

Zaman, J. A. B., Sauer, W. H., Alhusseini, M. I., Baykaner, T., Borne, R. T., Kowalewski, C. A. B., et al. (2018). Identification and characterization of sites where persistent atrial fibrillation is terminated by localized ablation. *Circ. Arrhythmia Electrophysiol.* 11, 1–12.

Zellerhoff, S., Pistulli, R., Mönnig, G., Hinterseer, M., Beckmann, B., Koebe, J., et al. (2009). Atrial arrhythmias in long−QT syndrome under daily life conditions: a nested case control study. *J. Cardiovasc. Electrophysiol.* 20, 401–407. doi: 10.1111/j.1540-8167.2008.01339.x

Zhao, J., Hansen, B. J., Wang, Y., Csepe, T. A., Sul, L. V., Tang, A., et al. (2017). Three-dimensional integrated functional, structural, and computational mapping to define the structural 'fingerprints' of heart-specific atrial fibrillation drivers in human heart ex vivo. *J. Am. Heart Assoc.* 6:e005922.

Conflict of Interest: The authors declare that the research was conducted in the absence of any commercial or financial relationships that could be construed as a potential conflict of interest.

frontiers in Physiology

ORIGINAL RESEARCH
published: 19 November 2020
doi: 10.3389/fphys.2020.583570

Apelin Inhibits Angiotensin II-Induced Atrial Fibrosis and Atrial Fibrillation via TGF-β1/Smad2/α-SMA Pathway

Wenkui Lv[1,2†], Ling Zhang[2,3†], Xinchun Cheng[4], Hongli Wang[3], Wen Qin[5], Xianhui Zhou[2,3] and Baopeng Tang[2,3*]*

[1] Heart Failure Department, The First Affiliated Hospital of Xinjiang Medical University, Urumqi, China, [2] Xinjiang Key Laboratory of Cardiac Electrophysiology and Cardiac Remodeling, The First Affiliated Hospital of Xinjiang Medical University, Urumqi, China, [3] Department of Pacing and Electrophysiological, The First Affiliated Hospital of Xinjiang Medical University, Urumqi, China, [4] Geriatrics Center, The People's Hospital of Xinjiang Uygur Autonomous Region, Urumqi, China, [5] Department of Histology and Embryology, School of Basic Medical Science, Xinjiang Medical University, Urumqi, China

OPEN ACCESS

Edited by:
Sanjiv M. Narayan,
Stanford University, United States

Reviewed by:
Tong Liu,
Tianjin Medical University, China
David R. Van Wagoner,
Case Western Reserve University, United States

***Correspondence:**
Baopeng Tang
tangbaopeng1111@163.com
Xianhui Zhou
zhouxhuiyf@163.com

[†] These authors have contributed equally to this work and share first authorship

Specialty section:
This article was submitted to Cardiac Electrophysiology, a section of the journal Frontiers in Physiology

Received: 15 July 2020
Accepted: 23 October 2020
Published: 19 November 2020

Citation:
Lv W, Zhang L, Cheng X, Wang H, Qin W, Zhou X and Tang B (2020) Apelin Inhibits Angiotensin II-Induced Atrial Fibrosis and Atrial Fibrillation via TGF-β1/Smad2/α-SMA Pathway. Front. Physiol. 11:583570. doi: 10.3389/fphys.2020.583570

Background: Angiotensin II (Ang II) could promote the development of atrial fibrosis in atrial fibrillation (AF). Apelin can inhibit the occurrence of myocardial fibrosis. However, the effect of apelin on Ang II-induced atrial fibrosis and subsequent AF still remains unknown.

Objective: In the present study, we examined the effect of apelin on the suppression of atrial fibrosis and subsequent AF, and investigated its underlying mechanisms.

Methods: Sprague-Dawley rats were treated for 2 weeks with Ang II (1080 μg/kg/24 h) and apelin-13 (140 μg/kg/24 h) using implantable mini-pumps. The incidence of AF induced by atrial pacing was determined. Atrial electrophysiological mapping was recorded by a 32-electrode microelectrode array. Blood was collected to measure the levels of Ang II and apelin. Atrial tissue samples were preserved to assess the pathohistological changes, DDR2 and α-SMA co-staining were performed, and the protein expression of Smad2 phosphorylation was evaluated.

Results: Apelin significantly inhibited Ang II-induced atrial fibrosis (HE:1.45 ± 0.11 vs 6.12 ± 0.16, $P < 0.001$; Masson:1.49 ± 0.25 vs 8.15 ± 0.23, $P < 0.001$; Picrosirius Red:1.98 ± 0.64 vs 9.59 ± 0.56, $P < 0.001$, respectively) and decreased the vulnerability of AF (inducibility of AF: $z = -4.40$, $P < 0.001$; total AF duration: $z = -4.349$, $P < 0.001$). Left atrial epicardial mapping studies demonstrated preservation of atrial conduction homogeneity by apelin. The protective effects of apelin from fibrotic remodeling were mediated by suppression of Smad2-dependent fibrosis.

Conclusion: Apelin potently inhibited Ang II-induced atrial fibrosis and subsequent vulnerability to AF induction via suppression TGF-β/Smad2/α-SMA pathway. Our results indicated that apelin might be an effective up-stream therapy for atrial fibrosis and AF.

Keywords: atrial fibrillation, apelin, angiotensin II, fibrosis, AF

INTRODUCTION

Atrial fibrillation (AF) is one of the most common arrhythmias, with high incidence rate and mortality. Atrial fibrosis is a typical manifestation of atrial structural remodeling, which promotes the occurrence and maintenance of AF, and significantly enhances the AF vulnerability (Andrade et al., 2014; Heijman et al., 2014). Angiotensin II (Ang II) can induce the proliferation of fibroblasts and the development of atrial fibrosis (Dzeshka et al., 2015; Hu et al., 2015).

Apelin is an endogenous peptide with strong positive inotropic effect. Apelin receptor shares 31% sequence identity with the human angiotensin type 1 (AT1) receptor, and the activation of the apelin receptor triggers various signaling pathways that exert protective cardiovascular effects (Marsault et al., 2019). More and more evidences show that apelin plays a protective role in the development of cardiovascular diseases (Cao et al., 2015; Zhong et al., 2017). Previous studies have found that apelin could inhibit the development of myocardial fibrosis (Huang et al., 2016; Xu et al., 2016). However, the effect and underlying mechanisms of apelin on AF and atrial fibrosis remain unclear.

MATERIALS AND METHODS

Ethics Statement

All the research procedures and the use of laboratory animals were in accordance with the Guide for the Care and Use of Laboratory Animals (NIH Publication 2011, eighth edition), and were approved by the Animal Care and Use Committee of the Xinjiang Medical University. All animals were supplied with filtered water and standard laboratory diet. They were placed in a room with constant temperature of 23°C and 12 h light-dark cycle.

Animal Model and Handling

48 male Sprague-Dawley (SD) rats (weighing 400–500 g, the Experimental Animal Center of Xinjiang Medical University, China) were randomly divided into three groups: control, Ang II and Ang II + apelin group. The osmotic mini-pumps were implanted subcutaneously (ALZET, Cupertino, CA, United States) in all animals for 2 weeks. Three groups were divided according to the different contents of osmotic mini-pumps as follows: Ang II group (Ang II, 1080 μg/kg/24h, Sigma-Aldrich, United States), Ang II + apelin group (Ang II 1080 μg/kg/24h, Sigma-Aldrich, United States and apelin 140 μg/kg/24h, Sigma-Aldrich, United States), control group (double distilled water). The dosage and the administration method of the drug were done according to the previous published studies (Scimia et al., 2012; Chagnon et al., 2017). Blood samples were collected at baseline and 2 weeks after drug administration in all the groups. Electrophysiological investigation were performed on all animals after 2 weeks of drugs administration. After that, the left atrial tissue was taken for staining and protein detection. All animal procedures were performed with ketamine anesthesia. Euthanasia was performed by intravascular pentobarbital overdose.

Electrophysiological Investigation

Atrial stimulation was performed as previously described by Rudolph et al. (2010) In brief, a quadrupolar electrophysiological catheter (5F, Boston Scientific Corporation, United States) was inserted via the esophagus into the atrium. Electrophysiological recording and atrial stimulation were performed using LEAD-7000 Electrophysiology Management System (Jinjiang Co. Ltd., China). Atrial burst stimulation was performed at pacing stimulus amplitudes of 2.0 mA for 30 s at S1S1 stimulation cycle lengths starting at 50 ms with 10 ms stepwise reduction down to 10 ms. A recovery period of 30 s was maintained between the stimulation process. Atrial fibrillation is defined as the appearance of rapid, scattered atrial electrograms accompanied by irregular AV-nodal conduction and ventricular rhythm with a duration of these electrograms of 1 s. The AF inducibility (the numbers of induced AF in a certain period of time) and duration (defined as the first sinus-rhythm P wave after AF to the last stimulus-spike) were analyzed.

Atrial Electrophysiological Mapping

The rats were placed on the operating table and connected to a ventilator. The thorax was opened and the heart was exposed. A 32-electrode microelectrode array (MEA, Multichannel Systems, Germany) was placed on the epicardial surface of the right atrium. Using a 128-channel, computer-assisted recording system to recorded electrograms. The inhomogeneity was reflected by the differences of activation time for each electrode with neighboring points, and the inhomogeneity index was obtained by calculating the largest difference at each electrode in the velocity-time curve according to the previous studies (Li et al., 1999; Shinagawa, 2002).

Ang II and Apelin Assay

Plasma levels of Ang II and apelin were quantified with apelin-13 EIA Kits (Sigma-Aldrich, United States) and Ang II EIA Kits (Sigma-Aldrich, United States) according to the manufacturer's instructions.

Hematoxylin-Eosin (HE), Masson's Trichrome and Picrosirius Red Staining

After the tissues of left atrial wall were obtained, it was immediately fixed with 4% paraformaldehyde at 4°C and then embedded in paraffin. Light microscopy was performed using semi-thin sections (2 μm) stained with HE and Masson's trichrome stains. The Picrosirius Red staining was performed using 4 μm sections. After dewaxing, rehydrating and staining with Wiegert's hematoxylin, the sections were stained in Picrosirius Red solution (0.5 g Sirius red F3B in 500 mL saturated aqueous picric acid solution) for 1 h. The sections were then washed in acidified water solution (5 mL acetic acid in 1 L water). Finally, sections were dehydrated in 100% ethanol, cleared in xylene and mounted in a resinous medium. Picrosirius Red stains the collagen red on a pale-yellow background in bright field

microscope, and collagen appears bright orange-red. The area of myocardial fibrosis was measured by a digital imaging system (ImageJ, NIH Image, United States).

Detection of Protein Expression by Western Blot Analysis

Membrane proteins were extracted from the tissue samples of the left atrium (LA) with 5 mmol/L Tris–HCl (pH 7.4), 2 mmol/L EDTA, 5 μg/mL leupeptin, 10 μg/mL benzamidine and 5 μg/mL soybean trypsin inhibitor. All procedures were performed at 4°C. Lysates were centrifuged at 10,000 *g* for 10 min, and supernatants (30 g protein/lane) were separated by SDS-PAGE on a 10% acrylamide gel. Gels were electroblotted onto a nitrocellulose membrane, then blocked with 2% non-fat dry milk and incubated with either anti-p-Smad-2 (Ser 465/467) (3108) and anti-Smad-2 (5339) (Cell Signaling Technology). The signals were scanned and semi quantitated using a digital imaging system (ImageJ, NIH Image, United States).

Co-staining of Atrial Tissue With DDR2 (Tyrosine Kinase Receptor for Fibrillar Collagen) and α-SMA (Marker of Myofibroblasts)

DDR2 and α-SMA co-staining was performed on tissue sections to determine the extent of fibrosis. Sections were incubated overnight in mouse anti-rat DDR2 antibody (1:100 dilution, Sigma-Aldrich, United States) with rabbit anti-rat α-SMA (1:500 dilution, Sigma-Aldrich, United States) and then incubated with goat anti-rabbit Alexa Fluor® 488 and goat anti-mouse Alexa Fluor® 594-conjugated secondary antibodies at a dilution of 1: 5000 and mounted with VectaShield® Antifade Mounting Medium with DAPI. Slides were visualized under fluorescent microscope (LeicaTCS SP8, Germany, atrial tissue, ×20).

Statistical Analysis

Data entry and analysis were done using the IBM® Statistical Package for the Social Sciences (SPSS) version 23. The normality of distribution of all the data were tested, and non-parametric tests were used if they were not normally distributed. The location and spread of continuous variables were presented as mean and standard deviation (SD) (if normal in distribution) or by the median (M) and inter-quartile range (skewed distribution). Hypothesis testing of the difference between the two groups of continuous variables was done using Student's *t*-test (normal distribution) or the Mann–Whitney test (skewed data). Null hypothesis was rejected at $P < 0.05$.

RESULTS

To verify the release of Ang II and apelin from the osmotic pumps, Ang II and apelin plasma levels were measured before and 2 weeks after drug administration in all the groups. Ang II plasma levels were significantly higher in both Ang II and Ang II + apelin groups compared with the corresponding group before administration (149.69 ± 15.87 vs 90.54 ± 16.02 pg/mL, $P < 0.001$; 140.90 ± 17.10 vs 86.33 ± 12.25 pg/mL, $P < 0.001$; respectively). There was no significant difference was observed in the plasma levels between Ang II and Ang II + apelin groups (149.69 ± 15.87 vs 140.90 ± 17.10 pg/ml, $P = 0.105$).The plasma levle of Apelin in the Ang II + apelin group was significantly higher than the baseline (2.37 ± 0.47 vs 1.36 ± 0.27 ng/mL, $P < 0.001$), and no significant difference was observed before and after the drug administration in Ang II group (1.34 ± 0.28 vs 1.31 ± 0.25 ng/mL, $P = 0.76$) (**Figure 1**).

Apelin Suppresses Atrial Fibrosis

Hematoxylin-Eosin, Masson's trichrome, and Picrosirius Red stained atrial sections revealed significantly greater atrial fibrosis in the Ang II group compared with the control group (6.12 ± 0.16 vs 1.24 ± 0.09, $P < 0.001$; 8.15 ± 0.23 vs 1.25 ± 0.11, $P < 0.001$; 9.59 ± 0.56 vs 2.11 ± 0.47, $P < 0.001$, respectively). On the other hand, HE, Masson's trichrome and Picrosirius Red stained atrial sections exhibited significant reduction in the levels of atrial fibrosis in Ang II + apelin group compared with Ang II group (1.45 ± 0.11 vs 6.12 ± 0.16, $P < 0.001$; 1.49 ± 0.25 vs 8.15 ± 0.23, $P < 0.001$; 1.98 ± 0.64 vs 9.59 ± 0.56, $P < 0.001$, respectively), and were in fact equivalent to the control group (1.45 ± 0.11 vs 1.24 ± 0.09, $P = 0.08$; 1.49 ± 0.25 vs 1.25 ± 0.11, $P = 0.06$; 1.98 ± 0.64 vs 2.11 ± 0.47, $P = 0.42$, respectively), (**Figure 2**).

Apelin Preserves Atrial Conduction Homogeneity

Microelectrode array results demonstrated significant increase in the inhomogeneity of Ang II group compared to the with control group (inhomogeneity index of Ang II group vs control group = 4.21 ± 0.32 vs 1.73 ± 0.26, $P < 0.001$),but there was no significant increase in Ang II + apelin group (inhomogeneity index of Ang II group vs Ang II + apelin group = 4.21 ± 0.32 vs 2.16 ± 0.35, $P < 0.001$), (**Figure 3** and **Supplementary Videos 1–3**).

Apelin Inhibits Fibrosis by Inhibition of TGF-β1/Smad2/α-SMA Pathway

Co-staining of atrial tissues with DDR2 and α-SMA revealed a significant increase in the fibroblasts in Ang II group compared with the control group, whereas this effect was almost completely blunted in the Ang II + apelin group (**Figure 4A**).

Western blot analysis demonstrated that the Smad2 phosphorylation was significantly attenuated in the Ang II + apelin group compared to the Ang II group (0.29 ± 0.09 vs 1.57 ± 0.23, $P < 0.001$) (**Figure 4B**).

Apelin Reduces AF Vulnerability

The AF vulnerability (including inducibility of AF and AF duration) was significantly increased in Ang II group compared with the control group (inducibility of AF: $z = -4.70$, $P < 0.001$; AF duration: $z = -4.746$, $P < 0.001$) while the Ang II + apelin group demonstrated reduced AF vulnerability than Ang II group (inducibility of AF: z = −4.40, P < 0.001; total time of AF episodes: $z = -4.349$, $P < 0.001$), (**Figure 5**).

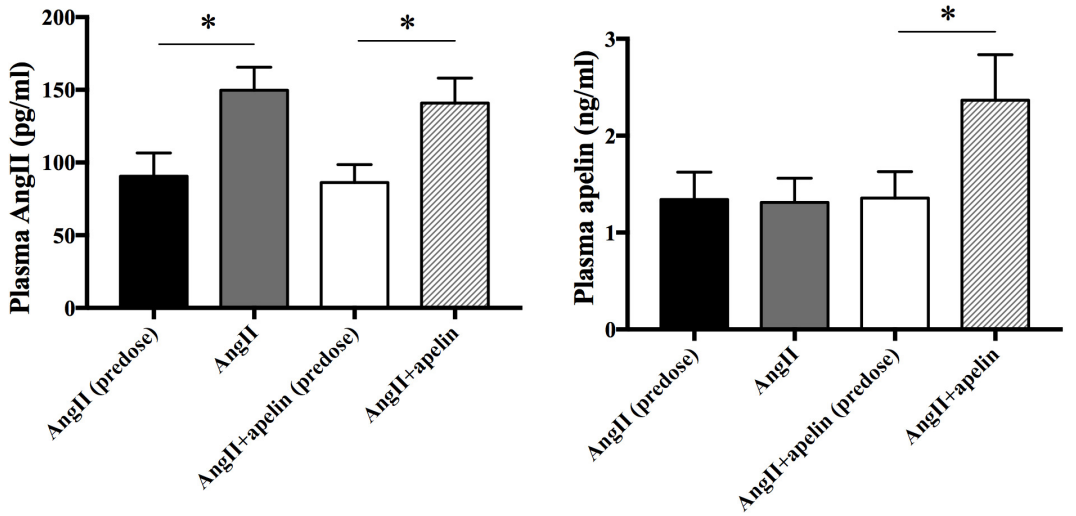

FIGURE 1 | Plasma Ang II and apelin levels. Ang II plasma levels were significantly higher in both Ang II (n = 16) and Ang II + apelin groups (n = 16) compared with the corresponding groups before administration. Apelin plasma levels were significantly higher in Ang II + apelin group than predose. *P < 0.001.

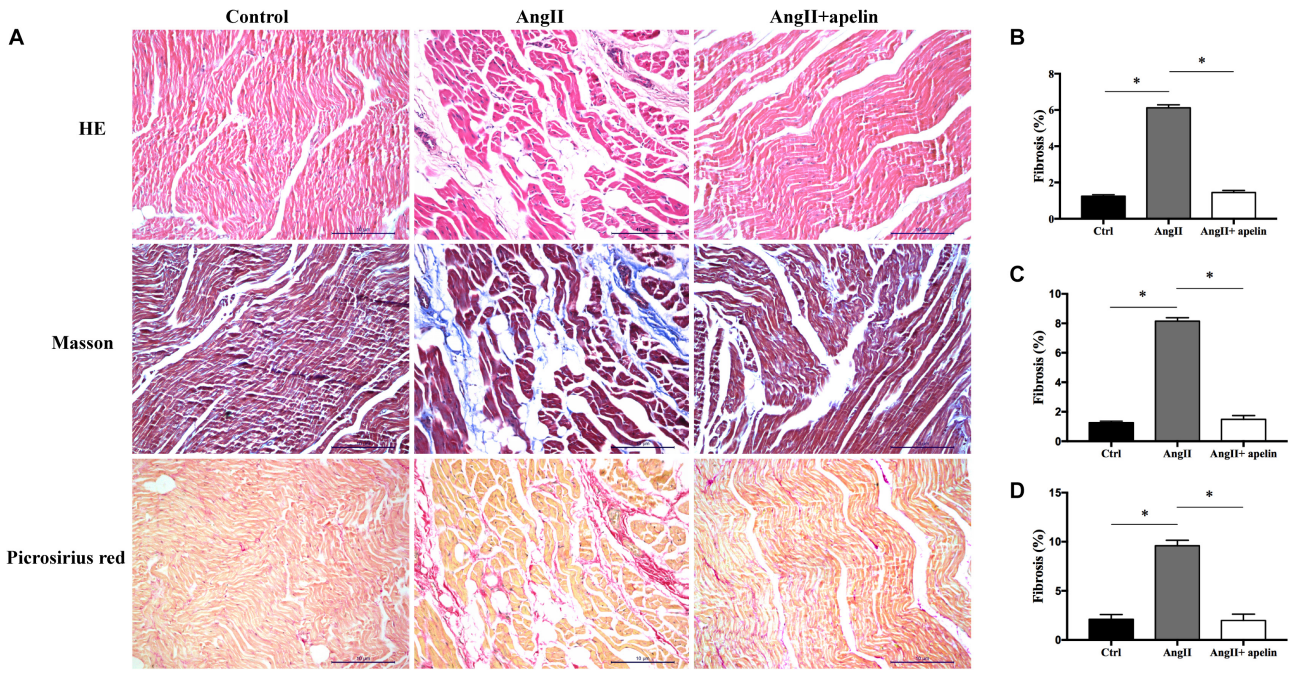

FIGURE 2 | Atrial fibrosis of control, Ang II and Ang II + apelin groups (n = 16 in each group). **(A)** Representative images of HE, Masson's trichrome staining and Picrosirius Red stained atrial sections. **(B–D)** Quantification of fibrotic areas of HE, Masson's trichrome and Picrosirius Red stained atrial sections, respectively. Ang II group showed a higher extent of atrial fibrosis, while concomitant apelin treatment led to a significant reduction of atrial fibrotic areas in Ang II + apelin group. Scale bar indicates 10 μm. *P < 0.001.

DISCUSSION

Atrial fibrillation is an arrhythmia that often leads to serious complications. Atrial remodeling includes electrical remodeling and structural remodeling, which are closely related to the occurrence and maintenance of AF. Atrial fibrosis is an important part of structural remodeling (Nattel and Harada, 2014; Opacic et al., 2016). In the present study, we observed that apelin administration suppressed atrial fibrosis as well as preserved atrial conduction homogeneity, and finally reduced AF vulnerability.

The expression of Ang II was increased in AF patients, and acted as a significant signaling mediator in the pathogenesis of atrial fibrosis (Dzeshka et al., 2015; Opacic et al., 2016).

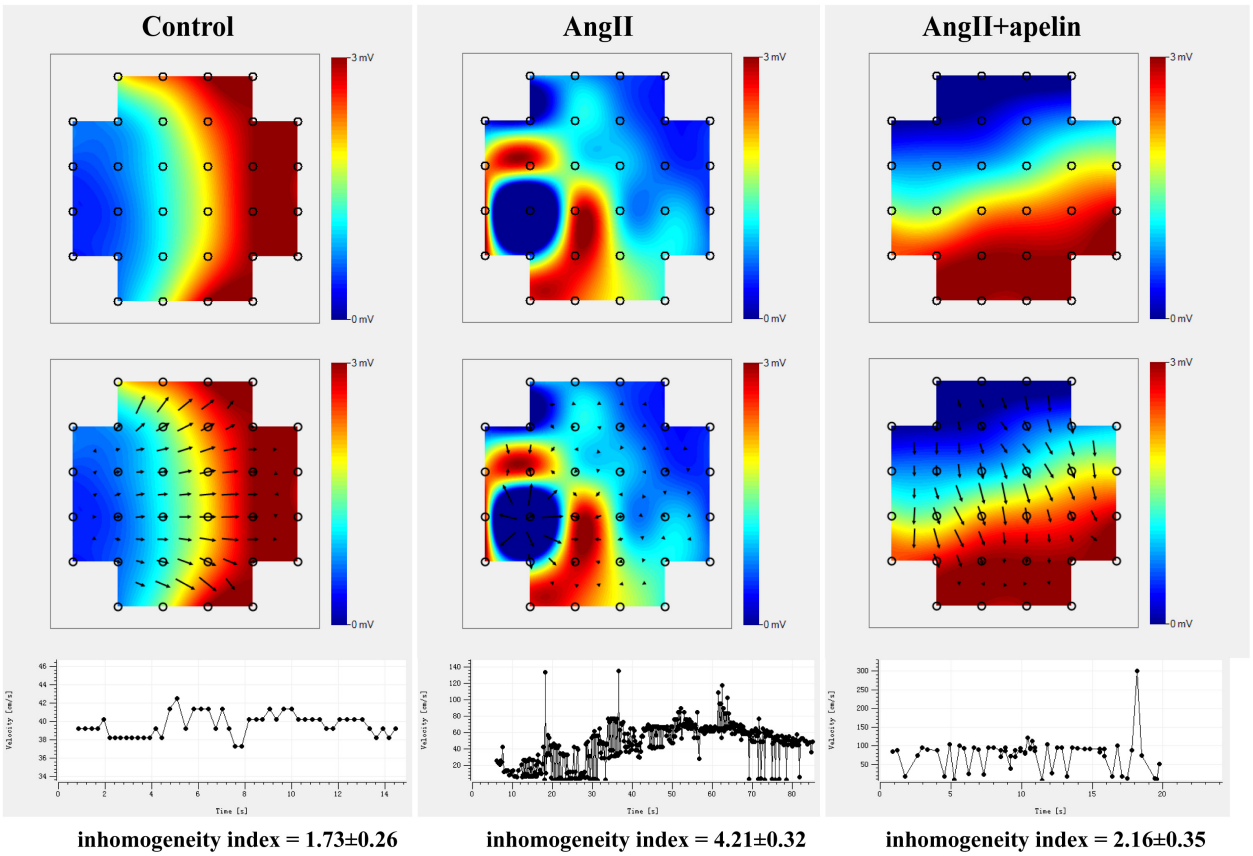

FIGURE 3 | Representative images of epicardial multi-electrode activation mapping. The arrow indicates the conduct direction. The images of epicardial multi-electrode activation mapping and velocity-time curve both demonstrated significant inhomogeneity increase in Ang II group compared with control group (inhomogeneity index of Ang II group vs. control group = 4.21 ± 0.32 vs 1.73 ± 0.26, $P < 0.001$), which was completely abolished in Ang II + apelin group (inhomogeneity index of Ang II group vs Ang II + apelin group = 4.21 ± 0.32 vs 2.16 ± 0.35, $P < 0.001$) ($n = 16$ in each group).

Rosin et al. (2013) demonstrated that Ang II could activate TGF-β1 synthesis, secretion, and downstream Smad2 signaling pathways, resulting in Smad2-dependent production of connective tissue growth factor. This in turn leads to the proliferation of fibroblast in the myocardium and promotes the differentiation of fibrocyte into myofibroblast, which eventually leads to the deposition of extracellular matrix (ECM). ACEI and ARB have been shown to block the activation of renin-angiotensin system (RAS) system, and block the atrial structural remodeling induced by Ang II, reducing the onset of AF. However, no study has reported the role of apelin in the inhibition of RAS system in AF.

In our study, apelin completely abolished the pro-fibrotic effects of Ang II treatment. Up to now, myofibroblasts are still the markers of pathological fibrosis and remodeling of myocardium. The process of differentiation from fibroblasts to myofibroblasts is crucial for promoting the deposition of ECM and increase the incidence of arrhythmia (Weber et al., 2013; Piek et al., 2016).

Furthermore, myofibroblasts also have the function of secreting angiotensin TGF-β1 and Ang II, which eventually leading to fibrosis.(Ghavami et al., 2015; Rudolph et al., 2015; Salvarani et al., 2017). Although it is not the only mechanism linking Ang II signaling and fibrosis, our study has found that Apelin could interrupt this vicious circle by mediating with Smad2-related suppression of myofibroblast differentiation, exerting the anti-fibrotic effect (**Figure 6**).

VALUE (Schmieder et al., 2008) and Val-HeFT (Maggioni et al., 2005) studies found that valsartan could reduce the incidence and recurrence rate of AF, but its underlying mechanism is unclear. In addition, Ellinor et al. (2006) have shown that valsartan could increase the plasma levels of apelin expression *in vivo*. It is unclear as to whether this effect of valsartan is achieved by the action of apelin. This is further confirmed by our present study results: valsartan increases the level of apelin *in vivo* and then inhibits Ang II-induced atrial fibrosis and subsequent vulnerability to AF. However, some studies (GISSI-AF Investigators et al., 2009) demonstrated that no significant improvement was observed in the prognosis of AF patients after using ARB drugs. The possible reason is that the beneficial influence of ARB is hard to work on the irreversible atrial remodeling.

Meanwhile, Parikh et al. (2013) found that the plasma Apelin level was significantly decreased in AF patients,

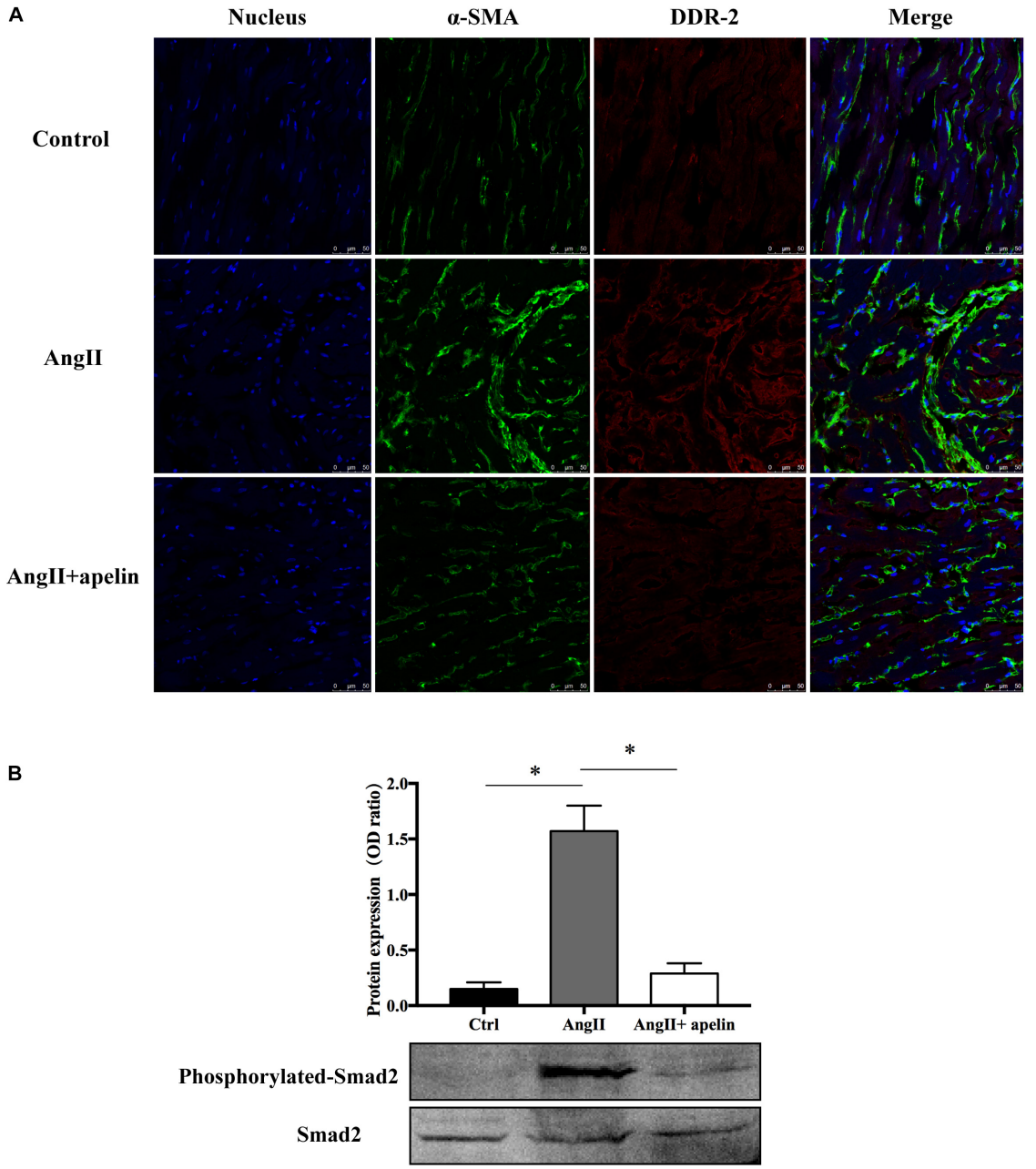

FIGURE 4 | Apelin inhibits fibrosis by inhibiting TGF-β1/Smad2/α-SMA pathway. **(A)** DDR2/a-SMA co-staining of murine atrial sections showed a significant higher amount of fibrosis in the atrial tissue of Ang II group compared with the control group, while apelin treatment reduced the fibrosis to the level of animals in the control group. Scale bar indicates 50 μm. **(B)** Apelin reduces TGF-β1-induced phosphorylation of Smad2, as detected by western blot. *$P < 0.001$ ($n = 16$ in each group).

which may be due to the disruption of apelin levels in atrial endocrine function during AF. If the above hypothesis is true, then apelin acts as a key factor, preventing the occurrence and development of AF. The decreased apelin levels in AF may be an underlying key factor that intervenes in the remodeling mechanisms leading to the phenomenon of "AF begets AF." Therefore, based on the above theory, supplementation of apelin in AF cohort might disrupt the vicious cycle.

LIMITATION

Our study has few limitations. Firstly, the mechanisms of AF are complex and unclear in clinical, we used a murine model of AF, and limitations occur when translating the present findings to human. Nevertheless, the key points of the present study were to evaluate the effect of apelin on atrial fibrosis and subsequent AF, for which the murine models have been widely used. Secondly, we did not evaluate the effect of apelin on Ang II-induced

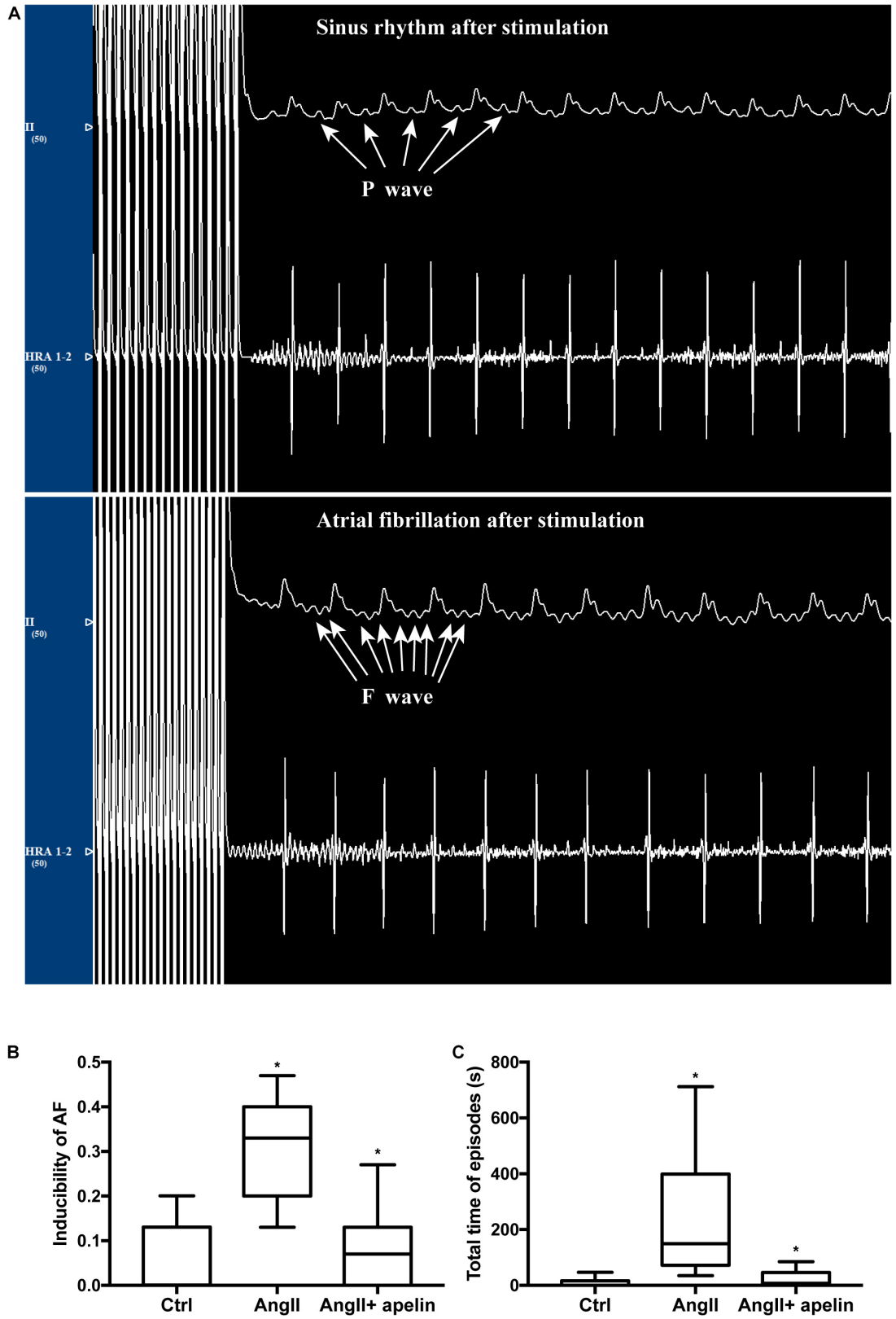

FIGURE 5 | Apelin attenuatation elevated AF vulnerability. **(A)** Representative figures of ECGs with and without atrial fibrillation episodes after stimulation. ECG interference caused by stimulus current could not be ruled out. **(B,C)** Ang II treatment led to a distinct elevation of inducibility of AF and the total time of AF episodes, whereas in the Ang II + apelin group, the inducibility of AF and total time of AF episodes are significantly decreased. *$P < 0.001$ ($n = 16$ in each group).

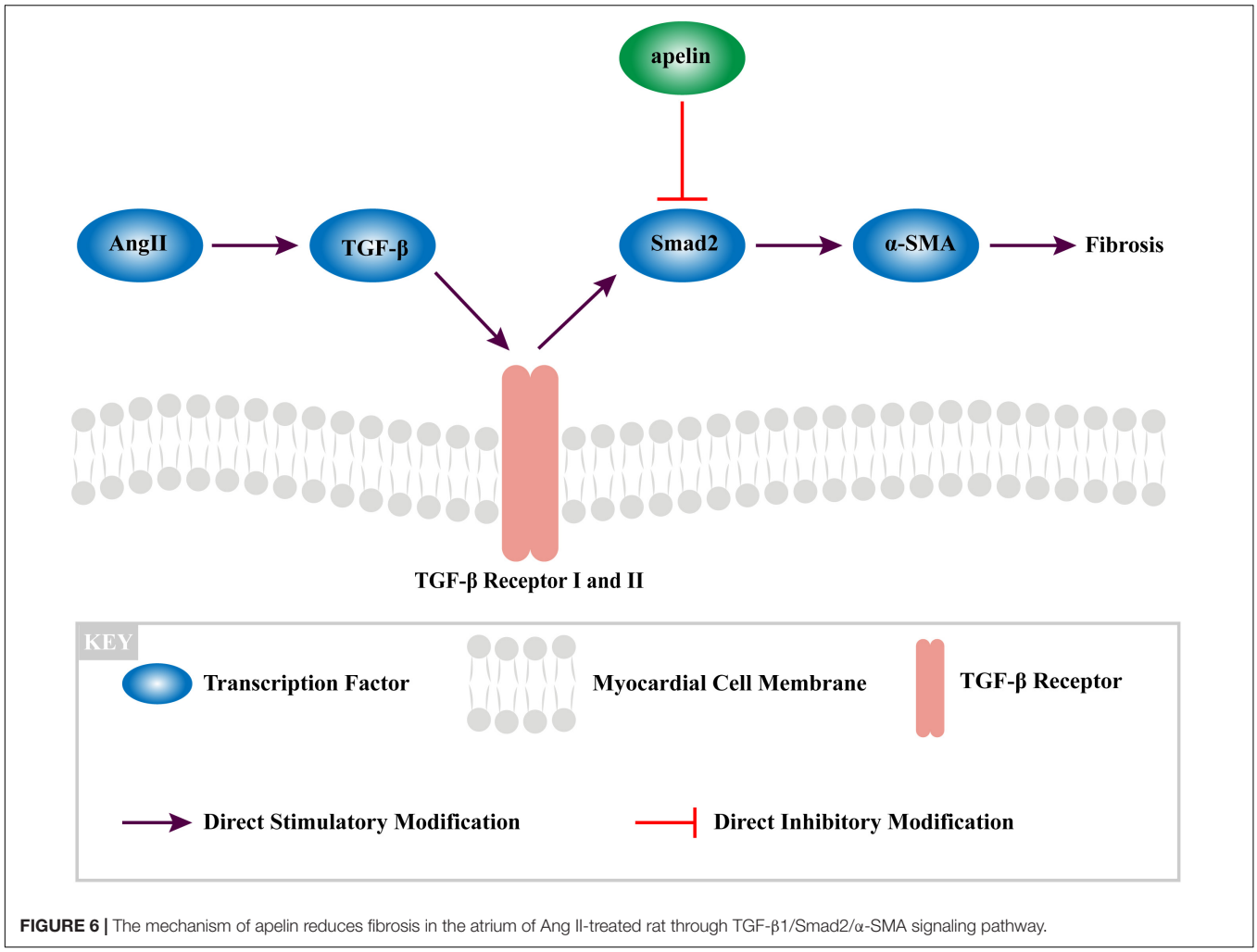

FIGURE 6 | The mechanism of apelin reduces fibrosis in the atrium of Ang II-treated rat through TGF-β1/Smad2/α-SMA signaling pathway.

atrial remodeling in dose-dependent manner. In future studies, various doses of apelin should be taken into consideration to further elucidate whether the inhibitory effect of apelin on atrial remodeling was dose-dependent. Thirdly, although apelin can prevent fibrosis, the fibrosis may not be reversed when it already exists. Therefore, for patients with persistent AF who already have severe atrial fibrosis, whether apelin has ideal effect needs to be further verified.

CLINICAL APPLICATION

Our findings suggested that apelin may be an effective up-stream treatment for atrial fibrosis. Further researches on the clinical use of apelin are necessary.

CONCLUSION

In recent years, many scholars have carried out in-depth researches on the treatment of atrial fibrosis and AF (Adam et al., 2015; Chen et al., 2015; Henry et al., 2015; Jalife and Kaur, 2015). But up to now, there is no effective treatment to inhibit atrial fibrosis (Dzeshka et al., 2015; Van Wagoner et al., 2015; Lüscher, 2017), however, apelin may serve as an effective upstream therapy for this unmet clinical need. In the current study, we found that apelin potently inhibits Ang II-induced atrial fibrosis and subsequent vulnerability to AF via supression of TGF-β1/Smad2/α-SMA pathway.

DATA AVAILABILITY STATEMENT

The original contributions presented in the study are included in the article/**Supplementary Material**, further inquiries can be directed to the corresponding author/s.

ETHICS STATEMENT

The use of animals and all procedures were in agreement with the Guide for the Care and Use of Laboratory Animals (NIH Publication 2011, eighth edition) and were approved by the Animal Care and Use Committee of the Xinjiang Medical University.

AUTHOR CONTRIBUTIONS

BT and XZ: work design. WL and LZ: experiments and data collection. XC, HW, and WQ: write the manuscript. All authors contributed to the article and approved the submitted version.

FUNDING

This work was supported by the National Natural Science Foundation of the People's Republic of China (grant nos. 81873488 and 81860067) and the Regional Natural Science Foundation of Xinjiang Uygur Autonomous Region (grant no. 2016D01C299).

SUPPLEMENTARY MATERIAL

The Supplementary Material for this article can be found online at: https://www.frontiersin.org/articles/10.3389/fphys.2020.583570/full#supplementary-material

REFERENCES

Adam, O., Zimmer, C., Hanke, N., Hartmann, R. W., Klemmer, B., Böhm, M., et al. (2015). Inhibition of aldosterone synthase (CYP11B2) by torasemide prevents atrial fibrosis and atrial fibrillation in mice. *J. Mol. Cell. Cardiol.* 85, 140–150. doi: 10.1016/j.yjmcc.2015.05.019

Andrade, J., Khairy, P., Dobrev, D., and Nattel, S. (2014). The clinical profile and pathophysiology of atrial fibrillation. *Circulat. Res.* 114, 1453–1468. doi: 10.1161/circresaha.114.303211

Cao, J., Li, H., and Chen, L. (2015). Targeting drugs to APJ receptor: the prospect of treatment of hypertension and other cardiovascular diseases. *Curr. Drug Targets* 16, 148–155. doi: 10.2174/1389450115666141128120053

Chagnon, F., Coquerel, D., Salvail, D., Eric, M., Robert, D., Mannix, A.-M., et al. (2017). Apelin compared with dobutamine exerts cardioprotection and extends survival in a rat model of endotoxin-induced myocardial dysfunction. *Crit. Care Med.* 45, e391–e398.

Chen, X.-Q., Liu, X., Wang, Q.-X., Zhang, M. J., Guo, M., Liu, F., et al. (2015). Pioglitazone inhibits angiotensin II-induced atrial fibroblasts proliferation via NF-κβ/TGF-β1/TRIF/TRAF6 pathway. *Exp. Cell Res.* 330, 43–55. doi: 10.1016/j.yexcr.2014.08.021

Dzeshka, M. S., Lip, G. Y., Snezhitskiy, V., and Shantsila, E. (2015). Cardiac fibrosis in patients with atrial fibrillation: mechanisms and clinical implications. *J. Am. Coll. Cardiol.* 66, 943–959.

Ellinor, P. T., Low, A. F., and Macrae, C. A. (2006). Reduced apelin levels in lone atrial fibrillation. *Eur. Heart J.* 27, 222–226. doi: 10.1093/eurheartj/ehi648

Ghavami, S., Cunnington, R., Gupta, S., Yeganeh, B., Filomeno, K. L., Freed, D. H., et al. (2015). Autophagy is a regulator of TGF-β1-induced fibrogenesis in primary human atrial myofibroblasts. *Cell Death Dis.* 6:e1696. doi: 10.1038/cddis.2015.36

GISSI-AF Investigators, Latini, R., Barlera, S., Franzosi, M. G., and Staszewsky, L. (2009). Valsartan for prevention of recurrent atrial fibrillation. *N. Engl. J. Med.* 360, 1606–1617. doi: 10.1056/nejmoa0805710

Heijman, J., Voigt, N., Nattel, S., and Dobrev, D. (2014). Cellular and molecular electrophysiology of atrial fibrillation initiation, maintenance, and progression. *Circulat. Res.* 114, 1483–1499. doi: 10.1161/circresaha.114.302226

Henry, B., Gabris, B., Li, Q., Martin, B., Giannini, M., Parikh, A., et al. (2015). Relaxin suppresses atrial fibrillation in 24 month old rats by reversing atrial fibrosis and upregulating sodium channels. *J. Am. Coll. Cardiol.* 65:A380.

Hu, Y.-F., Chen, Y.-J., Lin, Y.-J., and Chen, S.-A. (2015). Inflammation and the pathogenesis of atrial fibrillation. *Nat. Rev. Cardiol.* 12, 230–243. doi: 10.1038/nrcardio.2015.2

Huang, S., Chen, L., Lu, L., and Li, L. (2016). The apelin–APJ axis: a novel potential therapeutic target for organ fibrosis. *Clin. Chim. Acta* 456, 81–88. doi: 10.1016/j.cca.2016.02.025

Jalife, J., and Kaur, K. (2015). Atrial remodeling, fibrosis, and atrial fibrillation. *Trends Cardiovas. Med.* 25, 475–484. doi: 10.1016/j.tcm.2014.12.015

Li, D., Fareh, S., Leung, T. K., and Nattel, S. (1999). Promotion of atrial fibrillation by heart failure in dogs : atrial remodeling of a different sort. *Circulation* 100, 87–95. doi: 10.1161/01.cir.100.1.87

Lüscher, T. F. (2017). Atrial fibrillation beyond the arrhythmia: hypercoagulability, adipose tissue, and fibrotic remodelling. *Eur. Heart J.* 38, 1–3. doi: 10.1093/eurheartj/ehw674

Maggioni, A. P., Latini, R., Carson, P. E., Singh, S. N., Barlera, S., Glaze, R., et al. (2005). Valsartan reduces the incidence of atrial fibrillation in patients with heart failure: results from the Valsartan Heart Failure Trial (Val-HeFT). *Am. Heart J.* 149, 548–557. doi: 10.1016/j.ahj.2004.09.033

Marsault, E., Llorens -Cortes, C., Iturrioz, X., Chun, H. J., Lesur, O., Oudit, G. Y., et al. (2019). The apelinergic system: a perspective on challenges and opportunities in cardiovascular and metabolic disorders [J]. *Ann. N. Y. Acad. Sci.* 1455, 12–33. doi: 10.1111/nyas.14123

Nattel, S., and Harada, M. (2014). Atrial remodeling and atrial fibrillation: recent advances and translational perspectives. *J. Am. Coll. Cardiol.* 63, 2335–2345.

Opacic, D., van Bragt, K. A., Nasrallah, H. M., Schotten, U., and Verheule, S. (2016). Atrial metabolism and tissue perfusion as determinants of electrical and structural remodelling in atrial fibrillation. *Cardiovasc. Res.* 109, 527–541. doi: 10.1093/cvr/cvw007

Parikh, A., Patel, D. R., McTiernan, C. F., Xiang, W., Haney, J., Yang, L., et al. (2013). Relaxin suppresses atrial fibrillation by reversing fibrosis and myocyte hypertrophy, and increasing conduction velocity and sodium current in spontaneously hypertensive rat hearts. *Circulat. Res.* 113:301646.

Piek, A., de Boer, R., and Silljé, H. (2016). The fibrosis-cell death axis in heart failure. *Heart Fail. Rev.* 21, 199–211. doi: 10.1007/s10741-016-9536-9

Rosin, N. L., Falkenham, A., Sopel, M. J., Lee, T. D., and Légaré, J.-F. (2013). Regulation and role of connective tissue growth factor in AngII-induced myocardial fibrosis. *Am. J. Pathol.* 182, 714–726. doi: 10.1016/j.ajpath.2012.11.014

Rudolph, T. K., Ravekes, T., Klinke, A., Kai, F., Martin, M., Michaela, P., et al. (2015). Nitrated fatty acids suppress angiotensin II-mediated fibrotic remodelling and atrial fibrillation. *Cardiovasc. Res.* 109, 174–184. doi: 10.1093/cvr/cvv254

Rudolph, V., Andrié, R. P., Rudolph, T. K., Kai, F., Anna, K., Birgit, H.-H., et al. (2010). Myeloperoxidase acts as a profibrotic mediator of atrial fibrillation. *Nat. Med.* 16, 470–474. doi: 10.1038/nm.2124

Salvarani, N., Maguy, A., De Simone, S. A., Miragoli, M., Jousset, F., and Rohr, S. (2017). TGF-β 1 (Transforming Growth Factor-β 1) plays a pivotal role in cardiac myofibroblast arrhythmogenicity. *Circulation* 10:e004567.

Schmieder, R. E., Kjeldsen, S. E., Julius, S., Gordon, T. M., Alberto, Z., Hua, T. A., et al. (2008). Reduced incidence of new-onset atrial fibrillation with angiotensin ? receptor blockade: the VALUE trial. *J. Hypertens* 26, 403–411. doi: 10.1097/hjh.0b013e3282f35c67

Scimia, M. C., Hurtado, C., Ray, S., Scott, M., Ke, W., Jianming, W., et al. (2012). APJ acts as a dual receptor in cardiac hypertrophy. *Nature* 488, 394–398. doi: 10.1038/nature11263

Shinagawa, K. (2002). Dynamic nature of atrial fibrillation substrate during development and reversal of heart failure in dogs. *Circulation* 105, 2672–2678. doi: 10.1161/01.cir.0000016826.62813.f5

Van Wagoner, D. R., Piccini, J. P., Albert, C. M., Anderson, M. E., Benjamin, E. J., Brundel, B., et al. (2015). Progress toward the prevention and treatment of atrial fibrillation: a summary of the Heart Rhythm Society Research Forum on the Treatment and Prevention of Atrial Fibrillation, Washington, DC, December 9–10, 2013. *Heart Rhythm* 12:e5. doi: 10.1016/j.hrthm.2014.11.011

Weber, K. T., Sun, Y., Bhattacharya, S. K., Ahokas, R. A., and Gerling, I. C. (2013). Myofibroblast-mediated mechanisms of pathological remodelling of the heart. *Nat. Rev. Cardiol.* 10, 15–26. doi: 10.1038/nrcardio.2012.158

Xu, S., Li, Z., Jiang, H., Wu, H. B., Tao, D. S., Han, J. S., et al. (2016). Relationship between apelin and new-onset atrial fibrillation after coronary artery bypass grafting: a prospective cohort study and retrospective case-control clinical trial. *Clin. Trials Degenerat. Dis.* 1:58. doi: 10.4103/2468-5658.184745

Zhong, J.-C., Zhang, Z.-Z., Wang, W., McKinnie, S. M., Vederas, J. C., and Oudit, G. Y. (2017). Targeting the apelin pathway as a novel therapeutic approach for cardiovascular diseases. *Biochim. Biophys. Acta (BBA) Mol. Basis Dis.* 1863, 1942–1950. doi: 10.1016/j.bbadis.2016.11.007

Conflict of Interest: The authors declare that the research was conducted in the absence of any commercial or financial relationships that could be construed as a potential conflict of interest.

frontiers in Physiology

ORIGINAL RESEARCH
published: 26 November 2020
doi: 10.3389/fphys.2020.575846

Comparison of Unipolar and Bipolar Voltage Mapping for Localization of Left Atrial Arrhythmogenic Substrate in Patients With Atrial Fibrillation

Deborah Nairn[1†], Heiko Lehrmann[2†], Björn Müller-Edenborn[2], Steffen Schuler[1], Thomas Arentz[2], Olaf Dössel[1], Amir Jadidi[2†] and Axel Loewe[1†]*

[1] Institute of Biomedical Engineering, Karlsruhe Institute of Technology (KIT), Karlsruhe, Germany, [2] Department of Electrophysiology, University-Heart-Center Freiburg-Bad Krozingen, Bad Krozingen, Germany

OPEN ACCESS

Edited by:
Sanjiv M. Narayan,
Stanford University, United States

Reviewed by:
Prasanth Ganesan,
Stanford University, United States
Vijay S. Chauhan,
Peter Munk Cardiac Centre, Canada

***Correspondence:**
Deborah Nairn
publications@ibt.kit.edu

[†] These authors have contributed equally to this work

Specialty section:
This article was submitted to Cardiac Electrophysiology, a section of the journal Frontiers in Physiology

Received: 24 June 2020
Accepted: 20 October 2020
Published: 26 November 2020

Citation:
Nairn D, Lehrmann H, Müller-Edenborn B, Schuler S, Arentz T, Dössel O, Jadidi A and Loewe A (2020) Comparison of Unipolar and Bipolar Voltage Mapping for Localization of Left Atrial Arrhythmogenic Substrate in Patients With Atrial Fibrillation. Front. Physiol. 11:575846. doi: 10.3389/fphys.2020.575846

Background: Presence of left atrial low voltage substrate in bipolar voltage mapping is associated with increased arrhythmia recurrences following pulmonary vein isolation for atrial fibrillation (AF). Besides local myocardial fibrosis, bipolar voltage amplitudes may be influenced by inter-electrode spacing and bipole-to-wavefront-angle. It is unclear to what extent these impact low voltage areas (LVA) in the clinical setting. Alternatively, unipolar electrogram voltage is not affected by these factors but requires advanced filtering.

Objectives: To assess the relationship between bipolar and unipolar voltage mapping in sinus rhythm (SR) and AF and identify if the electrogram recording mode affects the quantification and localization of LVA.

Methods: Patients (n = 28, 66±7 years, 46% male, 82% persistent AF, 32% redo-procedures) underwent high-density (>1,200 sites, 20 ± 10 sites/cm^2, using a 20-pole 2-6-2 mm-spaced Lasso) voltage mapping in SR and AF. Bipolar LVA were defined using four different thresholds described in literature: <0.5 and <1 mV in SR, <0.35 and <0.5 mV in AF. The optimal unipolar voltage threshold resulting in the highest agreement in both unipolar and bipolar mapping modes was determined. The impact of the inter-electrode distance (2 vs. 6 mm) on the correlation was assessed. Regional analysis was performed using an 11-segment left atrial model.

Results: Patients had relevant bipolar LVA (23 ± 23 cm^2 at <0.5 mV in SR and 42 ± 26 cm^2 at <0.5 mV in AF). 90 ± 5% (in SR) and 85 ± 5% (AF) of mapped sites were concordantly classified as high or low voltage in both mapping modes. Discordant mapping sites located to the border zone of LVA. Bipolar voltage mapping using 2 vs. 6 mm inter-electrode distances increased the portion of matched mapping points by 4%. The unipolar thresholds (y) which resulted in a high spatial concordance can be calculated from the bipolar threshold (x) using following linear equations: $y = 1.06x + 0.26\,mV$ ($r = 0.994$) for SR and $y = 1.22x + 0.12\,mV$ ($r = 0.998$) for AF.

Conclusion: Bipolar and unipolar voltage maps are highly correlated, in SR and AF. While bipole orientation and inter-electrode spacing are theoretical confounders, their impact is unlikely to be of clinical importance for localization of LVA, when mapping is performed at high density with a 20-polar Lasso catheter.

Keywords: atrial fibrillation, bipolar voltage mapping, unipolar voltage mapping, arrhythmogenic substrate, low voltage areas

1. INTRODUCTION

Atrial fibrillation (AF) is the most common supraventricular cardiac arrhythmia characterized by an irregular heart rhythm and associated with an increased risk of heart failure, stroke, and mortality (Wang et al., 2003; Miyasaka et al., 2005; Go et al., 2014).

Pulmonary veins have been identified as major arrhythmogenic trigger sites for AF. Therefore, their isolation has become a widely used and effective treatment for AF (Haissaguerre et al., 1998). However, additional arrhythmogenic atrial substrate is present in 30–50% of persistent AF patients and may be responsible for the maintenance of the arrhythmia, resulting in increased AF recurrences after pulmonary vein isolation (PVI) in these patients (Verma et al., 2005, 2015). Procedural identification of arrhythmogenic AF sources with rapid, continuous, or repeated rotational activity has revealed their localization within fibrotic regions displaying low bipolar voltage <0.5 mV during AF (Jadidi et al., 2016, 2020; Seitz et al., 2017). Ablation of these atrial AF sources, in addition to PVI, improves the success rate in persistent AF patients from 30 to 50% with PVI only to 70% with additional selective ablation of arrhythmogenic low voltage areas (LVA) (Rolf et al., 2014; Jadidi et al., 2016; Blandino et al., 2017; Seitz et al., 2017).

Atrial arrhythmogenic fibrosis-rich areas are currently identified using imaging or bipolar voltage mapping. However, in addition to the underlying atrial fibrosis that affects the bipolar voltage (peak-to-peak amplitude of the electrogram), the angle of the bipolar recording electrodes (wavefront-to-bipole orientation), the distance between the electrodes and the electrode size may also influence the bipolar electrogram amplitudes (Schuler et al., 2013; Anter et al., 2015; Beheshti et al., 2018; Lin et al., 2018; Gaeta et al., 2019). Therefore, using bipolar electrograms can potentially cause areas of fibrotic and non-fibrotic tissue to be misclassified. On the other hand, unipolar electrogram voltage is unaffected by the catheter orientation and electrode distances. However, the signals are more susceptible to noise and ventricular far-field requiring advanced filtering (Frisch et al., 2020).

We aim to assess the differences in the extent and distribution of atrial LVA when comparing bipolar to unipolar voltage mapping in AF and sinus rhythm (SR). In this work, we evaluate the correlation between the two mapping methods and identify the corresponding unipolar thresholds that yield the highest concordance to the bipolar LVA. Additionally, we examine the impact of (1) the electrode distance, (2) the anatomical region of the left atrium, and (3) the extent of left atrial (LA) low voltage substrate on the correlation between unipolar and bipolar LVA.

2. METHODS

2.1. Study Cohort and Electro-Anatomical Mapping

A total of 28 patients with AF underwent high-density (>1,200 mapped sites per LA and rhythm, mapping density of 17 ± 7 sites per cm^2 in SR and 22 ± 11 per cm^2 in AF) voltage mapping using a 20-pole variable (15–20 mm diameter) Lasso-Nav mapping catheter (electrode size: 1 mm; spacing: 2-6-2 mm). The voltage mapping was performed using CARTO-3 (Biosense Webster, Diamond Bar, CA, USA) and carried out in both rhythms SR and AF prior to PVI. Bipolar voltage maps were acquired using all electrode spacings (2 and 6 mm). Patients were mapped first in the rhythm that they presented in and then cardioverted into SR or induced into AF to obtain the second map. 21/28 patients presented with clinical persistent AF, the remaining had SR at presentation. Nine of the 28 (32%) patients underwent a redo AF ablation procedure after a previous PVI procedure. The remaining 19 (68%) patients came for their first AF ablation procedure.

Electrograms recorded >7 mm from the geometry surface were excluded from the analysis to avoid poor contact points. Additionally, points containing only noise or pacing artifacts were removed based on manual assessment. The unipolar signals were processed by the Carto3 software, which uses standard clinical filtering with highpass and lowpass cutoff frequencies at 2 and 240 Hz to remove high and low frequency noise from the acquired EGM. Additionally, a notch filter was applied to clear the noise from the environment power lines. For the unipolar recordings Wilson's Central Terminal (WCT) was used as the reference electrode. Additionally, bandpass filtering was performed at 16–500 Hz for the bipolar signals. A window of interest was defined prior to the QRS complex to identify atrial activity and the voltage provided by CARTO-3 was obtained by taking the peak-to-peak value (local maximum − local minimum) of a single atrial beat in a 2.5 s second recording interval. This beat was identified to be, typically, the largest or second-largest beat in the signal, where the spread in the voltage within the time window differed in a range of 0–0.2 mV. A color interpolation of voltage values between the recorded electrode positions of <7 mm was then applied to the geometry automatically by CARTO-3.

2.2. Voltage Mapping in Sinus Rhythm

The QRS complex was excluded from the window-of-interest during LA voltage mapping. LVA were defined using cut-off values for bipolar peak-to-peak voltage in SR of <0.5 or <1.0 mV (Jadidi et al., 2016; Rodríguez-Mañero et al., 2018). Areas demonstrating low voltage when mapped with the 20-pole Lasso catheter were confirmed using a contact force-sensing mapping catheter with a contact threshold of >5 g.

2.3. Voltage Mapping in Atrial Fibrillation

Patients underwent voltage mapping in AF using the sharp peak in the surface QRS as the reference. The QRS complex was then excluded from the window-of-interest during LA voltage mapping. To ensure the highest accuracy of electrogram criteria, >1,200 points were acquired per LA and rhythm. Respiratory gating was performed and the atrial geometry was acquired at high adjustment settings (geometry acquisition by Lasso catheter was set to 18 on CARTO-3) to obtain the highest accuracy of the acquired atrial geometry. Presence and accurate localization of low voltage areas was confirmed by contact force-sensing catheters (>5 g). Bipolar low voltage zones were defined as <0.35 or <0.5 mV in AF, according to the findings in recent studies (Jadidi et al., 2016, 2020; Rodríguez-Mañero et al., 2018).

The voltage was defined as the peak-to-peak amplitude of a single AF beat. In AF, the window of interest was set to 90% of the mean AF cycle length in order to consider only a single AF beat. This beat was manually selected with special emphasis on having only a single depolarization wavefront (AF beat). The current voltage mapping software of CARTO-3.7 does not support automatic voltage mapping during AF. Use of the automatic CARTO-3 software for voltage mapping in AF may result in mapped sites without any underlying electrogram (including the isolelectric intervals only) or including multiple AF beats with inadequate peak-to-peak voltage measurements. Therefore, in the current study, AF voltage maps were acquired manually.

2.4. Analysis

To identify the correlation between the unipolar and bipolar maps, the sensitivity, and specificity were calculated. The bipolar map was considered as the "true condition" and the electrogram at each point of the unipolar map was classified depending on the unipolar voltage threshold. Points labeled as low voltage in the (ground truth) bipolar map were identified as true positive (unipolar voltage < threshold) or false negative (unipolar voltage > threshold) in the unipolar map. True negative and false positive classes were similarly defined for the points with a supra-threshold voltage in the bipolar map. The unipolar threshold was then varied between 0.1 and 4 mV, and a receiver operating characteristic (ROC) curve was created to identify the unipolar threshold which provides the best match to the bipolar map for each patient and rhythm.

The relationship between unipolar and bipolar voltage was further explored by examining the percentage of points on the maps, which were classified the same in both cases (low or high voltage). This analysis was performed based on the voltage map provided by CARTO-3 (interpolated map data). The data from the electrograms at the mapping sites were used directly to analyze the effect of inter-electrode spacing.

For each patient, the best unipolar threshold corresponding to a specific bipolar threshold was identified using the ROC curve. Using one common unipolar threshold for all patients rather than an individual threshold for each patient was evaluated and analyzed by calculating the percentage of points that matched in unipolar and bipolar.

Regional differences in the voltage have been found in patients, with the anteroseptal LA wall and roof displaying the common and most extensive LVA, followed by the posterior LA wall (Marcus et al., 2007; Müller-Edenborn et al., 2019). To examine what effect the regional differences may have on the correlation between unipolar and bipolar LVA, each LA was split into 11 anatomical regions. The regions are as follows: orifices to the four pulmonary veins (LIPV, LSPV, RIPV, RSPV), the region around the mitral valve (MV), the left atrial appendage (LAA), the anterior, posterior, and lateral wall, the roof, and the septum. The percentage of points which matched between the unipolar and bipolar map were calculated for each anatomical region, using the bipolar threshold of 0.5 mV in SR and 0.35 mV in AF and the best corresponding unipolar threshold for each patient, which range between 0.62 and 1.1 mV (SR) and 0.45 and 0.99 mV (AF).

A factor that may influence the correlation between bipolar and unipolar mapping is the level of low voltage substrate in patients. Therefore, the 28 patients were split into four subgroups depending on the extent of low voltage (<0.5 mV during SR in the bipolar map). The low voltage substrate extent was then determined as the percentage of the surface area. Each patient was categorized into one of the four groups: stage I (<5%), II (≥5% to <20%), III (≥20% to <30%) and IV (≥30%) as suggested by Oakes et al. (2009) and Yamaguchi et al. (2018). The match between unipolar and bipolar classification was then calculated for each category, in both rhythms.

The distance between the bipolar electrodes is known to affect the bipolar signals (voltage increases as the distance increases) (Beheshti et al., 2018). Several studies have examined this effect concerning the influence it may have on the identification of LVA (Anter et al., 2015; Mori et al., 2018). Thus, the data provided by CARTO-3 were split into three groups: (1) containing only information from the 2 mm electrode distances, (2) only 6 mm distances, and (3) containing both. The percentage of points that matched between unipolar and bipolar was then calculated, and the paired-sample *t*-test was used to calculate if the difference between the three sets was significant.

3. RESULTS

3.1. Patient Characteristics

Twenty-eight patients (66 ± 7 years old, 46% male, 82% persistent AF, 32% redo-procedures) underwent high-density (>1,200 sites, with a mapping density of 17 ± 7 sites per cm^2 in SR and 22 ± 11 per cm^2 in AF, using a 20-polar 2-6-2 mm-spaced Lasso, CARTO-3) voltage mapping in SR and AF prior to PVI. Further details on patients' characteristics are provided

TABLE 1 | Patient clinical demographics.

Patient characteristics	Total = 28
Rhythm at presentation (AF, %)	21 (75)
Persistent AF (%)	23 (82)
Age	66 ± 7
Male, *n* (%)	13 (46)
BMI (kg/m^2)	28 ± 4
Weight (kg)	84 ± 13
LVEF (%)	54 ± 10
LA diameter (AP, mm)	46 ± 5
IVSEDD (mm)	10 ± 2
SHD (%)	12 (43)
CHA_2DS_2-VASc score	2.2 ± 1.8
Hypertension (%)	16 (57)
LV systolic dysfunction (<45%)	9 (32)
Diabetes (%)	4 (14)
Renal failure (GFR<50 ml/min, %)	8 (29)
History of stroke (%)	1 (3.6)
Coronary artery disease (%)	3 (11)
Antiarhythmic therapy except betablocker (%)	14 (50)
Beta blocker therapy (%)	21 (75)
Amiodarone (%)	6 (21)
Flecainide (%)	5 (18)
Sotalol (%)	1 (3.5)
Dronedarone (%)	2 (7)
Redo procedure for AF	9 (32)

LVEF, left ventricular ejection fraction; SHD, structural heart disease; LV, left ventricular; BMI, body mass index; GFR, glomerular filtration rate.

TABLE 2 | Mapping information of patients included in the study.

Electro-anatomical mapping	SR	AF
Low voltage surface area [cm^2 (%)] (SR and AF < 0.5 mV)	23 ± 23 (31 ± 30)	42 ± 26 (52 ± 30)
Map points (pts)	1,536 ± 608	1,978 ± 925
Map points after processing (pts)	1,200 ± 632	1,639 ± 754
Bipolar voltage (mV)	1.15 ± 0.67	0.54 ± 0.22
Unipolar voltage (mV)	1.44 ± 0.71	0.73 ± 0.23

in **Table 1**. Additionally, information on the electro-anatomical mapping across all patients is provided in **Table 2**.

3.2. Spatial Distribution of Left Atrial Low Voltage Areas in Unipolar vs. Bipolar Mapping

The three-dimensional distribution patterns of the bipolar vs. unipolar LVA were highly concordant for all analyzed voltage thresholds and in all patients. 90 ± 5 and 85 ± 5% of mapped sites in SR and AF, respectively, were concordantly classified as low or high voltage both in bipolar vs. unipolar mapping mode. Discordant mapping sites located to the border zone of LVA.

Figure 1 illustrates the three-dimensional distribution patterns of the bipolar vs. unipolar LVA for a single patient with electrogram examples. LVA were found at the same positions in the unipolar and bipolar maps using a unipolar threshold of 0.78 mV when the bipolar threshold was 0.5 mV. The classification map, in **Figure 1** lower panels, identifies mapping sites where the maps disagree with regard to LVA in unipolar vs. bipolar mode. Such areas with different classification of LVA were mostly located at border zones, where the myocardial voltage amplitudes are changing from low to high voltage. The difference between the selected threshold value to the voltage values of miss-classified electrograms was found to be 0.3 ± 0.1 mV. **Figure 2** shows similar results for bipolar vs. unipolar voltage maps acquired during AF. Additionally, the three-dimensional distribution patterns of LVA in unipolar and bipolar voltage maps are illustrated for all 28 patients in **Supplementary Figures 1**, **2**. In these figures, the Pearson correlation coefficient between the bipolar and unipolar voltage maps prior to applying a threshold is shown for each patient. For both rhythms the correlation was found to be 0.88 ± 0.05, indicating a strong positive correlation between the mapping modalities independent of a specific threshold.

3.3. Spatial Correlation Between Unipolar vs. Bipolar Voltage Mapping—Regional Analysis

The overall three-dimensional distribution patterns of LA LVA during SR and AF (**Supplementary Figures 1**, **2**) reveal a very high spatial concordance with very similar localization of LVA when comparing bipolar and the best correlated unipolar voltage thresholds. Further detailed regional quantification of the amount of concordant LVA classification between unipolar vs. bipolar voltage mapping is reported in **Figure 3**. The figure shows regional correlation results when splitting the LA into 11 anatomical regions. The mean percentage of concordantly categorized electrograms for each anatomical region divided by the number of electrograms within the same region (across all patients) is presented on an example geometry. Additionally, the mean and standard deviation values for each region can be seen in **Table 3**. For both rhythms, the LAA was one of the regions showing the highest agreement between the unipolar and bipolar voltage maps with 98% match in SR and 95% in AF. The pulmonary veins also display high agreement (93–96% SR and 94–97% AF). A slightly lower but still high regional similarity between the unipolar and bipolar maps was found within the body of the LA: LA posterior wall, anterior wall and the septum (90, 90, and 91% in SR and 87, 87, and 91% in AF). The high regional correlation between unipolar and bipolar voltage maps is well-reflected by the distribution of LVA patterns on the high-density interpolated electro-anatomical voltage maps (**Supplementary Figures 1**, **2**). Independently of the underlying rhythm, the three-dimensional localization of the arrhythmogenic LVA is highly concordant and designates the

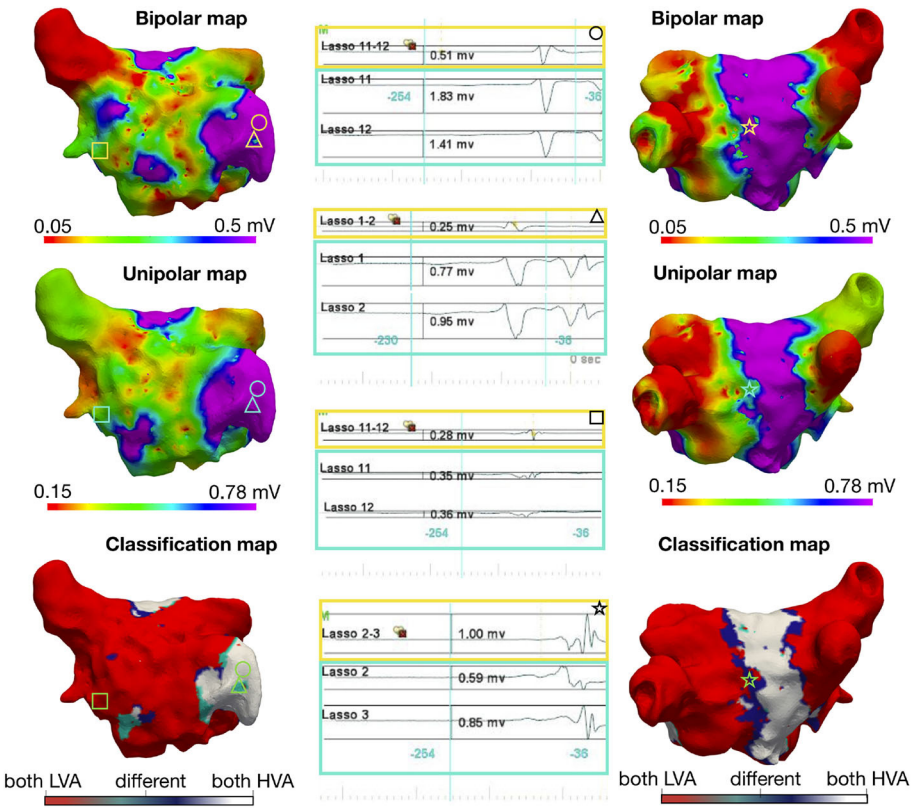

FIGURE 1 | Voltage mapping in sinus rhythm: Three-dimensional distribution of bipolar and unipolar LVA in a patient during SR with a bipolar threshold <0.5 mV. The top row indicates the bipolar map, the middle row shows the unipolar map, and the bottom row is a map of the point by point comparison between the two maps: if both points are below their indicated voltage thresholds (LVA), the point is colored red, if both are above [high voltage areas (HVA)] in white and with different classification (bipolar low voltage, unipolar high voltage) in dark-blue and (bipolar high voltage, unipolar low voltage) in turquoise. In the left column, the anterior view is shown and on the right the posterior view. Each geometric shape represents a point on the map where the corresponding signal is shown in the middle column. The upper unipolar threshold values were obtained by determining which threshold provided the best match of points between unipolar and bipolar. For visualization, the lower value was manually optimized to obtain the best visual match.

same regions as potential ablation targets in unipolar and bipolar voltage mapping mode.

3.4. The High Correlation Between Unipolar and Bipolar Voltage Maps Is Independent of the Underlying Extent of Low Voltage Substrate

The LA voltage maps of all 28 patients were categorized according to the extent of their LA low voltage substrate <0.5 mV in SR, as mentioned in section 2: seven patients in stage I, eight in stage II, five in stage III, and eight in stage IV. The low voltage surface area in SR at <0.5 mV bipolar threshold (mean ± standard deviation) in each group was: stage I: 3 ± 2%, stage II: 12 ± 5%, stage III: 27 ± 4%, stage IV: 37 ± 4%. The percentage of points that matched in the bipolar and unipolar voltage maps for patients with different levels of low voltage substrate is shown in **Supplementary Figure 3**. For all low-voltage substrate stages in both rhythms, the percentage of mapping points that matched was >85% (mean). The maximum difference between categories was 4%.

3.5. Specific Unipolar Voltage Thresholds Are Associated With High Correlation Between Unipolar vs. Bipolar Low Voltage Substrate

Figure 4 illustrates the ROC curves for the optimal unipolar voltage thresholds that result in the highest concordance of electrogram classifications to high and low voltage areas in both unipolar and bipolar maps for four previously described bipolar voltage thresholds. For each rhythm and voltage threshold, there was a high percentage of agreement (sensitivity and specificity >80% in all cases). The highest sensitivity and specificity values (93, 81%) were obtained when comparing the maps in SR using a bipolar threshold of 1 mV and a unipolar threshold of 1.31 mV. Sensitivity and specificity values were as follows for the other cases: SR with bipolar threshold of 0.5 mV (unipolar threshold 0.83 mV, 89%, 84%), AF 0.5 mV (unipolar 0.71 mV, 91%, 79%), and AF 0.35 mV (unipolar 0.54 mV, 85%, 82%).

To further examine the relationship between the bipolar and the unipolar voltage threshold, a set of SR and AF ROC curves were created for each bipolar threshold between 0.1 and

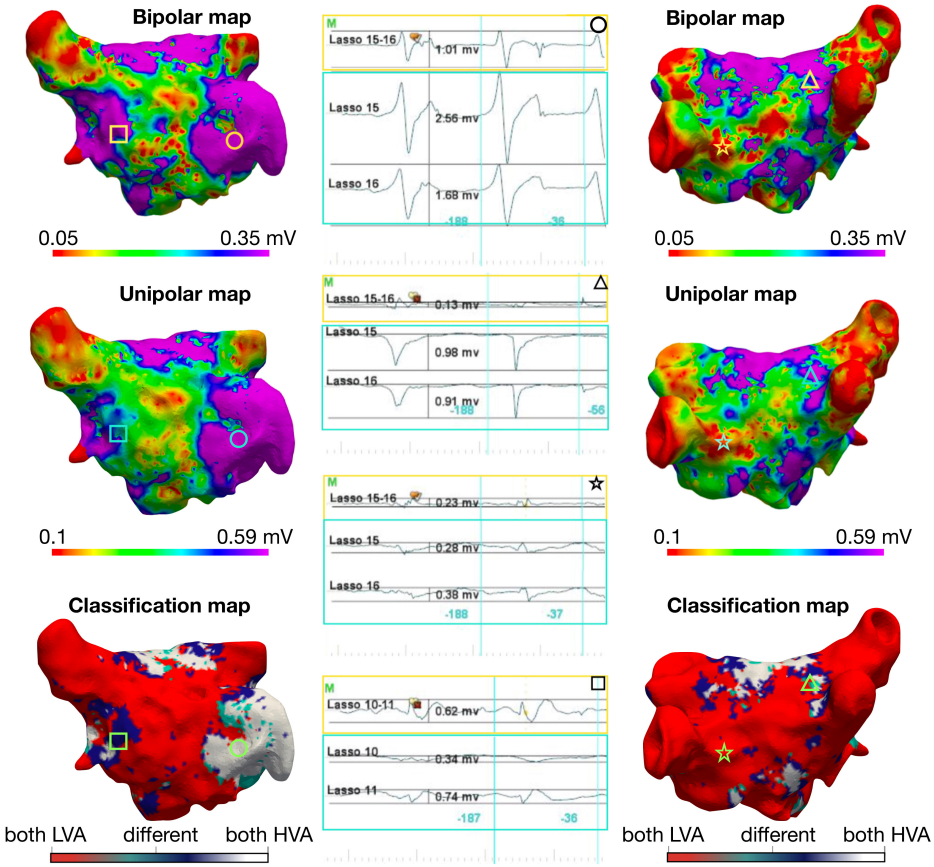

FIGURE 2 | Voltage mapping in atrial fibrillation: Three-dimensional distribution of bipolar and unipolar LVA in the same patient as **Figure 1** during AF with a bipolar threshold <0.35 mV. The top row indicates the bipolar map, the middle row shows the unipolar map, and the bottom row is a map of the point by point comparison between the two maps: if both points are below their indicated voltage thresholds (LVA), the point is colored red, if both are above [high voltage areas (HVA)] in white and with different classification (bipolar low voltage, unipolar high voltage) in dark-blue and (bipolar high voltage, unipolar low voltage) in turquoise. In the left column, the anterior view is shown and on the right the posterior view. Each geometric shape represents a point on the map where the corresponding signal is shown in the middle column. The electrogram marked with a triangle is an example of "voltage cancelation" in the bipolar recording (0.13 mV), while the voltages on both unipolar recordings are high (0.98 and 0.91 mV); this occurs because the unipolar electrograms have the same shape and same timing and their subtraction results in a near-zero bipolar voltage value.The upper unipolar threshold values was obtained by determining which threshold provided the best match of points between unipolar and bipolar. The lower value was selected manually to obtain the best visual match.

1 mV, in steps of 0.1 mV. In this way, the optimal unipolar threshold for each bipolar threshold was identified, which gave the highest classification match between the mapping modalities. The unipolar threshold values were then plotted against the bipolar threshold values, as shown in **Figure 5**. Linear regression yielded the following relations: $y = 1.06x + 0.26\,mV$ for SR and $y = 1.22x + 0.12\,mV$ for AF, where y is the unipolar threshold and x is the bipolar threshold in mV. The correlation coefficient between the two variables (bipolar and unipolar threshold) shows a strong positive correlation for both rhythms (0.994 in SR and 0.998 in AF). However, as there is spread between values for individual patients, the y-intercept cannot be as reliably determined as the slope of the relation. A simplified calculation of the corresponding unipolar threshold is provided by the addition of 0.3 vs. 0.2 mV to the bipolar voltage threshold in SR vs. AF, respectively (unipolar threshold error <0.07 mV in the bipolar threshold range between 0.1 and 1 mV).

3.6. Comparison of Unipolar and Bipolar Low Voltage Areas Using a Common vs. a Patient-Specific Unipolar Threshold

The difference between using one universal unipolar threshold for all patients (**Figure 4**), vs. patient-specific thresholds were evaluated to assess the variability in identifying low voltage areas. **Figure 6** illustrates that the increase in electrogram classification accuracy with the use of patient-specific vs. a common unipolar threshold is marginal (1–2%). For SR with a bipolar threshold 1 mV, the improvement in substrate classification changed from median of 92.7% using a common unipolar threshold to 92.9% using a patient-specific unipolar threshold. Using a Wilcoxon rank sum test, the difference between using one common threshold or individual thresholds was found to be not significant for either rhythm or bipolar threshold used. From **Figure 5** the best unipolar threshold for each patient can be seen in a

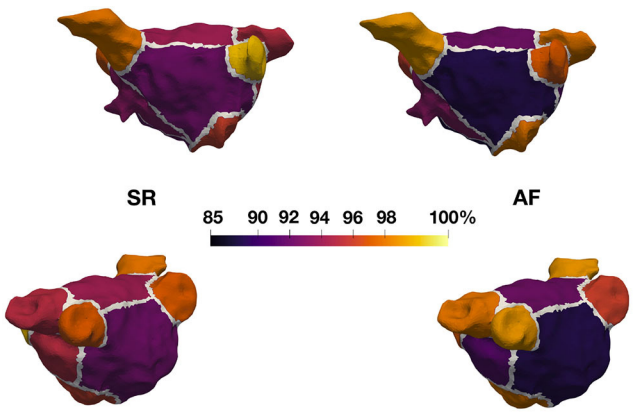

FIGURE 3 | Regional agreement of unipolar and bipolar substrate classification. Eleven anatomical regions were annotated in all 28 patient geometries and analyzed in SR and AF. Each region visualized on this example geometry is colored according to the mean percentage of concordantly categorized mapping sites (unipolar vs. bipolar voltage mapping) with regard to LVA.

TABLE 3 | Mean and standard deviation for the percentage of points that match in different anatomical regions of the LA [bipolar threshold of 0.5 mV in SR and 0.35 mV in AF and the best corresponding unipolar threshold for each patient, which range from 0.62 to 1.1 mV (SR) and 0.45 to 0.99 mV (AF)].

Anatomical region	SR (%)	AF (%)
LIPV	95 ± 6	97 ± 6
LSPV	93 ± 6	96 ± 3
RIPV	96 ± 6	97 ± 4
RSPV	95 ± 6	94 ± 7
MV	94 ± 5	96 ± 6
LAA	98 ± 3	95 ± 7
Anterior wall	90 ± 7	87 ± 8
Posterior wall	90 ± 8	87 ± 10
Lateral wall	93 ± 6	89 ± 7
Roof	92 ± 5	90 ± 7
Septum	91 ± 7	91 ± 7

range of 0.3 mV. However, the similarity between unipolar and bipolar mapping remains high regardless if a common threshold is used or a patient-specific one. This shows that within each patient, a classification margin exists of at most, ± 0.15 mV from the common threshold. Therefore, only a few data points have voltage values within this margin and are affected by changing the threshold in this range.

3.7. Impact of Bipolar Inter-electrode Distance on the Identified Low Voltage Substrate

We analyzed the impact of different inter-electrode distances on bipolar LVA distribution and its correlation to the corresponding unipolar voltage map. Therefore, LA electrograms were analyzed using each bipolar electrode distance (2, 6 mm and both) separately (see **Figure 7**). For both SR and AF, we found that when considering only the small bipoles (2 mm), 3–6% more mapping sites matched than when using the large bipoles (6 mm) or both together. Although the differences in LVA categorization remained small, they are statistically significant. Agreement of LVA categorization using the small bipoles was higher (SR 91%, AF 89% of mapping sites) than for mapping with the large or all bipoles in SR (88 and 87%) and in AF (83 and 85%) (p <0.001 for all cases). The optimal common unipolar threshold for each bipole distance is given in **Table 4**. The unipolar threshold for the all bipoles is slightly higher than reported in **Figure 5** (0.87 vs. 0.83 and 0.64 vs. 0.54 mV). This discrepancy is because this analysis was performed on the electrode signals directly rather than on the interpolated voltage map data. Only a 1% discrepancy in the median percentage of points that matched was seen when using the measured electrograms directly than the interpolated map data.

The best unipolar threshold for bipolar voltage maps (SR <0.5 mV) acquired with the small 2 mm distant electrode pairs was found to be higher (1.09 mV SR and 0.76 mV AF) than when using the large 6 mm distant electrode pairs (0.72 and 0.52 mV). **Supplementary Figure 4** shows the relationship between the bipolar and unipolar threshold when only using 2 mm bipoles (**Supplementary Figure 4A**) and 6 mm (**Supplementary Figure 4B**).

4. DISCUSSION

4.1. Main Findings

The current study on bipolar vs. unipolar voltage mapping reveals three main findings:

1. There is a high correlation in the spatial distribution of uni- and bipolar low voltage areas in sinus rhythm and atrial fibrillation.
2. Over 90% of LA electrograms are concordantly classified as high or low voltage using uni- or bipolar mode independently of the selected bipolar threshold. The remaining discordant electrograms locate to low voltage border zones without change of identified LVA.
3. Bipolar electrode distance has little impact on the agreement between unipolar and bipolar voltage maps.

Previous studies have suggested that diseased tissue can be identified in SR as bipolar voltage areas below 0.5 or 1 mV and similarly for AF with voltages below 0.35 or 0.5 mV (Jadidi et al., 2016; Yang et al., 2016; Rodríguez-Mañero et al., 2018). Our results reveal that for any given bipolar voltage threshold, a universal unipolar voltage threshold can be found that results in a highly similar unipolar voltage map with a spatial distribution of LA LVA that corresponds to the bipolar LVA. For a bipolar threshold of 0.5 mV in SR, a unipolar threshold of 0.83 mV was optimal. In AF, a unipolar threshold of 0.54 mV was found for a bipolar threshold of 0.35 mV. More generally, the unipolar threshold for identifying the same low voltage regions can be obtained by applying a linear transformation to the bipolar threshold being used. This threshold is dependent on the size of the bipolar electrode spacing (**Figure 5**, **Supplementary Figures 4A,B**). The linear regression

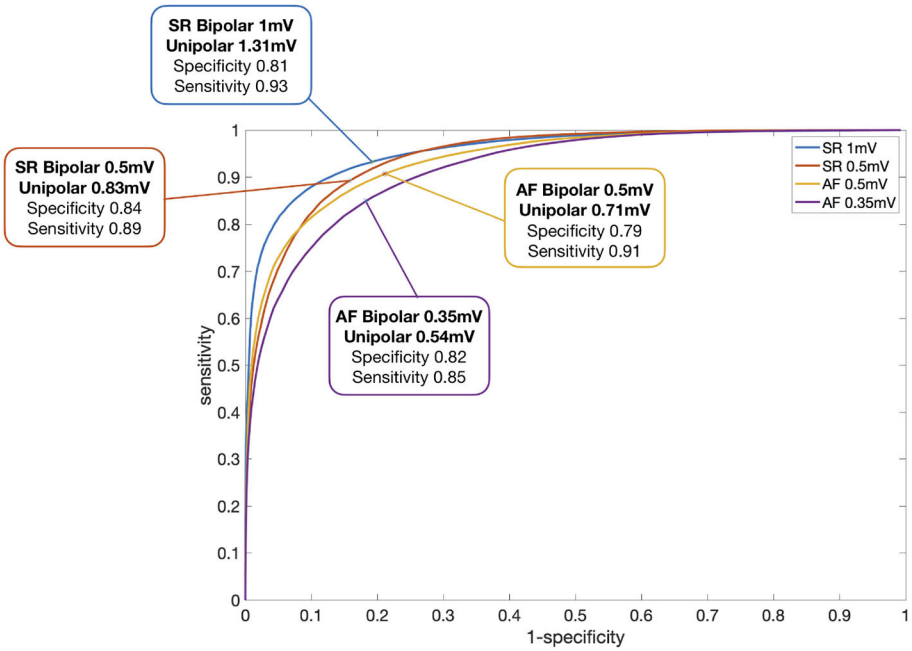

FIGURE 4 | ROC curve regarding identification of LVA for each rhythm and bipolar threshold. Each line represents the sensitivity and specificity for varying unipolar thresholds for the four different bipolar voltage thresholds that are reported in literature for SR and AF. The optimal unipolar thresholds for the corresponding bipolar thresholds were found for each patient and the median value of these patient specific thresholds is given in the figure.

lines describing the relationship differ between SR and AF, where lower unipolar thresholds were identified in AF than in SR. One possible reason for this can be that in AF, the propagation arrives at the electrodes from different directions. Therefore, the lower voltage values due to the catheter orientation are reduced in the bipolar AF map. Since there are fewer low voltage points, a lower unipolar threshold is needed to match the smaller bipolar low voltage areas.

Using patient-individual thresholds increases the agreement between unipolar and bipolar maps by up to 2%. In order to identify the optimal patient-specific unipolar threshold to a pre-selected bipolar threshold in clinical practice, the bipolar and unipolar voltage maps can be visualized side by side and the unipolar threshold can manually be adapted to a level at which the distribution of LVA show the best concordance/correlation to the bipolar voltage map. Our study revealed a very similar distribution of LVA during both mapping modes. Therefore, the utility of a unipolar voltage map beyond the bipolar map has to be assessed in future studies, eventually evaluating these correlations for other mapping catheters.

These high levels of correlation between the unipolar and bipolar map were seen in all four patient subgroups defined by the low voltage substrate extent with only little variation in accuracy of 5% between subgroups. Therefore, regardless of the low voltage substrate extent in a patient, the LVA will be identified in the same locations in both the bipolar and unipolar map.

Previous studies have shown that AF driver sites with acute AF termination frequently occur within LVA in bipolar mapping (Jadidi et al., 2016, 2020). Considering our findings, atrial sites displaying low voltage in the bipolar map will also display these regions in the unipolar map, thus indicating that an important criterion for AF source localization during high-density Lasso mapping is reduced electrogram voltage irrespective of the mapping modality (uni-/bipolar).

4.2. Impact of Electrode Spacing and Atrial Anatomical Region on Voltage Mapping

In this study, we split the voltage information into groups depending on the bipole pair that the signals were obtained from. Small bipolar inter-electrode distance (2 mm) yielded a significantly higher percentage of points being matched correctly in bipolar vs. unipolar voltage mapping, both in SR and AF. When using only the small bipoles, the signal collected from the bipolar pair is more localized, i.e., the region covered by the electrodes is smaller. The signal is less susceptible to influences of far-field, as presented by Takigawa et al. (2019). Therefore, mapping with the small distance electrode pairs improves the correlation between unipolar and bipolar mapping at 4% of mapping sites. Importantly, the optimal unipolar threshold has to be set to a higher value when bipolar mapping is done with small bipoles, resulting in larger LVA than mapping with large bipoles. In contrast, voltage maps acquired with large-spaced bipoles integrate high-voltage far-field signals from adjacent healthier myocardium and therefore, large-spaced bipolar maps under detect low voltage tissue. The unipolar voltage map, therefore, has to be set to a lower threshold to display the smaller LVA of the large-spaced bipolar map.

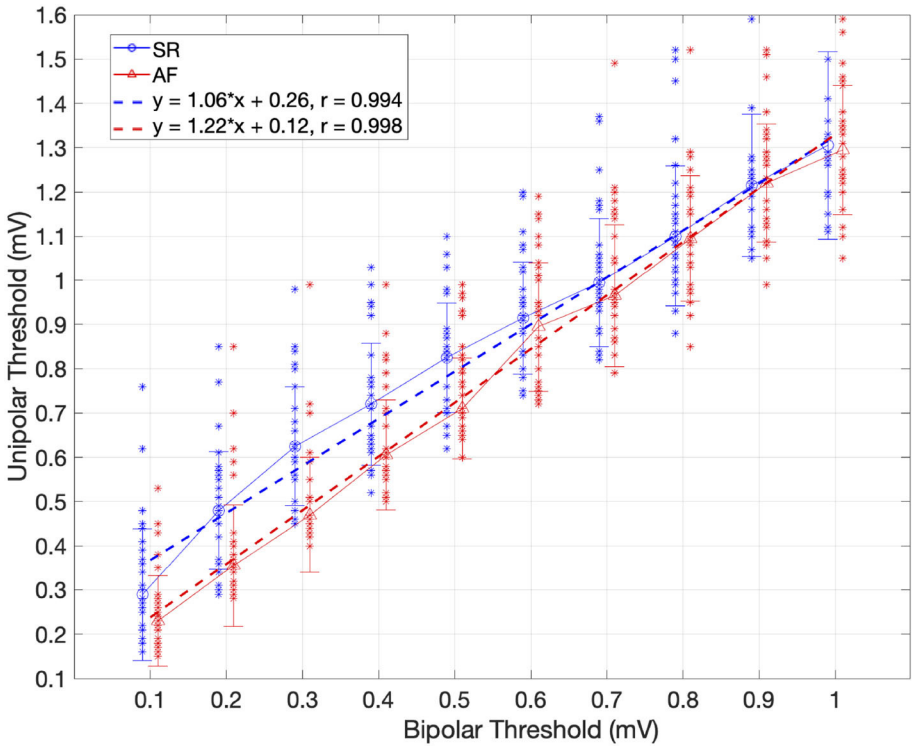

FIGURE 5 | Relationship between the bipolar and unipolar threshold in SR (blue) and AF (red). The unipolar threshold with highest concordance to the bipolar map is shown for different bipolar thresholds and each individual patient (blue and red dots for SR and AF, respectively). Standard deviation is represented by bars. The optimal unipolar threshold is identified as the optimal point on the ROC curve of each bipolar threshold using all patients. Linear regression shown as dotted lines, depending on the rhythm (SR blue, AF red). Pearson correlation coefficient (r) is provided. For every unipolar threshold, >89% of points matched in SR and >86% in AF.

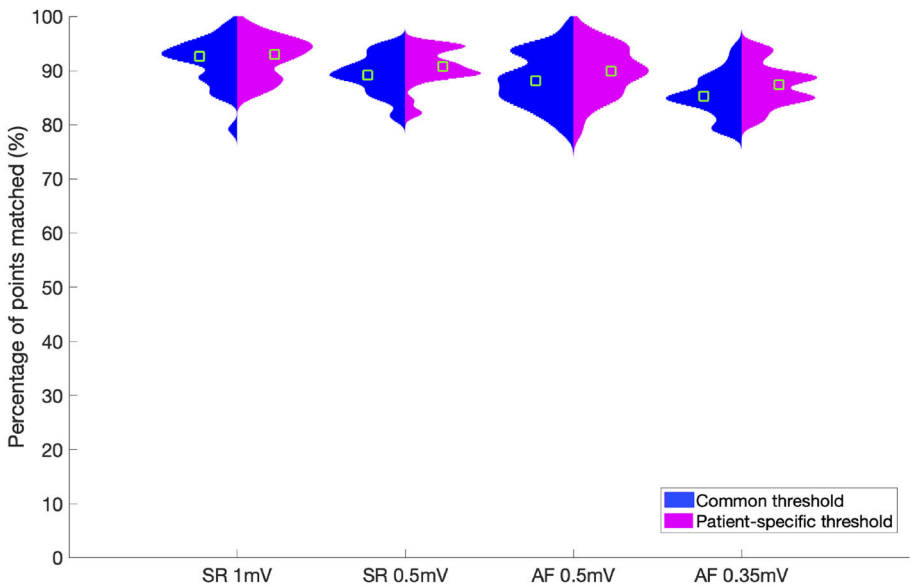

FIGURE 6 | Violin plot showing the percentage of points which match between unipolar and bipolar classification. The results are shown for each rhythm and corresponding bipolar threshold over all patients. Results for a common unipolar threshold for all patients are shown in blue. Results for patient-individual unipolar thresholds are shown in pink. The green squares indicate the median value for each set.

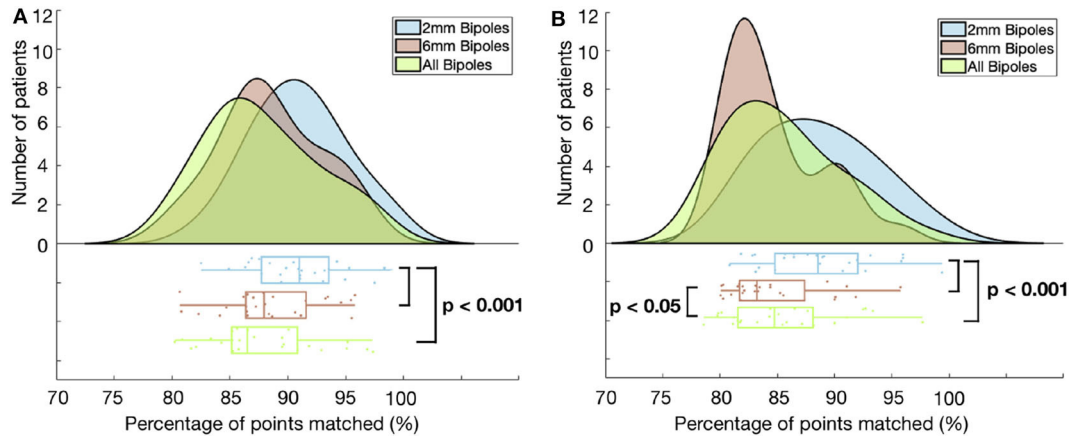

FIGURE 7 | Histogram and corresponding boxplot showing the percentage of points matched in SR **(A)** and AF **(B)** for each of the three electrode distance categories. Each category is shown in a different color: 2 mm (blue), 6 mm (red), all (green). *p*-value calculated with paired-sample *t*-test.

TABLE 4 | Rhythm-specific unipolar threshold corresponding to each bipolar threshold for each group of bipolar electrode distance.

	SR Threshold (mV)		AF Threshold (mV)	
Distance (mm)	**Bipolar**	**Unipolar**	**Bipolar**	**Unipolar**
2	0.5	1.09	0.35	0.76
6	0.5	0.72	0.35	0.52
All	0.5	0.87	0.35	0.64

Recent studies revealed a preferential anatomical distribution of LA LVA that more frequently affects the LA antero-septal area, followed by the LA roof and LA posterior wall (Corradi et al., 2005; Marcus et al., 2007; Müller-Edenborn et al., 2019). Therefore, it is more likely that LVA are present in these regions. From our analysis of assessing the different LA regions separately, we see that some of the lowest similarity between bipolar and unipolar signals exist in the posterior wall (90% SR, 87% AF match), the anterior wall (90% SR, 87% AF), and the septum (91% SR, 91% AF). This finding can be explained by the higher rate of occurrence of LVA in these regions, as this also means that more border zones are present and mismatch between unipolar and bipolar classification mainly occurred in border zones (**Figure 1**). In other areas such as the pulmonary veins, we typically have low voltage across the entire region and, therefore, fewer border zones, which leads to less mismatch in these regions.

4.3. Possible Reasons for the High Similarity Between Unipolar and Bipolar Low Voltage Distribution Patterns

Our findings show a high agreement between the bipolar and unipolar mapping when using high-density multi-electrode mapping with a 20-pole Lasso catheter. However, from simulation studies, it is known that the angle of the bipolar electrode pair in relation to the propagation direction and the size and distance between the electrodes are known to affect the bipolar voltage amplitude (Schuler et al., 2013; Beheshti et al., 2018). A recent study has shown that for 2 and 6 mm distant electrodes in simulated and clinical data, the amplitude of the bipolar electrogram goes from a maximum value at 0° to the propagation of a planar wavefront to close to 0 mV at 90° (Gaeta et al., 2019). Therefore, one can hypothesize that the bipolar voltage map would not present the same information as the unipolar voltage due to the direction dependence. Despite these factors, in our study, the majority of points (90%) were consistently categorized as either low or high voltage in both unipolar and bipolar. Small differences, which are clinically irrelevant, only exist at the border zones of the low voltage to high voltage threshold. Therefore, it is crucial to understand why the majority of points on the map have the same classification in both maps when the bipolar electrograms are influenced by various factors of the catheter. Here we discuss potential reasons why the theory-based expectations about the effects of using a bipolar catheter are hardly met by what was empirically identified in this study.

The simulation studies show that when the electrode orientation is perpendicular to the propagation, the bipolar voltage is 0 mV. This situation is shown in **Figure 2** by the electrograms marked with a triangle. However, the high overall correlation between the high-density unipolar vs. bipolar maps indicates that this situation rarely occurs in practice. One explanation may be the following: In the clinical setting of the 1–5 mm thick atrial wall with multiple layers of myocardial fibers, it may be extremely rare that the wavefront is uniformly parallel to the mapping bipole. Instead, the waves always contain some degree of curvature in the three-dimensional space, so that the electrodes do not receive the signal at the same time point, which would result in a voltage >0 mV. Thus, the effect of the bipolar orientation is likely to be less pronounced in clinical mapping settings than what is presented in idealized simulations with homogeneous tissue and (almost) perfectly planar wavefronts.

Another possible explanation for obtaining such a high correlation is due to the maps containing a high density of points. Thus, points in close proximity can be obtained from the catheter at various bipole orientations. Therefore, when interpolation of voltages is applied in the electro-anatomical maps, areas with low and high voltage points caused by the orientation of the catheter may result in an averaged value. Thus, some points which are affected by the catheter orientation may cancel out by near-by adjacent mapping points with different orientations to the wavefront. The use of interpolated vs. non-interpolated voltage maps yielded similar levels of agreement, suggesting that this effect does not notably contribute. During ongoing AF with changing wavefront directions, the direction dependency of the bipolar voltage maps should be further reduced (in comparison to regular rhythms).

Additionally, if the unipolar voltages at points in the diseased tissue are much smaller than the threshold or much larger than the threshold in healthy regions, then there is a substantial classification margin. This would result in the distortion of the bipolar voltages due to the unknown orientation of electrodes to still be within this margin and the classification to be the same for the bipolar and unipolar map. For the points in which the voltages are close to the threshold values, the classification is more susceptible to changes in the voltage due to the orientation or the distance between the electrodes. Furthermore, if the two electrodes used to calculate the bipolar voltage have slightly different distances to the endocardium, the bipolar voltage would be reduced. However, for unipolar voltages with a large amplitude, then this difference would cause the bipolar voltage to be reduced but not substantial enough to cause the value to fall below the threshold. In **Figure 1**, the bipolar voltage maps show more patchy/irregular areas than the unipolar map. This shows that the bipolar map may be affected by factors such as wavefront-to-bipole orientation in these areas. However, most regions are far enough from the threshold for the orientation of the catheter to affect the classification.

Finally, the unipolar threshold was identified to provide the best correlation between the unipolar and the bipolar map based on the standard bipolar threshold used in practice. This, however, may not lead to the best unipolar threshold for identifying true areas of fibrotic tissue. Future investigations will help to unravel which of the aforementioned potential reasons contribute most to the agreement between both mapping modalities. Nevertheless, this study has shown that with appropriate settings and the identical catheter, the same LVA can be identified when using the bipolar or unipolar map.

5. LIMITATIONS

In this study, CARTO-3 was used for electro-anatomic voltage mapping, with a Lasso catheter of 2 and 6 mm inter-electrode spacing. Since only one type of catheter was used, it may be that our results are not applicable when using other catheters or mapping systems. However, we expect similar results with high-density maps acquired using a PentaRay or OctaRay catheter, where the mapping conditions such as electrode size, inter-electrode distance, and the parallel orientation of bipoles to endocardium are similar as in the current mapping study. We aimed at having high-density maps with a sufficient number of data points across the entire atria. For some patients, more points were taken at specific areas of interest; therefore, the distribution of points was not always equal between patients. However, it was ensured that the mapping density was sufficiently high (17 and 22 mapping sites per cm^2 for SR and AF maps, respectively) to allow for regional analysis of the voltage maps. In this work, only one atrial beat was considered per mapped LA site (without averaging of multiple consecutive beats). However, due to the high density of the acquired maps, the atrial tissue was characterized by numerous mapping points that were recorded within a short distance from each other and contributed to the final voltage distribution maps in CARTO-3.

6. CONCLUSION

Bipolar and unipolar voltage maps are highly correlated both in SR and AF. Both mapping modes identify the same atrial sites as low voltage substrate. Small differences in low voltage classification may occur at the border zone of low voltage areas, without relevant impact on their spatial distribution patterns. Voltage mapping using small (2 mm) bipoles slightly improves the agreement between unipolar and bipolar low voltage areas. While bipole orientation and inter-electrode spacing are theoretical confounders, their impact is not of clinical importance, when mapping is performed at high density with a 20-polar Lasso catheter.

DATA AVAILABILITY STATEMENT

The data analyzed in this study is subject to the following licenses/restrictions: To protect the safety of the patients, the data used for this study can not be provided. However, the figures within the article and **Supplementary Material** show detailed analyses for all patients used. Requests to access these datasets should be directed to: Deborah Nairn, deborah.nairn@kit.edu.

ETHICS STATEMENT

The studies involving human participants were reviewed and approved by University Hospital of Freiburg Ethics Committee. The patients provided their written informed consent to participate in this study.

AUTHOR CONTRIBUTIONS

DN, HL, AJ, and AL designed the study and analyzed the results. HL and AJ collected the data. SS developed the automatic tool for sectioning the atria. DN carried out the data analysis and produced the initial draft of the manuscript. All

authors critically revised the manuscript and approved the final submitted manuscript.

FUNDING

We gratefully acknowledge financial support by Deutsche Forschungsgemeinschaft (DFG) through DO637/22-3 and by the Ministerium für Wissenschaft, Forschung und Kunst Baden-Württemberg through the Research Seed Capital (RiSC) program. We acknowledge support by the KIT-Publication Fund of the Karlsruhe Institute of Technology.

SUPPLEMENTARY MATERIAL

The Supplementary Material for this article can be found online at: https://www.frontiersin.org/articles/10.3389/fphys.2020.575846/full#supplementary-material

REFERENCES

Anter, E., Tschabrunn, C. M., and Josephson, M. E. (2015). High-resolution mapping of scar-related atrial arrhythmias using smaller electrodes with closer interelectrode spacing. *Circ. Arrhyth. Electrophysiol.* 8, 537–545. doi: 10.1161/CIRCEP.114.002737

Beheshti, M., Magtibay, K., Massé, S., Porta-Sanchez, A., Haldar, S., Bhaskaran, A., et al. (2018). Determinants of atrial bipolar voltage: Inter electrode distance and wavefront angle. *Comput. Biol. Med.* 102, 449–457. doi: 10.1016/j.compbiomed.2018.07.011

Blandino, A., Bianchi, F., Grossi, S., Biondi-Zoccai, G., Conte, M. R., Gaido, L., et al. (2017). Left atrial substrate modification targeting low-voltage areas for catheter ablation of atrial fibrillation: a systematic review and meta-analysis. *Pacing Clin. Electrophysiol.* 40, 199–212. doi: 10.1111/pace.13015

Corradi, D., Callegari, S., Benussi, S., Maestri, R., Pastori, P., Nascimbene, S., et al. (2005). Myocyte changes and their left atrial distribution in patients with chronic atrial fibrillation related to mitral valve disease. *Hum. Pathol.* 36, 1080–1089. doi: 10.1016/j.humpath.2005.07.018

Frisch, D., Oesterlein, T. G., Unger, L. A., Lenis, G., Wakili, R., Schmitt, C., et al. (2020). Mapping and removing the ventricular far field component in unipolar atrial electrograms. *IEEE Trans. Biomed. Eng.* 67, 2905–2915. doi: 10.1109/TBME.2020.2973471

Gaeta, S., Bahnson, T. D., and Henriquez, C. (2019). Mechanism and magnitude of bipolar electrogram directional sensitivity: characterizing underlying determinants of bipolar amplitude. *Heart Rhythm* 17(5 Pt A), 777–785. doi: 10.1016/j.hrthm.2019.12.010

Go, A. S., Mozaffarian, D., Roger, V. L., Benjamin, E. J., Berry, J. D., Blaha, M. J., et al. (2014). Heart disease and stroke statistics-2014 update: a report from the American heart association. *Circulation* 129, e28–e292. doi: 10.1161/01.cir.0000441139.02102.80

Haissaguerre, M., Jaïs, P., Shah, D. C., Takahashi, A., Hocini, M., Quiniou, G., et al. (1998). Spontaneous initiation of atrial fibrillation by ectopic beats originating in the pulmonary veins. *N. Engl. J. Med.* 339, 659–666. doi: 10.1056/NEJM199809033391003

Jadidi, A., Nothstein, M., Chen, J., Lehrmann, H., Dössel, O., Allgeier, J., et al. (2020). Specific electrogram characteristics identify the extra-pulmonary vein arrhythmogenic sources of persistent atrial fibrillation-characterization of the arrhythmogenic electrogram patterns during atrial fibrillation and sinus rhythm. *Sci. Rep.* 10:9147. doi: 10.1038/s41598-020-65564-2

Jadidi, A. S., Lehrmann, H., Keyl, C., Sorrel, J., Markstein, V., Minners, J., et al. (2016). Ablation of persistent atrial fibrillation targeting low-voltage areas with selective activation characteristics. *Circ. Arrhyth. Electrophysiol.* 9:e002962. doi: 10.1161/CIRCEP.115.002962

Lin, C.-Y., Te, A. L. D., Lin, Y.-J., Chang, S.-L., Lo, L.-W., Hu, Y.-F., et al. (2018). High-resolution mapping of pulmonary vein potentials improved the successful pulmonary vein isolation using small electrodes and inter-electrode spacing catheter. *Int. J. Cardiol.* 272, 90–96. doi: 10.1016/j.ijcard.2018.06.062

Marcus, G. M., Yang, Y., Varosy, P. D., Ordovas, K., Tseng, Z. H., Badhwar, N., et al. (2007). Regional left atrial voltage in patients with atrial fibrillation. *Heart Rhythm* 4, 138–144. doi: 10.1016/j.hrthm.2006.10.017

Miyasaka, Y., Barnes, M. E., Gersh, B. J., Cha, S. S., Seward, J. B., Bailey, K. R., et al. (2005). Time trends of ischemic stroke incidence and mortality in patients diagnosed with first atrial fibrillation in 1980 to 2000: report of a community-based study. *Stroke* 36, 2362–2366. doi: 10.1161/01.STR.0000185927.63746.23

Mori, H., Kato, R., Ikeda, Y., Goto, K., Tanaka, S., Asano, S., et al. (2018). The influence of the electrodes spacing of a mapping catheter on the atrial voltage substrate map. *J. Cardiol.* 72, 434–442. doi: 10.1016/j.jjcc.2018.04.012

Müller-Edenborn, B., Chen, J., Allgeier, J., Didenko, M., Moreno-Weidmann, Z., Neumann, F.-J., et al. (2019). Amplified sinus-p-wave reveals localization and extent of left atrial low-voltage substrate: implications for arrhythmia freedom following pulmonary vein isolation. *Europace* 22, 240–249. doi: 10.1093/europace/euz297

Oakes, R. S., Badger, T. J., Kholmovski, E. G., Akoum, N., Burgon, N. S., Fish, E. N., et al. (2009). Detection and quantification of left atrial structural remodeling with delayed-enhancement magnetic resonance imaging in patients with atrial fibrillation. *Circulation* 119, 1758–1767. doi: 10.1161/CIRCULATIONAHA.108.811877

Rodríguez-Mañero, M., Valderrábano, M., Baluja, A., Kreidieh, O., Martínez-Sande, J. L., Garc-Seara, J., et al. (2018). Validating left atrial low voltage areas during atrial fibrillation and atrial flutter using multielectrode automated electroanatomic mapping. *JACC Clin. Electrophysiol.* 4, 1541–1552. doi: 10.1016/j.jacep.2018.08.015

Rolf, S., Kircher, S., Arya, A., Eitel, C., Sommer, P., Richter, S., et al. (2014). Tailored atrial substrate modification based on low-voltage areas in catheter ablation of atrial fibrillation. *Circ. Arrhythm. Electrophysiol.* 7, 825–833. doi: 10.1161/CIRCEP.113.001251

Schuler, S., Keller, M. W., Oesterlein, T., Seemann, G., and Dössel, O. (2013). "Influence of catheter orientation, tissue thickness and conduction velocity on the intracardiac electrogram," in *Biomedical Engineering/Biomedizinische Technik, Vol. 58* (Berlin: De Gruvter). Available online at: https://www.degruyter.com/view/journals/bmte/bmte-overview.xml?tab_body=editorialContent-78027

Seitz, J., Bars, C., Théodore, G., Beurtheret, S., Lellouche, N., Bremondy, M., et al. (2017). AF ablation guided by spatiotemporal electrogram dispersion without pulmonary vein isolation: a wholly patient-tailored approach. *J. Am. Coll. Cardiol.* 69, 303–321. doi: 10.1016/j.jacc.2016.10.065

Takigawa, M., Relan, J., Martin, R., Kim, S., Kitamura, T., Cheniti, G., et al. (2019). Detailed analysis of the relation between bipolar electrode spacing and far- and near-field electrograms. *JACC Clin. Electrophysiol.* 5, 66–77. doi: 10.1016/j.jacep.2018.08.022

Verma, A., Jiang, C.-Y., Betts, T. R., Chen, J., Deisenhofer, I., Mantovan, R., et al. (2015). Approaches to catheter ablation for persistent atrial fibrillation. *N. Engl. J. Med.* 372, 1812–1822. doi: 10.1056/NEJMoa1408288

Verma, A., Wazni, O. M., Marrouche, N. F., Martin, D. O., Kilicaslan, F., Minor, S., et al. (2005). Pre-existent left atrial scarring in patients undergoing pulmonary vein antrum isolation: an independent predictor of procedural failure. *J. Am. Coll. Cardiol.* 45, 285–292. doi: 10.1016/j.jacc.2004.10.035

Wang, T. J., Larson, M. G., Levy, D., Vasan, R. S., Leip, E. P., Wolf, P. A., et al. (2003). Temporal relations of atrial fibrillation and congestive heart failure and

their joint influence on mortality: the Framingham heart study. *Circulation* 107, 2920–2925. doi: 10.1161/01.CIR.0000072767.89944.6E

Yamaguchi, T., Tsuchiya, T., Fukui, A., Kawano, Y., Otsubo, T., Takahashi, Y., et al. (2018). Impact of the extent of low-voltage zone on outcomes after voltage-based catheter ablation for persistent atrial fibrillation. *J. Cardiol.* 72, 427–433. doi: 10.1016/j.jjcc.2018.04.010

Yang, G., Yang, B., Wei, Y., Zhang, F., Ju, W., Chen, H., et al. (2016). Catheter ablation of nonparoxysmal atrial fibrillation using electrophysiologically guided substrate modification during sinus rhythm after pulmonary vein isolation. *Circ. Arrhythm. Electrophysiol.* 9:e003382. doi: 10.1161/CIRCEP.115.003382

Conflict of Interest: The authors declare that the research was conducted in the absence of any commercial or financial relationships that could be construed as a potential conflict of interest.

frontiers in Physiology

ORIGINAL RESEARCH
published: 15 December 2020
doi: 10.3389/fphys.2020.594654

Impact of Left Atrial Bipolar Electrogram Voltage on First Pass Pulmonary Vein Isolation During Radiofrequency Catheter Ablation

*Lohit Garg, Naga Venkata K. Pothineni, J. Michael Daw, Matthew C. Hyman, Jeffrey Arkles, Cory M. Tschabrunn, Pasquale Santangeli and Francis E. Marchlinski**

Electrophysiology Section, Cardiovascular Division, Hospital of the University of Pennsylvania, Philadelphia, PA, United States

OPEN ACCESS

Edited by:
Atul Verma, University of Toronto, Canada

Reviewed by:
David R. Van Wagoner, Case Western Reserve University, United States
Yasuo Okumura, Nihon University, Japan
Claudio Tondo, Centro Cardiologico Monzino (IRCCS), Italy

***Correspondence:**
Francis E. Marchlinski francis.marchlinski@pennmedicine.upenn.edu

Specialty section:
This article was submitted to Cardiac Electrophysiology, a section of the journal Frontiers in Physiology

Received: *14 August 2020*
Accepted: *09 November 2020*
Published: *15 December 2020*

Citation:
Garg L, Pothineni NVK, Daw JM, Hyman MC, Arkles J, Tschabrunn CM, Santangeli P and Marchlinski FE (2020) Impact of Left Atrial Bipolar Electrogram Voltage on First Pass Pulmonary Vein Isolation During Radiofrequency Catheter Ablation. Front. Physiol. 11:594654. doi: 10.3389/fphys.2020.594654

Background: First pass pulmonary vein isolation (PVI) is associated with durable isolation and reduced recurrence of atrial fibrillation (AF).

Objective: We sought to investigate the relationship between left atrial electrogram voltage using multielectrode fast automated mapping (ME-FAM) and first pass isolation with radiofrequency ablation.

Methods: We included consecutive patients (pts) undergoing first time ablation for paroxysmal AF (pAF), and compared the voltage characteristics between patients with and without first pass isolation. Left atrium (LA) adjacent to PVs was divided into 6 regions, and mean voltages obtained with ME-FAM (Pentaray, Biosense Webster) in each region and compared. LA electrograms with marked low voltage (<0.5 mV) were identified and the voltage characteristics at the site of difficult isolation was compared to the voltage in adjacent region.

Results: Twenty consecutive patients (10 with first pass and 10 without) with a mean age of 63.3 ± 6.2 years, 65% males, were studied. Difficult isolation occurred on the right PVs in eight pts and left PVs in three pts. The mean voltage in pts without first pass isolation was lower in all 6 regions; posterior wall (1.93 ± 1.46 versus 2.99 ± 2.19; $p < 0.001$), roof (1.83 ± 2.29 versus 2.47 ± 1.99; $p < 0.001$), LA-LPV posterior (1.85 ± 3.09 versus 2.99 ± 2.19, $p < 0.001$), LA-LPV ridge (1.42 ± 1.04 versus 1.91 ± 1.61; $p < 0.001$), LA-RPV posterior (1.51 ± 1.11 versus 2.30 ± 1.77, $p < 0.001$) and LA-RPV septum (1.55 ± 1.23 versus 2.31 ± 1.40, $p < 0.001$). Patients without first pass isolation also had a larger percentage of signal with an amplitude of <0.5 mV for each of the six regions (12.8% versus 7.5%). In addition, the mean voltage at the site of difficult isolation was lower at 8 out of 11 sites compared to mean voltage for remaining electrograms in that region.

Conclusion: In patients undergoing PVI for paroxysmal AF, failure in first pass isolation was associated with lower global LA voltage, more marked low amplitude signal (<0.5 mV) and lower local signal voltage at the site with difficult isolation. The results suggest that a greater degree of global and segmental fibrosis may play a role in ease of PV isolation with radiofrequency energy.

Keywords: first pass isolation, voltage mapping, atrial fibrillation, pulmonary vein isolation, atriopathy

INTRODUCTION

Pulmonary vein isolation (PVI) with catheter ablation is an effective therapy for paroxysmal atrial fibrillation (pAF) and is recommended for drug refractory symptomatic pAF (January et al., 2014). Durability of PVI is important and reconnection of previously isolated pulmonary veins (PVs) is associated with higher risk of recurrent AF (Callans et al., 2004; Lemola et al., 2004; Nilsson et al., 2006; Natale et al., 2010; January et al., 2014). There are several factors responsible for reconnection of pulmonary veins, including non-contiguous lesions, transmurality of lesion, and presence of scar based on electroanatomic mapping. In patients undergoing ablation for pAF, a left atrial scar can be reproducibly identified in the sinus rhythm using a voltage range of 0.2–0.45 mV, correlating with delayed enhancement abnormalities identified on cardiac magnetic resonance imaging (Sanders et al., 2003; Verma et al., 2005; Kapa et al., 2014; Squara et al., 2014). Previous studies have reported that in patients with pAF, there is wide range (2–15%) of low voltage (<0.5 mV) areas (Anter et al., 2015; Liang et al., 2017). Some reports suggest that the left atrium with a bipolar voltage between 0.5 and 1.3 mV can also be considered as a transitional zone with moderate atrial fibrosis (Lin et al., 2014; Saini et al., 2017). First pass isolation during initial catheter ablation has been shown to be associated with durable PVI and a lower risk of recurrence (Sandorfi et al., 2018; Yamaguchi et al., 2020). The impact of presence of low electrogram voltage on first pass isolation has not been investigated. In this study, we aimed to determine the relationship between the left atrial bipolar electrogram voltage obtained with multielectrode fast automated mapping (ME-FAM) in sinus rhythm and first pass isolation with radiofrequency catheter ablation.

MATERIALS AND METHODS

Study Population

We identified consecutive patients who underwent first time ablation with radiofrequency for symptomatic pAF with a standard ablation technique. Patients with complete ME-FAM performed in sinus rhythm were included. Patient demographics, clinical and procedural characteristics were assessed. All patients provided written informed consent for both the ablation procedure we well as inclusion of demographic information and procedural data in a medical research registry that was approved by the University of Pennsylvania Health System's Institutional Review Board.

EAM Technique

Our technique of AF mapping and ablation has been previously described (Squara et al., 2015; Liang et al., 2017). Briefly, 7 Fr- decapolar catheters were advanced into the coronary sinus and posterior right atrium along the crista terminalis. A 64-element phased-array intracardiac echocardiography (ICE) catheter (AcuNav, ACUSON, Mountain View, CA, United States) was used to assist for transseptal access, catheter manipulation, and real-team monitoring of complications. Intravenous heparin with a target activated clotting time of >350 s was administered before obtaining left atrial access. Two transseptal punctures were performed through which the ablation and a multipolar mapping catheter with 2-6-2 inter electrode spacing (PentaRay, Biosense Webster) were advanced into the left atrium. ME-FAMs were created for each patient during sinus rhythm, using CARTO 3 (Biosense Webster) prior to ablation (**Figure 1**).

Atrial electrograms were captured by setting the window of interest as the cycle length of sinus rhythm and using the proximal coronary sinus electrogram as a reference. Only patients with detailed LA mapping with >1000 points uniformly distributed were included in the study. Points were acquired in the auto-freeze mode if the stability criteria in space (6 mm) and local activation time (0.5 ms) were met. Mapping was performed with an equal distribution of points using a fill-threshold of 5–10 mm. Routinely, the regions adjacent to the PVs including the posterior wall, the roof between the superior veins, and the anterior aspect of the PV antrum were more densely sampled. Intracardiac echocardiography, orthogonal fluoroscopy, electrogram characteristics (far field appearing signals), and a dedicated impedance-based tissue proximity algorithm (TPI, Biosense Webster) were utilized to monitor for adequate contact. Signals were filtered at 30–400 Hz and displayed at 100 mm/s.

The PVI was performed by an experienced operator with coronary sinus and/or right ventricular pacing under general anesthesia, with high frequency low volume (JET) ventilation to optimize stability, and a target contact force of 10–25 gm. Ablation was performed utilizing an open irrigated contact force catheter (Thermocool SmartTouch SF, Biosense Webster) routinely with wide antral circumferential ablation with a power of 30–40 W for 30 s anteriorly and 30 W for 10 to 15 s posteriorly while carefully monitoring electrogram amplitude change and

Abbreviations: PVI, pulmonary vein isolation; AF, atrial fibrillation; ME-FAM, multielectrode fast automated mapping; LA, left atrium; LPV, left pulmonary vein; RPV, right pulmonary vein; CMR, cardiac magnetic resonance; LGE, late gadolinium enhancement.

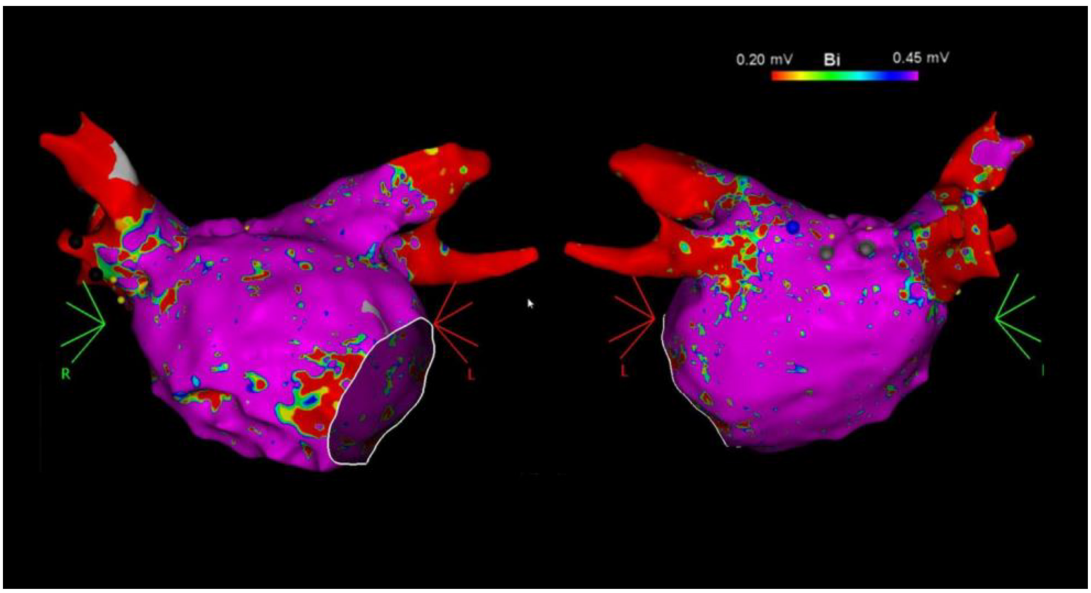

FIGURE 1 | Example of left atrial bipolar voltage maps (0.20–0.45 mV) in the anterior **(left)** and posterior **(right)** views recorded with the multielectrode catheter prior to catheter ablation.

impedance. An esophageal temperature probe was used during ablation on the posterior wall with careful monitoring of the temperature and power/duration titration when any increase in temperature was observed. All ablation lesions were labeled as 3 mm VisiTags and the interlesion distance was <5 mm with no visible gap on electroanatomic map. First pass isolation was considered as entrance and exit block of a PV after completion of index wide antral circumferential ablation around the vein.

LA Regional Electrogram Voltages

Left atrial electrogram voltages were reviewed offline from ME-FAM maps obtained prior to the administration of any ablation lesions during the index procedure. To compare the regional voltage characteristics, the LA adjacent to the pulmonary veins was divided into six distinct regions (**Figure 2**). These regions included the posterior wall between the PV antrum, the adjacent LA roof, the posterior wall adjacent to the left pulmonary veins (Post LPV), the LPV ridge, the posterior wall adjacent to the right pulmonary vein (Post RPV), and the LA septum adjacent to the septal RPV. Each region extended approximately 5–10 mm in width. All points with ME-FAM in each of the LAs were collected and the mean voltage with standard deviation was calculated for each region. The site of difficult isolation was identified based on a review of the electroanatomic maps. All the bipolar electrogram signal amplitudes at sites ($\sim$ 0.5–1.0 cm^2) of difficult isolation during the initial mapping and prior to ablation were assessed and mean voltage was calculated for comparison with mean voltage for the remaining points in that LA region. Based on prior work (Sanders et al., 2003; Kapa et al., 2014), a voltage cutoff of <0.5 mV was considered abnormal and consistent with increase LA fibrosis.

Statistical Analysis

Patient clinical and demographic characteristics were compared using χ^2 or *t*-tests, as appropriate. Results are reported as percentages for categorical variables or means ± standard deviations for continuous variables. Mean LA segments voltages were calculated using all abstracted voltages in ME-FAM maps for both groups (Group 1: First pass isolation and Group 2: No first pass isolation). Paired *t*-tests were used to compare mean segment voltages between the two groups. All statistical analyses were performed using IBM SPSS Statistics 26.0 (IBM Corp, Armonk, NY, United States). All *P*-values were 2-sided with a significance threshold of 0.05.

RESULTS

Patient Characteristics

Sixty consecutive patients who underwent catheter ablation for paroxysmal AF were screened. Of these, 20 patients (10 in each group; Group 1: First pass isolation and Group 2: No first pass isolation) had detailed ME-FAM obtained during sinus rhythm over all six regions and were included in the analysis. The baseline patient characteristics are summarized in **Table 1** and were comparable in two groups. Only the mean age was greater in patients with first pass isolation (65.4 years in group 1 versus 61.2 years in group 2; $p = 0.026$).

Segmental Bipolar Voltage Characteristics and Site of Difficult Isolation

A total of 1986 electrograms were sampled in patients with first pass isolation compared to 2984 electrograms in the group

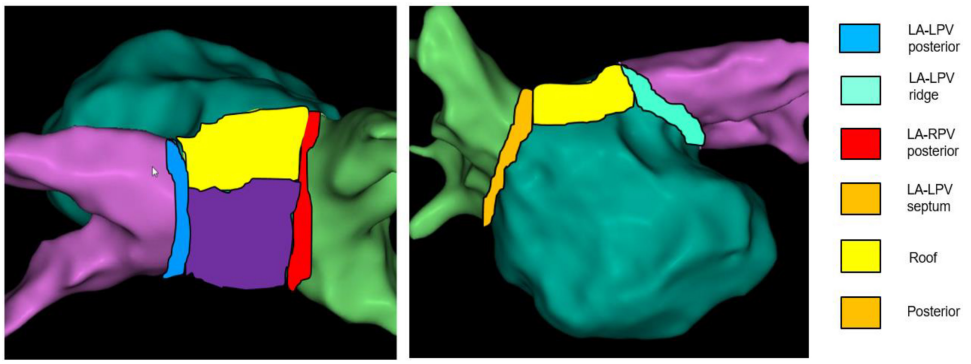

FIGURE 2 | Regionalization of the left atrium. Schematic of six regions of pulmonary vein antrum sampled for voltage comparisons is provided.

TABLE 1 | Patients' baseline characteristics at the time of ablation.

Characteristics	First pass (n = 10)	No first pass (n = 10)	p-value
Age (years)	65.4 ± 4.4	61.2 ± 11.3	0.026
Male (%)	7 (70%)	6 (60%)	0.639
BMI (kg/m^2)	29.3 ± 3.2	30.2 ± 6.2	0.119
Paroxysmal AF	5 (50%)	5 (50%)	1
CHADSVASC	1.7 ± 1.3	2.4 ± 1.4	0.851
HTN	4 (40%)	6 (60%)	0.371
Diabetes	1 (10%)	2 (20%)	0.136
OSA	2 (20%)	1 (10%)	0.531
CAD	2 (20%)	3 (30%)	0.606
Stroke	0 (0%)	1 (10%)	0.305
CHF	2 (20%)	3 (30%)	0.606
Atrial flutter ablation	5 (50%)	6 (60%)	0.653
Mean LVEF	55.0 ± 9	55 ± 7	0.279
LA diameter (cm)	4.2 ± 0.7	4.7 ± 0.9	0.459

TABLE 2 | Comparison of mean segmental bipolar voltage in two groups.

Segment	First pass isolation	No first pass	p-value
Posterior wall	2.99 ± 2.19	1.93 ± 1.46	<0.001
Roof	2.47 ± 1.99	1.83 ± 2.29	<0.001
RPV-septum	2.31 ± 1.40	1.55 ± 1.23	<0.001
LPV-ridge	1.91 ± 1.61	1.42 ± 1.04	<0.001
LPV posterior	2.5 ± 4.7	1.85 ± 3.09	<0.001
RPV posterior	2.30 ± 1.77	1.51 ± 1.11	<0.001

without first pass isolation during sinus rhythm. The number of points sampled per LA region is summarized in **Table 3**. The mean segmental voltage characteristics are summarized in **Table 2**. Mean bipolar voltages obtained with ME-FAM were lower in all 6 segments in patients without first pass isolation compared to patients with first pass isolation; posterior wall (1.93 ± 1.46 versus 2.99 ± 2.19; $p < 0.001$), roof (1.83 ± 2.29 versus 2.47 ± 1.99; $p < 0.001$), LA-LPV posterior (1.85 ± 3.09 versus 2.99 ± 2.19, $p < 0.001$), LA-LPV ridge (1.42 ± 1.04 versus 1.91 ± 1.61; $p < 0.001$), LA-RPV posterior (1.51 ± 1.11 versus 2.30 ± 1.77, $p < 0.001$), and LA-RPV septum (1.55 ± 1.23 versus 2.31 ± 1.40, $p < 0.001$). The patients without first pass isolation also had a higher percentage of low voltage electrograms (<0.5 mV) in all 6 LA regions as depicted in **Table 3**.

Out of 10 patients who had no first pass isolation, the site of difficult isolation was located on the RPVs in eight patients (Posterior carina in 6 and septal carina in 2) and the LPVs were reconnected in three patients (posterior carina/roof). The mean voltage at the site of the difficult isolation was numerically lower compared to mean voltage for rest of same region at 8 of the 11 sites (**Figure 3**).

DISCUSSION

In patients undergoing initial catheter ablation for pAF, we documented that patients without first pass isolation have lower mean left atrial electrogram voltage as well as more scar burden as indexed by the percent signals <0.5 mV compared to patients who had first pass isolation. Mean voltage at the site of a difficult isolation was also typically lower compared to the mean voltage for the rest of the electrograms in that region. These observations have clinical implications and suggest that indices of global and segmental increases in fibrosis may identify patients with more difficulty achieving first pass isolation with radiofrequency ablation. This came as somewhat of a surprise because we had originally believed that more difficult to isolate segments might actually have larger amplitude signals because of the associated increase in LA thickness or muscle bundle size.

Pulmonary vein isolation is the most effective ablation strategy for AF management. With advances in technology and experience with catheter ablation, durability of PVI has improved over the past decade. However, PV reconnection continues to be a common occurrence accounting for the majority of recurrent AF ablation procedures. First pass isolation, defined as an entrance and exit block of a PV after the completion of wide antral circumferential ablation around the vein appears to be a reliable index for achieving long-term chronic PV isolation. Various techniques such as ablation index, contact force, overlapping lesions to minimize inter lesion distance, closing visual gaps in lesion sets, etc., have been proposed to increase the rate of first pass isolation (Taghji et al., 2018). When first pass isolation is not achieved, further mapping and ablation of the persistent

TABLE 3 | Number of electrograms in each region and comparison of percentage of low voltage electrograms (<0.5 mV) based on ability to achieve first pass isolation.

	First pass isolation		Without first pass isolation	
	Number of electrograms (Mean ± SD)	Low voltage electrograms	Number of electrograms (Mean ± SD)	Low voltage electrograms
Posterior wall	68 ± 51	49/685 (7.1%)	93 ± 70	103/933 (11.0%)
Roof	27 ± 21	15/263 (5.7%)	46 ± 40	66/451 (14.6%)
LA-RPV septum	28 ± 17	17/281 (6.0%)	35 ± 23	64/348 (18.4%)
LA-RPV posterior	20 ± 7	22/311 (7.0%)	47 ± 36	54/395 (13.6%)
LA-LPV ridge	26 ± 15	22/193 (11.4%)	39 ± 14	95/473 (20.0%)
LA-LPV posterior	31 ± 22	25/253 (9.9%)	40 ± 26	46/384 (12.0%)

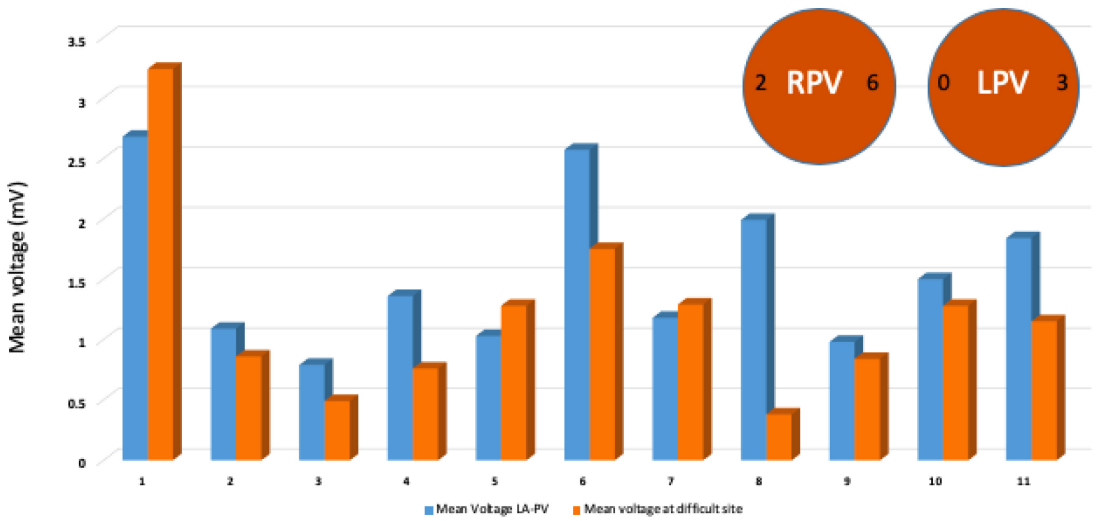

FIGURE 3 | Mean voltage at the site of failure of first pass isolation compared to mean voltage at the remaining sites from same LA-PV junction region. Descriptive analysis and comparison performed and illustrated by bar graphs of mean voltage showing lower baseline voltage at 8 of 11 sites of persistent PV connections. Typical location of persistent PV connection at posterior or anterior carina after first pass isolation highlighted by circles.

PV connection site can be challenging due to local edema from prior ablation lesions. Various factors such as catheter stability, respiratory variations, power delivered, and tissue characteristics affect optimal lesion delivery. In this context, low atrial bipolar voltage as a marker of left atrial fibrosis is proposed as a potential contributor that may affect the biophysics of energy delivery during RFA.

Specific voltage thresholds to define atrial scarring have not been histologically validated (Sim et al., 2019). In a study of 20 patients with paroxysmal AF, Kapa et al. (2014) evaluated thresholds for atrial scarring and reported different cut offs for different segments of the left atrium. A threshold of <0.2 mV for the posterior wall and pulmonary vein/left atrial junctions, and <0.45 mV for all other atrial segments correlated best with scarring defined by late gadolinium enhancement on cardiac magnetic resonance imaging. In a study of atrial voltage in non-AF patients presenting for left sided accessory pathway ablation, Lin et al. reported a threshold of 0.4 mV to represent low voltage (Lin et al., 2014). However, these studies were performed with point by point mapping using a 3.5 mm bipolar electrode at the tip of an ablation catheter. In the current era of multipolar mapping, voltage thresholds to define abnormal substrate vary considerably. Liang et al. (2017) compared point by point mapping to ME-FAM in assessing left atrial voltage in patients presenting for repeat AF ablation, using a voltage cut off of <0.2 mV to define a dense scar. In that study, mean voltage in multiple segments of the left atrium (septum, posterior wall, right PV-LA junction) were significantly higher with ME-FAM compared to point by point mapping (Liang et al., 2017). Higher mapping resolution with multipolar catheters such as PentaRay (Biosense Webster) has been shown to identify higher voltage segments within an area of scarring (Anter et al., 2015).

In this relatively small number of patients, we also noted that difficulty in achieving first pass isolation is more common in the RPVs compared to LPVs, with the RPV carina being the most common site of difficulty. The RPVs have also been shown to have higher rates of spontaneous and provoked reconnection after achieving first pass isolation in prior studies (Andrade et al., 2020). Importantly, patients with acute PV reconnections also have lower arrhythmia-free survival long-term. The RPV carina presents a particularly challenging region during PVI. The presence of an epicardial connection between the RPV carina

and the RA has been postulated as a potential mechanism of difficulty to achieve successful ablation (Yoshida et al., 2019). The septopulmonary bundle which is a broad band of epicardial fibers tends to connect at the RPV carina. Sites of difficult ablation of the RPV in our study showed that mean voltage at the site of difficult isolation along the RPVs was significantly lower compared to mean bipolar voltage of the remaining sites in that region segment, pointing toward scar/fibrosis in these regions that impede energy delivery at least on the posterior aspect of the carina. Early identification of these sites on sinus rhythm voltage could help direct energy delivery targeting higher ablation indices in these regions and more redundancy of lesions. This hypothesis will require additional investigation.

Limitations

The cohort size for our study was relatively small and included only patients presenting for first time catheter ablation for pAF and may not apply to patients with persistent forms of AF. All maps were created in sinus rhythm; the results might not be reproducible if voltage maps are created in AF or atrial flutter. There was heterogeneity and large standard deviation in LA-LPV posterior despite adequate sampling. Some of this variability may be related to the gaps in myocardium noted posteriorly. The sampling was greater in patients without first pass isolation, however, low voltage regions were diffuse and involved all regions. We do not routinely assess for late gadolinium enhancement (LGE) with pre-ablation cardiac MRI, therefore we were unable to make comparisons between ME-FAM derived low voltage regions versus LA scar as seen on CMR in this patient series. We have previously reported a correlation between LGE on CMR and voltage <0.5 mV with point by point mapping (Kapa et al., 2014). Further studies are required to compare an LA scar identified by ME-FAM and LGE abnormalities on CMR. Finally, we only included cases performed with PentaRay catheter in this series, our findings may not apply to LA voltage abnormalities identified using other multipolar mapping catheters or the larger tipped ablation catheter.

CONCLUSION

This study established that lower global LA voltage, and more low voltage signals (<0.5 mV), which suggest an increase in LA fibrosis, may identify patients with anticipated difficulty in achieving first pass isolation using radiofrequency ablation. Antral PV segments with difficult first pass isolation appear to be associated with lower rather than higher signal amplitude. The identification of relative low voltage areas could potentially guide optimal ablation energy delivery to achieve durable first pass isolation. Additional study is required to determine if there is a global voltage threshold effect which identifies risk and whether energy titration in higher risk patients can be used to improve the likelihood of first pass isolation and its relationship to long term success.

DATA AVAILABILITY STATEMENT

The raw data supporting the conclusions of this article will be made available by the authors, without undue reservation.

ETHICS STATEMENT

The studies involving human participants were reviewed and approved by the University of Pennsylvania Health System's Institutional Review Board. The patients/participants provided their written informed consent to participate in this study.

AUTHOR CONTRIBUTIONS

LG, NP, and FM contributed to the design and implementation of the project, analysis of the results, and writing of the final manuscript. MH, JA, CT, and PS contributed in interpreting the results and worked on the manuscript. All authors discussed the results and commented on the manuscript.

FUNDING

This study was supported by the Richard T. and Angela Clark Innovation Fund in Cardiac Electrophysiology and the Mark S. Marchlinski Electrophysiology Research and Education Fund.

REFERENCES

Andrade, J. G., Deyell, M. W., Nattel, S., Khairy, P., Dubuc, M., Champagne, J., et al. (2020). Prevalence and clinical impact of spontaneous and adenosine-induced pulmonary vein reconduction in the Contact-Force vs. Cryoballoon atrial fibrillation ablation (CIRCA-DOSE) study. *Heart Rhythm.* 17, 897–904. doi: 10.1016/j.hrthm.2020.01.017

Anter, E., Tschabrunn, C. M., and Josephson, M. E. (2015). High-resolution mapping of scar-related atrial arrhythmias using smaller electrodes with closer interelectrode spacing. *Circ. Arrhythm. Electrophysiol.* 8, 537–545. doi: 10.1161/circep.114.002737

Callans, D. J., Gerstenfeld, E. P., Dixit, S., Zado, E., Vanderhoff, M., Ren, J. F., et al. (2004). Efficacy of repeat pulmonary vein isolation procedures in patients with recurrent atrial fibrillation. *J. Cardiovasc. Electrophysiol.* 15, 1050–1055. doi: 10.1046/j.1540-8167.2004.04052.x

January, C. T., Wann, L. S., Alpert, J. S., Calkins, H., Cigarroa, J. E., Cleveland, J. C. Jr., et al. (2014). AHA/ACC/HRS guideline for the management of patients with atrial fibrillation: a report of the American College of Cardiology/American Heart Association Task Force on Practice Guidelines and the Heart Rhythm Society. *J. Am. Coll. Cardiol.* 64, e1–e76.

Kapa, S., Desjardins, B., Callans, D. J., Marchlinski, F. E., and Dixit, S. (2014). Contact electroanatomic mapping derived voltage criteria for characterizing left atrial scar in patients undergoing ablation for atrial fibrillation. *J. Cardiovasc. Electrophysiol.* 25, 1044–1052. doi: 10.1111/jce.12452

Lemola, K., Hall, B., Cheung, P., Good, E., Han, J., Tamirisa, K., et al. (2004). Mechanisms of recurrent atrial fibrillation after pulmonary vein isolation by

segmental ostial ablation. *Heart Rhythm.* 1, 197–202. doi: 10.1016/j.hrthm.2004.03.071

Liang, J. J., Elafros, M. A., Muser, D., Pathak, R. K., Santangeli, P., Supple, G. E., et al. (2017). Comparison of left atrial bipolar voltage and scar using multielectrode fast automated mapping versus point-by-point contact electroanatomic mapping in patients with atrial fibrillation undergoing repeat ablation. *J. Cardiovasc. Electrophysiol.* 28, 280–288. doi: 10.1111/jce.13151

Lin, Y., Yang, B., Garcia, F. C., Ju, W., Zhang, F., Chen, H., et al. (2014). Comparison of left atrial electrophysiologic abnormalities during sinus rhythm in patients with different type of atrial fibrillation. *J. Interv. Card. Electrophysiol.* 39, 57–67. doi: 10.1007/s10840-013-9838-y

Natale, A., Raviele, A., Al-Ahmad, A., Alfieri, O., Aliot, E., Almendral, J., et al. (2010). Venice Chart International Consensus document on ventricular tachycardia/ventricular fibrillation ablation. *J. Cardiovasc. Electrophysiol.* 21, 339–379.

Nilsson, B., Chen, X., Pehrson, S., Kober, L., Hilden, J., and Svendsen, J. H. (2006). Recurrence of pulmonary vein conduction and atrial fibrillation after pulmonary vein isolation for atrial fibrillation: a randomized trial of the ostial versus the extraostial ablation strategy. *Am. Heart J.* 152, 537.e1–537.e8.

Saini, A., Huizar, J. F., Tan, A., Koneru, J. N., Ellenbogen, K. A., and Kaszala, K. (2017). Scar Homogenization in Atrial Fibrillation Ablation: Evolution and Practice. *J. Atr. Fibrillation.* 10:1645.

Sanders, P., Morton, J. B., Davidson, N. C., Spence, S. J., Vohra, J. K., Sparks, P. B., et al. (2003). Electrical remodeling of the atria in congestive heart failure: electrophysiological and electroanatomic mapping in humans. *Circulation* 108, 1461–1468. doi: 10.1161/01.cir.0000090688.49283.67

Sandorfi, G., Rodriguez-Manero, M., Saenen, J., Baluja, A., Bories, W., Huybrechts, W., et al. (2018). Less pulmonary vein reconnection at redo procedures following radiofrequency point-by-point antral pulmonary vein isolation with the use of contemporary catheter ablation technologies. *JACC Clin. Electrophysiol.* 4, 1556–1565. doi: 10.1016/j.jacep.2018.09.020

Sim, I., Bishop, M., O'Neill, M., and Williams, S. E. (2019). Left atrial voltage mapping: defining and targeting the atrial fibrillation substrate. *J. Interv. Card. Electrophysiol.* 56, 213–227. doi: 10.1007/s10840-019-00537-8

Squara, F., Frankel, D. S., Schaller, R., Kapa, S., Chik, W. W., Callans, D. J., et al. (2014). Voltage mapping for delineating inexcitable dense scar in patients undergoing atrial fibrillation ablation: a new end point for enhancing pulmonary vein isolation. *Heart Rhythm.* 11, 1904–1911. doi: 10.1016/j.hrthm.2014.07.027

Squara, F., Liuba, I., Chik, W., Santangeli, P., Maeda, S., Zado, E. S., et al. (2015). Electrical connection between ipsilateral pulmonary veins: prevalence and implications for ablation and adenosine testing. *Heart Rhythm.* 12, 275–282. doi: 10.1016/j.hrthm.2014.11.003

Taghji, P., El Haddad, M., Phlips, T., Wolf, M., Knecht, S., Vandekerckhove, Y., et al. (2018). Evaluation of a strategy aiming to enclose the pulmonary veins with contiguous and optimized radiofrequency lesions in paroxysmal atrial fibrillation: a pilot study. *JACC Clin. Electrophysiol.* 4, 99–108. doi: 10.1016/j.jacep.2017.06.023

Verma, A., Wazni, O. M., Marrouche, N. F., Martin, D. O., Kilicaslan, F., Minor, S., et al. (2005). Pre-existent left atrial scarring in patients undergoing pulmonary vein antrum isolation: an independent predictor of procedural failure. *J. Am. Coll. Cardiol.* 45, 285–292. doi: 10.1016/j.jacc.2004.10.035

Yamaguchi, J., Takahashi, Y., Yamamoto, T., Amemiya, M., Sekigawa, M., Shirai, Y., et al. (2020). Clinical outcome of pulmonary vein isolation alone ablation strategy using visitag surpoint in non-paroxysmal atrial fibrillation. *J. Cardiovasc. Electrophysiol.* 31, 2592–2599. doi: 10.1111/jce.14673

Yoshida, K., Baba, M., Shinoda, Y., Harunari, T., Tsumagari, Y., Koda, N., et al. (2019). Epicardial connection between the right-sided pulmonary venous carina and the right atrium in patients with atrial fibrillation: a possible mechanism for preclusion of pulmonary vein isolation without carina ablation. *Heart Rhythm.* 16, 671–678. doi: 10.1016/j.hrthm.2018.11.017

Conflict of Interest: The authors declare that the research was conducted in the absence of any commercial or financial relationships that could be construed as a potential conflict of interest.

frontiers in Physiology

ORIGINAL RESEARCH
published: 23 December 2020
doi: 10.3389/fphys.2020.605671

Transcriptomic Bioinformatic Analyses of Atria Uncover Involvement of Pathways Related to Strain and Post-translational Modification of Collagen in Increased Atrial Fibrillation Vulnerability in Intensely Exercised Mice

Yena Oh[1,2,3,4†], Sibao Yang[1,5†], Xueyan Liu[1,5], Sayantan Jana[6], Farzad Izaddoustdar[2], Xiaodong Gao[1], Ryan Debi[1], Dae-Kyum Kim[7,8], Kyoung-Han Kim[3,4], Ping Yang[5], Zamaneh Kassiri[6], Robert Lakin[1] and Peter H. Backx[1,2]**

[1] Department of Biology, York University, Toronto, ON, Canada, [2] Department of Physiology, University of Toronto, Toronto, ON, Canada, [3] Department of Cellular and Molecular Medicine, Faculty of Medicine, University of Ottawa, Ottawa, ON, Canada, [4] University of Ottawa Heart Institute, Ottawa, ON, Canada, [5] Department of Cardiology, China-Japan Union Hospital of Jilin University, Changchun, China, [6] Department of Physiology, Cardiovascular Research Center, University of Alberta, Edmonton, AB, Canada, [7] Donnelly Centre, University of Toronto, Toronto, ON, Canada, [8] Lunenfeld-Tanenbaum Research Institute, Sinai Health System, Toronto, ON, Canada

Atrial Fibrillation (AF) is the most common supraventricular tachyarrhythmia that is typically associated with cardiovascular disease (CVD) and poor cardiovascular health. Paradoxically, endurance athletes are also at risk for AF. While it is well-established that persistent AF is associated with atrial fibrosis, hypertrophy and inflammation, intensely exercised mice showed similar adverse atrial changes and increased AF vulnerability, which required tumor necrosis factor (TNF) signaling, even though ventricular structure and function improved. To identify some of the molecular factors underlying the chamber-specific and TNF-dependent atrial changes induced by exercise, we performed transcriptome analyses of hearts from wild-type and TNF-knockout mice following exercise for 2 days, 2 or 6 weeks of exercise. Consistent with the central role of atrial stretch arising from elevated venous pressure in AF promotion, all 3 time points were associated with differential regulation of genes in atria linked to mechanosensing (focal adhesion kinase, integrins and cell-cell communications), extracellular matrix (ECM) and TNF pathways, with TNF appearing to play a permissive, rather than causal, role in gene changes. Importantly, mechanosensing/ECM genes were only enriched, along with tubulin- and hypertrophy-related genes after 2 days of exercise while being downregulated at 2 and 6 weeks, suggesting that early reactive strain-dependent remodeling with exercise yields to compensatory adjustments. Moreover, at the later time points, there was also downregulation of both collagen genes and genes involved in collagen turnover, a pattern mirroring aging-related fibrosis. By comparison, twofold fewer genes were differentially regulated in ventricles vs.

OPEN ACCESS

Edited by:
Flavia Ravelli,
University of Trento, Italy

Reviewed by:
David R. Van Wagoner,
Case Western Reserve University, United States
Marja Steenman,
INSERM U1087 L'unité de recherche de l'institut du thorax, France

***Correspondence:**
Robert Lakin
lakinrob@yorku.ca
Peter H. Backx
pbackx@yorku.ca

† These authors share first authorship

Specialty section:
This article was submitted to Cardiac Electrophysiology, a section of the journal Frontiers in Physiology

Received: *12 September 2020*
Accepted: *26 November 2020*
Published: *23 December 2020*

Citation:
Oh Y, Yang S, Liu X, Jana S, Izaddoustdar F, Gao X, Debi R, Kim D-K, Kim K-H, Yang P, Kassiri Z, Lakin R and Backx PH (2020) Transcriptomic Bioinformatic Analyses of Atria Uncover Involvement of Pathways Related to Strain and Post-translational Modification of Collagen in Increased Atrial Fibrillation Vulnerability in Intensely Exercised Mice. Front. Physiol. 11:605671. doi: 10.3389/fphys.2020.605671

atria, independently of TNF. Our findings reveal that exercise promotes TNF-dependent atrial transcriptome remodeling of ECM/mechanosensing pathways, consistent with increased preload and atrial stretch seen with exercise. We propose that similar preload-dependent mechanisms are responsible for atrial changes and AF in both CVD patients and athletes.

Keywords: atrial fibrillation (AF), RNA sequencing (RNA-seq), tumor necrosis factor, inflammation, collagen, mechanotransduction, heart, exercise

INTRODUCTION

Atrial fibrillation (AF) is the most common supraventricular tachyarrhythmia seen in clinical practice (Calkins et al., 2018), with its prevalence predicted to double by 2060 (Krijthe et al., 2013). AF is easily identified in electrocardiographic (ECG) recordings by the presence of rapid rates (typically > 110 beats/min) coupled with regular-irregular QRS complexes and is associated with impaired cardiac output regulation, non-pumping "quivering" atria, and an increased risk of stroke. The etiology of AF is complex, with most patients being elderly and also suffering from cardiovascular diseases (esp., hypertension, heart failure, valve disease) or having increased risk for cardiovascular disease (sleep apnea, hyperthyroidism, obesity, and diabetes) (Odutayo et al., 2016; Staerk et al., 2017). A common physiological feature of all these conditions, including aging, is increased filling pressures (De Jong et al., 2011; Park et al., 2014) which is believed to drive the atrial fibrosis, inflammation and hypertrophy invariably seen in AF patients. The importance of addressing the AF epidemic is highlighted by the > twofold increase in all-cause mortality seen in patients with AF.

Paradoxically, the risk of AF is also increased in veteran endurance athletes (Mont et al., 2002; Redpath and Backx, 2015), despite well-established evidence of beneficial physiological remodeling of the ventricles. Although the underlying basis for exercise-induced AF and its differential effects on the atria and ventricles are unclear, it is well known that intense exercise is associated with marked elevations in filling pressure (Reeves et al., 1990). Moreover, rodent models have established that endurance exercise causes atrial fibrosis, inflammation, and hypertrophy (Guasch et al., 2013; Aschar-Sobbi et al., 2015), as seen in persistent AF patients (Oakes et al., 2009; Qu et al., 2009; Gramley et al., 2010). We previously demonstrated that the exercise-induced atrial changes were prevented by pharmacological and genetic blockade of tumor necrosis factor (TNF), a mechanosensitive and pro-inflammatory cytokine (Aschar-Sobbi et al., 2015; Lakin et al., 2019). However, when TNF blockade was introduced 3 weeks after the beginning of intense exercise, cardioprotection was lost, suggesting that pathways linked to exercise-induced adverse atrial remodeling occur early in the response to exercise.

In this study, we performed bioinformatic analyses of transcriptomic changes in atria and ventricles induced by endurance exercise in wild-type and TNF knockout mice. Our results demonstrate that exercise induces TNF-dependent differential activation (enrichment) of pathways associated with mechanosensitive ECM remodeling that are time-dependent and differ between atria and ventricles, in a manner consistent with preferential stretch of atria in response to exercise-induced elevations in venous pressure. Our findings provide insight into the chamber-specific roles of TNF and mechanical strain in cardiac changes induced by exercise and support the general conclusion that exercise-induced adverse atrial remodeling is preload-dependent as seen in AF associated with aging and poor cardiovascular health.

MATERIALS AND METHODS

Experimental Animals and Endurance Exercise Training Models

This study was carried out in accordance with the recommendations of the Canadian Council of Animal Care. The protocol was approved by the Division of Comparative Medicine at the University of Toronto and York University Animal Care Committee. Mice swam for 2 days (4-sessions), 2 or 6 weeks against water currents in containers, as described previously (Aschar-Sobbi et al., 2015). For the 6 week group, 6 week old CD1 male mice (body weight = 28–34 g, Charles River Laboratories) were acclimatized by swimming twice daily for 30 min (separated by 4 h) after which the duration of the swims was increased by 10 min per day until the duration reach 90 min per swim. Thereafter, the mice swam 2 times per day for 90 min/session for 6 weeks. The swim protocol was similar for the 2 week group, except mice only swam for 2 weeks after acclimatization. These 2 week mice were bred in-house after backcrossing TNF knockout (TNF-KO) mice (c57b, Taconic model #1921) into a CD1 background a minimum of 8 times. After reaching 10 weeks of age, wild-type (WT) mice and their TNF-KO littermates were acclimatized as described for the 6 week mice and swam for 2 weeks. The breeding and housing for the 2 day group were as described for the 2 week group. At 10–12 weeks of age, these mice were familiarized for 3 days with a 10 min swim per day, followed by two consecutive days of twice daily, 90 min swims. The sedentary mice for all groups consisted of the age-matched animals who were placed in swim containers without a water current for 5 min each session to ensure similar handling.

Tissue Harvesting

Prior to harvesting of atrial and ventricular tissue, 0.2 ml of heparin was injected intraperitoneally to prevent blood clotting. After 5 min, mice were anesthetized using 2.5% isoflurane and

sacrificed via cervical dislocation. Hearts were quickly excised and placed into cold phosphate-buffered saline (PBS) to prevent protein or RNA degradation as well as cell apoptosis. In cold PBS, the left atrial appendage (LAA) and left ventricular (LV) free wall were separated and collected for RNA extraction. For our 2 day swim protocol, tissue was harvested 2 h after last swim. For 2 and 6 week studies, tissue was harvested 24 h after the last swim session.

RNA Extraction

Total RNA was extracted for both atria and ventricles using RNeasy Mini Kit (Qiagen), where the silica membrane used for this protocol removes RNA shorter than 200 nucleotides, including 5S/5.8S rRNAs, microRNAs and all tRNAs. All RNA samples were stored at −80°C until use. Initial RNA quantity and quality analyses were done using the Nanodrop2000 spectrophotometer (Thermo Fisher Scientific). The integrity and concentration of the RNA was determined with capillary electrophoresis by Agilent 2100 (Bioanalyzer, Agilent Technologies, Santa Clara, CA, United States) and was performed by the UHN Princess Margaret Genomics Centre (MaRS Centre, TMDT, Toronto, ON, Canada).

RNA Library Preparation and Sequencing (RNAseq)

Both cDNA library generation and RNA sequencing were performed by the Donnelly Sequencing Centre at the University of Toronto (Toronto, ON, Canada) using Illumina's TruSeq stranded mRNA enrichment for library preparation. cDNA was generated from amplified mRNA, which was purified from total RNA. To purify mRNA, oligoT and 3′ poly A tails were hybridized to mRNA only during transcription in the nucleus. Magnetic beads linked to poly T oligo were used to selectively isolate mRNA. The purified mRNA was then fragmented by chemical shear and size selection was performed to generate mRNA fragments > 100 bps. Fragmented mRNA was reversed transcribed by reverse transcriptase and random primers to generate first strand cDNA. Second strand cDNA generated using DNA polymerase I and RNase H. Adapters were ligated on cDNA fragments, followed by enrichment using PCR to generate the final mRNA-derived cDNA library. For 2 week study samples, HiSeq2500 single-end sequencing was performed at 51 cycles. For 2 day study samples, NextSeq500 single-end sequencing was performed at 75 cycles. Technical replicates were generated by running each sample across 2 lanes to ensure there is no technical variability.

Analysis of RNA-Sequencing and Microarray Data

For RNA sequencing (RNA-seq), raw sequencing data were processed using the UseGalaxy server (Afgan et al., 2016). Quality control assessments were performed using FastQC version 0.11.7 (Wingett and Andrews, 2018). Technical replicates were concatenated, then aligned to the mus musculus 10 (mm10) reference genome and quantified using Salmon 0.9.1 with default options (Kim et al., 2015; Patro et al., 2017; Srivastava et al., 2019). A gene was considered differentially expressed if the p-value was less than 0.05 using Student's t-test. Principal component analysis (PCA) was performed to identify the variance that lies between samples. R script was used for PCA analysis (Ringner, 2008; Jolliffe and Cadima, 2016). An example analysis is shown in **Supplementary Figure 1**. For our microarray analysis, normalized and processed microarray datasets from sedentary and 6 week exercise left atrial appendages (LAA) were acquired from ArrayExpress (E-MTAB-3106) (Aschar-Sobbi et al., 2015).

Gene Set Enrichment Analysis (GSEA 4.0.3) was used to identify differentially expressed gene sets ($p < 0.05$ and FDR < 0.20) (Subramanian et al., 2005). The C2 curated gene sets (c2 Canonical pathways) and C5 GO gene sets were used for the GSEA analysis. Weighted enrichment statistic was used and Signal2Noise metric was used for ranking genes. Nominal P-values of each gene set were given using 10,000 and 1,000 permutations of gene sets for analysis using c2 canonical pathway database and c5 GO database, respectively. Gene sets with fewer than 15 genes or more than 500 genes were excluded. Enrichment maps were generated to visually identify clusters of gene sets on Cytoscape 3.4.0 using the gene sets that were statistically different ($p < 0.05$ and FDR < 0.20) between two groups. Edge and node cut-off values were set to 0.375 (default) and 0.1, respectively. Wordcloud version 3.1.3 was used to annotate clusters. The "difference-of-the-difference" analysis was conducted to identify TNF-dependent pathways by subtracting the gene sets that were significantly differentially regulated between sedentary and swim in WT samples from those differentially regulated between sedentary and swim in KO samples.

Heat maps and hierarchal clustering of genes were performed with MATLAB (version 2016a), using all genes belonging to ECM, focal adhesion, integrin and cell-cell communication-related gene sets. Comparisons of transcripts per kilobase million (TPM) expression for individual genes from RNA-seq between two groups utilized unpaired (two-tailed) t-test, and genes with P-values of less than 0.05 were considered significant. All genes in the heat maps are significantly different between sedentary and swim WT ($p < 0.05$).

Telemetric Hemodynamics

Radiofrequency emitting hemodynamic telemetry devices (Data Sciences International, Inc.) were implanted sub-dermally into the interscapularis region. A fluid-filled catheter was inserted into the right common carotid artery and advanced into the left ventricle. After 7 days of recovery, a 30 min baseline recording preceded an acute, 90 min swim exercise bout. Left ventricular end-diastolic pressure (LVEDP) was used as an index of left atrial pressure. Data were analyzed using Ponemah Physiological Platform analysis software (Data Sciences International, Inc.).

Cardiac Electrical Remodeling and Arrhythmia Vulnerability

Electrical properties and arrhythmia inducibility were assessed as previously described (Aschar-Sobbi et al., 2015). For these measurements, mice were anesthetized (1.5% isoflurane and oxygen mixture) followed by isolation of the right jugular

vein and insertion of a 2.0F octapolar recording/stimulation EP catheter (CI'BER Mouse, Numed), which was subsequently advanced into the right ventricle. Programmed electrical stimulations were delivered to the right atria or right ventricle to assess arrhythmia inducibility. All stimulations were delivered at a magnitude of 1.5 times capture threshold and 1 ms pulse duration. Effective refractory periods (ERPs) were determined by delivering nine pulses at 20 ms below the R-R interval followed by an extra stimulation. The S2 coupling interval was initially delivered above capture (∼40 ms) and reduced by 5 ms increments and adjusted until capture was achieved. For arrhythmia induction, 27 pulses at 40 ms intervals were applied to each chamber and reduced at 2 ms decrements to 20 ms. In the absence of inducibility, a second protocol of 20 trains (every 1.5 s) of 20 pulses (2 ms duration) at a 20 ms interpulse interval were applied. Only reproducible episodes of rapid, chaotic, and continuous atrial or ventricular activity of more than 10 s were defined as a sustained arrhythmic event.

Histology and Macrophage Infiltration

For histology, hearts were perfused with PBS containing 1% KCl followed by 4% paraformaldehyde (PFA) in 0.01 M PBS and stored overnight in 4% PFA in 0.01 M PBS at 4°C. Hearts were then embedded in paraffin and 5 μm thin sections were stained with Picrosirius red (PSR) for collagen visualization and quantification. Collagen expression was quantified using ImageJ software as the ratio of positively stained tissue area to total tissue area of each section using the threshold method (Hadi et al., 2011). To quantify macrophage infiltration, antibodies against mouse Mac-3 (1:200, BD Pharminogen, Cat.#553322) were used with the streptavidin-biotin diaminobenzidine chromogen detection method (Vector Laboratories). Mac-3-positive cells were counted in at least three different left atrial appendage sections (100 μm apart) in each replicate and normalized to the total tissue area of each slice. Images were acquired using Metamorph software (Molecular Devices) and analyzed using ImageJ software.

In vitro ADAM17 Enzymatic Activity Assay

In vitro ADAM17 enzymatic activity was measured, as previously described (Shen et al., 2018). Briefly, atrial protein was extracted using a lysis buffer with a high yield of membrane-bound proteins (Cacodylic acid 10mM, NaCl 150 nM, ZnCl2 1 μM, CaCl2 20 mM, NaN3 1.5 mM, Triton X-100 1%, pH 5.0). Mca-Pro-Leu-Ala-Gln-Ala-Val-Dpa-Arg-Ser-Ser-Ser-Arg-NH2 fluorogenic peptide substrate III (R&D Systems, ES003) was used as the substrate for ADAM17. Mca-Pro-Leu-OH (Bachem, M-1975) calibration standard was used to calculate the conversion factor, and recombinant mouse ADAM17 (R&D Systems, 2978-AD) served as a positive control. The ADAM17 activity assay was carried out per the R&D systems protocol. A total amount of 5 μg protein was used for ADAM17 enzymatic activity assay, which was run as a kinetic assay mode for 2 h. Each sample was run in triplicates. ADAM17 activity is expressed as pmol/min/μg tissue protein.

Gelatin Zymography

MMP2 and MMP9 activity levels were assessed by *in vitro* gelatin zymography, as previously described (Jana et al., 2020). In brief, equal amounts (20 μg) of non-reduced atrial tissue lysate were run on 8% SDS-PAGE gel containing 1 mg/ml gelatin. Following electrophoresis, gels were renatured with 2.5% Triton X-100 buffer for 60 min (room temperature). The gels were then put in calcium assay buffer (50 mM Tris-Cl, pH 7.5, 5 mM CaCl2, 150 mM NaCl) and incubated overnight (37°C). Gels were then stained with 0.05% Coomassie Blue G-250, and grayscale images were scanned and inverted for densitometric quantification. Band intensity was quantified using the inbuilt ImageQuant TL software (Version 7.0 GE Healthcare) and normalized to a loading control.

Immunofluorescent Analyses

Left atrial tissue from each heart was flash-frozen in mounting compound (OCT). Immunohistochemical staining was performed on 5 μm sections (all other staining). Immunostaining for OPN (ab8448; Abcam), SPARC (MAB941, R&D Systems), and GAPDH (#2118. Cell Signaling Technology) were performed on frozen OCT sections, as previously described (Sakamuri et al., 2016).

Protein Extraction and Western Blot Analyses

Flash-frozen atria were freeze-crushed in tissue lysis buffer containing EDTA-free protease inhibitor cocktails and processed for protein extraction and immunoblotting as previously described (Sakamuri et al., 2016). Antibodies used for immunoblotting were as follows: OPN (ab8448; Abcam), SPARC (MAB941, R&D Systems), and GAPDH (#2118, Cell Signaling Technology). Band intensities were quantified using densitometry analysis software (ImageQuant TL 7.0; GE) and values were normalized to GAPDH expressions for each sample.

Statistics

Statistical analyses of transcriptional changes are described above. Unpaired (two-tailed) *t*-test was used to assess differences in ADAM17 activity, gel zymography, and western blot analyses. *P*-values of less than 0.05 were considered significant.

RESULTS

Consistent with previous work (Aschar-Sobbi et al., 2015), 6 weeks of swimming increased ($P < 0.001$) AF inducibility (**Figure 1A**), which was associated with increased ($P < 0.003$) left atrial (LA) inflammatory (Mac-3+) cell infiltrations (**Figures 1B,C**) and fibrotic remodeling (**Figures 1D,E**), as well as hypertrophy (not shown) in left atrial appendages (LAA). By contrast, the left ventricle (LV) showed enhanced function without fibrosis (**Figures 1D,E**), inflammation (data not shown) nor increased arrhythmia vulnerability in response to exercise, consistent with a chamber-specific effect of intense exercise.

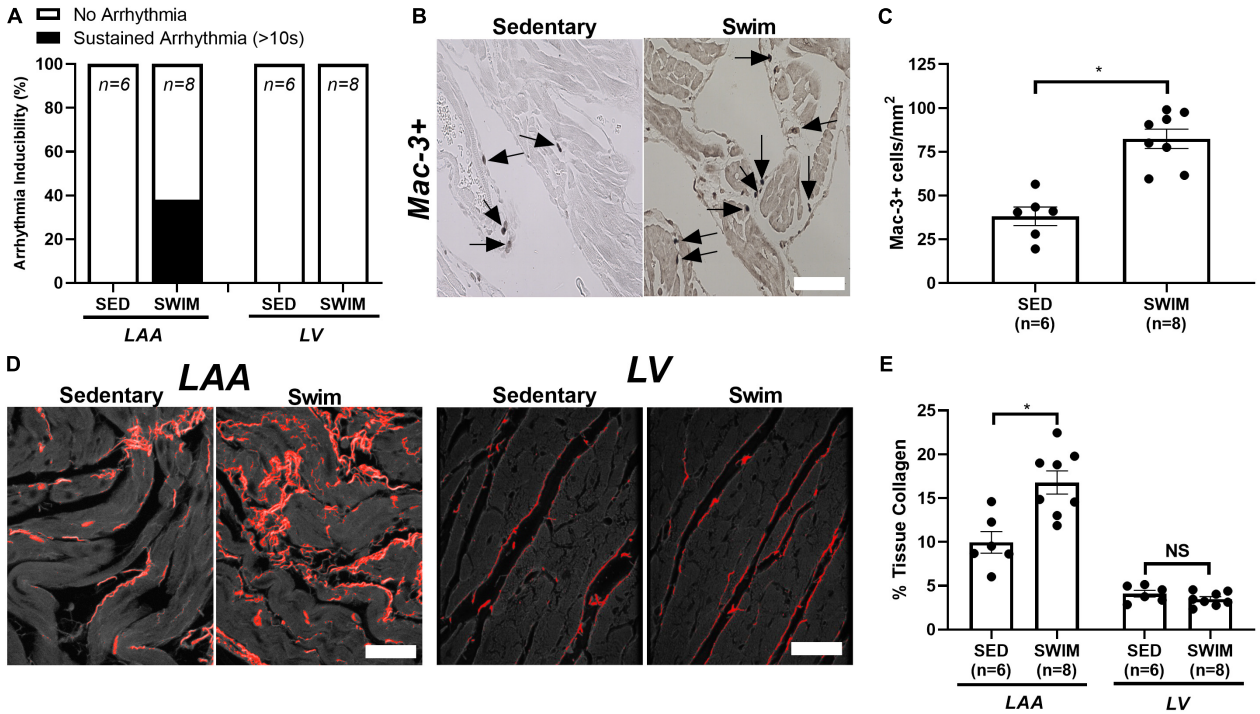

FIGURE 1 | Intense exercise-induced adverse atrial remodeling and atrial fibrillation (AF) vulnerability. **(A)** 6 week swim exercise training is associated with increased atrial fibrillation (AF) inducibility, with no evidence of left ventricular (LV) arrhythmia vulnerability, compared to sedentary mice. **(B,C)** Swim exercise was associated with increased inflammatory cell infiltration (macrophage, Mac-3+) compared to sedentary mice. **(D,E)** Increased fibrosis (%tissue collagen) was observed in the left atrial appendage (LAA) with 6 week swim exercise compared to sedentary mice, with no elevations in fibrosis observed in the LV. Data presented as mean ± SEM. $^*P < 0.05$.

Our previous microarray data from atria of mice after 6 weeks (Aschar-Sobbi et al., 2015) revealed exercise-induced transcriptional changes consistent with increases in inflammatory genes. As shown in **Supplementary Figures 2,3**, additional bioinformatics analyses verified enrichment in exercised atria of gene sets/clusters associated with inflammation ($P < 0.05$, FDR < 0.2) along with pathways involved in cell cycle regulation, mitochondrial fatty acid, and biological oxidation as well as metabolism/processing of DNA, RNA, and amino acids. Additionally, gene sets linked to mechanosensitive pathways (i.e., focal adhesion kinases (FAK), integrins, cell-cell communication) as well as extracellular matrix (ECM) remodeling (i.e., collagen formation, degradation, biosynthesis, assembly, cross-linking, and matrisome enzymes) were also differentially regulated between WT exercised and sedentary atria. However, despite the elevations in atrial fibrosis after 6 week of exercise, transcriptional levels of individual collagen genes (i.e., *Col1a1*, *Col3a1*, and *Col4a1*) were paradoxically reduced in WT exercised atria.

The unexpected lack of transcriptional elevations in collagen genes, combined with the inability of TNF blockade to prevent atrial fibrosis when started 3 weeks after exercise initiation (Aschar-Sobbi et al., 2015), suggests that pathways driving fibrosis are engaged early following exercise initiation. Therefore, we investigated the transcriptome responses after 2 weeks of exercise. In order to get greater gene coverage, we used deep RNA sequencing (RNA-seq) for these studies. Since TNF gene disruption prevented adverse atrial changes and exercise-induced AF in a chamber-dependent manner, RNA-seq was performed on atria and ventricles from both WT and TNF-KO mice. We first present the transcriptome changes with exercise in atria and discuss the ventricular results thereafter. For clarity, we illustrate our bioinformatic results by displaying each differentially regulated gene set as an individual dot (blue for enriched in swim and red enriched in sedentary). All closely related gene sets were represented by lines using Cytoscape 3.4.0 which allowed gene sets to be grouped into "gene clusters" with common and overlapping function and/or genes. To help focus our discussion, our graphic representations did not include clusters of gene sets with 2 or fewer related gene sets. The total number of differentially regulated gene sets and the number of gene sets in each cluster are presented in each figure.

Transcriptional Responses in Atria After 2 Weeks of Exercise

Principal component analysis (PCA) showed (an expected) distinct separation between atria and ventricles (**Supplementary Figure 1**). Surprisingly, there was little separation between WT and TNF-KO, regardless of chamber or exercise status. A remarkable feature of PCA results is the much larger effect of exercise on atrial vs. ventricular transcriptomes, for either genotype. These findings establish that exercise has a far greater

impact on atrial vs. ventricular transcriptomes while TNF ablation has a relatively minor impact on exercise-induced changes in either chamber.

The specific gene sets that were differentially affected in WT atria by 2 weeks of exercise are represented in **Figure 2** and **Supplementary Table 1**. The 2 week results in the TNF-KO mice are presented later. These analyses identified 112 differentially regulated ($P < 0.05$ and FDR < 0.2) gene sets, with 64 of these falling into clusters with common function (**Figure 2A**). Of these, gene sets linked to ATP synthesis and oxidative phosphorylation were enriched with swimming, which is not unexpected given the known cardiac bioenergetic adaptations to exercise (Vega et al., 2017). More interesting perhaps, was the finding that ∼28% of the differentially regulated gene sets were linked to mechanosensing (i.e., integrin/focal adhesion signaling), cell-cell communication, and ECM (i.e., collagen turnover, cross-linking, and matrisome remodeling), compared to only 15% after 6 weeks of exercise. As discussed later, differential regulation of these gene sets seems highly relevant because atrial stretch is central to AF pathogenesis (Vranka et al., 2007; Remes et al., 2008). Nevertheless, these gene sets were enriched in sedentary atria of WT mice (see **Supplementary Table 2** for separation of these gene sets into different functional categories). Importantly, the expression levels of the major cardiac collagen types did not vary between the groups, suggesting that fibrotic responses to exercise after 2 weeks are limited to collagen turnover and stability (discussed below). Consistent with this notion, notch as well as the closely related Ephrin-related pathways were also enriched in the atria of WT sedentary compared to swim mice, which both play central roles in early embryogenesis (Sanz-Ezquerro et al., 2017) and are associated with hypertrophy and fibrosis in the heart as well as other tissues (Su et al., 2017).

Despite the protective effects of TNF blockade on the atrial changes induced by exercise, the 2 week WT exercised atria did not show clear evidence of differential regulation of genes related to inflammation or TNF signaling, although several TNF-related pathways were just beyond our cut off criteria [NFκB-IKK ($P = 0.04$, FDR = 0.327), RelA ($P = 0.06$, FDR = 0.329), TNFR1 ($P = 0.08$, FDR = 0.384), and IL1R ($P = 0.10$, FDR = 0.384)]. By contrast, TNF-related gene sets [e.g., Toll-like receptor, interleukin, and TNF-related pathways (NF-κB and p38 MAPK)] were differentially regulated between swim and sedentary atria from TNF-KO mice, with enrichment in the sedentary group (**Figure 2B** and **Supplementary Table 1**). It is important to note that the number of gene sets related to ECM/mechanosensing was far less (i.e., 2 vs. 30) and did not form clusters in TNF-KO compared to WT mice, which aligns with the absence of exercised-induced atrial fibrosis when TNF is inhibited. Although at first glance this pattern of differential regulation with exercise in TNF-KO atria seems unexpected, we provide additional data below supporting the conclusion that TNF plays a permissive, rather than a primary role, in exercise-mediated atrial remodeling.

The TNF-dependence of the gene sets that are differentially regulated with exercise are summarized in **Figure 2C** as the "difference-of-the-difference" results (see section "Materials and Methods"). These analyses reveal, not unexpectedly, that exercise induces TNF-dependent changes in gene sets involved with ECM/mechanosensing, collagen production/turnover, fatty acid metabolism, oxidative phosphorylation as well as notch and ephrin signaling, with all these gene sets being enriched in the atria of WT compared to TNF-KO mice. To better understand the involvement of TNF in exercise-induced atrial remodeling, we further assessed the TNF-dependence of specific differentially regulated genes by generating heat maps of genes related to mechanotransduction and ECM (**Figure 3**). For these purposes, genes were separated into TNF-dependent (cluster 1 genes, whose expression differed in WT only) vs. TNF-independent genes (cluster 2 genes whose expression differ in both genotypes). As shown in **Figure 3**, far more genes were regulated in a TNF-dependent than a TNF-independent manner. Since TNF-KO abrogates atrial fibrosis as well as AF inducibility, we focused our attention initially on TNF-dependent collagen/ECM/mechanosensing genes (**Supplementary Table 2**). Of these, *Mmp2* and *Mrc2* are reduced in atria after 2 weeks of exercise which is of particular interest because these genes are also reduced in the age-related fibrosis of multiple tissues (Podolsky et al., 2020) and AF is strongly linked to aging (Heeringa et al., 2006).

It is also worth stating that many specific ECM/mechanosensing-related genes whose expression was downregulated in TNF-dependent manner with exercise have been linked previously to AF and ECM remodeling, including *Comp* (Zou et al., 2018; Thomas et al., 2019), *Thbs2* (Yang et al., 2000), *Ltbp1* and *Fbn1* (Zhang et al., 2020; **Figure 3** and **Table 1**). On the other hand, most genes linked to collagen production (i.e., *Col1a1*, *Col1a2*, *Col3a1*) were TNF-independent. Since TNF-KO abrogates fibrosis and AF inducibility, these results suggest (see section "Discussion") that the cluster 2 genes are not central to the adverse atrial changes induced by exercise. In light of the impact of TNF on atria induced by exercise, it is worth pointing out that only two genes, *Comp* (TNF-dependent) and *PIK3R2* (TNF-independent) are upregulated with exercise in swim WT vs. swim TNF-KO atria (see Discussion). Additional gene sets and individual genes linked to ECM/mechanosensing and/or AF are listed in **Table 1** and **Supplementary Tables 1–3**, respectively.

Transcriptional Responses in Atria After 2 Days of Exercise

The observation that ECM/FAK/integrin gene sets pathways were generally enriched in sedentary atria at 2 and 6 weeks, despite atrial fibrosis at 6 weeks in exercised mice, prompted us to perform RNAseq measurements in hearts after only 2 days of exercise (i.e., 4-sessions of 90 min swims). Consistent with 2 week data, PCA showed the expected separation between atria and ventricles (**Supplementary Figure 1**). Surprisingly, while there were distinct separations between exercise and sedentary atrial samples, this was not true in ventricles, suggesting a much smaller effect of exercise on ventricular transcriptomic remodeling. Moreover, there was overlap between WT and TNF-KO, regardless of chamber or exercise status, suggesting TNF ablation may have a minor impact on acute exercise-induced changes.

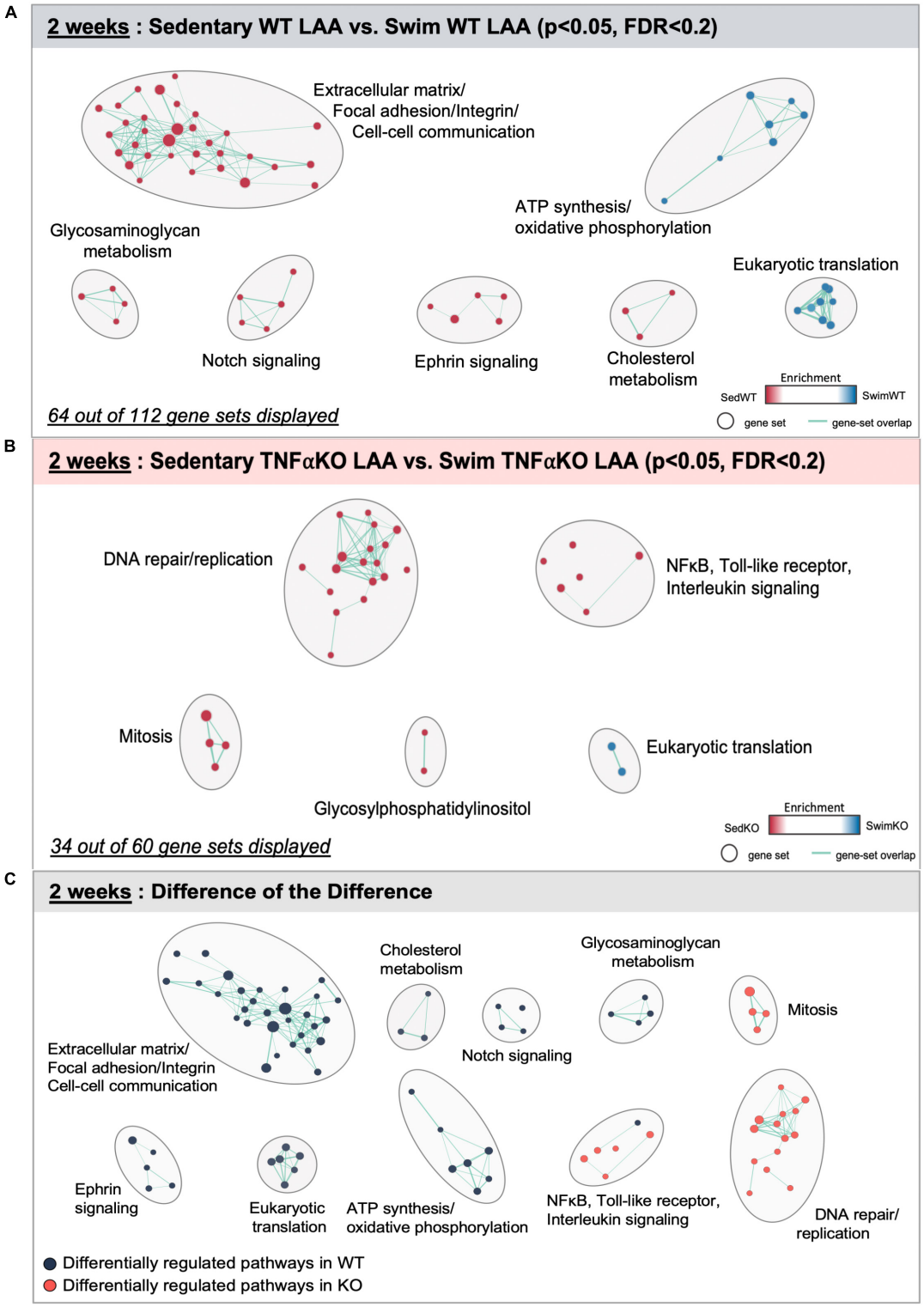

FIGURE 2 | Differentially regulated pathways in the atria of 2 week swim exercised wild-type (WT) and tumor necrosis factor (TNF) knockout (KO) mice. **(A)** Gene set enrichment analysis (GSEA) and enrichment mapping showing clusters of differentially regulated pathways in the left atrial appendage (LAA) between WT 2 week swim (blue dots) and sedentary (red dots) mice. **(B)** Enrichment map showing clusters of differentially regulated pathways in the left atrial appendage (LAA) of TNF-KO 2 week swim and sedentary mice. **(C)** Enrichment map of the difference of the difference analysis revealing clusters of exercise-induced differentially regulated pathways in WT (blue dots) vs. TNF-KO (orange dots) mice. Only gene sets that form clusters are shown for clarity, with connecting lines indicating gene set overlap. Nominal *P*-value < 0.05, false discovery rate (FDR) < 0.20.

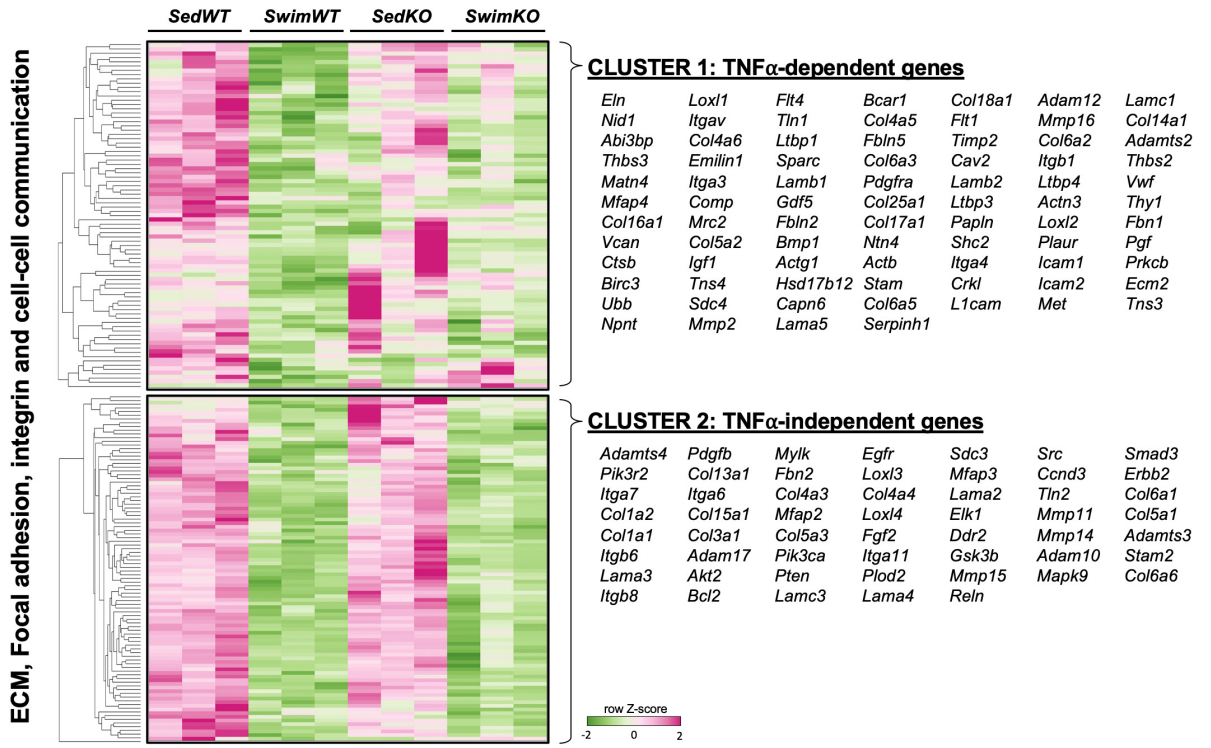

FIGURE 3 | Heat map and clustering analysis of the tumor necrosis factor (TNF)-dependence of extracellular matrix (ECM)-, integrin-, and cell-cell communication-associated genes in 2 week swim exercised mice. Heat map and cluster analysis of individual genes belonging to ECM-, integrin-, and/or cell-cell communication-associated gene sets that are TNF-dependent (cluster 1) or TNF-independent (cluster 2). Note that all individual genes were enriched in sedentary (Sed) vs. swim mice. TNF-dependent (cluster 1) is: SedWT vs. SwimWT ($P < 0.05$) and SedKO vs. Swim KO (not $P < 0.05$). TNF-independent (cluster 2) is: SedWT vs. SwimWT ($P < 0.05$) and SedKO vs. SwimKO ($P < 0.05$).

The results of our GSEA analyses for mice after 2 days of exercise are summarized in **Figure 4** and **Supplementary Table 4**. The data reveals that 101 gene sets were differentially regulated ($P < 0.05$, FDR < 0.2) between swim (total of 61 differentially regulated gene sets) vs. sedentary (40 gene sets) atria in WT mice, with 60 sets clustering into common pathways (**Figure 4A**). Importantly, unlike what was seen after 2 and 6 weeks of exercise, ECM/mechanosensing gene sets were now more enriched in exercise vs. sedentary atria (**Supplementary Table 4**). Acute exercise also induced enrichment in gene sets related to actin/tubulin folding, which cross-talks to many hypertrophic signaling pathways (i.e., MAPK/FGFR1/2) linked to dilated and hypertrophic cardiomyopathy (Caporizzo et al., 2019), as well as IQGAPs, PAKs, and AMPK activation (see section "Discussion") (Hedman et al., 2015; Daskalopoulos et al., 2016). On the other hand, TNF-related gene sets in acute exercise were only differentially regulated in TNF-KO atria (**Figure 4B**) with reductions in many specific pro-inflammatory genes in exercised mice [i.e., toll-like receptor 10 ($p < 0.008$, FDR = 0.178), IL-2 ($p = 0.018$, FDR = 0.187), IL-2-STAT5 ($p = 0.018$, FDR = 0.240), TAK1 ($P < 0.037$, FDR = 0.278), and NFκB ($P < 0.005$, FDR = 0.124)].

The difference-of-the-difference analyses after 2 day exercise clearly establish that gene sets involved in mechanosensitive pathways are uniquely differentially enriched in exercised WT atria, while TNF-related signaling and DNA replication/repair pathways are uniquely enriched in sedentary KO mice (**Figure 4C**). Heat maps of differentially ($P < 0.05$) regulated genes revealed (**Figure 5**) a distinct pattern after 2 days of exercise compared to 2 weeks. Now, many TNF-dependent genes linked to ECM remodeling as well as AF are upregulated with exercise in WT atria compared to sedentary, including *Mmp14* (Simmers et al., 2016), *Fgf2* (i.e., fibroblast growth factor 2, which activates p38 and induces cardiac hypertrophy as well as fibrosis) (Itoh and Ohta, 2013), *Gsk3*β (Sugden et al., 2008), and *Tln1* (Manso et al., 2013). On the other hand, only *Fgf2* was upregulated ($P = 0.0142$) in WT vs. KO exercised atria, suggesting TNF-dependent activation of FGF signaling pathways may be important early responses that regulate exercise-induced atrial remodeling. Nonetheless, these results suggest that acute exercise leads to TNF-dependent and TNF-independent transcriptome changes affecting ECM remodeling. Additional genes and their links to ECM/mechanosensing and/or AF are listed in **Table 2**.

Transcriptional Changes in Ventricles With Exercise

As mentioned, after 2 weeks of exercise, PCA showed relatively small effects of exercise on ventricles (compared to atria) at all-time points. Before directly comparing LV

TABLE 1 | Differentially regulated genes with 2 weeks exercise of the ECM-receptor, integrin, and cell-cell communication pathways associated with hypertrophic remodeling and/or atrial fibrillation (AF).

Gene	Gene product	Directional change with swim exercise	Tumor necrosis factor (TNF) dependent?	Link(s) to fibrotic and/or hypertrophic remodeling and AF vulnerability
Adam10	A disintegrin and metalloprotease (ADAM) 10	↓	No	Processes membrane bound TNF to a soluble form, which in turn can induce MMPs and drive ECM remodeling (Manso et al., 2006; Murphy, 2008)
Adam12	A disintegrin and metalloprotease (ADAM) 12	↓	Yes	Regulator of MMPs and linked to prevention of cardiac hypertrophic and fibrotic remodeling through reductions in TGF-β- and integrinβ1-mediated FAK/Akt, ERK, and Smad signaling (Frangogiannis, 2012; Nakamura et al., 2020)
Adam17	A disintegrin and metalloprotease (ADAM) 17	↓	No	A metalloprotease and disintegrin, also known as TNF-α converting enzyme (TACE), that cleaves TNF to its soluble form and has been implicated in pressure overload-induced hypertrophic and fibrotic remodeling (Xu et al., 2016) and AF vulnerability (Weeke et al., 2014)
Adamts2	Adamts2	↓	Yes	Extracellular enzyme that activates pro-collagens I, II, III, and V (Wang et al., 2017b), and is a regulator of MMPs linked to cardiac hypertrophic and fibrotic remodeling in pressure-overload (Dong et al., 2013)
Bcl2	B-cell lymphoma 2	↓	No	Increased expression of BCL-2/BCL-2-associated X protein (BAX) linked to fibrosis and apoptosis in AF (Xu et al., 2013; Diao et al., 2016)
Bmp1	Bone morphogenetic protein 1	↓	Yes	A peptidase that cleaves the C-terminal pro-peptides of procollagen I, II, and III and mediates the proteolytic activation of lysyl oxidase LOX (Rodriguez and Martinez-Gonzalez, 2019)
Col4a4, Col5a1, and Col5a3	Collagen type IV, alpha 4 chain; collagen type V, alpha 1 chain; and collagen type V, alpha 3 chain	↓	No	Collagen transcripts linked to AF and rhythm outcome following ablation (Husser et al., 2016)
Col6a6	Collagen type VI Alpha 6 Chain	↓	No	Collagen protein encoding gene containing multiple von Willebrand factor (vWF) domains. Linked to extracellular matrix (ECM)-receptor interactions and is upregulated in AF (Zou et al., 2018)
Ctsb	Cathepsin B	↓	Yes	Lysosomal cysteine proteases localized in lysosomes and endosomes that function to degrade cellular substrates (Turk et al., 2000). Stimulated by TNF and linked to hypertrophic and fibrotic cardiac remodeling (Cheng et al., 2012b). Upregulated in AF (Thomas et al., 2019)
Erbb2	HER-2; receptor tyrosine kinase	↓	No	A receptor involved in physiological cardiac adaptations and hypertrophic remodeling through the activation of MAPK, PI3K/Akt and Src/FAK signaling pathways (Vermeulen et al., 2016)
Fbln2	Fibulin-2	↓	Yes	ECM glycoprotein involved in angiotensin-II-mediated TGF-β signaling and cardiac hypertrophy (Zhang et al., 2014)
Fbn1	Fibrillin 1	↓	Yes	Large ECM glycoprotein and constituent of the myocardial ECM that is linked to reactive and reparative fibrotic remodeling (Bouzeghrane et al., 2005) and is upregulated in AF (Zhang et al., 2020)
Igf1	Insulin-like growth factor-1	↓	Yes	A hormone that has pleiotropic actions in the heart and mediated eccentric hypertrophy through PI3K- and MAPK-dependent mechanisms (Lavandero et al., 1998)

(Continued)

TABLE 1 | Continued

Gene	Gene product	Directional change with swim exercise	Tumor necrosis factor (TNF) dependent?	Link(s) to fibrotic and/or hypertrophic remodeling and AF vulnerability
Itga4, Itgb1, Itgb6	Integrin alpha-4, beta-1, and beta-6 precursors	↓	No	ECM proteins involved in mechanotransduction linked to AF incidence and rhythm outcome following ablation (Husser et al., 2016)
Ltbp1, *Ltbp3,* and *Ltbp4*	Latent transforming growth factor (TGF)- β binding proteins	↓	Yes	Family of secreted multidomain proteins that bind to and regulate TGFβ-dependent activation and pro-fibrotic remodeling (Goumans and Ten Dijke, 2018) as well as AF (Thomas et al., 2019; Zhang et al., 2020)
Mfap4	Microfibril-associated protein 4	↓	Yes	A matricellular protein associated with AF and atrial fibrotic remodeling (Zhang et al., 2019)
Pgf	Placental growth factor	↓	Yes	A member of the VEGF (vascular endothelial growth factor) family known to induce cardiac fibroblasts to secrete TNF and other pro-hypertrophic factors (Accornero and Molkentin, 2011)
Pdgfb	Platelet-derived growth factor subunit B	↓	No	Increased PDGF-B expression linked to focal cardiac fibrosis and moderate cardiac hypertrophy (Gallini et al., 2016)
Pdgfra	Platelet-derived growth factor α receptor	↓	Yes	Cardiac mast cells synthesize and release PDGF-A and mediates both fibrosis and AF in pressure-overloaded hearts (Liao et al., 2010; Wang et al., 2017a)
Plod2	Procollagen-lysine, 2-oxoglutarate 5-dioxygenase 2 (PLOD2)	↓	No	Lysyl hydroxylase linked to both TNF- and TGFβ1-mediated pyridinoline cross-linking inherent to fibrotic cardiac remodeling (van der Slot et al., 2005)
Pten	Phosphatase and tensin homolog (PTEN)	↓	No	A protein linked to increased pathological hypertrophy and progression to heart failure in response to biomechanical stress (Oudit et al., 2008)
Reln	Reelin	↓	No	A large secreted ECM glycoprotein that regulates pathways associated with ECM-receptor interaction and focal adhesion and its expression is linked to AF (Husser et al., 2016; Zhao et al., 2018; Zou et al., 2018)
Sdc4	Syndecan-4	↓	Yes	A transmembrane (type I) heparan sulfate proteoglycan that interacts with the ECM and is a primary determinant in collagen cross-linking and LOX induction in pressure-overload hearts (Herum et al., 2015)
Serpinh1	Heat shock protein 47 (HSP47)	↓	Yes	A chaperone protein for collagen involved in cardiac injury-induced fibrosis and reductions in hypertrophy in cardiac pressure-overload (Khalil et al., 2019)
Sparc	Secreted protein acidic and cysteine rich (Sparc)	↓	Yes	A matricellular protein that is activated by several MMPs (i.e., MMP-2) and is elevated in cardiac hypertrophy and fibrosis in pressure-overload (Bradshaw et al., 2009) and aging (Bradshaw et al., 2010)
Src	Proto-ongogene tyrosine-protein kinase Src	↓	No	A tyrosine kinase that phosphorylates FAK (Frame et al., 2010) and is activated in response to integrin clustering and activation as well as LOX-mediated ECM remodeling (Schneider et al., 2008)
Thbs2	Thrombospondin-2	↓	Yes	A matricellular protein involved in myocardial matrix integrity (Schroen et al., 2004) and linked to protection against inflammatory-induced cardiac injury and dysfunction (Papageorgiou et al., 2012)
Tln1	Talin-1	↓	Yes	A ubiquitously expressed protein localized to costameres that become more prominent during mechanical stress-induced cardiac hypertrophy and fibrosis (Manso et al., 2013) and is upregulated in AF (Weeke et al., 2014)
Vwf	von Willebrand factor	↓	Yes	A prothrombotic plasma marker and index of endothelial damage and dysfunction that is prominently linked to AF incidence, rhythm outcome following ablation (Husser et al., 2016) and stroke risk (Zhong et al., 2018; Ye et al., 2020)

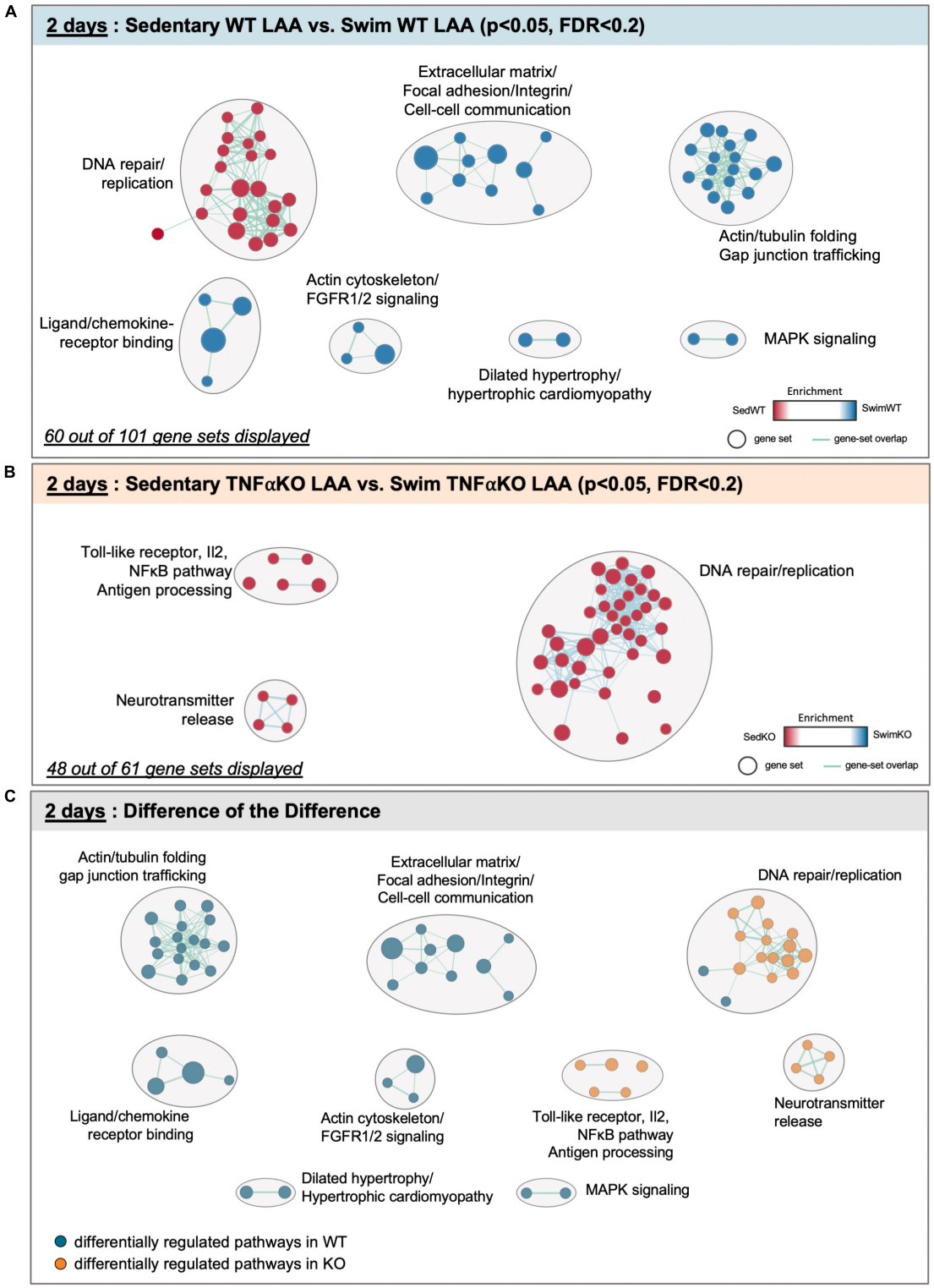

FIGURE 4 | Differentially regulated pathways in the atria of 2 day swim exercised wild-type (WT) and tumor necrosis factor (TNF) knockout (KO) mice. **(A)** Gene set enrichment analysis (GSEA) and enrichment mapping showing clusters of differentially regulated pathways in the left atrial appendage (LAA) between WT 2 day swim (blue dots) and sedentary (red dots) mice. **(B)** Enrichment map showing clusters of differentially regulated pathways in the LAA of TNF-KO 2 day swim (blue dots) and sedentary (red dots) mice. **(C)** Enrichment map of the difference of the difference analysis revealing clusters of exercise-induced differentially regulated pathways in WT (blue dots) vs. TNF-KO (orange dots) mice. Only gene sets that form clusters are shown for clarity, with connecting lines indicating gene set overlap. Nominal *P*-value < 0.05, false discovery rate (FDR) < 0.20.

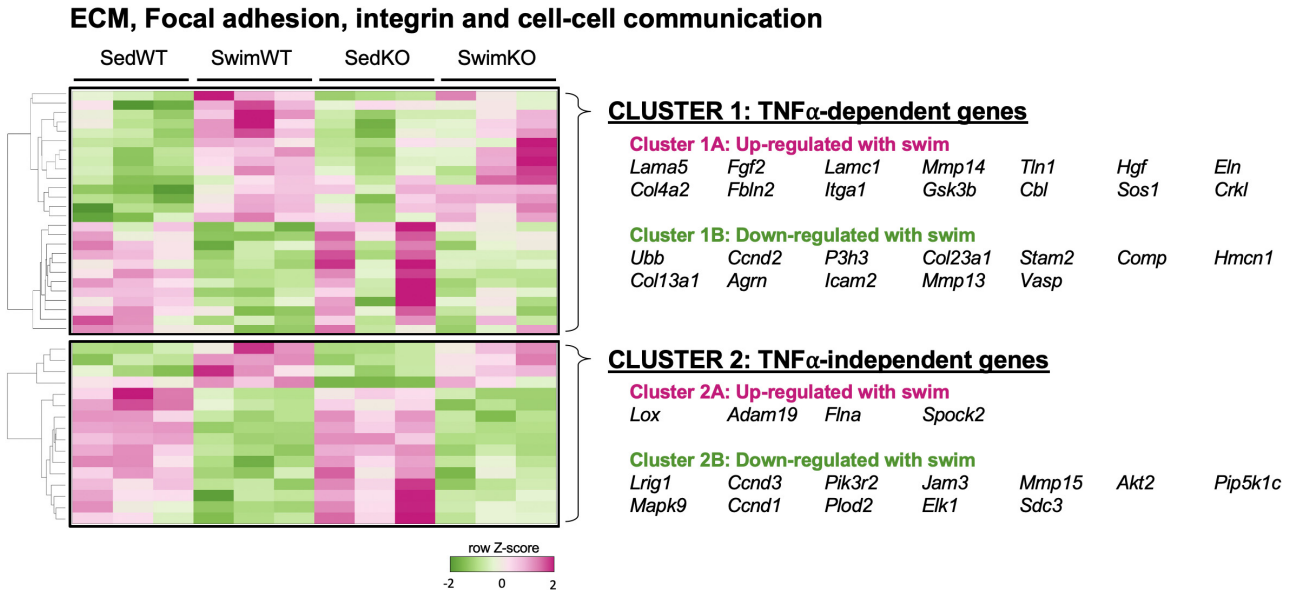

FIGURE 5 | Heat map and clustering analysis of the tumor necrosis factor (TNF)-dependence of extracellular matrix (ECM)-, integrin-, and cell-cell communication-associated genes in 2 day swim exercised mice. Heat map and cluster analysis of up- or down-regulation of individual genes belonging to ECM-, integrin-, and/or cell-cell communication-associated gene sets that are TNF-dependent (cluster 1) or TNF-independent (cluster 2) in 2 day swim mice. TNF-dependent (cluster 1) is: SedWT vs. SwimWT ($P < 0.05$) and SedKO vs. Swim KO (not $P < 0.05$). TNF-independent (cluster 2) is: SedWT vs. SwimWT ($P < 0.05$) and SedKO vs. SwimKO ($P < 0.05$).

and LA transcriptomic remodeling, we present the effects of exercise on LV genetic plasticity. After 2 weeks, genes sets associated with oxidative phosphorylation and ribosome translation were enriched in exercised WT mice while the genes sets related to ECM/mechanosensing (as in atria) and cardiomyopathy (i.e., HCM, DCM, ARVC), as well as notch, ephrin/Rho GTPases, and MAPK signaling were enriched in sedentary atria (**Supplementary Figure 4A**). By comparison, TNF-KO mice showed enrichment of gene sets linked to amino acid metabolism and TCA cycle with exercise while gene sets associated with ECM/mechanosensing, chemokine, interleukin, and T-cell/B-cell receptor pathways were enriched in the sedentary group (**Supplementary Figure 4B**). Interestingly, after performing the difference-of-the-difference analyses (**Supplementary Figure 4C**) the majority of gene sets that remained were related to TNF-mediated signaling with differential regulation in TNF-KO mice, suggesting that TNF also serves a role in LV remodeling with exercise, albeit less than in LA.

The results above establish that the gene sets inked to ECM/mechanosensitive pathways are quite similar after 2 weeks of exercise between the LA and LV (i.e., **Figure 2C** and **Supplementary Figure 4C**), even though the exercise-induced remodeling is different between the chambers. To more directly assess the differential effects of exercise and TNF on chamber-specific transcriptomic remodeling at 2 weeks, a modified difference-of-the-difference analysis was performed in which TNF-dependent pathways were determined by subtracting the gene sets that were significantly differentially regulated between swim in WT and KO samples within each chamber from those differentially regulated between LA and LV samples. As shown in **Figure 6A**, the number of TNF-dependent differentially regulated gene sets with exercise is far smaller for LVs (i.e., 4) vs. LAs (i.e., 43) at 2 weeks, with little overlap between the gene sets between chambers (i.e., 12). Indeed, while ECM/mechanosensitive pathways were enriched in both the LAs and LVs of sedentary mice at 2 weeks, direct comparisons between chambers highlight the predominance of TNF-dependent differentially gene sets (**Figure 6B**), including ECM/integrin signaling, dilated/hypertrophic cardiomyopathy, and actin/tubulin folding, in the atria, which reinforces the chamber-specific effects of both exercise and TNF on transcriptome remodeling.

The differential impact of exercise on the LA and LV is also apparent in 2 day acutely exercised mice. Indeed, while we found clear evidence of ECM/mechanosensitive pathway enrichment in WT mice at 2 days in the atria (discussed above), when we assessed ventricular changes after 2 day acute exercise, only 16 gene sets were differentially regulated in WT LVs with most of the pathways linked to cell cycle and DNA replication processes (**Supplementary Figure 5A**). By contrast, exercised LV from TNF-KO mice had far greater numbers (211) of differentially regulated gene sets, including ECM/integrin, gap junction and actin/tubulin folding, as well as cell cycle and DNA repair/replication (**Supplementary Figure 5B**), all of which were enriched in sedentary mice. The difference-of-the-difference analysis (**Supplementary Figure 5C**) confirmed enrichment of the above pathways in TNF-KO compared to WT mice. Indeed, heat map and cluster analysis (**Supplementary Figure 6**) identified only three genes linked to ECM/mechanosensing,

TABLE 2 | Differentially regulated genes with acute (2 day) exercise of the ECM-receptor, integrin, and cell-cell communication pathways associated with hypertrophic remodeling and/or atrial fibrillation (AF).

Gene	Gene product	Directional change with swim exercise	Tumor necrosis factor (TNF) dependent?	Link(s) to fibrotic and/or hypertrophic remodeling and atrial fibrillation
Ccnd3	Cyclin D3	↓	No	A protein shown to be upregulated during hypertrophic growth (Busk et al., 2002) and linked to the pathogenesis of AF (Li et al., 2019)
Elk1	Elk-1	↓	No	A transcription factor that is phosphorylated via MEK/ERK kinases and plays a role in cardiac hypertrophy (Babu et al., 2000) as well as regulating stretch-mediated atrial natriuretic factor (ANF) expression (Mahida, 2013)
Fgf2	Fibroblast growth factor 2	↑	Yes	A multifunctional polypeptide that is upregulated by stress (Kardami et al., 2004) and involved in p38 MAPK-mediated cardiac hypertrophy (Tanaka et al., 1999) as well as fibrosis (Itoh and Ohta, 2013)
Gsk3β	Glycogen synthase kinase 3 beta	↑	Yes	An enzyme that serves as a hub for the regulation of both physiological and pathological hypertrophic and fibrotic remodeling (Lal et al., 2015) via TNF-related pathways (Sugden et al., 2008)
Itga1	Integrin, alpha 1	↑	Yes	Cell-cell and cell-matrix adhesion (ECM-receptor interactions), upregulated in AF and linked to rhythm outcome of AF catheter ablation (Husser et al., 2016)
Lama5	Laminin subunit alpha-5	↑	Yes	A component of the ECM, specifically basement membranes, that is upregulated in AF (Husser et al., 2016)
Mmp13	Matrix metalloproteinase 13	↓	Yes	A matrix metalloproteinase and collagenase that targets collagens I and III and is linked to cardiac hypertrophy and fibrosis in pressure overload hearts (Spinale, 2002)
Plod2	Procollagen-lysine, 2-oxoglutarate 5-dioxygenase 2 (PLOD2)	↓	No	Lysyl hydroxylase linked to both TNF- and TGFβ1-mediated pyridinoline cross-linking inherent to fibrotic cardiac remodeling (van der Slot et al., 2005)
Tln1	Talin-1	↑	Yes	A protein mediating cell-cell adhesion linked to AF (Weeke et al., 2014) and becomes more prominent at costameres during mechanical stress and modulates hypertrophic and fibrotic remodeling (Manso et al., 2013)

Mmp16, *Dst,* and *Reln*, that were upregulated in a TNF-dependent manner with acute swim, compared to the 14 genes identified in the LA. The absence of enrichment of gene sets linked to ECM/mechanosensitive pathways in the LV and their upregulation in the LA with 2 day acute exercise supports our contention that strain-dependent signaling mediates exercise-induced atrial remodeling.

Acute Effects of Exercise on Atrial Pressures and Collagen Metabolism/Remodeling

Since AF is primarily observed in cardiovascular conditions associated with elevated diastolic filling pressures (De Jong et al., 2011), we previously postulated (Aschar-Sobbi et al., 2015) that elevated filling pressures seen with exercise may explain the increased incidence of AF in endurance athletes. Consistent with this conjecture, we found that diastolic filling pressures increase from 10 mmHg to ∼45 mmHg within the first 10 min after mice begin swimming exercise (**Figure 7**). Thereafter the pressure falls to ∼20 mmHg over the next 30–50 min after which the filling pressure steadily rise to 40–45 mmHg after 90 min. Such increases in venous filling pressures would be expected to preferentially stretch the thin-walled and compliant atria, which may explain our observation of mechanosensitive and compensatory hypertrophic pathways being disproportionately activated in LAs compared to LVs.

Taken together, our findings demonstrate prominent time-dependent transcriptional changes in genes related to strain-dependent pathways in response to exercise. However,

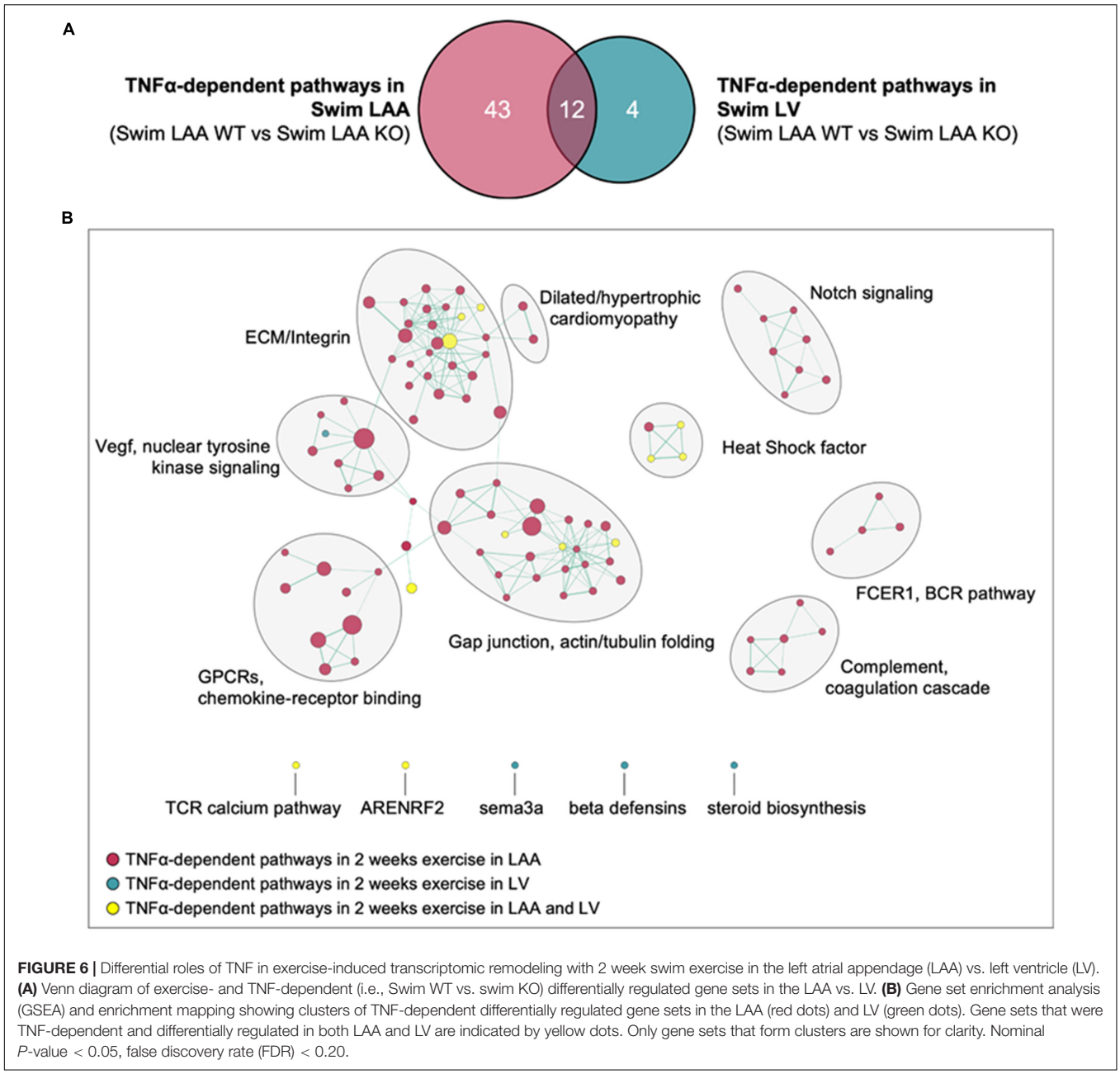

FIGURE 6 | Differential roles of TNF in exercise-induced transcriptomic remodeling with 2 week swim exercise in the left atrial appendage (LAA) vs. left ventricle (LV). **(A)** Venn diagram of exercise- and TNF-dependent (i.e., Swim WT vs. swim KO) differentially regulated gene sets in the LAA vs. LV. **(B)** Gene set enrichment analysis (GSEA) and enrichment mapping showing clusters of TNF-dependent differentially regulated gene sets in the LAA (red dots) and LV (green dots). Gene sets that were TNF-dependent and differentially regulated in both LAA and LV are indicated by yellow dots. Only gene sets that form clusters are shown for clarity. Nominal P-value < 0.05, false discovery rate (FDR) < 0.20.

despite the induction of fibrosis by exercise, the absence of increased collagen expression at all-time points following exercise led us to explore the potential contribution of factors that have previously been shown to mediate post-translational changes in collagen maturation and deposition in the heart. For these studies, we used the 2 day mice and made the measurements 2 h following the final 90 min exercise bout, consistent with our RNA-seq measurements. Given that soluble TNF is required for exercise-induced atrial changes (Lakin et al., 2019), we first measured the activity of TNF-converting enzyme (TACE, or ADAM17), which is upregulated with mechanical stretch and releases active (soluble) TNF (Zhan et al., 2007). Indeed, TACE activity tended to be increased (P = 0.211) with swim (142 ± 4 pmol/min/μg, n = 5) compared to sedentary mice (129 ± 8 pmol/min/μg, n = 6), suggesting activation. It is conceivable that earlier assessment would have displayed even greater TACE activity since we previously found upregulation of TNF-dependent p38 MAPK signaling within 10 min post-exercise (Aschar-Sobbi et al., 2015). We also measured MMP2 and MMP9 activity since these are increased with atrial stretch as well as in CV disease (Yabluchanskiy et al., 2013). We found that pro-MMP2 activity was increased (P = 0.0003) while pro-MMP9 activity tended (P = 0.098) to be increased in atria after swim completion in 2 day swim compared to sedentary mice (**Supplementary Figure 7A**), establishing increased collagen turnover with acute exercise.

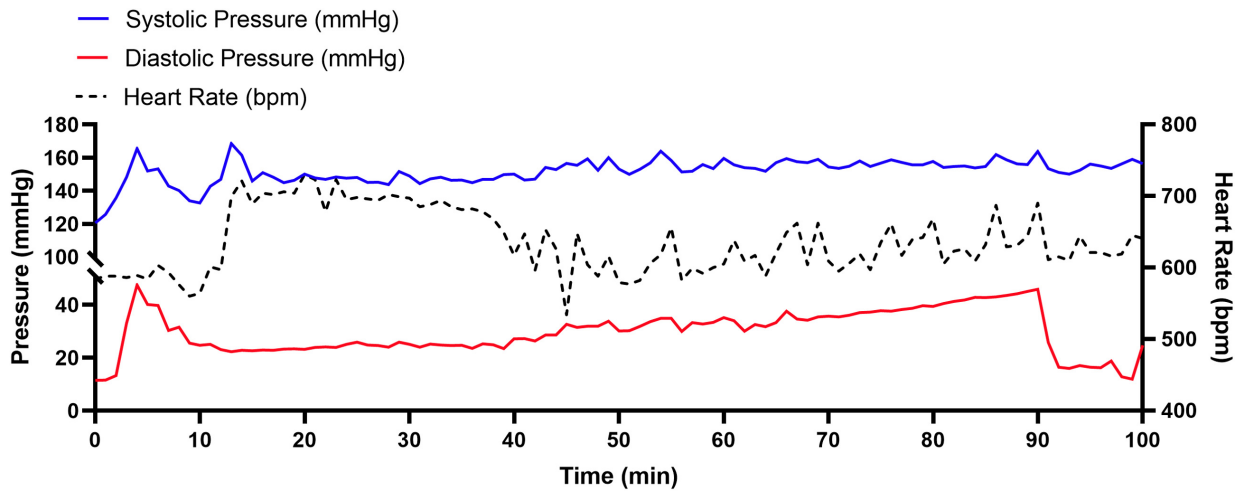

FIGURE 7 | Representative left ventricular (LV) hemodynamic changes measured by implantable pressure-telemetry during an acute swim bout in mice. During a 90 min swim bout, LV diastolic filling pressures (red) increase rapidly from a baseline of ∼10 mmHg to ∼45 mmHg within the first 10 min. Thereafter, the pressure falls to ∼20 mmHg, only to rise steadily to ∼40–45 mmHg by the end of the 90 min swim.

Since previous studies reported increases in matricellular proteins that mediate post-synthetic collagen turnover in several models (Frangogiannis, 2012; McDonald et al., 2018), we also measured osteopontin (OPN) and SPARC expression levels. Although SPARC expression in atria was unaffected by acute exercise ($P = 0.562$), OPN was decreased ($P = 0.006$), suggesting these matricellular proteins contribute minimally to adverse atrial remodeling in the early response to exercise.

A schematic overview of the time-dependent and atrial-specific exercise-induced TNF-dependent transcriptomic changes mediating adverse atrial remodeling and AF vulnerability in response to increased filling pressures and atrial stretch are shown in **Figure 8**.

DISCUSSION

The transcriptional changes in WT atria were generally similar after 2 vs. 6 weeks of exercise, with about 50% of the differentially regulated gene sets related to ECM and mechanosensing enriched in sedentary mice. We believe that changes in gene sets associated with ECM/mechanosensitive pathways at these time points are relevant because elevated venous filling pressures (i.e., preloads) are seen invariably in virtually all AF conditions (Vranka et al., 2007; Remes et al., 2008), including intense exercise (Reeves et al., 1990; Aschar-Sobbi et al., 2015). Such elevations in filling pressure are expected to favor atrial vs. ventricular stretch and thereby preferentially driving stretch-dependent atrial remodeling (De Jong et al., 2011). This would help explain the appearance of fibrosis in atria but not ventricles. Moreover, the number of differentially regulated genes/gene sets related to ECM/mechanosensing were ∼twofold greater after 2 weeks vs. 6 weeks of exercise suggesting that the atrial responses to exercise adapt and diminish with time, as expected with the appearance of fibrosis. A puzzling finding, however, is the absence of increased collagen mRNA levels in exercised atria at either time point, despite the fibrosis after 6 weeks of exercise. This was surprising because fibrosis seen in most cardiac conditions (i.e., heart failure, hypertension, and cardiomyopathies) is associated with elevated collagen mRNA (Frangogiannis, 2019). The absence of elevated collagen mRNA in fibrotic exercised atria is similar to the discordant pattern seen with age- (Horn and Trafford, 2016; Podolsky et al., 2020) and stress-related (Kandalam et al., 2011) fibrosis in several tissues. As discussed below, we believe these findings have important implications on the mechanisms underlying adverse atrial changes and AF, regardless of the inciting factors.

Consistent with the TNF-dependence of adverse atrial changes with exercise, TNF- and inflammation-related gene sets were differentially regulated after 2 weeks of exercise (similar to 6 weeks of exercise) with the number of differentially regulated gene sets being ∼twofold less in TNF-KO vs. WT atria. On the other hand, after 2 weeks of exercise atria from sedentary TNF-KO mice, but not WT mice, showed enrichment in TNF-related inflammatory gene sets. Since adverse atrial changes do not occur in TNF-KO mice, it appears that TNF plays a permissive role in exercise-induced inflammation rather than being a primary factor. By contrast, the primary exercise-induced gene changes in TNF-KO atria are related to DNA replication and repair, whose significance will require further studies. Collectively, the differences in atrial transcriptome remodeling after 2 weeks of exercise are consistent with the pleiotropic actions of TNF (Tracey and Cerami, 1994).

To gain insight into possible mechanisms underlying the TNF-dependent atrial changes induced by 2 weeks of exercise, we examined transcript levels of individual genes between the 4 groups. Consistent with our enrichment maps, the bulk of the differentially regulated genes related to ECM/mechanotransduction had lower expression levels in exercised atria of both WT and KO mice. Moreover, most

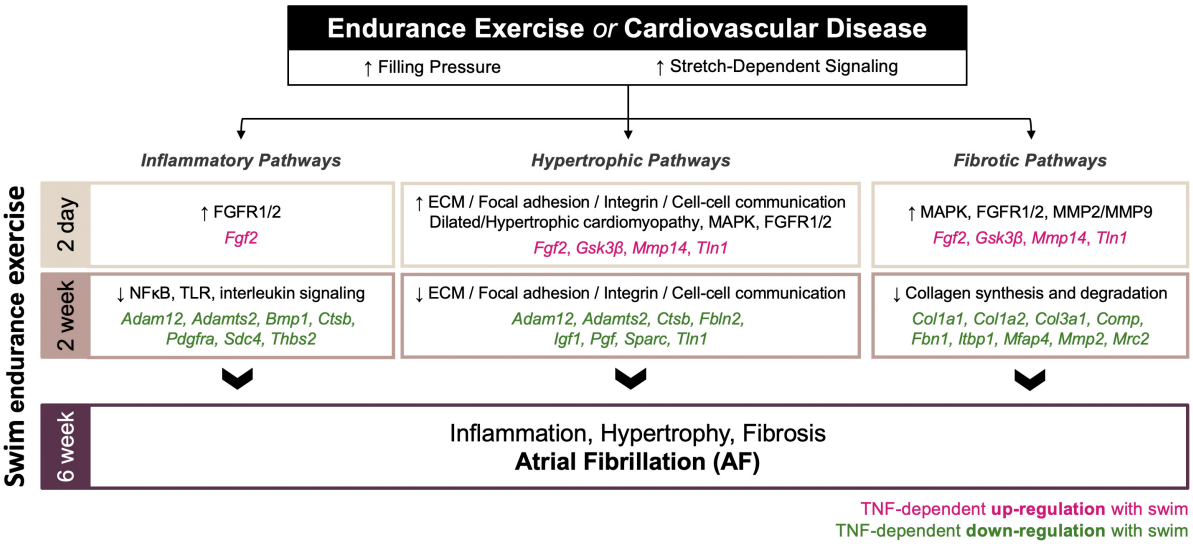

FIGURE 8 | Schematic overview of the time-dependent and atrial-specific exercise-induced tumor necrosis factor (TNF)-dependent transcriptional responses to elevated venous filling pressures and atrial stretch mediating adverse atrial remodeling (inflammation, fibrosis, hypertrophy) and atrial fibrillation (AF) vulnerability.

of these genes have been linked to increased tissue fibrosis, despite the absence of atrial fibrosis and AF inducibility in exercised TNF-KO mice, which suggests that many of these gene changes are likely of limited relevance in driving exercise-induced fibrosis (Chou et al., 1996; Sivasubramanian et al., 2001). However, it is noted in previous studies that reductions in the metalloproteinase, *Mmp2*, and the canonical collagen endocytic receptor (Engelholm et al., 2003), *Mrc2* (which are both TNF-dependent genes that are reduced in WT exercised atria), are linked to age-dependent fibrosis (Podolsky et al., 2020). These TNF-dependent changes are particularly interesting since atrial fibrosis and AF are generally seen with aging (Gramley et al., 2009; Ravassa et al., 2019), and AF is especially prevalent in veteran endurance athletes (Karjalainen et al., 1998; Mont et al., 2002). Also, these *Mmp2* reductions paralleled reductions in *Mmp14*, albeit independently of TNF, which has been associated with AF (Simmers et al., 2016) and shown to activate MMP-2 (Jr and Nagase, 2000). On the other hand, when we directly compared WT and TNF-KO swim atria, the majority of genes were increased in exercised atria from TNF-KO relative to WT, with the only gene that was increased in a TNF-dependent manner after 2 weeks of exercise in WT atria was *Comp*, which is a biomarker for cardiac fibrosis and hypertrophic remodeling (Huang et al., 2013; Zhao et al., 2018). *Comp* is involved in non-collagen ECM-receptor interaction (Rosenberg et al., 1998) and appears from multiple studies to contribute to the pathogenesis of AF (Zou et al., 2018; Thomas et al., 2019).

As the ECM/mechanosensitive pathways did not show enrichment at 2 and 6 weeks in our exercised mice, we also performed RNAseq measurements after only 2 days of exercise. Importantly, at this time point gene sets associated with ECM/mechanosensitive as well as hypertrophic signaling pathways were enriched in exercised atria from WT mice, which would appear to align with the elevated filling pressures seen in exercise and AF-related conditions (Reeves et al., 1990; De Jong et al., 2011; Aschar-Sobbi et al., 2015). Of particular note is the enrichment of tubulin folding and MAPK pathways in exercised WT (but not TNK-KO) atria. Tubulin assembly/disassembly in microtubules is involved in mechanosensing (White, 2011) in a number of cell types and is interdependent on MAPKs (Samaj et al., 2004), particularly p38 kinases (Ramkumar et al., 2018). These results suggest that strain-dependent signaling via microtubule assembly/disassembly may play a role in driving early atrial responses to atrial stretch occurring during exercise, possibly in concert with the recruitment of TNF-dependent transduction, consistent with TNF's mechanosensing properties (Kroetsch et al., 2017). Microtubule involvement is consistent with the pioneering studies by George Cooper (4th) who showed that p21-activated kinase-1 (Pak1)-dependent microtubule assembly plays a central role in the early response to pressure overload and mechanical stretch in right ventricular cardiomyocytes (Cheng et al., 2012a). Indeed, Pak1 regulates exercise-induced cardiac hypertrophy (Davis et al., 2015), which aligns nicely with our 2 day atrial analyses showing exercise-induced upregulation of *Flna* (filamen A), a cytoprotective protein that is upregulated with mechanical stress (D'Addario et al., 2003) and is essential for actin/cytoskeletal dynamics (Vadlamudi et al., 2002) through interdependent p38- (D'Addario et al., 2002) and Pak1-mediated signaling (Zhang et al., 1995; Shifrin et al., 2012). We also found enrichment of other pathways, including IQGAPs and AMPKs, in acutely exercised WT atria which are involved in the early compensatory responses to pressure overload stimuli that may be harbingers of fibrotic remodeling in the long-term (Hermida et al., 2013; Hedman et al., 2015; Daskalopoulos et al., 2016). Taken together, these observations suggest that the loss of TNF leads to an inhibitory modulation of mechanosensitive signaling pathways which is consistent with the stretch-dependence of TNF

activation (Kroetsch et al., 2017) and the regulation of FAK by TNF (Funakoshi-Tago et al., 2003; Murphy et al., 2019) via MAPK signaling and IL-6 expression (Schlaepfer et al., 2007). Given the absence of exercise-induced adverse atrial remodeling and AF with TNF inhibition, our results suggest stretch-activation of TNF may tip the scales toward maladaptive compensatory remodeling that is unique to the atria.

As in the 2 week group, far fewer gene sets (61 vs. 101) were differentially regulated with 2 day exercise in TNF-KO vs. WT mice. In particular, TNF-KO mice again showed enrichment of NF-κB, toll-like receptor, and interleukin pathways in the sedentary group, further supporting a permissive role for TNF in regulating exercise-induced atrial changes. With regards to individual genes, our analyses showed that fewer atrial genes were differentially regulated between swim WT and KO mice. Of these, the differentially regulated genes related to ECM/mechanosensitive include *Mmp14*, *Tln*1, *Lox*, and *Gsk3*β as well as *Fgf2*, the latter being the only gene upregulated in a TNF-dependent manner exclusively in exercised WT mice. The presence of only one TNF-dependent differentially regulated gene in the WT compared to TNF-KO exercise group is unexpected given the increased filling pressures we observed with swim. However, exercise is an intermittent hemodynamic overload stimulus (Moreira-Goncalves et al., 2015), and the nature and time course of cardiac transcriptomic remodeling in response to mechanical stretch is highly dependent on stretch duration (Rysa et al., 2018). Therefore, as we only looked at atrial transcriptomic remodeling 2 h following the last acute swim bout, and focused our analysis on genes linked to mechanotransduction and ECM remodeling, a larger window is likely necessary to capture the full impact of swim exercise on stretch-induced transcriptomic remodeling and enzyme activity (i.e., TACE/ADAM17, pro-MMP2).

Relative to atria, the number of genes sets in ventricles that were differentially regulated in response to exercise was much smaller. This is not unexpected because ventricles are far less compliant than atria due to differences in ECM as well as wall thickness (La Gerche et al., 2011) in agreement with our previous studies showing that exercise activates p38 in atria but not ventricles (Aschar-Sobbi et al., 2015). Presumably, preferential atrial stretch underlies prominent bi-atrial enlargement in athletes (D'Andrea et al., 2010; D'Ascenzi et al., 2016, 2018) as well as pronounced atrial hypertrophy and fibrosis in our exercised mice. These responses would be expected to normalize atrial wall stress which explains nicely the evolving pattern of time-dependent exercised-induced atrial changes in stretch-dependent signaling pathways in the current study.

Given the link between TNF and mechanical stress, it is tempting to speculate that the degree of TNF elevation with elevated filling pressures and its effects on mechanosensitive signaling cascades may determine the threshold between compensatory (i.e., physiological) or maladaptive transcriptomic activation early in the response to exercise training. This would be consistent with the pleiotropic functions of TNF (Tracey and Cerami, 1994). Indeed, TNF and its downstream factors such as NFκB and p38 can promote protective and pathophysiological responses (Schumacher and Naga Prasad, 2018). Moreover, time-dependent adaptations (i.e., hypertrophy and fibrosis) may serve to blunt or normalize acute elevations in wall stress with exercise, which would explain enrichment in ECM/mechanosensitive genes in sedentary mice over time and compensatory deactivation of stretch-mediated remodeling. This would further promote an early transition to reduced collagen transcription, mimicking fibrotic processes seen in aging wherein collagen expression is also not increased (Podolsky et al., 2020).

Implications

AF increases strongly with age, CVD and conditions associated with poor cardiovascular health (i.e., diabetes, obesity, and metabolic syndrome). Even though physical activity reduces AF risk (Drca et al., 2014; Malmo et al., 2016), endurance athletes, especially elite veteran athletes, have AF risks rivaling that seen with hypertension and other CVD conditions (Mont et al., 2002; Redpath and Backx, 2015; Goodman et al., 2018). In CVD patients, persistent AF is invariably associated with atrial fibrosis, inflammation and hypertrophy, along with variable electrical changes (Daoud et al., 1996; Xu et al., 2004; Nattel and Harada, 2014). Although historically AF in athletes has often been referred to as "lone AF" (Calvo et al., 2016) because of the absence of CVD, the term is no longer considered appropriate since AF is associated with a multitude of conditions (Wyse et al., 2014). In this regard, animal studies have established, and some human studies suggest, that intense exercise leads to adverse atrial changes resembling those seen in persistent AF patients. In this regard, our studies reveal that exercise induces dynamic transcriptional adaptations involving, in particular, pronounced changes in strain-dependent pathways related to ECM/integrin/focal adhesion. These observations seem particularly relevant since elevated filling pressures and atrial stretch are both prominent features of aging, CVD and exercise. A novel and remarkable finding of our analyses was the link between genes associated with collagen turnover, rather than collagen transcripts, and fibrosis in exercised atria, a pattern that mirrors aging-related fibrosis (Podolsky et al., 2020). This is especially interesting because the strongest predictor of AF is age (Staerk et al., 2018). Moreover, our findings revealed TNF plays a permissive rather than primary role in exercise-mediated atrial structural and transcriptomic remodeling.

TNF involvement in exercise-induced structural and transcriptional adaptations are of particular interest because TNF has been implicated in the pathogenesis of AF (Ren et al., 2015) and persistent AF is associated with elevated atrial TNF levels and inflammatory infiltrates (Li et al., 2010; Guo et al., 2012). Collectively, the many common atrial features between persistent AF patients and exercised mice suggests to us that AF and adverse remodeling seen with intense exercise and CVD share common mechanisms. Thus, while our findings of an arrhythmogenic substrate requires confirmation in athletes presenting with AF, the genetic changes seen in our studies may have broader implications for the general AF population. By comparison, ventricular responses to exercise were relatively muted, although the differentially regulated gene sets were similar to those in the atria, consistent with clinical and

epidemiological evidence for exercise-induced arrhythmogenic remodeling being chamber-specific (Guasch et al., 2018).

Limitations

Obviously the use of whole tissue samples prevents us from determining the individual contributions of cardiomyocytes, endothelial cells, and fibroblasts to the transcriptomic remodeling induced by exercise which would be highly desirable since TNF is a mechanosensitive cytokine expressed in cardiomyocytes (Kapadia et al., 1997; Sun et al., 2007), fibroblasts (Yokoyama et al., 1999), and endothelial cells (Yin et al., 2017).

Although the studies presented here were limited to male mice, we have plan to examine the effects of exercise on female mice. It is worth noting that even though female athletes remain underrepresented generally in previous studies examining exercise-induced AF (Andersen et al., 2013), several studies have found a reduced incidence of AF in females (Mohanty et al., 2016) making our future studies potentially highly relevant.

Our studies were limited to only three time points leaving many uncertainties regarding the evolving effects of intense exercise. Nevertheless, our results showed time-dependent adaptations to exercise with generally comparable responses at the 2 and 6 week time points, suggestive of compensatory adaptations in fibrotic, hypertrophic and inflammatory pathways. In this regard, we did not extend our swim training beyond 6 weeks given the clear evidence of adverse atrial remodeling and increased AF vulnerability at this time point. However, given the presence of inflammatory infiltrates and enrichment of TNF-mediated inflammatory signaling pathways at 6 weeks of exercise, it is conceivable that the arrhythmogenic substrate and the degree of AF vulnerability may be more pronounced if we were to extend our exercise protocol. We cannot rule out increased collagen synthesis or mechanisms involved in post-translational modifications/deposition (i.e., SPARC/OPN, LOXs) or degradation (i.e., MMPs) as contributing to exercise-induced atrial remodeling, which might not have been fully captured at 2 day, 2 or 6 week exercise.

While we used microarray analyses for 6 week data and RNAseq for the other time points to assess exercise-induced transcriptional changes, our analyses focused on RNAseq data at the earlier time points. In this regard, it was reassuring to find that the 6 weeks microarray results align well with the 2 week RNAseq results, thus robustly supporting the compensatory nature of the atrial responses to exercise at the later time points.

CONCLUSION

Our results demonstrate clear exercise-induced TNF-dependent differential activation (enrichment) of pathways associated with mechanosensitive ECM remodeling, which are both time-dependent and differ between atria and ventricles in a manner consistent with preferential stretch of atria in response to exercise-induced elevations in venous pressure. Our findings provide insight into the chamber-specific roles of TNF and mechanical strain in cardiac changes induced by exercise, which supports the general conclusion that exercise-induced adverse atrial remodeling and AF vulnerability is linked to elevated filling pressures, consistent with AF associated with aging and poor cardiovascular health. The common atrial features between persistent AF patients and exercised mice suggests that AF and adverse remodeling seen with intense exercise may share common mechanisms, which may have broader implications for the general AF population.

DATA AVAILABILITY STATEMENT

The data generated in this study can be found in the BioProject database (accession: PRJNA663094).

ETHICS STATEMENT

The animal study was reviewed and approved by the Division of Comparative Medicine at the University of Toronto and York University Animal Care Committee (ACC).

AUTHOR CONTRIBUTIONS

Experiments were performed at York University Department of Biology, the University of Toronto Department of Physiology, and the University of Alberta Department of Physiology. YO, SY, RL, and PB were responsible for the conception and design of the work, the acquisition, analysis, and interpretation for the work, drafting the work, and revising it critically for important intellectual content. XL, SJ, FI, XG, RD, and D-KK were involved in acquisition, analysis, and interpretation of data for the work. All authors approved the final version of this manuscript and agreed to be accountable for all aspects of the work.

FUNDING

This work was supported by the Queen Elizabeth II/Heart and Stroke Foundation of Ontario Graduate Scholarships in Science and Technology Award, Queen Elizabeth II Scholarship in Science and Technology (QEII-GSST), and University of Ottawa Heart Institute Endowed Scholarship to YO, the Natural Science Funding from the Science and Technology Department of Jilin Province, China (No. 20200201562JC) to SY, the Canadian Institutes of Health Research (CIHR) Fellowship to RL, the Natural Sciences and Engineering Research Council of Canada (NSERC) Discovery Grant to K-HK, the Canadian Institutes of Health Research, Operating grant (MOP125950 and MOP119339) and a Canada Research Chair in Cardiovascular Biology to PB, and the Canadian Foundation for Innovation, John Evans Leader Award to PB.

SUPPLEMENTARY MATERIAL

The Supplementary Material for this article can be found online at: https://www.frontiersin.org/articles/10.3389/fphys.2020.605671/full#supplementary-material

REFERENCES

Accornero, F., and Molkentin, J. D. (2011). Placental growth factor as a protective paracrine effector in the heart. *Trends Cardiovasc. Med.* 21, 220–224. doi: 10.1016/j.tcm.2012.05.014

Afgan, E., Baker, D., Van Den Beek, M., Blankenberg, D., Bouvier, D., Cech, M., et al. (2016). The Galaxy platform for accessible, reproducible and collaborative biomedical analyses: 2016 update. *Nucleic Acids Res.* 44, W3–W10.

Andersen, K., Farahmand, B., Ahlbom, A., Held, C., Ljunghall, S., Michaelsson, K., et al. (2013). Risk of arrhythmias in 52 755 long-distance cross-country skiers: a cohort study. *Eur. Heart J.* 34, 3624–3631. doi: 10.1093/eurheartj/eht188

Aschar-Sobbi, R., Izaddoustdar, F., Korogyi, A. S., Wang, Q., Farman, G. P., Yang, F., et al. (2015). Increased atrial arrhythmia susceptibility induced by intense endurance exercise in mice requires TNFalpha. *Nat. Commun.* 6:6018.

Babu, G. J., Lalli, M. J., Sussman, M. A., Sadoshima, J., and Periasamy, M. (2000). Phosphorylation of elk-1 by MEK/ERK pathway is necessary for c-fos gene activation during cardiac myocyte hypertrophy. *J. Mol. Cell Cardiol.* 32, 1447–1457. doi: 10.1006/jmcc.2000.1185

Bouzeghrane, F., Reinhardt, D. P., Reudelhuber, T. L., and Thibault, G. (2005). Enhanced expression of fibrillin-1, a constituent of the myocardial extracellular matrix in fibrosis. *Am. J. Physiol. Heart Circ. Physiol.* 289, H982–H991.

Bradshaw, A. D., Baicu, C. F., Rentz, T. J., Van Laer, A. O., Boggs, J., Lacy, J. M., et al. (2009). Pressure overload-induced alterations in fibrillar collagen content and myocardial diastolic function: role of secreted protein acidic and rich in cysteine (SPARC) in post-synthetic procollagen processing. *Circulation* 119, 269–280. doi: 10.1161/circulationaha.108.773424

Bradshaw, A. D., Baicu, C. F., Rentz, T. J., Van Laer, A. O., Bonnema, D. D., and Zile, M. R. (2010). Age-dependent alterations in fibrillar collagen content and myocardial diastolic function: role of SPARC in post-synthetic procollagen processing. *Am. J. Physiol. Heart Circ. Physiol.* 298, H614–H622.

Busk, P. K., Bartkova, J., Strom, C. C., Wulf-Andersen, L., Hinrichsen, R., Christoffersen, T. E., et al. (2002). Involvement of cyclin D activity in left ventricle hypertrophy in vivo and in vitro. *Cardiovasc. Res.* 56, 64–75. doi: 10.1016/s0008-6363(02)00510-2

Calkins, H., Hindricks, G., Cappato, R., Kim, Y. H., Saad, E. B., Aguinaga, L., et al. (2018). 2017 HRS/EHRA/ECAS/APHRS/SOLAECE expert consensus statement on catheter and surgical ablation of atrial fibrillation: executive summary. *Europace* 20, 157–208.

Calvo, N., Ramos, P., Montserrat, S., Guasch, E., Coll-Vinent, B., Domenech, M., et al. (2016). Emerging risk factors and the dose-response relationship between physical activity and lone atrial fibrillation: a prospective case-control study. *Europace* 18, 57–63. doi: 10.1093/europace/euv216

Caporizzo, M. A., Chen, C. Y. X., and Prosser, B. L. (2019). Cardiac microtubules in health and heart disease. *Exp. Biol. Med.* 244, 1255–1272. doi: 10.1177/1535370219868960

Cheng, G., Kasiganesan, H., Baicu, C. F., Wallenborn, J. G., Kuppuswamy, D., and Cooper, G. T. (2012a). Cytoskeletal role in protection of the failing heart by beta-adrenergic blockade. *Am. J. Physiol. Heart Circ. Physiol.* 302, H675–H687.

Cheng, X. W., Shi, G. P., Kuzuya, M., Sasaki, T., Okumura, K., and Murohara, T. (2012b). Role for cysteine protease cathepsins in heart disease: focus on biology and mechanisms with clinical implication. *Circulation* 125, 1551–1562. doi: 10.1161/circulationaha.111.066712

Chou, D. H., Lee, W., and Mcculloch, C. A. (1996). TNF-alpha inactivation of collagen receptors: implications for fibroblast function and fibrosis. *J. Immunol.* 156, 4354–4362.

D'Addario, M., Arora, P. D., Ellen, R. P., and Mcculloch, C. A. G. (2002). Interaction of p38 and Sp1 in a mechanical force-induced, beta(1), integrin-mediated transcriptional circuit that regulates the actin-binding protein filamin-A. *J. Biol. Chem.* 277, 47541–47550. doi: 10.1074/jbc.m207681200

D'Addario, M., Arora, P. D., Ellen, R. P., and Mcculloch, C. A. G. (2003). Regulation of tension-induced mechanotranscriptional signals by the microtubule network in fibroblasts. *J. Biol. Chem.* 278, 53090–53097. doi: 10.1074/jbc.m309027200

D'Andrea, A., Riegler, L., Cocchia, R., Scarafile, R., Salerno, G., Gravino, R., et al. (2010). Left atrial volume index in highly trained athletes. *Am. Heart J.* 159, 1155–1161. doi: 10.1016/j.ahj.2010.03.036

Daoud, E. G., Bogun, F., Goyal, R., Harvey, M., Man, K. C., Strickberger, S. A., et al. (1996). Effect of atrial fibrillation on atrial refractoriness in humans. *Circulation* 94, 1600–1606. doi: 10.1161/01.cir.94.7.1600

D'Ascenzi, F., Anselmi, F., Focardi, M., and Mondillo, S. (2018). Atrial enlargement in the Athlete's heart: assessment of atrial function may help distinguish adaptive from pathologic remodeling. *J. Am. Soc. Echocardiogr.* 31, 148–157. doi: 10.1016/j.echo.2017.11.009

D'Ascenzi, F., Solari, M., Anselmi, F., Maffei, S., Focardi, M., Bonifazi, M., et al. (2016). Atrial chamber remodelling in healthy pre-adolescent athletes engaged in endurance sports: a study with a longitudinal design. The CHILD study. *Int. J. Cardiol.* 223, 325–330. doi: 10.1016/j.ijcard.2016.08.231

Daskalopoulos, E. P., Dufeys, C., Bertrand, L., Beauloye, C., and Horman, S. (2016). AMPK in cardiac fibrosis and repair: actions beyond metabolic regulation. *J. Mol. Cell Cardiol.* 91, 188–200. doi: 10.1016/j.yjmcc.2016.01.001

Davis, R. T., Simon, J. N., Utter, M., Mungai, P., Alvarez, M. G., Chowdhury, S. A. K., et al. (2015). Knockout of p21-activated kinase-1 attenuates exercise-induced cardiac remodelling through altered calcineurin signalling. *Cardiovasc. Res.* 108, 335–347. doi: 10.1093/cvr/cvv234

De Jong, A. M., Maass, A. H., Oberdorf-Maass, S. U., Van Veldhuisen, D. J., Van Gilst, W. H., and Van Gelder, I. C. (2011). Mechanisms of atrial structural changes caused by stretch occurring before and during early atrial fibrillation. *Cardiovasc. Res.* 89, 754–765. doi: 10.1093/cvr/cvq357

Diao, S. L., Xu, H. P., Zhang, B., Ma, B. X., and Liu, X. L. (2016). Associations of MMP-2, BAX, and Bcl-2 mRNA and protein expressions with development of atrial fibrillation. *Med. Sci. Monit.* 22, 1497–1507. doi: 10.12659/msm.895715

Dong, C., Li, H. J., Chang, S., Liao, H. J., Zhang, Z. P., Huang, P., et al. (2013). A disintegrin and metalloprotease with thrombospondin motif 2 may contribute to cirrhosis in humans through the transforming growth factor-beta/SMAD pathway. *Gut Liver* 7, 213–220. doi: 10.5009/gnl.2013.7.2.213

Drca, N., Wolk, A., Jensen-Urstad, M., and Larsson, S. C. (2014). Atrial fibrillation is associated with different levels of physical activity levels at different ages in men. *Heart* 100, 1037–1042. doi: 10.1136/heartjnl-2013-305304

Engelholm, L. H., List, K., Netzel-Arnett, S., Cukierman, E., Mitola, D. J., Aaronson, H., et al. (2003). uPARAP/Endo180 is essential for cellular uptake of collagen and promotes fibroblast collagen adhesion. *J. Cell Biol.* 160, 1009–1015. doi: 10.1083/jcb.200211091

Frame, M. C., Patel, H., Serrels, B., Lietha, D., and Eck, M. J. (2010). The FERM domain: organizing the structure and function of FAK. *Nat. Rev. Mol. Cell Biol.* 11, 802–814. doi: 10.1038/nrm2996

Frangogiannis, N. G. (2012). Matricellular proteins in cardiac adaptation and disease. *Physiol. Rev.* 92, 635–688. doi: 10.1152/physrev.00008.2011

Frangogiannis, N. G. (2019). Cardiac fibrosis: cell biological mechanisms, molecular pathways and therapeutic opportunities. *Mol. Aspects Med.* 65, 70–99. doi: 10.1016/j.mam.2018.07.001

Funakoshi-Tago, M., Sonoda, Y., Tanaka, S., Hashimoto, K., Tago, K., Tominaga, S., et al. (2003). Tumor necrosis factor-induced nuclear factor kappaB activation is impaired in focal adhesion kinase-deficient fibroblasts. *J. Biol. Chem.* 278, 29359–29365. doi: 10.1074/jbc.m213115200

Gallini, R., Lindblom, P., Bondjers, C., Betsholtz, C., and Andrae, J. (2016). PDGF-A and PDGF-B induces cardiac fibrosis in transgenic mice. *Exp. Cell Res.* 349, 282–290. doi: 10.1016/j.yexcr.2016.10.022

Goodman, J. M., Banks, L., Connelly, K. A., Yan, A. T., Backx, P. H., and Dorian, P. (2018). Excessive exercise in endurance athletes: Is atrial fibrillation a possible consequence? *Appl. Physiol. Nutr. Metab.* 43, 973–976. doi: 10.1139/apnm-2017-0764

Goumans, M. J., and Ten Dijke, P. (2018). TGF-β signaling in control of cardiovascular function. *Cold Spring Harb. Perspect. Biol.* 10:a022210. doi: 10.1101/cshperspect.a022210

Gramley, F., Lorenzen, J., Knackstedt, C., Rana, O. R., Saygili, E., Frechen, D., et al. (2009). Age-related atrial fibrosis. *Age* 31, 27–38. doi: 10.1007/s11357-008-9077-9

Gramley, F., Lorenzen, J., Koellensperger, E., Kettering, K., Weiss, C., and Munzel, T. (2010). Atrial fibrosis and atrial fibrillation: the role of the TGF-beta1 signaling pathway. *Int. J. Cardiol.* 143, 405–413. doi: 10.1016/j.ijcard.2009.03.110

Guasch, E., Benito, B., Qi, X., Cifelli, C., Naud, P., Shi, Y., et al. (2013). Atrial fibrillation promotion by endurance exercise: demonstration and mechanistic exploration in an animal model. *J. Am. Coll. Cardiol.* 62, 68–77. doi: 10.1016/j.jacc.2013.01.091

Guasch, E., Mont, L., and Sitges, M. (2018). Mechanisms of atrial fibrillation in athletes: what we know and what we do not know. *Neth. Heart J.* 26, 133–145. doi: 10.1007/s12471-018-1080-x

Guo, Y., Lip, G. Y., and Apostolakis, S. (2012). Inflammation in atrial fibrillation. *J. Am. Coll. Cardiol.* 60, 2263–2270.

Hadi, A. M., Mouchaers, K. T., Schalij, I., Grunberg, K., Meijer, G. A., Vonk-Noordegraaf, A., et al. (2011). Rapid quantification of myocardial fibrosis: a new macro-based automated analysis. *Cell Oncol.* 34, 343–354. doi: 10.1007/s13402-011-0035-7

Hedman, A. C., Smith, J. M., and Sacks, D. B. (2015). The biology of IQGAP proteins: beyond the cytoskeleton. *EMBO Rep.* 16, 427–446. doi: 10.15252/embr.201439834

Heeringa, J., Van Der Kuip, D. A., Hofman, A., Kors, J. A., Van Herpen, G., Stricker, B. H., et al. (2006). Prevalence, incidence and lifetime risk of atrial fibrillation: the Rotterdam study. *Eur. Heart J.* 27, 949–953. doi: 10.1093/eurheartj/ehi825

Hermida, N., Markl, A., Hamelet, J., Van Assche, T., Vanderper, A., Herijgers, P., et al. (2013). HMGCoA reductase inhibition reverses myocardial fibrosis and diastolic dysfunction through AMP-activated protein kinase activation in a mouse model of metabolic syndrome. *Cardiovasc. Res.* 99, 44–54. doi: 10.1093/cvr/cvt070

Herum, K. M., Lunde, I. G., Skrbic, B., Louch, W. E., Hasic, A., Boye, S., et al. (2015). Syndecan-4 is a key determinant of collagen cross-linking and passive myocardial stiffness in the pressure-overloaded heart. *Cardiovasc. Res.* 106, 217–226. doi: 10.1093/cvr/cvv002

Horn, M. A., and Trafford, A. W. (2016). Aging and the cardiac collagen matrix: novel mediators of fibrotic remodelling. *J. Mol. Cell Cardiol.* 93, 175–185. doi: 10.1016/j.yjmcc.2015.11.005

Huang, Y., Xia, J., Zheng, J., Geng, B., Liu, P., Yu, F., et al. (2013). Deficiency of cartilage oligomeric matrix protein causes dilated cardiomyopathy. *Basic Res. Cardiol.* 108:374.

Husser, D., Büttner, P., Ueberham, L., Dinov, B., Sommer, P., Arya, A., et al. (2016). Genomic contributors to rhythm outcome of atrial fibrillation catheter ablation – pathway enrichment analysis of GWAS data. *PLoS One* 11:e0167008. doi: 10.1371/journal.pone.0167008

Itoh, N., and Ohta, H. (2013). Pathophysiological roles of FGF signaling in the heart. *Front Physiol* 4:247. doi: 10.3389/fphys.2013.00247

Jana, S., Chute, M., Hu, M., Winkelaar, G., Owen, C. A., Oudit, G. Y., et al. (2020). ADAM (a disintegrin and metalloproteinase) 15 deficiency exacerbates Ang II (Angiotensin II)-induced aortic remodeling leading to abdominal aortic aneurysm. *Arterioscler. Thromb. Vasc. Biol.* 40, 1918–1934. doi: 10.1161/ATVBAHA.120.314600

Jolliffe, I. T., and Cadima, J. (2016). Principal component analysis: a review and recent developments. *Philos. Trans. A Math. Phys. Eng. Sci.* 374:20150202. doi: 10.1098/rsta.2015.0202

Jr, J. W., and Nagase, H. (2000). *Activation of the Zymogen Forms of MMPs*. New York, NY: Oxford University Press.

Kandalam, V., Basu, R., Moore, L., Fan, D., Wang, X., Jaworski, D. M., et al. (2011). Lack of tissue inhibitor of metalloproteinases 2 leads to exacerbated left ventricular dysfunction and adverse extracellular matrix remodeling in response to biomechanical stress. *Circulation* 124, 2094–2105. doi: 10.1161/circulationaha.111.030338

Kapadia, S. R., Oral, H., Lee, J., Nakano, M., Taffet, G. E., and Mann, D. L. (1997). Hemodynamic regulation of tumor necrosis factor-alpha gene and protein expression in adult feline myocardium. *Circ. Res.* 81, 187–195. doi: 10.1161/01.res.81.2.187

Kardami, E., Jiang, Z. S., Jimenez, S. K., Hirst, C. J., Sheikh, F., Zahradka, P., et al. (2004). Fibroblast growth factor 2 isoforms and cardiac hypertrophy. *Cardiovasc. Res.* 63, 458–466. doi: 10.1016/j.cardiores.2004.04.024

Karjalainen, J., Kujala, U. M., Kaprio, J., Sarna, S., and Viitasalo, M. (1998). Lone atrial fibrillation in vigorously exercising middle aged men: case-control study. *BMJ* 316, 1784–1785. doi: 10.1136/bmj.316.7147.1784

Khalil, H., Kanisicak, O., Vagnozzi, R. J., Johansen, A. K., Maliken, B. D., Prasad, V., et al. (2019). Cell-specific ablation of Hsp47 defines the collagen-producing cells in the injured heart. *JCI Insight* 4:e128722.

Kim, D., Langmead, B., and Salzberg, S. L. (2015). HISAT: a fast spliced aligner with low memory requirements. *Nat. Methods* 12, 357–360. doi: 10.1038/nmeth.3317

Krijthe, B. P., Kunst, A., Benjamin, E. J., Lip, G. Y., Franco, O. H., Hofman, A., et al. (2013). Projections on the number of individuals with atrial fibrillation in the European Union, from 2000 to 2060. *Eur. Heart J.* 34, 2746–2751. doi: 10.1093/eurheartj/eht280

Kroetsch, J. T., Levy, A. S., Zhang, H., Aschar-Sobbi, R., Lidington, D., Offermanns, S., et al. (2017). Constitutive smooth muscle tumour necrosis factor regulates microvascular myogenic responsiveness and systemic blood pressure. *Nat. Commun.* 8:14805.

La Gerche, A., Heidbuchel, H., Burns, A. T., Mooney, D. J., Taylor, A. J., Pfluger, H. B., et al. (2011). Disproportionate exercise load and remodeling of the athlete's right ventricle. *Med. Sci. Sports Exerc.* 43, 974–981. doi: 10.1249/mss.0b013e31820607a3

Lakin, R., Polidovitch, N., Yang, S., Guzman, C., Gao, X., Wauchop, M., et al. (2019). Inhibition of soluble TNFalpha prevents adverse atrial remodeling and atrial arrhythmia susceptibility induced in mice by endurance exercise. *J. Mol. Cell Cardiol.* 129, 165–173. doi: 10.1016/j.yjmcc.2019.01.012

Lal, H., Ahmad, F., Woodgett, J., and Force, T. (2015). The GSK-3 family as therapeutic target for myocardial diseases. *Circ. Res.* 116, 138–149. doi: 10.1161/circresaha.116.303613

Lavandero, S., Foncea, R., Perez, V., and Sapag-Hagar, M. (1998). Effect of inhibitors of signal transduction on IGF-1-induced protein synthesis associated with hypertrophy in cultured neonatal rat ventricular myocytes. *FEBS Lett.* 422, 193–196. doi: 10.1016/s0014-5793(98)00008-8

Li, J., Solus, J., Chen, Q., Rho, Y. H., Milne, G., Stein, C. M., et al. (2010). Role of inflammation and oxidative stress in atrial fibrillation. *Heart Rhythm* 7, 438–444. doi: 10.1016/j.hrthm.2009.12.009

Li, Y., Tan, W., Ye, F., Xue, F., Gao, S., Huang, W., et al. (2019). Identification of microRNAs and genes as biomarkers of atrial fibrillation using a bioinformatics approach. *J. Int. Med. Res.* 47, 3580–3589. doi: 10.1177/0300060519852235

Liao, C. H., Akazawa, H., Tamagawa, M., Ito, K., Yasuda, N., Kudo, Y., et al. (2010). Cardiac mast cells cause atrial fibrillation through PDGF-A-mediated fibrosis in pressure-overloaded mouse hearts. *J. Clin. Invest.* 120, 242–253. doi: 10.1172/jci39942

Mahida, S. (2013). Transcription factors and atrial fibrillation. *Cardiovasc. Res.* 101, 194–202. doi: 10.1093/cvr/cvt261

Malmo, V., Nes, B. M., Amundsen, B. H., Tjonna, A. E., Stoylen, A., Rossvoll, O., et al. (2016). Aerobic interval training reduces the burden of atrial fibrillation in the short term: a randomized trial. *Circulation* 133, 466–473. doi: 10.1161/circulationaha.115.018220

Manso, A. M., Elsherif, L., Kang, S. M., and Ross, R. S. (2006). Integrins, membrane-type matrix metalloproteinases and ADAMs: potential implications for cardiac remodeling. *Cardiovasc. Res.* 69, 574–584. doi: 10.1016/j.cardiores.2005.09.004

Manso, A. M., Li, R., Monkley, S. J., Cruz, N. M., Ong, S., Lao, D. H., et al. (2013). Talin1 has unique expression versus talin 2 in the heart and modifies the hypertrophic response to pressure overload. *J. Biol. Chem.* 288, 4252–4264. doi: 10.1074/jbc.m112.427484

McDonald, L. T., Zile, M. R., Zhang, Y., Van Laer, A. O., Baicu, C. F., Stroud, R. E., et al. (2018). Increased macrophage-derived SPARC precedes collagen deposition in myocardial fibrosis. *Am. J. Physiol. Heart Circ. Physiol.* 315, H92–H100.

Mohanty, S., Mohanty, P., Tamaki, M., Natale, V., Gianni, C., Trivedi, C., et al. (2016). Differential association of exercise intensity with risk of atrial fibrillation in men and women: evidence from a meta-analysis. *J. Cardiovasc. Electrophysiol.* 27, 1021–1029. doi: 10.1111/jce.13023

Mont, L., Sambola, A., Brugada, J., Vacca, M., Marrugat, J., Elosua, R., et al. (2002). Long-lasting sport practice and lone atrial fibrillation. *Eur. Heart J.* 23, 477–482. doi: 10.1053/euhj.2001.2802

Moreira-Goncalves, D., Henriques-Coelho, T., Fonseca, H., Ferreira, R., Padrao, A. I., Santa, C., et al. (2015). Intermittent cardiac overload results in adaptive hypertrophy and provides protection against left ventricular acute pressure overload insult. *J. Physiol.* 593, 3885–3897. doi: 10.1113/jp270685

Murphy, G. (2008). The ADAMs: signalling scissors in the tumour microenvironment. *Nat. Rev. Cancer.* 8, 929–941.

Murphy, J. M., Jeong, K., Rodriguez, Y. A. R., Kim, J. H., Ahn, E. E., and Lim, S. S. (2019). FAK and Pyk2 activity promote TNF-alpha and IL-1beta-mediated pro-inflammatory gene expression and vascular inflammation. *Sci. Rep.* 9:7617.

Nakamura, Y., Kita, S., Tanaka, Y., Fukuda, S., Obata, Y., Okita, T., et al. (2020). A disintegrin and metalloproteinase 12 prevents heart failure by regulating

cardiac hypertrophy and fibrosis. *Am. J. Physiol. Heart Circ. Physiol.* 318, H238–H251.

Nattel, S., and Harada, M. (2014). Atrial remodeling and atrial fibrillation: recent advances and translational perspectives. *J. Am. Coll. Cardiol.* 63, 2335–2345.

Oakes, R. S., Badger, T. J., Kholmovski, E. G., Akoum, N., Burgon, N. S., Fish, E. N., et al. (2009). Detection and quantification of left atrial structural remodeling with delayed-enhancement magnetic resonance imaging in patients with atrial fibrillation. *Circulation* 119, 1758–1767. doi: 10.1161/circulationaha.108.811877

Odutayo, A., Wong, C. X., Hsiao, A. J., Hopewell, S., Altman, D. G., and Emdin, C. A. (2016). Atrial fibrillation and risks of cardiovascular disease, renal disease, and death: systematic review and meta-analysis. *BMJ* 354:i4482. doi: 10.1136/bmj.i4482

Oudit, G. Y., Kassiri, Z., Zhou, J., Liu, Q. C., Liu, P. P., Backx, P. H., et al. (2008). Loss of PTEN attenuates the development of pathological hypertrophy and heart failure in response to biomechanical stress. *Cardiovasc. Res.* 78, 505–514. doi: 10.1093/cvr/cvn041

Papageorgiou, A. P., Swinnen, M., Vanhoutte, D., Vandendriessche, T., Chuah, M., Lindner, D., et al. (2012). Thrombospondin-2 prevents cardiac injury and dysfunction in viral myocarditis through the activation of regulatory T-cells. *Cardiovasc. Res.* 94, 115–124. doi: 10.1093/cvr/cvs077

Park, J., Joung, B., Uhm, J. S., Young Shim, C., Hwang, C., Hyoung Lee, M., et al. (2014). High left atrial pressures are associated with advanced electroanatomical remodeling of left atrium and independent predictors for clinical recurrence of atrial fibrillation after catheter ablation. *Heart Rhythm* 11, 953–960. doi: 10.1016/j.hrthm.2014.03.009

Patro, R., Duggal, G., Love, M. I., Irizarry, R. A., and Kingsford, C. (2017). Salmon provides fast and bias-aware quantification of transcript expression. *Nat. Methods* 14, 417–419. doi: 10.1038/nmeth.4197

Podolsky, M. J., Yang, C. D., Valenzuela, C. L., Datta, R., Huang, S. K., Nishimura, S. L., et al. (2020). Age-dependent regulation of cell-mediated collagen turnover. *JCI Insight* 5:e137519.

Qu, Y. C., Du, Y. M., Wu, S. L., Chen, Q. X., Wu, H. L., and Zhou, S. F. (2009). Activated nuclear factor-kappaB and increased tumor necrosis factor-alpha in atrial tissue of atrial fibrillation. *Scand. Cardiovasc. J.* 43, 292–297. doi: 10.1080/14017430802651803

Ramkumar, A., Jong, B. Y., and Ori-Mckenney, K. M. (2018). ReMAPping the microtubule landscape: how phosphorylation dictates the activities of microtubule-associated proteins. *Dev. Dyn.* 247, 138–155. doi: 10.1002/dvdy.24599

Ravassa, S., Ballesteros, G., and Diez, J. (2019). Aging and atrial fibrillation: a matter of fibrosis. *Aging (Albany NY)* 11, 9965–9966. doi: 10.18632/aging.102501

Redpath, C. J., and Backx, P. H. (2015). Atrial fibrillation and the athletic heart. *Curr. Opin. Cardiol.* 30, 17–23. doi: 10.1097/hco.0000000000000130

Reeves, J. T., Groves, B. M., Cymerman, A., Sutton, J. R., Wagner, P. D., Turkevich, D., et al. (1990). Operation Everest II: cardiac filling pressures during cycle exercise at sea level. *Respir. Physiol.* 80, 147–154. doi: 10.1016/0034-5687(90)90078-d

Remes, J., Van Brakel, T. J., Bolotin, G., Garber, C., De Jong, M. M., Van Der Veen, F. H., et al. (2008). Persistent atrial fibrillation in a goat model of chronic left atrial overload. *J. Thorac. Cardiovasc. Surg.* 136, 1005–1011. doi: 10.1016/j.jtcvs.2008.05.015

Ren, M., Li, X., Hao, L., and Zhong, J. (2015). Role of tumor necrosis factor alpha in the pathogenesis of atrial fibrillation: a novel potential therapeutic target? *Ann. Med.* 47, 316–324. doi: 10.3109/07853890.2015.1042030

Ringner, M. (2008). What is principal component analysis? *Nat. Biotechnol.* 26, 303–304.

Rodriguez, C., and Martinez-Gonzalez, J. (2019). The role of Lysyl oxidase enzymes in cardiac function and remodeling. *Cells* 8:1483. doi: 10.3390/cells8121483

Rosenberg, K., Olsson, H., Morgelin, M., and Heinegard, D. (1998). Cartilage oligomeric matrix protein shows high affinity zinc-dependent interaction with triple helical collagen. *J. Biol. Chem.* 273, 20397–20403. doi: 10.1074/jbc.273.32.20397

Rysa, J., Tokola, H., and Ruskoaho, H. (2018). Mechanical stretch induced transcriptomic profiles in cardiac myocytes. *Sci. Rep.* 8:4733.

Sakamuri, S. S., Takawale, A., Basu, R., Fedak, P. W., Freed, D., Sergi, C., et al. (2016). Differential impact of mechanical unloading on structural and nonstructural components of the extracellular matrix in advanced human heart failure. *Transl. Res.* 172, 30–44. doi: 10.1016/j.trsl.2016.02.006

Samaj, J., Baluska, F., and Hirt, H. (2004). From signal to cell polarity: mitogen-activated protein kinases as sensors and effectors of cytoskeleton dynamicity. *J. Exp. Bot.* 55, 189–198. doi: 10.1093/jxb/erh012

Sanz-Ezquerro, J. J., Munsterberg, A. E., and Stricker, S. (2017). Editorial: signaling pathways in embryonic development. *Front. Cell Dev. Biol.* 5:76. doi: 10.3389/fcell.2017.00076

Schlaepfer, D. D., Hou, S., Lim, S. T., Tomar, A., Yu, H., Lim, Y., et al. (2007). Tumor necrosis factor-alpha stimulates focal adhesion kinase activity required for mitogen-activated kinase-associated interleukin 6 expression. *J. Biol. Chem.* 282, 17450–17459. doi: 10.1074/jbc.m610672200

Schneider, S., Weydig, C., and Wessler, S. (2008). Targeting focal adhesions:*Helicobacter* pylori-host communication in cell migration. *Cell Commun. Signal* 6:2. doi: 10.1186/1478-811x-6-2

Schroen, B., Heymans, S., Sharma, U., Blankesteijn, W. M., Pokharel, S., Cleutjens, J. P., et al. (2004). Thrombospondin-2 is essential for myocardial matrix integrity: increased expression identifies failure-prone cardiac hypertrophy. *Circ Res* 95, 515–522. doi: 10.1161/01.res.0000141019.20332.3e

Schumacher, S. M., and Naga Prasad, S. V. (2018). Tumor necrosis factor-alpha in heart failure: an updated review. *Curr. Cardiol. Rep.* 20:117.

Shen, M., Hu, M., Fedak, P. W. M., Oudit, G. Y., and Kassiri, Z. (2018). Cell-specific functions of ADAM17 regulate the progression of thoracic aortic aneurysm. *Circ. Res.* 123, 372–388. doi: 10.1161/circresaha.118.313181

Shifrin, Y., Pinto, V. I., Hassanali, A., Arora, P. D., and Mcculloch, C. A. (2012). Force-induced apoptosis mediated by the Rac/Pak/38 signalling pathway is regulated by filamin A. *Biochem. J.* 445, 57–67. doi: 10.1042/bj20112119

Simmers, M. B., Cole, B. K., Ogletree, M. L., Chen, Z., Xu, Y., Kong, L. J., et al. (2016). Hemodynamics associated with atrial fibrillation directly alters thrombotic potential of endothelial cells. *Thromb. Res.* 143, 34–39. doi: 10.1016/j.thromres.2016.04.022

Sivasubramanian, N., Coker, M. L., Kurrelmeyer, K. M., Maclellan, W. R., Demayo, F. J., Spinale, F. G., et al. (2001). Left ventricular remodeling in transgenic mice with cardiac restricted overexpression of tumor necrosis factor. *Circulation* 104, 826–831. doi: 10.1161/hc3401.093154

Spinale, F. G. (2002). Matrix metalloproteinases: regulation and dysregulation in the failing heart. *Circ. Res.* 90, 520–530. doi: 10.1161/01.res.0000013290.12884.a3

Srivastava, A., Malik, L., Smith, T., Sudbery, I., and Patro, R. (2019). Alevin efficiently estimates accurate gene abundances from dscRNA-seq data. *Genome Biol.* 20:65.

Staerk, L., Sherer, J. A., Ko, D., Benjamin, E. J., and Helm, R. H. (2017). Atrial fibrillation: epidemiology, pathophysiology, and clinical outcomes. *Circ. Res.* 120, 1501–1517. doi: 10.1161/circresaha.117.309732

Staerk, L., Wang, B., Preis, S. R., Larson, M. G., Lubitz, S. A., Ellinor, P. T., et al. (2018). Lifetime risk of atrial fibrillation according to optimal, borderline, or elevated levels of risk factors: cohort study based on longitudinal data from the Framingham Heart Study. *BMJ* 361:k1453. doi: 10.1136/bmj.k1453

Su, S. A., Yang, D., Wu, Y., Xie, Y., Zhu, W., Cai, Z., et al. (2017). EphrinB2 regulates cardiac fibrosis through modulating the interaction of Stat3 and TGF-beta/Smad3 signaling. *Circ. Res.* 121, 617–627. doi: 10.1161/circresaha.117.311045

Subramanian, A., Tamayo, P., Mootha, V. K., Mukherjee, S., Ebert, B. L., Gillette, M. A., et al. (2005). Gene set enrichment analysis: a knowledge-based approach for interpreting genome-wide expression profiles. *Proc. Natl. Acad. Sci. U.S.A.* 102, 15545–15550. doi: 10.1073/pnas.0506580102

Sugden, P. H., Fuller, S. J., Weiss, S. C., and Clerk, A. (2008). Glycogen synthase kinase 3 (GSK3) in the heart: a point of integration in hypertrophic signalling and a therapeutic target? A critical analysis. *Br. J. Pharmacol.* 153(Suppl. 1), S137–S153.

Sun, M., Chen, M., Dawood, F., Zurawska, U., Li, J. Y., Parker, T., et al. (2007). Tumor necrosis factor-alpha mediates cardiac remodeling and ventricular dysfunction after pressure overload state. *Circulation* 115, 1398–1407. doi: 10.1161/circulationaha.106.643585

Tanaka, K., Abe, M., and Sato, Y. (1999). Roles of extracellular signal-regulated kinase 1/2 and p38 mitogen-activated protein kinase in the signal transduction

of basic fibroblast growth factor in endothelial cells during angiogenesis. *Jpn. J. Cancer Res.* 90, 647–654. doi: 10.1111/j.1349-7006.1999.tb00796.x

Thomas, A. M., Cabrera, C. P., Finlay, M., Lall, K., Nobles, M., Schilling, R. J., et al. (2019). Differentially expressed genes for atrial fibrillation identified by RNA sequencing from paired human left and right atrial appendages. *Physiol. Genomics* 51, 323–332. doi: 10.1152/physiolgenomics.00012.2019

Tracey, K. J., and Cerami, A. (1994). Tumor necrosis factor: a pleiotropic cytokine and therapeutic target. *Annu. Rev. Med.* 45, 491–503. doi: 10.1146/annurev.med.45.1.491

Turk, B., Turk, D., and Turk, V. (2000). Lysosomal cysteine proteases: more than scavengers. *Biochim. Biophys. Acta* 1477, 98–111. doi: 10.1016/s0167-4838(99)00263-0

Vadlamudi, R. K., Li, F., Adam, L., Nguyen, D., Ohta, Y., Stossel, T. P., et al. (2002). Filamin is essential in actin cytoskeletal assembly mediated by p21-activated kinase 1. *Nat. Cell Biol.* 4, 681–690. doi: 10.1038/ncb838

van der Slot, A. J., Van Dura, E. A., De Wit, E. C., De Groot, J., Huizinga, T. W., Bank, R. A., et al. (2005). Elevated formation of pyridinoline cross-links by profibrotic cytokines is associated with enhanced lysyl hydroxylase 2b levels. *Biochim. Biophys. Acta* 1741, 95–102. doi: 10.1016/j.bbadis.2004.09.009

Vega, R. B., Konhilas, J. P., Kelly, D. P., and Leinwand, L. A. (2017). Molecular mechanisms underlying cardiac adaptation to exercise. *Cell Metab.* 25, 1012–1026. doi: 10.1016/j.cmet.2017.04.025

Vermeulen, Z., Segers, V. F., and De Keulenaer, G. W. (2016). ErbB2 signaling at the crossing between heart failure and cancer. *Basic Res. Cardiol.* 111:60.

Vranka, I., Penz, P., and Dukat, A. (2007). Atrial conduction delay and its association with left atrial dimension, left atrial pressure and left ventricular diastolic dysfunction in patients at risk of atrial fibrillation. *Exp. Clin. Cardiol.* 12, 197–201.

Wang, L., Yue, Y., Yang, X., Fan, T., Mei, B., Hou, J., et al. (2017a). Platelet derived growth factor alpha (PDGFRalpha) induces the activation of cardiac fibroblasts by activating c-Kit. *Med. Sci. Monit.* 23, 3808–3816. doi: 10.12659/msm.906038

Wang, X., Chen, W., Zhang, J., Khan, A., Li, L., Huang, F., et al. (2017b). Critical role of ADAMTS2 (a disintegrin and metalloproteinase with thrombospondin Motifs 2) in cardiac hypertrophy induced by pressure overload. *Hypertension* 69, 1060–1069. doi: 10.1161/hypertensionaha.116.08581

Weeke, P., Muhammad, R., Delaney, J. T., Shaffer, C., Mosley, J. D., Blair, M., et al. (2014). Whole-exome sequencing in familial atrial fibrillation. *Eur. Heart J.* 35, 2477–2483. doi: 10.1093/eurheartj/ehu156

White, E. (2011). Mechanical modulation of cardiac microtubules. *Pflugers Arch.* 462, 177–184. doi: 10.1007/s00424-011-0963-0

Wingett, S. W., and Andrews, S. (2018). FastQ Screen: a tool for multi-genome mapping and quality control. *F1000Res.* 7:1338. doi: 10.12688/f1000research.15931.1

Wyse, D. G., Van Gelder, I. C., Ellinor, P. T., Go, A. S., Kalman, J. M., Narayan, S. M., et al. (2014). Lone atrial fibrillation: does it exist? *J. Am. Coll. Cardiol.* 63, 1715–1723.

Xu, G. J., Gan, T. Y., Tang, B. P., Chen, Z. H., Mahemuti, A., Jiang, T., et al. (2013). Accelerated fibrosis and apoptosis with ageing and in atrial fibrillation: adaptive responses with maladaptive consequences. *Exp. Ther. Med.* 5, 723–729. doi: 10.3892/etm.2013.899

Xu, J., Cui, G., Esmailian, F., Plunkett, M., Marelli, D., Ardehali, A., et al. (2004). Atrial extracellular matrix remodeling and the maintenance of atrial fibrillation. *Circulation* 109, 363–368. doi: 10.1161/01.cir.0000109495.02213.52

Xu, J., Mukerjee, S., Silva-Alves, C. R., Carvalho-Galvao, A., Cruz, J. C., Balarini, C. M., et al. (2016). A disintegrin and metalloprotease 17 in the cardiovascular and central nervous systems. *Front. Physiol.* 7:469. doi: 10.3389/fphys.2016.00469

Yabluchanskiy, A., Ma, Y., Iyer, R. P., Hall, M. E., and Lindsey, M. L. (2013). Matrix metalloproteinase-9: Many shades of function in cardiovascular disease. *Physiology (Bethesda)* 28, 391–403. doi: 10.1152/physiol.00029.2013

Yang, Z., Kyriakides, T. R., and Bornstein, P. (2000). Matricellular proteins as modulators of cell-matrix interactions: adhesive defect in thrombospondin 2-null fibroblasts is a consequence of increased levels of matrix metalloproteinase-2. *Mol. Biol. Cell* 11, 3353–3364. doi: 10.1091/mbc.11.10.3353

Ye, Y. Z., Chang, Y. F., Wang, B. Z., Ma, Y. T., and Ma, X. (2020). Prognostic value of von Willebrand factor for patients with atrial fibrillation: a meta-analysis of prospective cohort studies. *Postgrad. Med. J.* 96, 267–276. doi: 10.1136/postgradmedj-2019-136842

Yin, J. C., Platt, M. J., Tian, X., Wu, X., Backx, P. H., Simpson, J. A., et al. (2017). Cellular interplay via cytokine hierarchy causes pathological cardiac hypertrophy in RAF1-mutant Noonan syndrome. *Nat. Commun.* 8:15518.

Yokoyama, T., Sekiguchi, K., Tanaka, T., Tomaru, K., Arai, M., Suzuki, T., et al. (1999). Angiotensin II and mechanical stretch induce production of tumor necrosis factor in cardiac fibroblasts. *Am. J. Physiol.* 276, H1968–H1976.

Zhan, M., Jin, B., Chen, S. E., Reecy, J. M., and Li, Y. P. (2007). TACE release of TNF-alpha mediates mechanotransduction-induced activation of p38 MAPK and myogenesis. *J. Cell Sci.* 120, 692–701. doi: 10.1242/jcs.03372

Zhang, H., Wu, J., Dong, H., Khan, S. A., Chu, M. L., and Tsuda, T. (2014). Fibulin-2 deficiency attenuates angiotensin II-induced cardiac hypertrophy by reducing transforming growth factor-β signalling. *Clin. Sci. (Lond.)* 126, 275–288. doi: 10.1042/cs20120636

Zhang, P. P., Sun, J., and Li, W. (2020). Genome-wide profiling reveals atrial fibrillation-related circular RNAs in atrial appendages. *Gene* 728:144286. doi: 10.1016/j.gene.2019.144286

Zhang, S. J., Han, J. H., Sells, M. A., Chernoff, J., Knaus, U. G., Ulevitch, R. J., et al. (1995). Rho-family gtpases regulate P38 mitogen-activated protein-kinase through the downstream mediator Pak1. *J. Biol. Chem.* 270, 23934–23936. doi: 10.1074/jbc.270.41.23934

Zhang, X., Li, H., Kou, W., Tang, K., Zhao, D., Zhang, J., et al. (2019). Increased plasma microfibrillar-associated protein 4 is associated with atrial fibrillation and more advanced left atrial remodelling. *Arch. Med. Sci.* 15, 632–640. doi: 10.5114/aoms.2018.74953

Zhao, J., Lv, T., Quan, J., Zhao, W., Song, J., Li, Z., et al. (2018). Identification of target genes in cardiomyopathy with fibrosis and cardiac remodeling. *J. Biomed. Sci.* 25:63.

Zhong, C., Xin, M., He, L., Sun, G., and Shen, F. (2018). Prognostic value of von Willebrand factor in patients with atrial fibrillation: a meta-analysis. *Medicine (Baltimore)* 97:e11269. doi: 10.1097/md.0000000000011269

Zou, R., Yang, M., Shi, W., Zheng, C., Zeng, H., Lin, X., et al. (2018). Analysis of genes involved in persistent atrial fibrillation: comparisons of 'Trigger' and 'Substrate' differences. *Cell Physiol. Biochem.* 47, 1299–1309. doi: 10.1159/000490225

Conflict of Interest: The authors declare that the research was conducted in the absence of any commercial or financial relationships that could be construed as a potential conflict of interest.

frontiers in Physiology

ORIGINAL RESEARCH
published: 06 January 2021
doi: 10.3389/fphys.2020.611266

Non-invasive Spatial Mapping of Frequencies in Atrial Fibrillation: Correlation With Contact Mapping

*Miguel Rodrigo[1,2], Kian Waddell[1], Sarah Magee[1], Albert J. Rogers[1], Mahmood Alhusseini[1], Ismael Hernandez-Romero[3], Alejandro Costoya-Sánchez[2], Alejandro Liberos[2] and Sanjiv M. Narayan[1]**

[1] Stanford University School of Medicine, Stanford, CA, United States, [2] ITACA Institute, Universitat Politècnica de València, Valencia, Spain, [3] Department of Signal Theory and Communications, Rey Juan Carlos University, Móstoles, Spain

Introduction: Regional differences in activation rates may contribute to the electrical substrates that maintain atrial fibrillation (AF), and estimating them non-invasively may help guide ablation or select anti-arrhythmic medications. We tested whether non-invasive assessment of regional AF rate accurately represents intracardiac recordings.

Methods: In 47 patients with AF (27 persistent, age 63 ± 13 years) we performed 57-lead non-invasive Electrocardiographic Imaging (ECGI) in AF, simultaneously with 64-pole intracardiac signals of both atria. ECGI was reconstructed by Tikhonov regularization. We constructed personalized 3D AF rate distribution maps by Dominant Frequency (DF) analysis from intracardiac and non-invasive recordings.

Results: Raw intracardiac and non-invasive DF differed substantially, by 0.54 Hz [0.13 – 1.37] across bi-atrial regions ($R^2 = 0.11$). Filtering by high spectral organization reduced this difference to 0.10 Hz (cycle length difference of 1 – 11 ms) [0.03 – 0.42] for patient-level comparisons ($R^2 = 0.62$), and 0.19 Hz [0.03 – 0.59] and 0.20 Hz [0.04 – 0.61] for median and highest DF, respectively. Non-invasive and highest DF predicted acute ablation success ($p = 0.04$).

Conclusion: Non-invasive estimation of atrial activation rates is feasible and, when filtered by high spectral organization, provide a moderate estimate of intracardiac recording rates in AF. Non-invasive technology could be an effective tool to identify patients who may respond to AF ablation for personalized therapy.

Keywords: atrial fibrillation, driver, dominant frequency, non-invasive mapping, Electrocardiographic imaging, basket mapping

OPEN ACCESS

Edited by:
Richard David Walton, Université de Bordeaux, France

Reviewed by:
Matthijs Cluitmans, Maastricht University, Netherlands
Laura R. Bear, Institut de Rythmologie et Modélisation Cardiaque (IHU-Liryc), France

***Correspondence:**
Sanjiv M. Narayan
sanjiv1@stanford.edu

Specialty section:
This article was submitted to Cardiac Electrophysiology, a section of the journal Frontiers in Physiology

Received: *28 September 2020*
Accepted: *04 December 2020*
Published: *06 January 2021*

Citation:
Rodrigo M, Waddell K, Magee S, Rogers AJ, Alhusseini M, Hernandez-Romero I, Costoya-Sánchez A, Liberos A and Narayan SM (2021) Non-invasive Spatial Mapping of Frequencies in Atrial Fibrillation: Correlation With Contact Mapping. Front. Physiol. 11:611266. doi: 10.3389/fphys.2020.611266

INTRODUCTION

Pharmacological and surgical therapies for atrial fibrillation (AF) continue to have suboptimal outcomes despite advances in anatomical mapping and catheter technology. Isolation of the pulmonary veins (PVI) is the cornerstone of ablation, yet its 1 year success is 40–70% depending on population, and it is unclear how this can be improved. The identification and elimination of regions of rapid atrial activity are plausible mechanistic sites and indicate drivers in optical imaging of human AF (Hansen et al., 2015) and clinical studies (Miller et al., 2017; Honarbakhsh et al., 2019). These fastest activated regions may lie near scar or fibrosis (Swartz et al., 2009), and can

be represented by Dominant Frequency (DF) (Atienza et al., 2014), which identifies the activation rate as the greatest spectral contribution. It would be useful to identify such atrial regions non-invasively to characterize AF patients, and potentially to plan whether ablation should include PVI alone, more extensive ablation, or potentially other therapeutic strategies.

Electrocardiographic Imaging (ECGI) enables non-invasive reconstruction of epicardial electrical activity and may non-invasively characterize AF. ECGI has been used to identify regions in AF with reentrant and focal patterns to guide ablation (Haissaguerre et al., 2014), and shows regional differences in rate and sites of high dominant frequency (DF) (Pedrón-Torrecilla et al., 2016). Nevertheless, the accuracy of ECGI has been questioned (Cluitmans et al., 2017; Duchateau et al., 2018), and the DF of AF estimated from ECGI has never been calibrated against direct measurements from contact catheters. Finally, existing commercial ECGI systems use 252 leads which introduce practical limitations for bedside use, and increase the chance that electrodes may lose contact at some regions of the torso.

We set out to calibrate ECGI obtained using our published practical reduced-lead method, against simultaneously recorded panoramic intracardiac measurements in AF. We also correlated analyses to the clinical endpoint of acute ablation success resulting in termination of AF.

MATERIALS AND METHODS

Patient Inclusion

We recruited 47 consecutive patients undergoing AF ablation with simultaneous intracardiac basket and ECGI torso mapping at two centers: Stanford Hospital (SH, CA, United States, $N = 17$) and Hospital General Universitario Gregorio Marañón (HGUGM, Madrid, Spain, $N = 30$). Patients from Stanford University ($N = 17$) received PVI and also substrate guided ablation. In this approach, lesions were applied for 15 to 30 s at sites of focal or rotational activity in AF (Miller et al., 2017) identified by a commercial mapping system (RhythmView, Abbott) from basket recordings. Patients from Spain received only PVI, regardless of perceived substrate. Both protocols were approved by each local Institutional Ethics Committee and all patients gave informed consent.

Electrophysiological Study

Classes I and III antiarrhythmic medications were discontinued for $>$ 5 half-lives prior to study ($>$ 30 days for amiodarone). Catheters were advanced to the right atrium (RA), coronary sinus, and transseptally to left atrium (LA). In patients arriving in sinus rhythm, AF was induced using burst pacing. Contact basket catheters (64 poles) were positioned in RA, then LA for AF mapping, based on 3-dimensional electroanatomic imaging (NavX, St Jude Medical, Sylmar, CA, United States).

Data Acquisition

Unipolar electrograms (EGM) from basket catheters were recorded at 1 kHz sampling frequency and filtered at 0.05 to 500 Hz. Raw electrograms comprising 64 basket and other intracardiac channels (e.g., coronary sinus) and 12-lead ECG were exported from Bard (LabSystem Pro), Prucka (GE Cardiolab) or Boston Scientific (Clearsign^{TM}) recorders for off-line analysis. Basket electrode positions and atrial anatomy meshes were extracted from the electro-anatomical navigation system (Ensite NavX System) that enabled atrial anatomy reconstruction (**Figure 1A**).

MRI/CT images were acquired 2–3 days prior to the ablation procedure, and segmented to provide atria and torso anatomy using ITK-SNAP (Yushkevich et al., 2006; **Figure 1B**). Surface ECG positions were registered on torso anatomy as we have described (Rodrigo et al., 2020). Anatomical models obtained with the different technologies were co-registered by using an algorithm based on rigid transformations guided by fiducial points manually marked in both atrial models (PVs, LAA, RAA, superior vena cava (SVC) and inferior vena cava (IVC)) or torso models (anterior and posterior axillae, nipples, low scapula and xiphoid appendix) (Rodrigo et al., 2020).

Electrocardiographic imaging was recorded with surface ECG leads at electrophysiological study. ECG electrodes were distributed as follows: 24 electrodes on the anterior, 24 on the posterior, 3 on each lateral side of the torso and 3 extra leads to obtain Wilson Central Terminal (**Figures 1C,D**). We used the same filtering as for intracardiac electrograms (0.05 to 500 Hz band-pass at 1 kHz) as previously described (Rodrigo et al., 2020).

Data Analysis

Simultaneous basket EGM and surface ECG signals were analyzed from 160 AF episodes (3 [2 – 5] per patient). Signals with duration 4.9 $\pm$ 1.4 s were used for Dominant Frequency (DF) analysis. A total of $N = 4566$ pairs of Intracardiac and non-invasive signals were analyzed. Surface electrode recordings were discarded if noisy or poor contact defined as those in which QRS complexes had signal-to-noise ratio $<$ 0 dBs.

For intracardiac analysis, we calculated bipolar electrograms by subtracting unipolar electrograms for successive pairs of electrodes along basket splines (for instance A1-2, A3-4). Intracardiac DFs were then calculated from the Power Spectral Density (PSD) curves of these bipolar EGM signals using a convolutional filter composed by a band-pass filter (2 to 20 Hz, Butterworth) (Rodrigo et al., 2014) and a Botteron and Smith filter (Botteron and Smith, 1996). The PSD of both filtered signals was obtained by Welch Periodogram (50% overlapping, 2 s-length Hamming window, 65.536 points) and both PSDs were multiplied to get the final convolutional PSD (de la Torre Costa et al., 2016). The dominant frequency was defined as the maximal contribution in the 3 to 8 Hz band, discarding peaks whose sub-harmonic contribution (at DF/2) was higher than 50% of the DF peak amplitude. Spectral organization of EGM signals was calculated using the regularity index (RI), which is the cumulative sum of PSD in a 0.5 Hz bandwidth surrounding the DF peak ($\pm$ 0.25 Hz) (Skanes et al., 1998; Li et al., 2017).

For ECGI analysis, a QRST removal algorithm based on principal component analysis (PCA) was first applied to each ECG channel (Guillem et al., 2013). Then, the ECG baseline

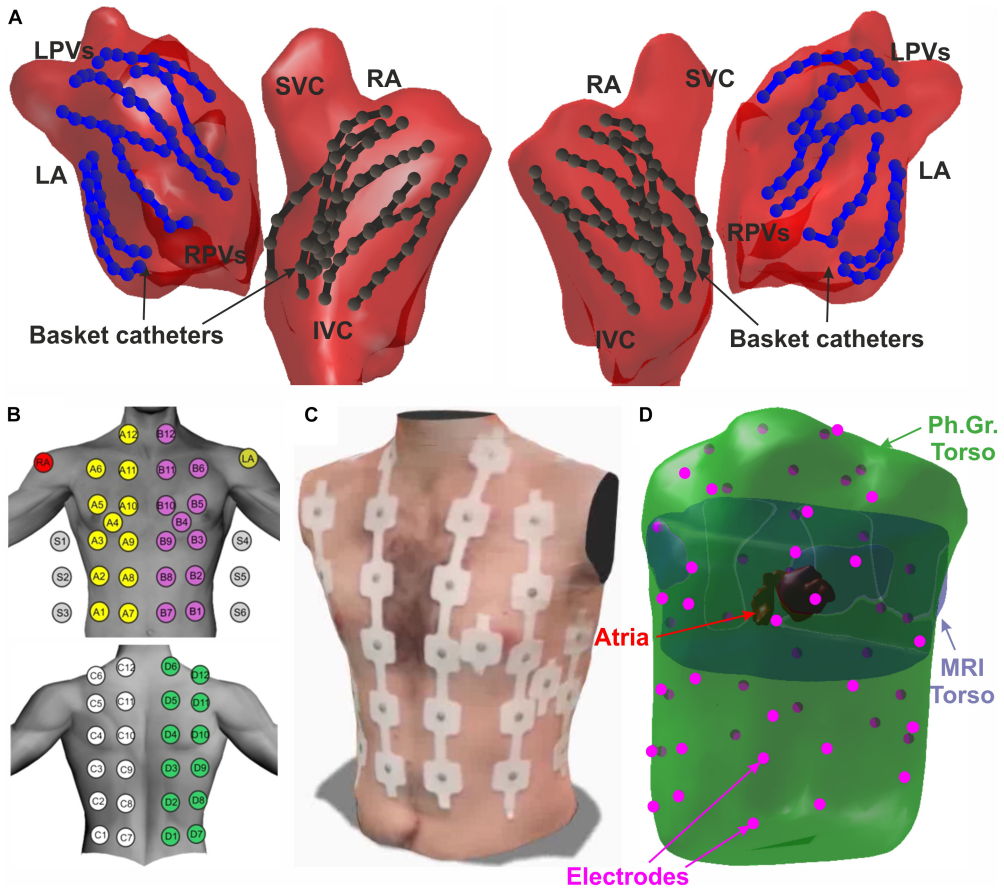

FIGURE 1 | Schematic view of the experiment set-up. **(A)** Atrial anatomy (red) with 2 basket catheters in left (blue) and right (black) atria. **(B)** Atrial anatomy segmentation from MRI scan. **(C)** Surface 57-ECG electrode distribution. **(D)** 3D meshes of the MRI torso (purple), photogrammetry torso (green), atrial anatomy (red), and BSPM electrodes (pink).

was estimated by decimation of raw signal (sample frequency of 50 Hz) and a posterior low-pass filtering (Butterworth 10th-order, cut-off frequency of 2 Hz). This baseline signal was interpolated to the original sample frequency and then subtracted from the original signal. ECG signals were then low-pass filtered with a 10th-order Butterworth filter with a cut-off frequency of 20 Hz. We estimated the inverse-computed Electrogram signals (ic-EGM) by applying the zero-order Tikhonov's method on the filtered surface signals over the torso and atrial anatomy. The optimal regularization parameter was chosen at the first local maximum value of the curvature of the L-curve (Rodrigo et al., 2017a). Non-invasive DFs in ic-EGM signals were identified on the PSD of raw reconstructed signals, which were already filtered on the ECG. The PSD of non-invasive signals was obtained by Welch Periodogram (50% overlapping, 2 s-length Hamming window, 65.536 points) and DF and RI was calculated as described for intracardiac recordings.

Median DF value was used to describe the overall DF values for each patient and/or episode. Highest DF (HDF), calculated as the 95% percentile of the intracardiac or non-invasive DF measures, respectively, were used to describe the fastest activation rate avoiding possible harmonic detection.

Ablation

Radiofrequency energy was delivered via an irrigated catheter (Cool-Flex/TactiCath/Sapphire-Blue, St Jude Medical) at 25 to 35 W. All patients received standard-of-care pulmonary vein isolation (PVI). Patients from Stanford center ($N = 17$) also received guided ablation, in whom lesions were applied for 15 to 30 s at sites of focal or rotational activity during AF guided by basket mapping and commercially available software (RhythmView, Abbott). Such potential driver sites were targeted if they were present for $>$ 50% of recorded tracings. Ablation covered areas of 2 to 3 cm^2 as described by Miller et al. (2017). PVI was performed by circumferential point-by-point ablation or cryoablation of left and right PV pairs (Artic Front, Medtronic Inc.) with verification of PV isolation using dedicated circular mapping catheters.

Performance Metrics and Statistical Analysis

Different measures were included to compare non-invasive vs. intracardiac DF measures. Relative Difference Measurement Star (RDMS) and Relative Absolute Error (RAE) metrics were used

to evaluate the relative difference between intracardiac and non-invasive DF measurements (Figuera et al., 2016). To evaluate the accuracy of non-invasive measures to identify sites of Highest DF (HDF) identified by intracardiac measures, we used the Weighted Underestimation Indicator (WUI), defined as the percentage of the intracardiac HDF region not detected non-invasively as HDF, and the Weighted Over-estimation Indicator (WOI), defined as the falsely detected non-invasive HDF areas as a percentage of the total non-invasive HDF region (Figuera et al., 2016). HDF regions for each AF epoch were defined as regions with DF within 0.5 Hz of HDF (i.e., > HDF −0.5 Hz), calculated for both invasive and non-invasive maps.

Continuous data are represented as mean ± SD, when normally distributed, or median [lower quartile – higher quartile] otherwise. Normality was evaluated using the Kolmogorov–Smirnov test. Comparisons between 2 groups were made with Student *t*-tests for independent samples if normally distributed, or if not normally distributed, with the Mann–Whitney *U*-test. Nominal values were expressed as n (%) and compared with χ^2 tests. Paired *t*-test was used for paired comparisons with continuous variables. A probability of < 0.05 was considered statistically significant. Repeated-measures one-way ANOVA test was used to compare patient-specific and global linear fits.

RESULTS

Patient demographics are shown in **Table 1**. Patients who underwent PVI and driver ablation had more comorbidities than other patients in the proportion of persistent AF cases, duration of AF history and demographics, with a higher rate of AF termination by ablation.

Non-invasive Identification of Atrial Activation Rate

An illustrative example of simultaneous intracardiac and non-invasive DF maps during an AF episode is depicted in **Figure 2**. In panel A, the DF values obtained from each basket electrode are projected onto the atrial surface and color-coded, with warm colors for higher frequencies. In this unusual episode with 2 basket catheters simultaneously placed in the left and right atria, the RA showed higher DF values of ∼7 Hz in the RA lateral wall, whereas the rest of the RA showed lower DF values ∼6 Hz and the LA ∼4.5–5 Hz.

The non-invasive ECGI AF rate map simultaneous to the basket recording (**Figure 2B**) shows a similarly located fastest region (7 Hz). This region covers a larger region on ECGI than on intracardiac maps, extending to much of RA and the septal LA. Remaining areas had lower frequencies around 5–6 Hz. Examples of intracardiac and non-invasive traces processed to obtain DF measures are shown in Panel C for signals #1 and #2 marked in Panels A and B, respectively. This patient received PVI only ablation, which did not terminate AF, and this right atrial site was not targeted.

A higher regularity index (RI) indicates that the frequency peak under consideration makes a greater contribution to the selected frequency range. In this study, RI identified intracardiac and non-invasive signals with more reliable DF measurements. In **Figure 2C**: the signal at position #1 on intracardiac and non-invasive traces showed periodic deflections every 140–150 ms, indicating 6.9 and 7.1 Hz yet with moderate RI = 0.20 and 0.17, respectively. The intracardiac signal at position #2 showed a clear spectral frequency of 4.6 Hz with a high RI value of 0.46, corresponding to observed deflections with period = 220 ms. Conversely, the ic-EGM trace at position #2 showed 2 similar spectral peaks at 3.3 and 6.1 Hz with low RI values of 0.07 and 0.08, respectively, which therefore may not faithfully represent the original signal periodicity. This is observed in the raw ic-EGM signal, in which no clear trend is observed at period = 300 ms (3.3 Hz) nor period = 165 ms (6.1 Hz).

Systematic Comparison of Raw Non-invasive and Basket DF

Supplementary Figure 1 summarizes the ability of non-invasive DF to estimate intracardiac DF in AF, examined by comparing 4566 non-invasive EGM vs. intracardiac-EGM pairs measured at the closest nodes of the atrial mesh to each intracardiac electrode (overall projection distance 4.4 ± 2.3 mm). Points with better agreement between intracardiac and non-invasive DFs (main diagonal) had higher values for intracardiac and non-invasive spectral regularity index (RI) (Skanes et al., 1998). Overall, the difference between non-invasive and invasive DF was 0.54 Hz [0.13 – 1.37] in absolute magnitude, or 11.3% [2.7 – 30.3] in relative magnitude (normalized to the intracardiac DF) with poor correlation ($R^2 = 0.11$).

Further analysis of RI indices are included in **Supplementary Figure 2**, where we provide additional analyses comparing intracardiac and non-invasive DFs and RIs. **Supplementary Figure 2A** shows low correlation between intracardiac and non-invasive RI, which may reflect different causes for intracardiac recordings (far field, low contact) than non-invasive recordings (ventricular contamination, poor surface coverage). Nevertheless, **Supplementary Figures 2A,B** show that DF estimated non-invasively differed from invasive indices less in patients with higher RI values, and more in patients with lower RI. This was true for intracardiac (**Supplementary Figure 2C**) and non-invasive (**Supplementary Figure 3D**) RI measurements. This reinforces our selection of this marker to estimate the reliability of DF estimates.

Systematic Comparison of Non-invasive and Basket DF, Filtered Using RI Threshold

We used RI calculated from spectral analysis, which measures stability of activation, as a filter to identify more stable signals. We used a RI threshold > 0.4 (intracardiac) and > 0.2 (non-invasive). RI thresholds were obtained by maximizing R^2 analysis on our dataset after thresholding. RI thresholds were higher for intracardiac than non-invasive signals as the total spectral content was lower for ECGI signals after spectral filtering.

Figure 3 shows intracardiac and non-invasive DF for pairs of tracings that fulfilled this RI threshold (967 signals from 123

TABLE 1 | Cohort demographics.

	All patients	PVI + Driver ablation (Stanford)	PVI Only (Spain)	*P*-value (Guided vs PVI)
N	47	17	30	–
Paroxysmal AF (%)	20 (43%)	3 (18%)	17 (57%)	**0.009**
Male (%)	21 (45%)	14 (82%)	7 (23%)	**<0.001**
Age (years)	63 ± 13	67 ± 9	61 ± 14	0.13
AF history (months)	55 ± 56	85 ± 70	36 ± 32	**0.01**
Previous ablations	1.1 ± 0.9	0.6 ± 1.0	1.4 ± 0.8	**0.004**
Acute termination (%)	12 (26%)	7 (41%)	5 (17%)	0.06
CHA2DS2-VASc Score	2.4 ± 1.5	2.5 ± 1.5	2.4 ± 1.6	0.80
Weight (kg)	78 ± 17	93 ± 14	70 ± 13	**<0.001**
Risk factors				
HTA (%)	24 (51%)	12 (71%)	12 (40%)	**0.04**
Diabetes (%)	8 (17%)	5 (29%)	3 (10%)	0.09
Obesity (%)	8 (17%)	4 (24%)	4 (13%)	0.37
Alcohol/Tabaquism (%)	9 (19%)	1 (6%)	8 (27%)	0.08
Cardiovascular diseases				
Valvulopaty (%)	13 (28%)	0 (0%)	13 (43%)	**0.001**
CAD (%)	6 (13%)	3 (18%)	3 (10%)	0.45
CHF (%)	5 (11%)	2 (12%)	3 (10%)	0.85
Dilated cardiomyopathy (%)	9 (19%)	6 (35%)	3 (10%)	0.04
Medications				
Class I/III antiarrhythmics	21 (45%)	7 (41%)	14 (47%)	0.72
Class II/IV antiarrhythmics	39 (83%)	15 (88%)	24 (80%)	0.47
Angiotensin Converting Enzyme Inhibitors (ACEI)/ Angiotensin Receptor Blockers (ARBs)	14 (30%)	7 (41%)	7 (23%)	0.82

Bold numbers are the statistically significant differences.

episodes and 42 patients). Panel A depicts intracardiac vs. non-invasive DF comparison, color-coded by patient number. The absolute and relative deviation between non-invasive and basket DF measures was 0.10 Hz [0.03 – 0.42] and 2.3% [0.7–8.9], respectively (Panels C and D), with $R^2 = 0.62$. These measures provided a Relative Difference Measurement Star (RDMS) of 0.075% [0.034 – 0.125]; and Relative Absolute Error (RAE) of 7.51% [3.77 – 14.4] across patients. We assessed inter-patient variability in the DF linear fit using repeated-measures one-way ANOVA to compare individual patients to the global linear regression fit. Notably, 19 out of 47 patients (40%) showed a significant difference ($p < 0.05$) between the patient-dependent and global trend fits.

Panel B shows median and highest DF (HDF) over both atria on a per-episode basis, calculated for 160 AF episodes (3 [2–5] per patient, 4.9 ± 1.4 s duration). Absolute and relative deviation between non-invasive and basket HDF measures were 0.20 [0.04 – 0.61] Hz and 3.5 [1.0 – 11.2]%, and the linear fitting $R^2 = 0.46$, whereas the deviation for median DF was 0.19 [0.03 – 0.59] Hz and 3.4 [0.7 – 11.8]% (Panels C and D) and the linear fitting was $R^2 = 0.52$. Highest DF and median DF were detected by ECGI with a difference from intracardiac electrodes of < 1.5 Hz except for 12/6 cases, respectively (1.2%/0.6%). Cases with deviations > 2.5 Hz had a poor number (< 10) of intracardiac/non-invasive signals to compare after RI threshold (**Supplementary Figures 3**, **4**).

We also measured the accuracy of non-invasive maps to identify high DF regions revealed by intracardiac recordings, using WUI and WOI. High DF regions detected by ECGI produced a median false positive area of 27.6% [0.0 – 77.8] (WOI metric), whereas non-HDF regions detected by ECGI produced a median false positive area of 0.0% [0.0 – 50.0] of intracardiac high DF area (WUI metric), compared with intracardiac high DF regions.

Ablation Outcome, Global and Regional Atrial Rate

We reasoned that patients more amenable to therapy may have more organized AF, and hence lower median DF. We further reasoned that within the lower overall DF milieu in such patients, sites of potential interest for targeted ablation may be the fastest, i.e., with highest DF.

Figure 4 shows simultaneous intracardiac and ECGI DF maps for two patients in whom AF did terminated acutely during ablation (**Figures 4A,B**) or did not terminate (**Figure 4C**). Intracardiac and non-invasive DF measures not fulfilling the RI threshold are depicted as gray. The first patient with acute termination during PVI + guided ablation showed slow rates across the atria: 3.9 Hz and 4.1 Hz of median DF and HDF in intracardiac maps, and 3.9 Hz and 4.1 Hz in ECGI maps, respectively. The second patient with acute termination during PVI only ablation showed also slow rates across the atria: 3.7 Hz and 4.0 Hz of median DF and HDF in intracardiac maps, and 3.7 Hz and 3.8 Hz in ECGI maps, respectively. Conversely, the third patient without AF termination during PVI only ablation

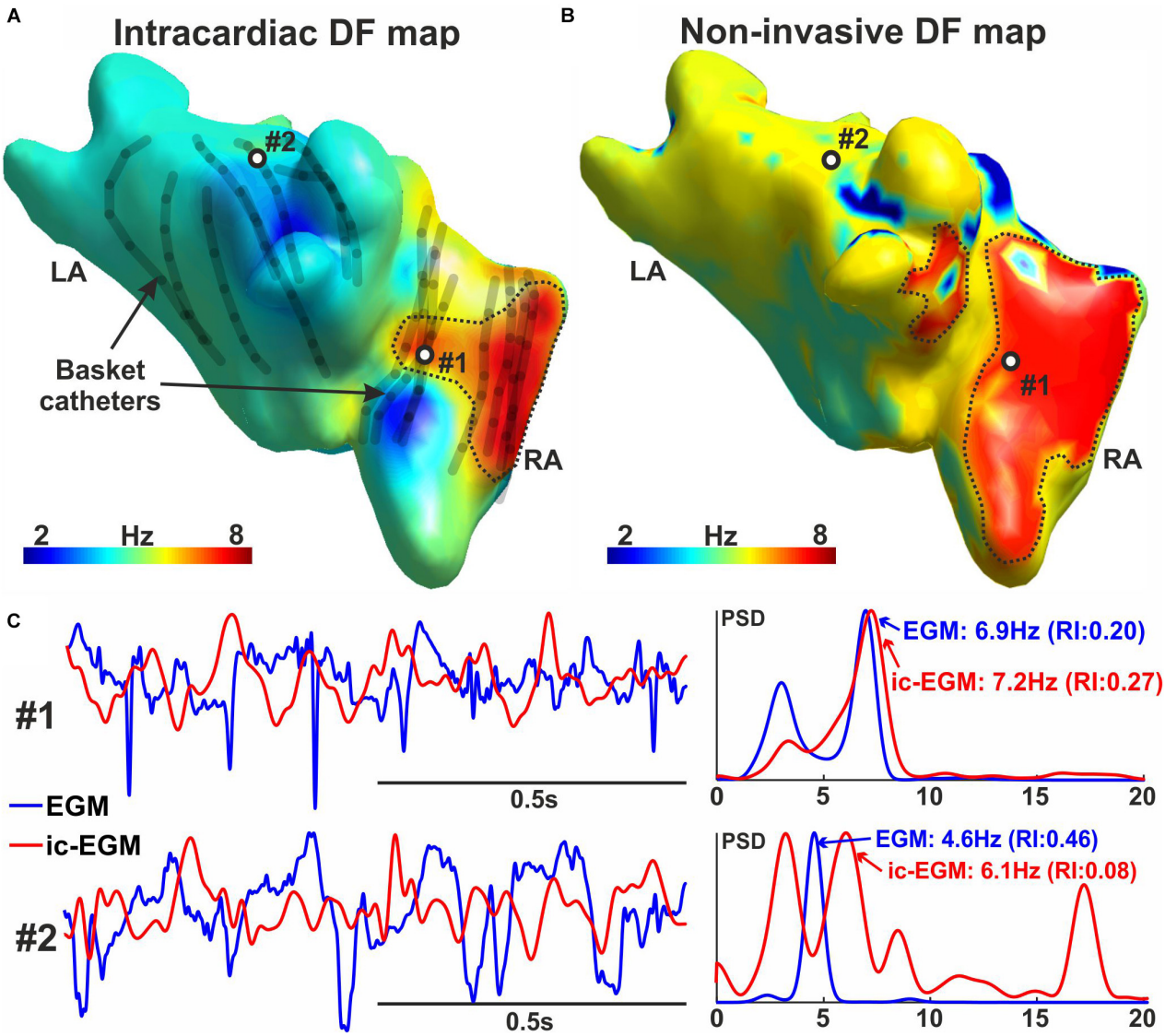

FIGURE 2 | Intracardiac and non-invasive DF map. **(A)** Intracardiac DF map. **(B)** Non-invasive DF map. **(C)** Intracardiac and non-invasive signals and Power Spectral Density (PSD) from points #1 and #2 marked in panels **(A,B)**.

had higher global activation rate: 6.0 Hz and 6.6 Hz for median DF and HDF, respectively, slightly faster in RA (∼6.5 Hz) than LA (∼6 Hz) as also shown on ECGI maps 6.5 Hz and 6.7 Hz, respectively). PVI ablation did not terminate AF in this patient.

Overall, **Figure 5** shows this trend for higher ECGI DF in patients in whom ablation did not acutely terminate AF compared to those with AF termination. The resolution of our maps did not identify high-DF spots at sites where ablation acutely terminated AF on intracardiac nor ECGI DF maps. It is not clear if this represents small numbers, an artifact of DF analysis, map resolution that missed a small site of high DF, or the actual physiology. Patients with acute AF termination thus showed slightly lower overall activation rates reconstructed non-invasively than patients with no acute termination, in median DF (5.0 ± 1.1 Hz vs. 5.3 ± 1.0 Hz, $p = 0.055$) and HDF (5.2 ± 1.1 Hz vs 5.6 ± 1.0, $p = 0.044$). No significant differences were found using this approach for classical AF classification such as paroxysmal and persistent patients (**Figure 5B**), neither in median DF (5.2 ± 1.2 Hz vs 5.2 ± 0.9 Hz, $p = 0.62$) nor in HDF (5.4 ± 1.2 Hz vs 5.5 ± 0.9 Hz, $p = 0.53$).

Non-invasive DF measures were also calculated between different patient groups in **Supplemental Figures 5, 6**. Differences between terminating and non-terminating patients where only present in persistent patients (median DF: 4.9 ± 0.9 Hz vs 5.4 ± 0.8 Hz, $p = 0.005$; highest DF: 5.1 ± 0.9 Hz vs 5.7 ± 0.9 Hz, $p = 0.002$). Paroxysmal patients did not show differences in median DF (5.1 ± 1.4 Hz vs 5.2 ± 1.1 Hz, $p = 0.98$) or Highest DF (5.4 ± 1.3 Hz vs 5.4 ± 1.1 Hz, $p = 0.90$).

Patients in whom AF terminated by ablation showed lower DF in non-invasive maps than patients in whom AF did

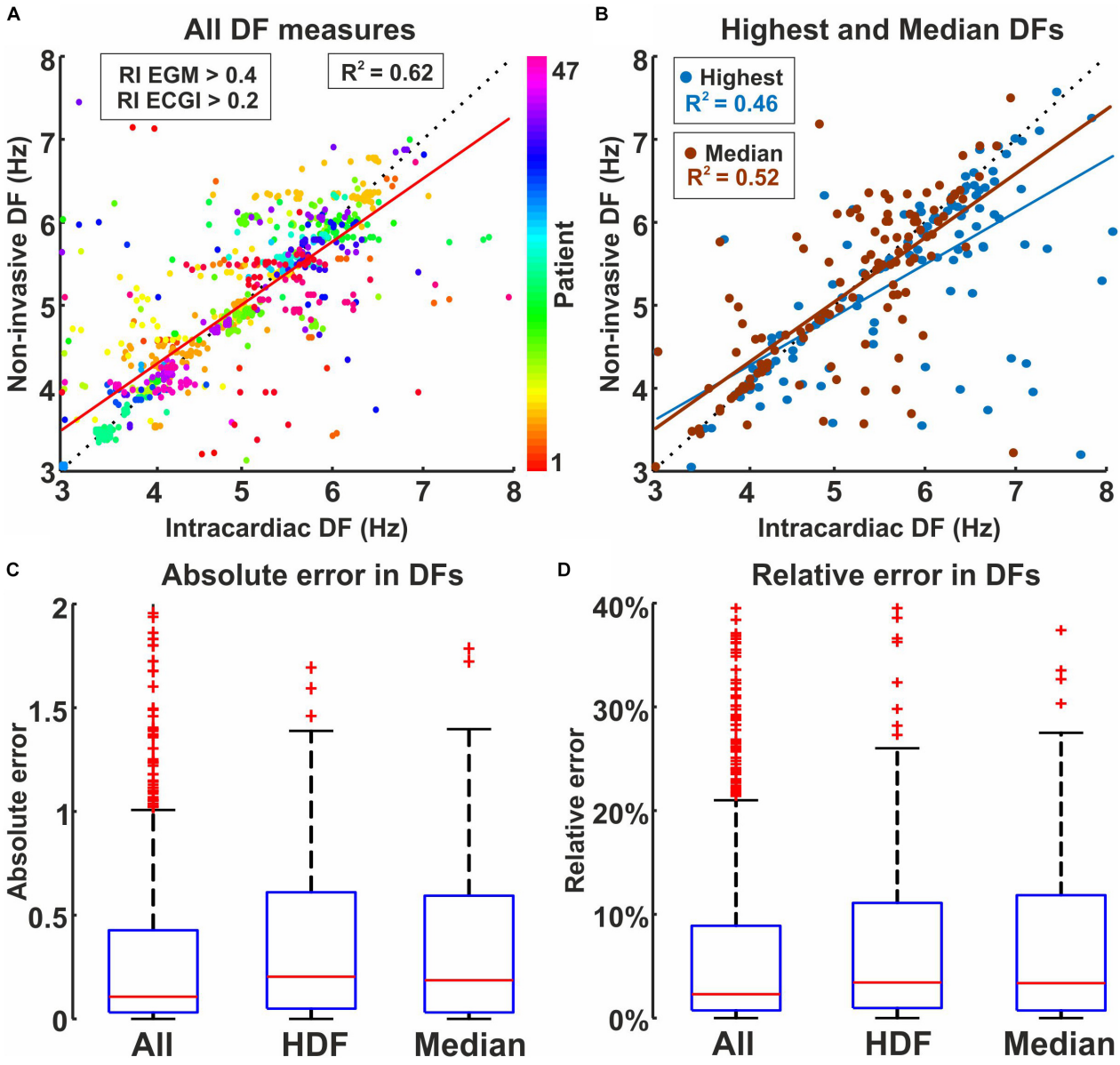

FIGURE 3 | Intracardiac and non-invasive DF measures filtered by spectral organization (RI). **(A)** Dispersion plot by patient, using RI (intracardiac) > 0.4 and RI (non-invasive) > 0.2. **(B)** Dispersion plot coded by highest DF (blue) and Median DF (red). **(C)** Absolute and **(D)** relative (% of intracardiac measure) difference for all electrodes, Highest DF and Median DF.

not terminate in both AF ablation protocols (**Supplementary Figure 6**). In patients receiving PVI + substrate ablation, median DF were 5.1 ± 1.1 Hz vs 5.5 ± 0.8 Hz, $p = 0.035$, while highest DF were 5.3 ± 1.0 Hz vs 5.7 ± 0.8 Hz, $p = 0.034$. Patients receiving PVI-only ablation showed a similar (but non-significant) trend for median DF of 4.7 ± 1.0 Hz vs 5.1 ± 1.0 Hz, $p = 0.18$ and for highest DF of 4.9 ± 1.1 Hz vs 5.4 ± 1.1 Hz, $p = 0.15$).

Finally, we examined DF between patients with and without AF termination from intracardiac data (**Figure 6**). In intracardiac recordings, patients with AF termination by ablation showed lower overall DF than patients without termination, for both median DF (4.5 ± 0.9 Hz vs 5.3 ± 0.8 Hz, $p < 0.001$) and highest DF (5.3 ± 1.1 Hz vs 5.8 ± 0.9 Hz, $p = 0.0018$). Similarly to non-invasive measures from **Figure 5B**, no significant differences were found in intracardiac DFs between paroxysmal and persistent patients (**Figure 6B**) in median DF (5.0 ± 0.9 Hz paroxysmal vs 5.0 ± 0.9 Hz persistent, $p = 0.72$) nor in highest DF (5.8 ± 1.2 Hz paroxysmal vs 5.6 ± 0.9 Hz persistent, $p = 0.27$).

DISCUSSION

In this study, simultaneous intracardiac and non-invasive measures of atrial activation rate in AF were compared in a

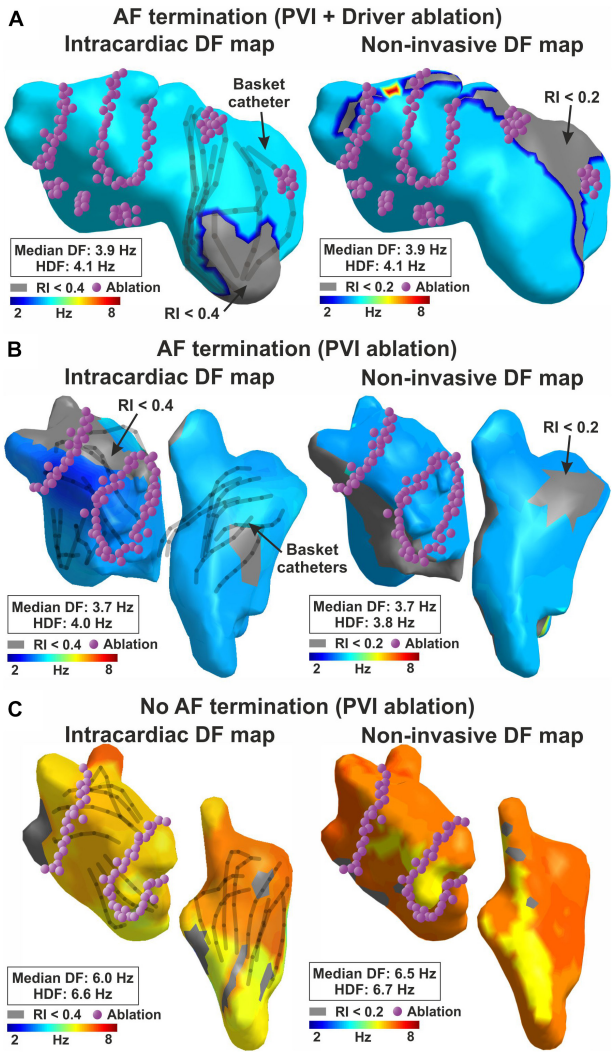

FIGURE 4 | Dominant frequency maps and acute AF termination. Intracardiac (left) and non-invasive (right) DF map for **(A)** a patient with acute AF termination during guided ablation; **(B)** a patient with acute AF termination during PVI ablation; **(C)** no acute AF termination during PVI ablation.

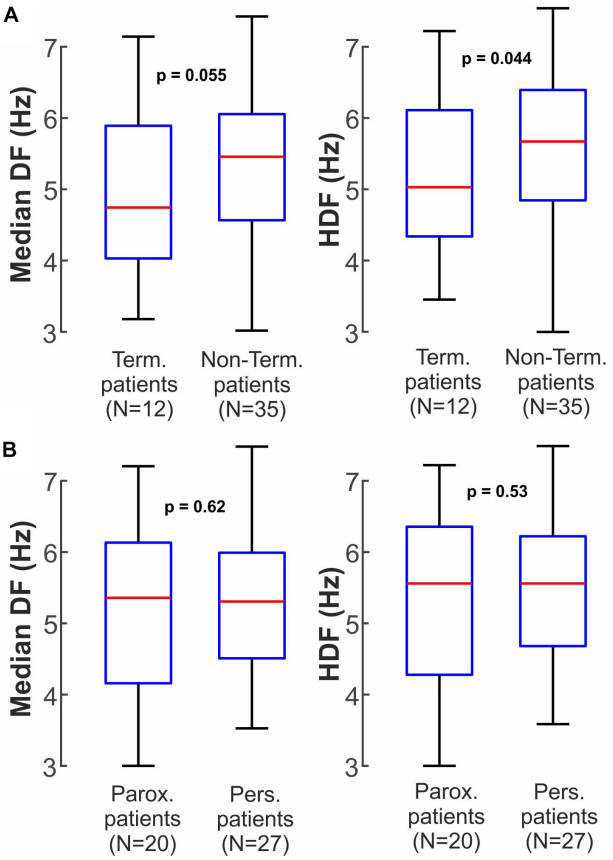

FIGURE 5 | Non-invasive clinical Dominant Frequency measures between different patient groups. **(A)** Median DF and HDF for patients in which ablation did or did not terminate AF. **(B)** Median DF and HDF for paroxysmal and persistent AF patients.

cohort representing diverse clinical types of AF. We found agreement between intracardiac and non-invasive measures of dominant frequency during AF, that was dramatically improved by secondary markers of stability such as regularity index. We identified spectral signatures, or 'phenotypes' for patients who did and did not achieve the clinical outcome of the acute AF termination by ablation. Future work should extend this to endpoints such as long-term freedom from arrhythmias, and compare these results using different filtering strategies.

Dominant Frequency and Atrial Fibrillation Management

Optical mapping of explanted hearts shows that atrial activation rate may play a fundamental role in maintaining AF (Kalifa et al., 2006; Filgueiras-Rama et al., 2012). In many studies, regions of higher activation rate appeared to drive fibrillatory activity in the rest of atrial tissue, and in some studies their ablation terminated AF (Sanders et al., 2005; Atienza et al., 2014). Of note, this was found in patients with paroxysmal AF but not those with persistent AF.

Electrical remodeling favoring progression of AF from paroxysmal to persistent then permanent may be linked with an increase in atrial activation rate (Martins et al., 2014). Therefore, patients presenting with lower DF measurements on the ECG have been linked with better long-term outcome of ablation procedures (Murase et al., 2020). Therapy based on the identification and ablation of fastest activated regions based on intracardiac estimation of DFs have been shown to be equivalent to pulmonary vein ablation (Atienza et al., 2014) particularly in relatively early paroxysmal AF.

Comparing the findings of this study to the prior literature, therefore, one could conclude that both lower global DF measurements and the existence of DF gradients within the atria can simultaneously predict ablation success. Further studies are needed to investigate whether previously reported DF gradients may be exaggerated by the use of adenosine, which is known to

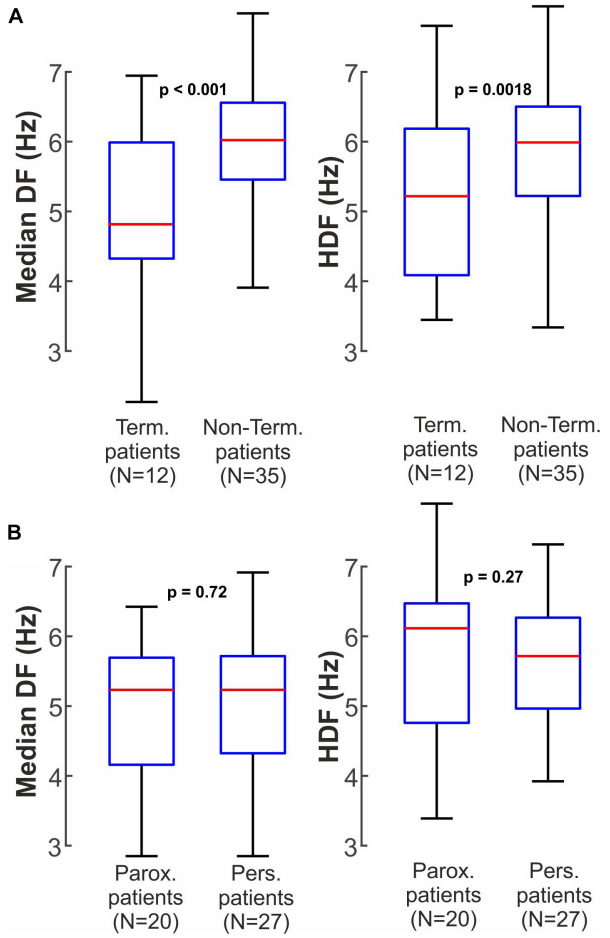

FIGURE 6 | Intracardiac clinical Dominant Frequency measures between different patient groups. **(A)** Median DF and HDF for patients in which ablation did or did not terminate AF. **(B)** Median DF and HDF for paroxysmal and persistent AF patients.

highlight differences in atrial activation rate (Atienza et al., 2006), and thus may not be expected in this study.

Early stages of AF exhibit lower activation frequencies and less complex propagation patterns. Notably, DF may better discriminate acute outcome in patients with persistent AF than paroxysmal AF. This supports differential electrical substrate remodeling detectable by DF, in which earlier AF (paroxysmal) show lower activation frequencies and less complex propagation than later stage AF. Lower activation frequency (longer cycle length) corresponds to larger wavelength and therefore a smaller number of co-existing wave-fronts (Kneller et al., 2005). These findings agree with other studies that lower complexity measured as number of different AF reentrant drivers correlates with better ablation outcomes (Haissaguerre et al., 2014; Rodrigo et al., 2020).

Non-invasive Identification of AF Activation Rate

Electrocardiographic imaging has been used to non-invasively map electrical activity of the whole epicardium. Haissaguerre et al. (2014) used this technique in 103 persistent AF patients to guide the ablation procedure, showing acute termination rate of 75% for persistent and 15% for long-standing AF patients, and showing that the number of targeted regions was related to the degree of AF progression, and inversely related to the probability of AF termination. These results agree with our findings.

Electrocardiographic imaging may be more robust in classifying AF patients than in quantifying and mapping specific propagation patterns in AF. Recent studies raise methodologic questions on the technical ability of ECGI to reconstruct cardiac electrical activity. Duchateau et al. showed that local activation time diverges between non-invasive and catheter-based epicardial recording (Duchateau et al., 2018). Methodologic factors such as bipolar vs. unipolar recordings, or biophysical limitations of the inverse resolution may prevent signals reconstructed by ECGI from having temporal and/or spatial precision that accurately represents local activations to reproduce isochronal maps (Rodrigo et al., 2017b; Rudy, 2019). Our findings show that non-invasively acquired frequency organization may be used to improve the accuracy of non-invasive cardiac mapping of AF. DF analysis in AF is intrinsically more stable than activation times, since it does not depend on a single fiducial point (activation time) to define a series of isochrones for activation or phase mapping. Frequency mapping summarizes a series of temporal voltage distributions in a single DF value, and thus should be more robust to biophysical limitations of the inverse problem than activation time. This was reported in previous studies in which we found that displacements and rotations greatly reduced agreement of inverse-solution computed signals with original signals, yet preserved frequency information as the concordance of the HDF region remained almost stable (Rodrigo et al., 2017a).

We found that spectral organization indicated by the Regularity Index (RI) is a useful index of the reliability of a specific estimated frequency. Lower RI implies lower energy of that DF peak, and filtering out such peaks improved the accuracy of non-invasive estimates. Low RI may result from factors that indicate non-local activity, including far field contributions, ventricular artifacts, low electrode contact or electrical noise. Local mechanisms such as wave fractionation or competing AF mechanisms may also produce low RI. Previous findings of our group and others suggest that intracardiac DF measurements can be affected by far-field contributions particularly when the basket electrodes are at a distance from the atrial wall (Martinez-Mateu et al., 2019, 2018). In the present study, we used bipolar recordings in order to diminish such far-field artifacts.

Clinical Perspective of Non-invasive AF Mapping

To date, non-invasive AF mapping through ECGI has been used to guide and plan AF ablation, specifically by identifying those atrial regions harboring reentrant drivers (Haissaguerre et al., 2014). This study broadens the application of non-invasive mapping to identify AF 'phenotypes' which may be relevant to acute and long-term success from therapy. Our results suggest that global measures such as median DF may also be valuable

markers of AF outcome, and future studies should evaluate whether this can be obtained from simpler approaches such as Body Surface Potential Maps or even the classical ECG. The current high resolution ECGI approach may be ultimately needed to classify long-term outcomes, a focus of ongoing studies, and to improve clinical phenotypes such as paroxysmal and persistent AF. Non-invasive activation rate mapping of AF may also help to tailor therapies including drugs to electrical phenotypes detected in specific patients. Clearly, prospective clinical trials are needed to test each of these hypotheses.

Limitations

Results from this paper were obtained with patients from 2 different institutions and under different AF therapies (PVI and guided ablation) and demographic differences. Nevertheless, results obtained for non-invasive DF mapping were consistent between and within each cohort, showing the robustness of non-invasive atrial activation rate mapping in different types of AF patients: paroxysmal, persistent, long-standing and valvular AF. On the other hand, the specific thresholds we used for RI filtering may differ in other cohorts. Finally, long-term clinical results of ablation in these patients vary with different ablation protocols. We selected AF termination as it is a common acute endpoint for ablation, and because it is independent on differences in post-ablation medications, long-term lesion recovery, drug adherence and AF progression.

CONCLUSION

Non-invasive characterization of atrial rate in AF, filtered by spectral measures of organization, identifies regional activation rates on intracardiac mapping. Non-invasive analysis could provide a mechanistic basis for clinical phenotypes such as patients who are likely to experience AF termination by ablation, or ultimately those who may experience long-term arrhythmia freedom from ablation or drug therapy.

DATA AVAILABILITY STATEMENT

The raw data supporting the conclusions of this article will be made available by the authors, without undue reservation.

ETHICS STATEMENT

The studies involving human participants were reviewed and approved by Stanford Hospital, Hospital General Universitario Gregorio Marañon. The patients/participants provided their written informed consent to participate in this study.

AUTHOR CONTRIBUTIONS

Only those who have made an important contribution to the study and are thoroughly familiar with the primary data are included as authors, and all authors are responsible for the contents and have read and approved the manuscript and conform to the Uniform Requirements for Manuscripts Submitted to Biomedical Journals published in Annals of Internal Medicine 1997; 126:36–47.

FUNDING

This work was supported in part by: Generalitat Valenciana Grants (APOSTD/2017 and APOSTD/2018) and projects (GVA/2018/103); the National Institutes of Health (R01 HL85537; R01 HL149134).

SUPPLEMENTARY MATERIAL

The Supplementary Material for this article can be found online at: https://www.frontiersin.org/articles/10.3389/fphys.2020.611266/full#supplementary-material

REFERENCES

Atienza, F., Almendral, J., Moreno, J., Vaidyanathan, R., Talkachou, A., Kalifa, J., et al. (2006). Activation of inward rectifier potassium channels accelerates atrial fibrillation in humans: evidence for a reentrant mechanism. *Circulation* 114, 2434–2442. doi: 10.1161/CIRCULATIONAHA.106.633735

Atienza, F., Almendral, J., Ormaetxe, J. M., Moya, A., Martínez-Alday, J. D., Hernández-Madrid, A., et al. (2014). Comparison of radiofrequency catheter ablation of drivers and circumferential pulmonary vein isolation in atrial fibrillation: a noninferiority randomized multicenter RADAR-AF trial. *J. Am. Coll. Cardiol.* 64, 2455–2467. doi: 10.1016/j.jacc.2014.09.053

Botteron, G. W., and Smith, J. M. (1996). Quantitative assessment of the spatial organization of atrial fibrillation in the intact human heart. *Circulation* 93, 513–518. doi: 10.1161/01.cir.93.3.513

Cluitmans, M. J. M., Bonizzi, P., Karel, J. M. H., Das, M., Kietselaer, B. L. J. H., de Jong, M. M. J., et al. (2017). In vivo validation of electrocardiographic imaging. *JACC Clin. Electrophysiol.* 3, 232–242. doi: 10.1016/j.jacep.2016.11.012

de la Torre Costa, J., Guillem, M. S., Climent, A. M., and Rodrigo, M. (2016). "Medida de la frecuencia dominante en registros eléctricos auriculares mediante filtrado convolucional," in *Proceedings of the Annual Congress of the Spanish Society of Biomedical Engineering*, Valencia, 290–293.

Duchateau, J., Sacher, F., Pambrun, T., Derval, N., Chamorro-Servent, J., Denis, A., et al. (2018). Performance and limitations of noninvasive cardiac activation mapping. *Heart Rhythm* 16, 435–442. doi: 10.1016/j.hrthm.2018.10.010

Figuera, C., Suárez-Gutiérrez, V., Hernández-Romero, I., Rodrigo, M., Liberos, A., Atienza, F., et al. (2016). Regularization techniques for ECG imaging during atrial fibrillation: a computational study. *Front. Physiol.* 7:466. doi: 10.3389/fphys.2016.00466

Filgueiras-Rama, D., Martins, R. P., Mironov, S., Yamazaki, M., Calvo, C. J., Ennis, S. R., et al. (2012). Chloroquine terminates stretch-induced atrial fibrillation more effectively than flecainide in the sheep heart. *Circ. Arrhythm. Electrophysiol.* 5, 561–570. doi: 10.1161/CIRCEP.111.966820

Guillem, M. S., Climent, A. M., Millet, J., Arenal, Á, Fernández-Avilés, F., Jalife, J., et al. (2013). Noninvasive localization of maximal frequency sites of atrial fibrillation by body surface potential mapping. *Circ. Arrhythm. Electrophysiol.* 6, 294–301. doi: 10.1161/CIRCEP.112.000167

Haissaguerre, M., Hocini, M., Denis, A., Shah, A. J., Komatsu, Y., Yamashita, S., et al. (2014). Driver domains in persistent atrial fibrillation. *Circulation* 130, 530–538. doi: 10.1161/CIRCULATIONAHA.113.005421

Hansen, B. J., Zhao, J., Csepe, T. A., Moore, B. T., Li, N., Jayne, L. A., et al. (2015). Atrial fibrillation driven by micro-anatomic intramural re-entry revealed by

simultaneous sub-epicardial and sub-endocardial optical mapping in explanted human hearts. *Eur. Heart J.* 36, 2390–2401. doi: 10.1093/eurheartj/ehv233

Honarbakhsh, S., Hunter, R. J., Ullah, W., Keating, E., Finlay, M., and Schilling, R. J. (2019). Ablation in persistent atrial fibrillation using stochastic trajectory analysis of ranked signals (STAR) mapping method. *J. Am. Coll. Cardiol. E.P.* 5, 817–829. doi: 10.1016/j.jacep.2019.04.007

Kalifa, J., Tanaka, K., Zaitsev, A. V., Warren, M., Vaidyanathan, R., Auerbach, D., et al. (2006). Mechanisms of wave fractionation at boundaries of high-frequency excitation in the posterior left atrium of the isolated sheep heart during atrial fibrillation. *Circulation* 113, 626–633. doi: 10.1161/CIRCULATIONAHA.105.575340

Kneller, J., Kalifa, J., Zou, R., Zaitsev, A. V., Warren, M., Berenfeld, O., et al. (2005). Mechanisms of atrial fibrillation termination by pure sodium channel blockade in an ionically-realistic mathematical model. *Circ Res.* 96, e35–e47. doi: 10.1161/01.RES.0000160709.49633.2b

Li, X., Salinet, J. L., Almeida, T. P., Vanheusden, F. J., Chu, G. S., Ng, G. A., et al. (2017). An interactive platform to guide catheter ablation in human persistent atrial fibrillation using dominant frequency, organization and phase mapping. *Comput. Methods. Programs Biomed.* 141, 83–92. doi: 10.1016/j.cmpb.2017.01.011

Martinez-Mateu, L., Romero, L., Ferrer-Albero, A., Sebastian, R., Matas, J. F. R., Jalife, J., et al. (2018). Factors affecting basket catheter detection of real and phantom rotors in the atria: a computational study. *PLoS Comput. Biol.* 14:e1006017. doi: 10.1371/journal.pcbi.1006017

Martinez-Mateu, L., Romero, L., Saiz, J., and Berenfeld, O. (2019). Far-field contributions in multi-electrodes atrial recordings blur distinction between anatomical and functional reentries and may cause imaginary phase singularities_a computational study. *Comput. Biol. Med.* 108, 276–287. doi: 10.1016/j.compbiomed.2019.02.022

Martins, R. P., Kaur, K., Hwang, E., Ramirez, R. J., Willis, B. C., Filgueiras-Rama, D., et al. (2014). Dominant frequency increase rate predicts transition from paroxysmal to long-term persistent atrial fibrillation. *Circulation* 129, 1472–1482. doi: 10.1161/CIRCULATIONAHA.113.004742

Miller, J. M., Kalra, V., Das, M. K., Jain, R., Garlie, J. B., Brewster, J. A., et al. (2017). Clinical benefit of ablating localized sources for human atrial fibrillation: the Indiana University FIRM registry. *J. Am. Coll. Cardiol.* 69, 1247–1256. doi: 10.1016/j.jacc.2016.11.079

Murase, Y., Inden, Y., Shibata, R., Yanagisawa, S., Fujii, A., Ando, M., et al. (2020). The impact of the dominant frequency of body surface electrocardiography in patients with persistent atrial fibrillation. *Heart Vessels* 35, 967–976. doi: 10.1007/s00380-020-01563-7

Pedrón-Torrecilla, J., Rodrigo, M., Climent, A. M., Liberos, A., Pérez-David, E., Bermejo, J., et al. (2016). Noninvasive estimation of epicardial dominant high-frequency regions during atrial fibrillation. *J. Cardiovasc. Electrophysiol.* 27, 435–442. doi: 10.1111/jce.12931

Rodrigo, M., Climent, A. M., Hernández-Romero, I., Liberos, A., Baykaner, T., Rogers, A. J., et al. (2020). Noninvasive assessment of complexity of atrial fibrillation: correlation with contact mapping and impact of ablation. *Circ. Arrhythm. Electrophysiol.* 13:e007700. doi: 10.1161/CIRCEP.119.007700

Rodrigo, M., Climent, A. M., Liberos, A., Fernández-Avilés, F., Berenfeld, O., Atienza, F., et al. (2017a). Highest dominant frequency and rotor positions are robust markers of driver location during noninvasive mapping of atrial fibrillation: a computational study. *Heart Rhythm* 14, 1224–1233. doi: 10.1016/j.hrthm.2017.04.017

Rodrigo, M., Climent, A. M., Liberos, A., Fernández-Avilés, F., Berenfeld, O., Atienza, F., et al. (2017b). Technical considerations on phase mapping for identification of atrial reentrant activity in direct- and inverse-computed electrograms. *Circ. Arrhythm. Electrophysiol.* 10:e005008. doi: 10.1161/CIRCEP.117.005008

Rodrigo, M., Guillem, M. S., Climent, A. M., Pedrón-Torrecilla, J., Liberos, A., Millet, J., et al. (2014). Body surface localization of left and right atrial high-frequency rotors in atrial fibrillation patients: a clinical-computational study. *Heart Rhythm* 11, 1584–1591. doi: 10.1016/j.hrthm.2014.05.013

Rudy, Y. (2019). Letter to the Editor-ECG imaging and activation mapping. *Heart* 16, e50–e51. doi: 10.1016/j.hrthm.2019.02.001

Sanders, P., Berenfeld, O., Hocini, M., Jaïs, P., Vaidyanathan, R., Hsu, L. F., et al. (2005). Spectral analysis identifies sites of high-frequency activity maintaining atrial fibrillation in humans. *Circulation* 112, 789–797. doi: 10.1161/CIRCULATIONAHA.104.517011

Skanes, A. C., Mandapati, R., Berenfeld, O., Davidenko, J. M., and Jalife, J. (1998). Spatiotemporal periodicity during atrial fibrillation in the isolated sheep heart. *Circulation* 98, 1236–1248. doi: 10.1161/01.cir.98.12.1236

Swartz, M. F., Fink, G. W., Lutz, C. J., Taffet, S. M., Berenfeld, O., Vikstrom, K. L., et al. (2009). Left versus right atrial difference in dominant frequency, K(+) channel transcripts, and fibrosis in patients developing atrial fibrillation after cardiac surgery. *Heart Rhythm* 6, 1415–1422. doi: 10.1016/j.hrthm.2009.06.018

Yushkevich, P. A., Piven, J., Hazlett, H. C., Smith, R. G., Ho, S., Gee, J. C., et al. (2006). User-guided 3D active contour segmentation of anatomical structures: significantly improved efficiency and reliability. *Neuroimage* 31, 1116–1128. doi: 10.1016/j.neuroimage.2006.01.015

Conflict of Interest: MR, IH-R, and AL: equity from Corify Care SL. SN: compensation for services from up to date, Abbott Laboratories, American College of Cardiology Foundation. Intellectual property rights from University of California Regents and Stanford University. Grant support from the National Institutes of Health (R01 HL83359, R01 HL149134, and K24 HL103800).

The remaining authors declare that the research was conducted in the absence of any commercial or financial relationships that could be construed as a potential conflict of interest.

Advantages of publishing in Frontiers

OPEN ACCESS
Articles are free to read for greatest visibility and readership

FAST PUBLICATION
Around 90 days from submission to decision

HIGH QUALITY PEER-REVIEW
Rigorous, collaborative, and constructive peer-review

TRANSPARENT PEER-REVIEW
Editors and reviewers acknowledged by name on published articles

Frontiers
Avenue du Tribunal-Fédéral 34
1005 Lausanne | Switzerland

Visit us: www.frontiersin.org
Contact us: frontiersin.org/about/contact

REPRODUCIBILITY OF RESEARCH
Support open data and methods to enhance research reproducibility

DIGITAL PUBLISHING
Articles designed for optimal readership across devices

FOLLOW US
@frontiersin

IMPACT METRICS
Advanced article metrics track visibility across digital media

EXTENSIVE PROMOTION
Marketing and promotion of impactful research

LOOP RESEARCH NETWORK
Our network increases your article's readership